Investigation of the Effects of High Pressure Pulses on Biological Samples

Chiara Bo

Imperial College London

Department of Physics

This dissertation is submitted for the degree of Doctor of Philosophy

Abstract

The increase in survivability in modern conflict has been accompanied by an increase in casualties with multiple and complex blast injuries which are associated with long term complications such as heterotopic ossification. Improving treatments for these complications requires the development of a cellular and molecular understanding of the effects of blast on live biological samples which in the past has been limited by the lack of experimental capabilities.

This thesis describes the development and characterisation of experimental platforms to study the effects of high intensity pressure waves on cells and tissues. A confined Split Hopkinson Pressure Bar (SHPB) system has been developed, allowing cells in suspension or in a monolayer to be subjected to pressure waves in the order of tens of MPa and duration of hundreds of microseconds. The confinement chamber has been designed to enable recovery of the biological samples for cellular and molecular analysis, such as cell survivability, viability, metabolic activity and morphological changes post compression.

The SHPB platform, coupled with quasi-static experiments, has also been used to determine stress-strain curves of porcine skin tissue samples under uniaxial compression at low, medium and high strain rates. Three phenomenological models have been used to fit the experimental data at different strain rates and the results compared. The recovered samples have been examined using histological techniques to study morphological changes induced by uniaxial compression. Finally, a shock tube-bio set up has been developed and characterised to replicate primary blast damage on cell monolayers by generating single air blast in the order of kPa and few milliseconds duration. This platform permits investigation of a different pressure-time regime compared to the SHPB system and to analyse post-traumatic changes induced in biological samples.

To conclude, different experimental platforms have been successfully developed to study the effects of pressure pulses on biological samples.

Acknowledgments

Many are the people to thank. First of all I would like to express my gratitude to the supervisor of this research, Dr. Bill Proud, for his support, and to the Atomic Weapons Establishment for funding my research. I am very grateful to my co-supervisors, Dr. Kate Brown and Prof. Sara Rankin: they have provided assistance in numerous ways, being excellent scientific reference models and supporting me with constant encouragement. I wish to thank all the members of the Institute of Shock Physics, the Centre for Blast Injury Studies and the Rankin's group for assistance with the experiments and for their advice and scientific contributions which are much appreciated. I am also grateful to the technicians of Imperial College London and the Surfaces, Microstructure and Fracture Group at the Cavendish Laboratory for their help with a great many practical matters in experimental set-up. I would also like to acknowledge Prof. A. Williams who provided me with the opportunity to conduct the experiments presented in chapter 6.

A big thanks to my friend Emi and Lara, who patiently listened to my struggles through this journey. Thanks to Seb and Andrea for our lunch breaks, and to the Belly Dance society who kept my social life somehow active in the past three years.

The biggest thank goes to my husband Vinicio, no need to explain why.

Contents

List of Figures

List of Tables

List of Symbols

Chapter 2 and 3

C_0	sound velocity
u	displacement
E_B	bar Young's modulus
ρ	density
ε	strain
ε_i	incident strain
ε_r	reflected strain
ε_t	transmitted strain
$\dot{\varepsilon}$	strain rate
L_S	specimen length
A	surface area (subscript B for bar, S for specimen)
F	force
σ	stress
σ_x	longitudinal stress
σ_r	radial stress
P	pressure
Z	mechanical impedance
z	specific mechanical impedance (Z/A)
ω_0	radial frequency
C_k	wave velocity of the k_{th} component
Λ_k	wave length of the k_{th} component
r	bar radius
Φ_k	phase of the k_{th} component
Δt	transit time
Δx	dispersion correction distance / gauges stand off distance
v_0	striker impact velocity
t_L / τ_P	impact pulse duration
V	voltage
$\overline{V}$	average voltage of impact pulse
k	SHPB calibration parameter
b	SHPB calibration parameter
d	bar diameter
SNR	signal to noise ratio
Re	Reynold's number
μ	dynamic viscosity coefficient

D	hydraulic diameter
τ_S	specimen transit time
R	adimensional parameter for stress equilibrium
b/a	outer/inner radial ratio
ε_θ	hoop strain
σ_θ	hoop stress
GF	gauge factor
ΔR	change in resistance
R_0	nominal resistance
v	velocity of bar/specimen interface
l	instantaneous sample length
E_C	chamber Young's modulus
R_i	chamber's inner radius
R_o	chamber's outer radius
ς	deviation from expected values
I_P	pressure impulse
Chapter 5	
W_S	shock velocity
H	entalpy
γ	specific heat ratio
R	universal gas constant
T	temperature
M	Mach number
a	speed of sound in gas
ν	gas particle velocity
Chapter 6	
W	energy potential
λ_k	principal stretches
$\overline{\lambda_k}$	principal deviatoric stretches
μ_i	shear parameters
α_i	exponential parameters
D_i	bulk parameters
σ_k	principal stresses
p	static pressure
C_1 / C_2	material constants
b	strain stiffening parameter
F	force
A	surface area
J_m	limited chain extensibility parameter
k	material elastic constant
η	damping coefficient
$\dot{\varepsilon}$	strain rate
σ_{ENG}	engineering stress
σ_{TRUE}	true stress

Chapter 1

Introduction

1.1 Motivation and objectives

Blast injury is a hallmark of modern military conflit and treatment of the wounds in survivors represent a huge clinical challenge. The use of improvised explosive devices (IEDs) and technological improvements in equipment, aimed at mitigating the effects of blast, have resulted in a change in the pattern of injuries seen in survivors [1]. Specifically, there has been an increase of survivors with multiple extremity injuries, with a distinct correlation between injury patterns observed and the environment in which they were sustained [2]. In addition, the high pressure pulses and high strain rate deformation of hard and soft tissues from the blast results in injuries and tissue dysfunction uncommon in civilian injuries.

Understanding the damage that high-intensity pressure waves induce in human tissues is a critical step towards improving the treatment of blast injury patients. Development of appropriate experimentally-based models for this type of traumatic damage is needed as a mean of providing fundamental information about cellular and molecular processes affected by the blast wave. Moreover, simplified blast injury models could facilitate studies correlating biological outcomes with blast parameters to define tolerance criteria. The difficulties in handling live biological samples and the lack of appropriate equipment have limited the research on the effects of pressure waves on biological tissues.

The main objective of this project was to study injury processes induced by high-pressure

waves on live biological samples at a cellular and tissue level.

In this context the key project aims were:

- to develop and characterize experimental apparati for subjecting live biological samples to compression waves representative of blast injuries;
- to assess pressure wave-induced damage at the cellular level by studying the viability and functional responses of live biological samples subjected to the pressure pulse;
- to characterise the influence of strain rate on the mechanical response and morphological damage of a soft biological tissue.

1.2 Thesis structure

In chapter 2 a review of the physics of blast waves, their effects on the human body and current models to study blast injuries are presented with particular focus on *in vitro* models.

In chapter 3 a modified Split Hopkinson Pressure Bar (SHPB) system designed for dynamic cell pressurisation experiments is presented. The SHPB is a mechanical apparatus composed of a series of metal bars which are subjected to stress wave propagation due to the impact of a projectile. This system is generally used for characterisation of the dynamic stress-strain response of materials. The modified apparatus devised for live biological samples is critically assessed, the data analysis software is explained in detail and the necessity of dispersion correction is investigated. Finally values of peak pressure and impulsive pressurisation are summarised for the cell pressurisation experiments.

Chapter 4 describes the biological outcomes of high-intensity pressure pulses experiments on cell cultures. Cellular damage is investigated in terms of cell viability for different cell suspensions, as a function of cell density, peak pressure and impulsive pressurisation. Functional studies on the effects of pressure pulses on mesenchymal stem cells are also reported. Cell damage increased as a function of peak pressure and impulsive pressurisation, and the effects of blast conditioned medium on healthy cells suggest possible influence of blast-induced release of injury signals.

Chapter 5 presents the shock tube *in vitro* model to study primary blast injuries on adherent cells in culture. A shock tube is a device used to replicate blast waves in the laboratory; it generates a shock wave by bursting a diaphragm under the influence of high pressure. The shock tube system is briefly characterised and the set up used to determine the overpressure sensed by the biological samples is analysed. Preliminary experiments on the effects of overpressure on monolayers of mesenchymal stem cells are finally reported. In chapter 6 the mechanical properties of porcine skin tissue in compression are studied for different strain rates of loading. The material properties of skin samples harvested from different anatomical regions are investigated and three different hyperelastic models are compared to fit the stress-stretch curves experimentally obtained. Moreover, the potential of histological analysis of recovered samples to inform tissue deformation and damage is considered.

1.3 Statement of originality

This is to certify that, to the best of my knowledge, the content of this thesis is my own work. This thesis has not been submitted for any degree or other purposes. I certify that the intellectual content of this thesis is the product of my own work and that all the assistance received in preparing this thesis and sources have been acknowledged.

1.4 Publications

- Chiara Bo, Jens Balzer, Katherine A Brown, Stephen M Walley and William G Proud, Development of a chamber to investigate high-intensity compression waves upon live cell cultures, *The European Physical Journal Applied Physics* **55**(3), 31201: p1-p5, 2011.

- Chiara Bo, Jens Balzer, Mark Hahnel, Sara M Rankin, Katherine A Brown, and William G Proud, Cellular characterization of compression-induced damage in live biological samples, In *Proceedings of the Conference of the American Physical So-*

ciety Topical Group on Shock Compression of Condensed Matter, Chicago, Illinois, USA, June 26 - July 1, 2011, **1426**, 153-156.

- Katherine A Brown, Chiara Bo, Arul Ramasamy, Spiros Masouros, Nicolas Newell, Adam Hill, Jon Clasper, Anthony Bull, and William G Proud, Prospect for Studying How High-Intensity Compression Waves Cause Damage in Human Blast Injuries, In *Proceedings of the Conference of the American Physical Society Topical Group on Shock Compression of Condensed Matter, Chicago, Illinois, USA, June 26 - July 1, 2011*, **1426**, 131-134.

- C. Bo, J. Balzer, S. Godfrey, M. Francois, J. L. Saffell, S. M. Rankin, W. G. Proud, and K. A. Brown, Pressure pulse induced damage in live biological samples, In *EPJ Web of Conferences, 10th International Conference on the Mechanical and Physical Behavior of Materials under Dynamic Loading, Freiburg, Germany, 2012*, **26**, 03006: p1-p5.

- Bo, C., Newell, N., Nguyen, T-T. N., Butler, B., Wilgeroth, J., Balzer, J., Masouros, S. D., Bull, A. M. J., Phillips, A. T. M., Jardine, A. P., Williams, A., Rankin, S., Brown, K. A. & Proud, W.G., Understanding the Effects of Blast on Biological Systems, In *Proceedings of the 16^{th} Seminar on New Trends in Research of Energetic Materials, Czech Republic, 2013*, 52-65.

- C. Bo, A. Williams, S. M. Rankin, W.G. Proud, K.A. Brown, Integrated experimental platforms to study blast injuries: a bottom-up approach, submitted to *18th APS Topical Conference on Shock Compression of Condensed Matter Proceedings, Seattle, USA, 2013.*

- Katherine A Brown, Chiara Bo, Benjamin J Butler, Samuel Godfrey, Jens Balzer, Sara M Rankin, Jane Saffell Andrew P Jardine, Alun Williams and William G Proud, Applications of Hopkinson pressure bars for studying cells and tissues under blast injury conditions, submitted to *Phylosophical Transaction of the Royal Society - A*, 2013.

Chapter 2

Background

2.1 Blast waves

Blast waves usually originate from explosions, the rapid expansion of gas. The reaction products from the explosive or driving gas push against the surrounding ambient-pressure air and produces a pressure wave, known as the blast front. This pressure wave expands rapidly outward. This front increases the density of the air through which it passes, hence the pressure wave travels faster than in ambient-pressure air (velocity ≥ 330 m s^{-1}) [3]. The speed of the gas moving behind the blast front, in the so-called "blast wind", can be as high as 5555 m s^{-1} [5]. As the explosive gases continue to expand outwards, a period of relative low pressure develops (negative-pressure phase) as a result of the void created by the displaced air, before atmospheric pressure is re-established [4]. The general shape of the loading pulse for an ideal free field explosion, as shown in Fig. 2.1 A, can be described as a sharp rise to a peak blast overpressure, BOP, followed by an exponential decay. This is analytically described by the Friedlander waveform [5]:

$$P(t) = P_s(1 - t/t_0)^{(-bt/t_0)} \tag{2.1}$$

where P_s is the peak overpressure, t_0 is the duration of the positive pressure and b is a decay constant that governs the rate at which the pressure decreases. The explosive compression process generates a shock wave, which travels through the surrounding media at

a speed higher than the speed of sound in the uncompressed media, and that is characterized by a discontinuous and adiabatic jump in the state variables (e.g. pressure, density, temperature). A free-field shock wave expands in 3 dimensions, but can be approximated as a planar wave for far-field conditions. In the next section the governing relations for 1-D shock wave theory are summarised.

The duration, profile and peak pressure of a blast depend on the size, the nature and the container of the explosive charge. The presence of obstacles induces reflected waves which can complicate the pressure profile, increasing the energy associated with the blast overpressure [3], as shown in Fig. 2.1 A. In a cluttered urban or vehicle environment, a casualty will experience a number of waves, those directly arising from the charge and those reflected from a wide variety of surfaces and arriving from different directions [6].

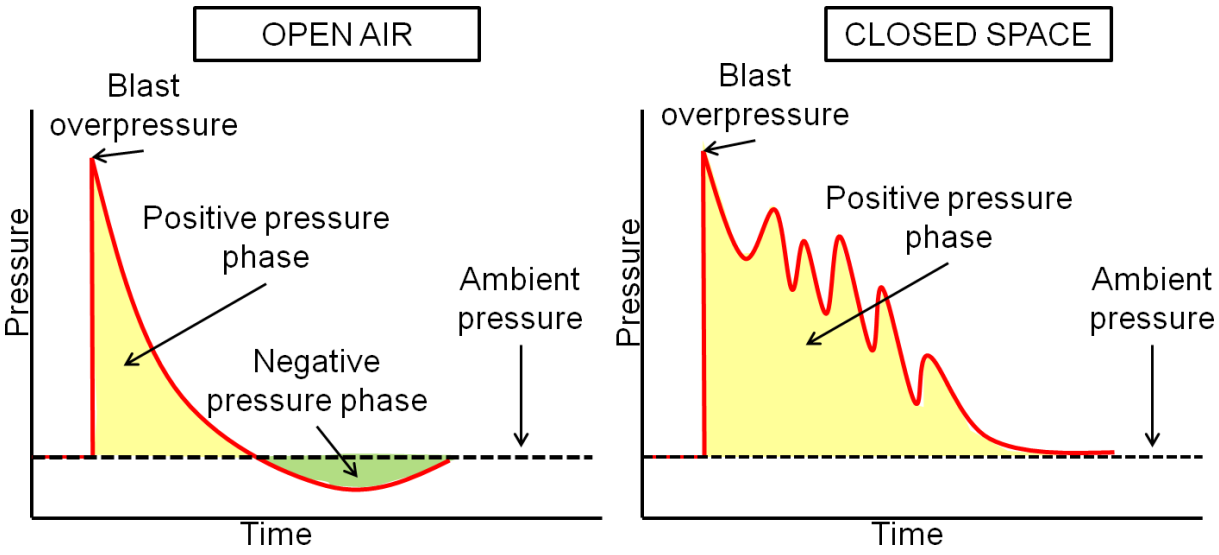

Figure 2.1: **Ideal shape of blast waves.** Left, generalised open air pressure time profile of a blast wave: the graph shows an initial instantaneous pressure rise followed by the development of an underpressure wave. Right, generalised enclosed space pressure time profile of a blast wave: the initial pressure rise is followed by a complex pressure curve characterised by multiple peaks attributable to reflected pressure waves.

The blast loading, described as a force per unit area, is usually not the same on all parts of an object such as a person or a building. The pressure exerted by the blast wave on a structure depends upon its geometry and its orientation. Moreover, factors that will determine the level of damage caused by a blast wave are the distance from the explosive and the energy coupling. Intuitively, the further from the explosive the less energy will be

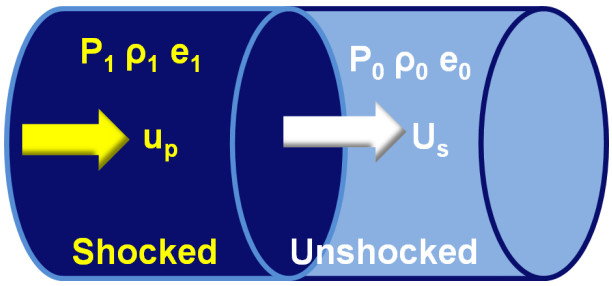

Figure 2.2: **One dimensional shock wave in a medium** Control volume used for derivation of Rankine-Hugoniot jump conditions showing the ambient state (0) and the shocked state (1)

transferred to the body either reducing brisance, stress transmission, and heave. Scaling equations have been developed to relate the effects of large explosive charges over tens of meters to those of small charges at close range. These relations depend on the mass of the charge and on the cube of the distance between the charge and the target, which represent the expansion of the volume over which the blast wave energy is dispersed [6]. Energy coupling, hence stress transmission, depends mainly on two material properties: strength and mechanical impedance [3]. The first one is a measure of the maximum stress that the material can sustain before it permanently deforms, while the second one is a measure of how much a material resists motion when subjected to a given force and is defined as the product of density and sound speed of the material [6].

2.2 Shock wave theory

A shock wave is a traveling wavefront across which a discontinuous, adiabatic jump in state variables takes place. Shock wave theory was developed in the mid to late XIX century, the main contributors were Stokes, Rayleigh, Rankine and Hugoniot [7]. Under the assumption of hydrodynamics, the material is regarded as a fluid which has no strength nor resistance to shear deformation, with body forces such as gravity negligible and in absence of phase changes, the governing relations for 1-D shock wave theory are described by the Rankine-Hugoniot equations, which describe changes in the state variables across a shock front. If we consider a control volume in which a shock front is moving with shock velocity U_s, as shown in Fig. 2.2, the conservation relations, assuming the material in the

unshocked state is stationary, can be expressed as:

$$\text{Conservation of Mass} \qquad \rho_0 U_s = \rho_1 (U_s - u_p) \tag{2.2}$$

$$\text{Conservation of Momentum} \qquad P_1 - P_0 = \rho_0 U_s u_p \tag{2.3}$$

$$\text{Conservation of Energy} \qquad e_1 - e_0 = \frac{1}{2}(P_1 + P_0)(\frac{1}{\rho_0} - \frac{1}{\rho_1}) \tag{2.4}$$

where u_p, ρ, P and e are the particle velocity, density, pressure and energy per unit mass and the indexes 0 and 1 represent the unshocked and shocked states respectively. If we consider the case of a shock front moving in an ideal gas (a gas with constant specific heats), the conservation equations can be expressed in terms of Mach number M, temperature T, specific heat ratio γ, pressure and density. The Mach number M is defined as the ratio of the velocity of a flow in the gas and the local speed of sound a, which for the gas in the unshocked state equals to $M_0 = \frac{U_s}{a_0}$. The sound speed in the unshocked gas is defined as $a_0 = \sqrt{\gamma R T_0}$ where R is the universal gas constant per unit mass of gas. Hence, the pressure, temperature and density in the shock front of an ideal gas can be calculated knowing the pressure, temperature and density in the unshocked state and the shock velocity using the equations:

$$\frac{P_1}{P_0} = \frac{2\gamma M_0^2 - (\gamma - 1)}{(\gamma + 1)} \tag{2.5}$$

$$\frac{\rho_1}{\rho_0} = \frac{M_0^2(\gamma + 1)}{(\gamma - 1)M_0^2 + 2} \tag{2.6}$$

$$\frac{T_1}{T_0} = \frac{(\gamma M_0^2 - \frac{\gamma - 1}{2})(\frac{M_0^2(\gamma - 1)}{2} + 1)}{(\frac{\gamma + 1}{2})^2 M_0^2} \tag{2.7}$$

This equations are particularly useful in a laboratory context when 1-D experiments want to be designed to replicate blast conditions seen in the battlefield, for example using a shock tube.

2.3 Blast injuries

2.3.1 Past & current history

The effects of blast injuries on soldiers killed by an explosion were first reported by Rusca [8] in 1914, who later identified in animal experiments the cause of death as pulmonary embolism. Since lethal injuries were usually not visible, casualties from WWI were thought to be affected by nervous system disorders. The increased number of casualties in WWII due to explosions highlighted the need for research into blast injuries [8]. After WWII, particularly in the USA, biological effects of blast events were investigated: reports from the Defense Atomic Support Agency were published that included attempts to define biomedical criteria for assessing blast-related hazards [9, 10]. In one of these reports [9] Clayton highlighted the importance of approaching the topic from both physically and biologically oriented points of view. Particularly he expressed the need: to define biologically relevant physical parameters and how these parameters quantitatively affect loading forces; to generate animal models to identify and quantify critical biological responses; and to study a variety of acute and chronic health problems associated with diagnosis, therapy, casualty care and rehabilitation of blast injury casualties. Since then considerable progress has been made, especially about the physical characterization of the blast events and the pathophysiology of life threatening blast injuries [11].

The casualties of bombings in recent conflicts are usually young people, in their 20's, early 30's, who experience long periods in hospital and require prolonged rehabilitation [12]. In current conflicts, in which IEDs pose the most prevalent single threat to troops in theater [1], extremities are the most frequently injured body region. Analysis of injury patterns in 53 IED-casualties a British field hospital in Iraq in 2006 indicated that 86.7% of injuries were sustained to the lower limbs [2]. This finding is also consistent with data presented by Owens *et al.* [13] who reported data describing the distribution of injuries from 1566 casualties with 6609 combat wounds from conflicts in Iraq sustained between 2001 and 2005. Table 1.1 summarizes their findings, which indicate that the highest number of injuries occur to the lower extremities. The low percentage of thorax wounds

Body region	% Injuries
Head	8%
Eyes	6%
Face	10%
Neck	3%
Thorax	6%
Abdomen	11%
Extremity	54%

Table 2.1: **Distribution of blast injuries per body region** Adapted from [13]

reported in Table 2.1 suggests that personnel protective equipment may be responsible for the lower incidence of injuries to this region of the body but this requires further investigation [13]. In addition, incidence levels of injury are reported by Ramasamy *et al.* for open field compared to in-vehicle injuries [14]. Ramasamy *et al.* [15] reviewed medical documentation and radiographs of surviving casualties injured by an explosive blast. They found a distinct correlation between the pattern of injury and the environment in which the explosion occurred. Casualties subjected to blast in enclosed spaces showed predominant tertiary injuries (described in section 2.3.2.3). These types of injuries arise from subjecting bone to external loads that results in the nucleation, multiplication and growth of micro-cracks that lead to fractures [16]. In the open space, casualties were mostly subejected to secondary fracture patterns, related to the fragments propelled by the explosion [15].

Of the limb injuries, soft tissue injuries are the most prominent (53%), followed by fractures (26%) [17]. In these terrible scenarios often the only available course of treatment is amputation. In a recent retrospective of study of US soldiers injured in Afghanistan and Iraq, over 950 soldiers have sustained a combat-related amputation [18]. While the majority of these combat-related amputations were reported to occur during acute treatment of injuries, more than 15% of amputations occured in later phases of treatment [18]. These amputations were possibly related to complications associated with these limb injuries that included a high incidence of infection, nerve injury, chronic pain and heterotopic ossification (HO; discussed in more detail in section 2.3.3). These factors hinder the process of tissue healing and rehabilitation. In particular HO is expected to affect up to 64% of patients, representing a significant source of disability [19].

2.3.2 Pathophysiology

2.3.2.1 Introduction

The physical processes involved in the body's response to a blast event are very complex. Due to the sudden increase in environmental pressure the body's external surface moves rapidly, the organs with high air content are compressed, and tissue damage occurs when the strength of the tissue is overcome [3]. Traumatic amputation of limbs occurs when casualties are located in the immediate vicinity of the explosive and penetrating injuries, fractures and burns add to an already tremendous scenario.

Peak overpressure in conjunction with its duration (impulse), the environment in which the explosion occurs (free field versus confined space), wave form, body mass and the proximity of the target to the explosions are amongst the factors that can influence the type of injuries produced [17]. Soft tissues in the human body have generally low strength and impedance which favours the energy coupling between the high pressure gases and the tissue, causing substantial damage. The principal damage mechanisms associated with blast events are due to the direct effects of the shock wave and the differential acceleration of body parts of different densities and sound speeds.

Blast injuries due to exploding missiles were first classified by Zuckerman [20] into four groups:

- **Primary blast injuries:** those resulting from exposure of the body to environmental pressure variations accompanying the blast wave;
- **Secondary blast injuries:** penetrating and non-penetrating injuries due to fragments/projectiles propelled by blast force;
- **Tertiary blast injuries:** caused by the acceleration of the entire body against mobile or fixed objects;
- **Quaternary blast injuries:** all other injuries not covered by the previous groups as chemical poisoning, burns, etc.

2.3.2.2 Primary blast injuries

Gas filled structures in the body are the most susceptible to primary blast mechanism. The sudden loading of a blast force distorts air-containing organs because the change in pressure happens so rapidly that there is insufficient time to allow equilibration of internal pressures in these organs to occur. The tympanic membrane is very commonly injured after a blast. However, this type of injury does not represent a marker for more serious primary blast injuries and it usually heals spontaneously [17]. In contrast, blast lung is a major cause of mortality for blast victims both at the scene of the explosion and among initial survivors. Blast waves impact upon the lung, which results in tearing, haemorrhage, contusion, and edema of lung tissues [21]. Primary injuries have been reported also in relation with the musculoskeletal system [15]: the blast wave interacts and transfer energy to tissues of different mechanical impedance causing shear and axial stresses which, if they exceed the tensile failure stress of the tissue, can cause fracture and lacerations. In the case of musculoskeletal system the most severe primary injuries are associated with traumatic amputations.

2.3.2.3 Secondary and tertiary blast injuries

The majority of injuries seen in survivors are thought to be secondary and tertiary blast-related injuries [17]. Secondary injuries include penetrating ballistic or blunt trauma injuries with associated laceration. These injuries are characterised by extensive wound contamination that increases the incidence of infection. Tertiary injuries include fracture and traumatic amputation. These injuries can occur throughout the body but are mainly reported to occur in the extremities [17].

Blast Traumatic Brain Injury (bTBI), usually caused by a penetrating or closed head injury, has been described as a classical example of secondary and tertiary blast injury [17, 20]. Recent studies on blast induced neurotrauma however, suggest that blast wave effects associated with primary blast injury [17] may also contribute to the development of bTBI [17]. These observations have led to the current view that coupled mechanisms contribute to the bTBI syndrome: brain tissue first responds to the blast

wave (primary mechanism); then, the head may also be penetrated by high speed fragments (secondary mechanism) and finally the acceleration of the body against surrounding objects can cause head trauma [22].

2.3.3 Complications

Post-traumatic effects of blast waves include recurrent infections [23], neurotrauma, post-traumatic stress disorder [24], trauma induced coagulopathy [25], and heterotopic ossification (HO) [19, 26], but the correlation of these complications with specific blast injury mechanisms is not well established. There is some evidence that primary blast injury mechanisms may play an important role in generating heterotopic ossification since this complication is rarely observed in civilian traumatic injuries [19].

HO consists of the formation of mature lamellar bone in non-osseous tissue. HO has been observed following trauma, surgical intervention to elbow or acetabular fractures, total hip arthroplasty, and/or neurologic injury [27]. A higher incidence of HO has been consistently reported in combat-related injuries compared to civilian trauma injuries [19]. A complete understanding of the etiology of HO does not exist. HO has been described as a pathological wound repair process and preliminary studies have focused on the identification and characterization of the progenitor cell population responsible for the initiation of ectopic bone lesions that occur as a result of extremity trauma [28]. Different progenitor cell lines have been suggested to play an important role in the initiation of HO and include mesenchymal stem cells (MSCs), multipotent progenitor cells (MPCs) [28,29] and progenitor cells of a vascular lineage [30]. Nesti *et al.* [29] isolated and cultured mesenchymal progenitor cells from debrided muscle from soldiers who had sustained traumatic injuries. This study also demonstrated that these cells had the potential to differentiate into osteoblasts, adipocytes and chondrocytes. In a related study, Jackson *et al.* [28] compared the osteogenic potential of MPCs and MSCs derived from traumatized muscle tissue. They observed that, although both cell lines showed the same osteoprogenitor phenotype and increase alkaline phosphatase (ALP) activity, under osteogenic induction, MPCs, unlike MSCs, showed a significant level of proliferation even when cultured in

osteogenic medium. Potter *et al.* [26], reported that MPCs cultured with wound effluent, without exposure to osteogenic induction media, did not show bone formation. These data suggest that a combination of factors including the recruitment of MPCs and MSCs in wounded tissues and the presence of osteogenic factors released by the trauma could contribute to the formation of ectopic bone in severely injured limbs.

It has been shown that HO is generally associated with inflammatory responses. The same study by Potter *et al.* [26] carried out on 24 high-energy wounded patients, quantified the amounts of cytokines and chemokines present in serum and wound effluent obtained from these individuals. In serum two cytokines and one chemokines, IL-6, IL-10 and human MPC-1 respectively, were upregulated compared to a control group. Of particular interest was the observed delay in the upregulation of IL-10. According to the authors, this delay suggests a persistent systemic inflammation in the wound region and that time-dependent disregulation of pro- and anti-inflammatory responses in a traumatized limb may play an important role in the development of HO.

2.4 Blast-related experimental studies

2.4.1 Animal/organ studies

Some attempts to estimate the tolerance of the human body to overpressure have been made, mainly using a range of animals. Richmond *et al.* [31] reported lethality curves for different animals as a function of overpressure and duration of the stimulus in open air experiments. From their calculations a stimulus of the duration of 400 ms with a peak overpressure of 600 psi would cause 99% lethality for mammals of 70 kg weight. The most important conclusion of their study related to the peak pressure/duration of the stimulus: the more gradual the rise time to the peak, the greater the tolerance to the stimulus; and an increase in body mass was generally associated with a higher rate of survival. In a more recent study by Bass *et al.* [32] a revised model for injury threshold was developed and new injury risk assessment curves were analysed. The results suggested an injury threshold level of few MPa for stimuli in the order of ms duration [32].

Lung damage has been studied in sheep using shock tubes. Non-lethal single or multiple blast exposures, showed pulmonary contusion in the form of minor petechial changes on the lung surface. At low peak pressures diffuse hemorrhaging involving almost 60% of the lung lobes was observed, and edema was present in lungs subjected to the highest sublethal peak pressures applied [33,34]. The authors also reported significant cardiopulmonary and blood gas changes that correlated with the level of blast exposure, and cardiac injury sustained, possibly related to the formation of air emboli or myocardial contusion. Similar types of experiments have also demonstrated damage to the central nervous system [35], the visual system and the gastrointestinal system [17]. Elsayed and Gorbunov [36] also observed evidence of oxidative stress arising from blast overpressure based upon depletion of antioxidants in blood from rats obtained 1 h after a single blast exposure of 62 kPa.
Traumatic brain injury (TBI) has also been investigated using shock tube-driven blast overpressure [37]. Particularly, Reneer *et al.* [37] investigated the primary effects of blast on brain tissue in rats subjected to peaks pressure ranging from 100-200 kPa. They observed enlarged brain surface vessels and hematomas, the latter appearing at peak pressures from 150 kPa.
Musculoskeletal tissue has also been investigated under blast overpressure in animal models. Goat hind limb bones were exposed to near field blast, 0.5 m source-target distance, and the fracture patterns were analyzed [38]. Femoral fractures were associated with high-axial forces, while tibial fractures were caused by bending stresses. The authors also described computer model of blast-related mass displacement of the body with movement of the limbs relative to the torso. This model indicated that direct shock wave coupling into a limb exposed to near-field blast was the primary mechanism for bone injury [38].

2.4.2 Cell-based studies

Blast injuries, as classified by Zuckerman [20], also result in damage to biological samples at a smaller length scale, *i.e.* at the cellular level.
Most of the blast-related cell-based studies found in literature focus on the tertiary type of injury in relation to TBI, where acceleration of the skull results in shear stresses applied

to the different brain tissues. In this case *in vitro* studies focus on mimicking shearing of tissues or cell monolayers, by stretching samples below level known to cause cellular structural failure [22]. The main findings of these studies are that the severity of cellular injury depends on both the magnitude of stress and the rate of application [39,40] and that the response of the cells to external stimuli depends on the mechanical properties of the cells, which can vary with the cell line used, the culture conditions etc [39]. Early studies on astrocytes by Ellis [41] suggested that cell death was not caused by cell lysis, but by mechanically initiated intracellular events. More recent studies on astrocytes, neuron and microglia show that when these cells are subjected to mechanical stresses they release the S100B protein and that exogenous S100B can contribute to the injury/repair process reducing delayed neuronal injury when added to the cultures at 6 or 24 h after injury [42]. Secondary blast injuries have been mimicked *in vitro* by scratching cells monolayers with a stylus, or by direct laceration of single cells using laser microsurgery [22].

In general, however, very little is known about primary blast effects at the cellular level. The only literature describing cellular damage due to transient pressure involves studies related to extracorporeal shock wave lithotripsy, or reports of a few laser-driven shock wave or shock tube systems designed to study cell injury. A summary of these studies, including a description of the techniques and the biological effects produced on cell cultures due to stress waves, are described below.

2.4.2.1 Extracorporeal shock wave treatment

Extracorporeal shock waves (ESW) are non-invasive acoustic waves applied as pulsed energy in medical applications. ESW treatment was first introduced as a non-invasive means of disintegrating kidney stones [43]. Typical parameters for shock waves used in lithotripsy applications are 35-120 MPa amplitude, 1-3 μs compression phase duration with a high energy density at the focal point up to 1 mJ mm^{-2} [43]. The use of ESW has further extended into orthopedics treatment for musculoskeletal disorders such as tendinopathies [44], and as a mean to improve fracture healing [43]. Lower energy densities are usually used for treatment of musculoskeletal disorders.

ESW can also cause damage to living tissues. Damage to biological tissues depends on the energy density used and on the rate of administration. The same acoustic energy administered with few pulses of high energy generates more extensive tissue damage compared to administering many low energy pulses [43]. In all organs that have been exposed to ESW treatment, the predominant effect observed has been damage to blood vessels that results in bleeding. Cardiac arrhythmia and nerve excitation have also been observed, the latter being also reproduced in *in vitro* studies [45]. In animal studies high intensity ESW have been shown to fracture rat bone, while lower intensity administration doses can stimulate osteogenesis [46].

At the cellular level ESW have been shown to cause damage and to induce other cellular and molecular processes such as the stimulation of osteoblast activity [47], haemoglobin release from erythrocytes [48], growth and differentiation of bone- marrow stromal cells [49]. Both *in vivo* and *in vitro* experiments suggest cavitation as the main mechanism of cellular damage and membrane permeabilization [50]. The precise mechanism is still not clear but bubble expansion, or collapse, and rebound are proposed. Along with cavitation, jetting of liquid has been postulated as source of cell injury [51]. Cell lysis, 5-95%, has been observed in cell suspensions subjected to shock waves and the level of lysis appears to depend upon the number of discharges administered and the accompanying energy density [43]. Cellular destruction and reduced viability has also been observed in suspended and immobilized cell cultures that have been subjected to ESW [51]. Cellular components such as the cell membrane and different organelles are also known to be affected by shock waves. Steinbach *et al.* [52] identified energy densities thresholds for different cell component, organelles and membranes, using laser scanning microscopy following specific fluorescence staining. In Table 1.2 are summarized the results of the study showing that the plasma membrane is the most sensitive cell component to ESW.

Specific effects of ESW upon membrane function and viability have also been studied in some detail. Transient cell membrane permeabilization due to shock waves have been demonstrated by internalization of molecules of different dimensions in the cell cytoplasm that correlated with shock wave administration [53]. Howard and Sturtevant [54] per-

Cellular Component	Damage Threshold mJ mm^{-2}	Identification Method
Plasma Membrane	0.12	Permeability to PI
Vimetin (cytoskeleton)	0.21	FITC-Vimetin antibody
Mitochondria	0.33	DIO staining
Nuclei	0.50	DAPI staining

Table 2.2: **Cellular components damaged by shock waves.** Adapted from [52]

formed experiments on thin polymeric membrane using ESW and identified two different effects as source of membrane failure: a direct mechanism due to rapid compression that results in shearing and tearing of inhomogeneous tissues and an indirect effect due to pressurization caused by bubble collapsing. A computer simulation of shock-induced damage in lipid bilayers suggests that in liquid shock front velocities below 3000 m s^{-1} do not cause permanent damage to the patch, while a strong correlation between shock velocity and damage is observed for values of shock velocity above this threshold [55]. These results represent a starting point in understanding cell membrane failure due to shock waves.

2.4.2.2 Laser-driven shock waves

Devices capable of using a laser to produce shock waves have also been shown to induce damage in tissues and cell cultures. Structural and functional damage has been reported in cells subjected to laser shock waves with a strong correlation between the level of cell damage and the stress gradient [56]. Also, different cell lines have shown different damage thresholds, with rapidly dividing cells being the more susceptible to shock wave damage [56].

In an interesting study by Kodama *et al.* [53], human promyelocytic cells were subjected to pressure waves generated with three different devices: two different laser-based instruments and one shock tube. The stimuli from the different devices differed both in peak pressure and in impulse duration, with the shock tube being the device capable of producing the longest stimulus. In this study, increased membrane permeabilization detected using fluorophore internalization, along with a decrease in cell viability,were observed only in cells subjected to the shock tube-generated pressure wave, which had peak pressures

and duration of approximately 11.6 MPa and 40 μs. The authors identified the impulse delivered as the driving parameter for determination of the threshold level of damage [53]. Sondén *et al.* [57] developed a laser-driven flyer plate technique to generate shock waves in monolayers of endothelial cells. They reported rupture of cell membranes and increased levels of cell debris localized to the area where the laser beam was focused. In this experimental configuration, the level of cell damage did not appear to be affected by differences in peak pressures, stimuli durations or the number of repetition of each stimulus. These observations led the authors to propose that cavitation was the key destructive mechanism inducing cells subjected to shock waves to lyse [57].

2.4.2.3 Shock tube

In the past few years shock tubes have been adapted to develop *in vitro* models of blast injuries [58–60]. These studies have focused on determining cellular injury thresholds and cellular and molecular changes induced by pressure stimuli on cell cultures relevant to TBI. The shock tube is used to generate a 1-D shock wave that travels in a gas medium, so modifications were necessary to subject live biological samples to the overpressure generated with this apparatus. Arun *et al.* [59] used tissue culture plates sealed with adhesive membranes to contain cell cultures during exposure, while Panzer *et al.* [58] designed a fluid-filled receiver that contains the living culture during the overpressure experiments. Both methods reported increased levels of delayed cellular injury associated with cellular samples subjected to blast overpressure. Moreover, other cellular mechanism such as membrane permeabilisation [61] and reactive oxygen species formation [59] were reported by the authors.

2.4.2.4 Other techniques

Few more studies have been published regarding the development of *in vitro* techniques to study primary blast injuries. Leung *et al.* developed a barochamber to subject cell cultures grown in petri dishes to an overpressure [62]. Nienaber *et al.* used a modified Split Hopkinson Pressure Bar system to subject cell monolayers to a single pressure pulse

of few MPa [63]. These studies lack of a complete characterisation of the pressure stimuli and conditions the biological samples are subjected to and report only limited analysis of biological changes induced by pressure waves.

2.4.2.5 Final remarks

Among all these techniques, ESWT and laser driven shock waves were able to generate high pressure but relatively short pressure pulses (in the order of tens of microseconds) and usually multiple pulses were necessary to generate cellular damage levels as seen in blast injury of threshold levels 100 kPa - 10 MPa. On the other side, shock tube and SHPB techniques provided pressure levels in the order of blast injury threshold levels and with duration comparable to stimuli reported in blast events (hundred of microseconds to tens of millisencods). Moreover, the SHPB system is a flexible platform which can be used to test material properties of biological tissues at high dynamic stresses and strain rates. For these reasons, it was decided to develop and further characterise a modified SHPB system to subject live biological samples to controlled high pressure pulses, as well as a shock tube *in vitro* model of blast injury.

2.4.3 Material properties of tissues

In general biological tissues each have very different mechanical properties and are characterized by very complex mechanical behaviour. They show non-linear, anisotropic, viscoelastic and in some cases also viscoplastic behaviours. This is due to their inhomogeneous compositions and complex structure. They also vary from individual to individual. Soft biological tissues show a strong strain-rate dependency in their mechanical response to tensile or compressive loads [64–67].

In order to generate valid models of blast injuries and to design adequate protective devices, the mechanical properties of a number of tissues under dynamic conditions have been tested. The literature in this subject area includes studies of the mechanical properties of liver [64], stomach [64], skin [65], muscle [66], bone [67–69], and brain [70] using materials obtained from humans and animals. These materials were studied using strain

rates ranging from 10^{-2} s^{-1} up to 4×10^3 s^{-1}. The lower strain rate tests were typically conducted using conventional mechanical testing instruments, while modified split Hopkinson bar systems were developed for testing soft materials at high strain rates. A common observation from all these studies was that tissue stiffness increases with increasing strain rate. In bone tissue direct evidence of anisotropic response to compressive loads has also been reported [67].

The main difficulties encountered in high strain rate tests of biological materials are related to inertia effects. These effects can appear as a genuine mechanical response leading to an overestimation of the correct mechanical parameters, further complicated by the use of non-equilibrated specimens that cannot provide the constitutive behavior of the material. In addition, to represent *in vivo* conditions, tissues need to be correctly preserved in order to prevent dehydration and ageing effects.

All the reported tests described above have been conducted on dead tissue and hence only provide information about the mechanical responses of the materials in terms of bulk modulus and ultimate strength and, in certain cases, enabled the description of mechanisms of material failure. Only more recent studies have characterised the material properties of fresh soft tissues at high strain rates: a review of these studies is presented in Chapter 6.

2.5 Cell injury and death

Cells are generally able to adapt to shifts in environmental condition; when the cell's ability to maintain the normal homeostasis is overcome, cell injury occurs [71]. Cellular injury can be caused by different mechanisms and agents including lack of oxygen (hypoxia), free radicals, chemical agents, infectious agents, inflammatory and immune responses, genetic factors, insufficient nutrients, or physical trauma [71]. Physical traumas that lead to cellular injury include exposure to temperature extremes, changes in atmospheric pressure, ionizing radiation, illumination, mechanical stresses and noise. Injured cells may recover (reversible injury) or die (irreversible injury) [72]. If the oxygen supply is reduced, oxidative phosphorylation within mitochondria is disrupted and anaerobic glycolysis takes

place to maintain ATP reserves within cells [73]. If ATP production is disrupted or the plasma membrane is damaged then cell metabolism and maintenance of active transport processes that prevent fluid and solute influx are disrupted. The immediate consequence is cellular swelling resulting from the accumulation of excess water within the cell caused by the failure of transport mechanisms. Injured cells can fail to metabolize fatty acids leading to an accumulation of triglycerides within non-membrane bound cytoplasmic vacuoles, visible with light microscopy. Another indicator of cell injury is dystrophic calcification reaulting in the accumulation of calcium salts within damaged or dead cells. Free calcium in the cytosol can cause diminished cell-cell communication, modulation of the structure of the cytoskeleton, activation of phospholipase, and stimulation of macromolecular synthesis [72, 74].

Cells subjected to injury that cannot recover will die; two different mechanisms of cell death are recognised: necrosis and apoptosis [75]. Necrosis consists of the enzymic digestion of the cell and denaturation of proteins. Necrosis leads to dense clumping of cells and disruption of genetic material and the disruption of the plasma and organelle membranes. An inflammatory response is usually associated with necrotic processes. Apoptosis is a controlled mechanism of cell death that takes place both in normal and injured cells. Specific proteins are activated during apoptosis that breakdown cellular components required for normal cellular function (e.g. structural proteins in the cytoskeleton and nuclear proteins such as DNA repair enzymes) [76]. This process is highly selective so that single cells can be killed among an entire population. Also, apoptosis is usually not associated with inflammatory responses but with a rapid phagocytosis [76].

Chapter 3

A modified Split Hopkinson Pressure Bar system for cell pressurisation experiments

In this chapter a novel experimental setup developed to subject live biological samples to pressure pulses will be presented, specifically, a confinement chamber for a Split Hopkinson Pressure Bar (SHPB) system. This has been designed to contain liquid specimens during compressive loading. The theory behind SHPB experiments, the validation of the system, data analysis, characterisation and its limitations will be reported and discussed.

3.1 Split Hopkinson Pressure Bars

3.1.1 General principles of a SHPB system

The Hopkinson Pressure Bars (HPBs) were first developed by Bertram Hopkinson in 1914 to measure the pressure produced by explosives [77]. In 1949 they were used by Kolsky to characterise the dynamic response of materials in compression at high strain rates [78]. The design involved placing the sample between two bars - the Split Hopkinson Pressure Bar (SHPB). Since then several modifications have been used to test a variety of material types under compression, tension and shear. The compressive SHPB system

is generally composed by a gas gun and four bars; a striker bar (SB), an input bar (IB), an output bar (OB) and a momentum trap bar (MB). The SB, IB, OB and MB are supported by metal blocks as shown in Fig. 3.1. The bar material can vary depending

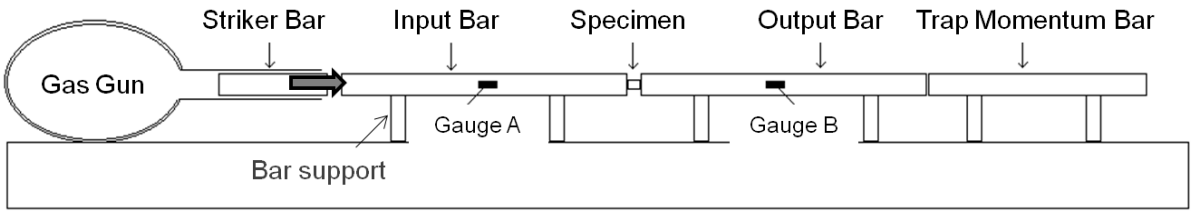

Figure 3.1: **Ideal SHPB compressive System.** Sketch of the different components of a typical SHPB system.

on the applications: usually bars are made of a high strength steel for studying metals, but aluminium, magnesium alloys and polymeric bars have also been used to test soft materials.

In a compression test the sample is sandwiched between the IB and the OB. The SB impacts the free end of the IB, this generates a longitudinal compression wave along the IB with an associated strain, ε_I. Once it reaches the IB-sample interface, part of the pulse is reflected back into the IB, ε_R, and part of it is transmitted to the sample. When the loading pulse has reached the sample-OB interface, part of it is then transmitted to the OB, ε_T, and part of it is transmitted back into the sample. Strain gauges applied on the surface of IB and OB are used to measure the time history of the pulses travelling along the bars. In Fig. 3.2 the wave propagation diagram is shown. The strain gauges position is chosen so that incident and reflected pulses don't overlap and the signals are recorded with high-speed digital oscilloscopes. In all cases the bars remain in their elastic regime and this allows a relatively simple analysis: the signal measured at the strain gauges location can be time shifted to obtain the bar stress and deformation at the IB and OB ends in contact with the sample. From these the deformation of and stress applied to the sample can be calculated.

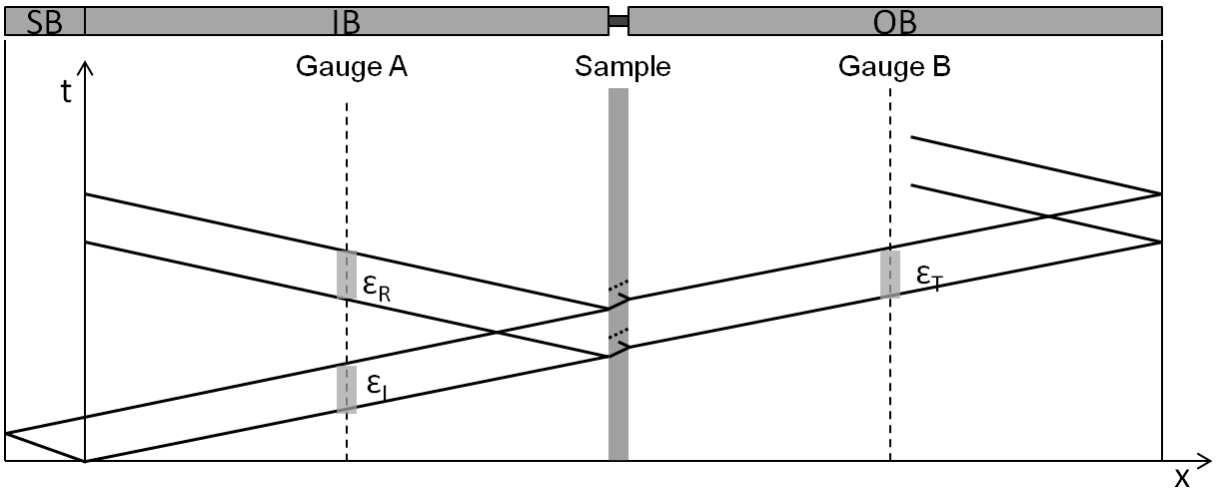

Figure 3.2: **Lagrangian wave profile for a typical compressive experiments** The incident, reflected and transmitted strain history is measured on the IB and OB at the coordinate x corresponding to the applied strain gauges.

3.1.2 Classical SHPB theory

Characteristic equations describing the stress - strain behavior of the material being tested in a Hopkinson bar system are derived from one-dimensional (1D) elastic wave propagation theory and are reported, for example, by Gray III [79, 80] and Gama [81]. The equation of motion for the IB and OB is given by:

$$C_0^2 \frac{\partial^2 u}{\partial x^2} = \frac{\partial^2 u}{\partial t^2} \tag{3.1}$$

where u is the displacement of a differential element of length dy in any position of the bar (including the extremities), C_0 is the wave velocity calculated as

$$C_0 = \sqrt{\frac{E_B}{\rho}} \tag{3.2}$$

where E_B is the bars Young's modulus and ρ the bars mass density. The solutions to Eq. (3.1) at the interfaces IB-sample and OB-sample as reported by Gama et al. [81], using D'Alambert's method, and assume respectively the forms:

$$u_1 = f(x - C_0 t) + g(x + C_0 t) \tag{3.3}$$

$$u_2 = h\,(x - C_0 t) \tag{3.4}$$

where f, g and h are arbitrary functions. 1D strain, by definition, is given by:

$$\varepsilon = \frac{\partial u}{\partial x} \tag{3.5}$$

hence the strain in the IB and OB can be derived by differentiating respectively Eq. (3.3) and (3.4) which gives:

$$\varepsilon_1 = f\prime + g\prime = \varepsilon_i + \varepsilon_r \tag{3.6}$$

$$\varepsilon_2 = h\prime = \varepsilon_t \tag{3.7}$$

where ε_i, ε_r and ε_t are respectively the incident, reflected and transmitted strains measured on the bars as illustrated in Fig. 3.3. The strain rate of the specimen $\dot{\varepsilon}_s$ can

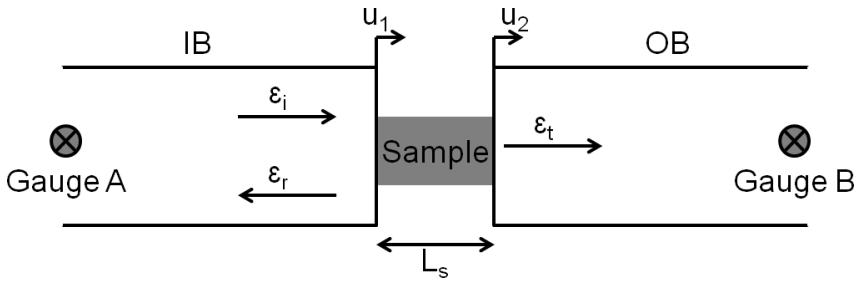

Figure 3.3: **Hopkinson bar wave transmission analysis** Expanded view of the bars - sample interfaces highlighting the longitudinal displacement of the bars (u_1 and u_2) as well as the bars' strain components (ε_i, ε_r and ε_t)

be calculated from the bars-specimen interface velocities $\dot{u}_1$ and $\dot{u}_2$ respectively for IB-specimen and OB-specimen interfaces. So, differentiating Eq. (3.3) and (3.4) with respect to t and substituting $f\prime$,$g\prime$ and $h\prime$ with Eq. (3.6)and (3.7), one obtains:

$$\dot{u}_1 = C_0(-f\prime + g\prime) = -C_0\,(\varepsilon_i - \varepsilon_r) \tag{3.8}$$

$$\dot{u}_2 = C_0(-h\prime) = -C_0\varepsilon_t \tag{3.9}$$

and consequently the strain rate, defined as

$$\dot{\varepsilon}_s\,(t) = \frac{\dot{u}_1 - \dot{u}_2}{L_s\,(t)} \tag{3.10}$$

where L_s is the instantaneous sample length, results

$$\dot{\varepsilon}_s(t) = -\frac{C_0}{L_s(t)}\left[\varepsilon_i(t) - \varepsilon_r(t) - \varepsilon_t(t)\right] \tag{3.11}$$

The strain in the specimen can hence be calculated by integration of the strain rate, so it results:

$$\varepsilon_s(t) = -\frac{C_0}{L_s}\int_0^t \left[\varepsilon_i(t) - \varepsilon_r(t) - \varepsilon_t(t)\right] dt \tag{3.12}$$

The average stress in the sample can be expressed in terms of the forces that acts at the IB-sample and OB-sample interfaces as:

$$\sigma_s(t) = \frac{F_1(t) + F_2(t)}{2A_s(t)} \tag{3.13}$$

where A_s is the instantaneous cross-sectional area of the specimen and F_1 and F_2 are by definition:

$$F_1 = A_B E_B \left(\varepsilon_i(t) + \varepsilon_r(t)\right) \tag{3.14}$$

$$F_2 = A_B E_B \varepsilon_t(t) \tag{3.15}$$

where A_B is the bar cross-sectional area. Substituting Eq. 3.14 and Eq. 3.14 in Eq. 3.13 the sample stress results:

$$\sigma_s(t) = \frac{A_B E_B}{2A_S}\left[\varepsilon_i(t) + \varepsilon_r(t) + \varepsilon_t(t)\right] \tag{3.16}$$

When the sample reaches dynamic stress equilibrium, after an initial ringing-up period, it reaches force equilibrium ($F_1 = F_2$) and it deforms uniformly. It follows that:

$$\varepsilon_i(t) + \varepsilon_r(t) = \varepsilon_t(t) \tag{3.17}$$

and thus the set of equations describing the strain rate, strain and stress in the specimen can be simplified as:

$$\dot{\varepsilon}_s(t) = \frac{2C_0}{L_s}\varepsilon_r(t) \tag{3.18}$$

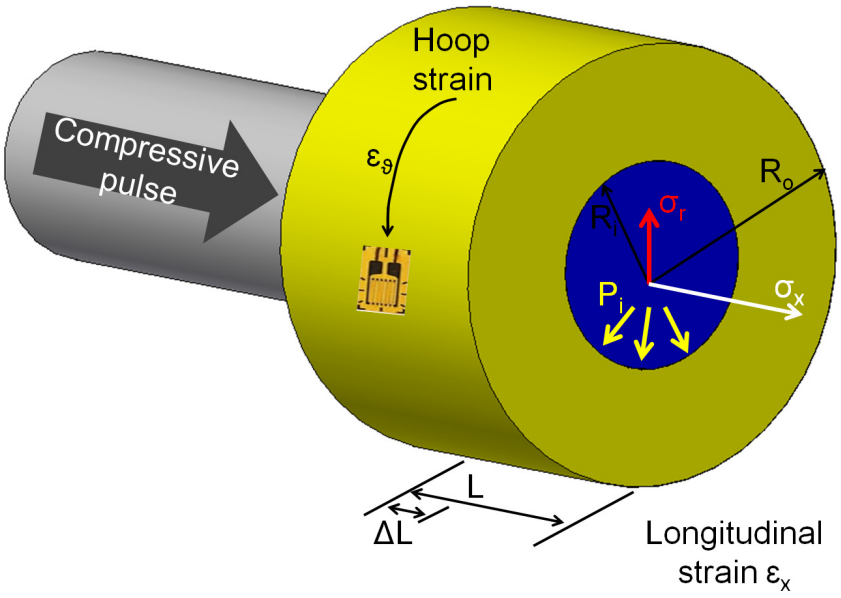

Figure 3.4: **Stress and strain components for confined compression experiments** Cut out of an ideal confined SHPB experiment, showing the compressive pulse travelling on the input bar (grey) in the direction of the sample (blue) confined by a jacket (yellow).

$$\varepsilon_s(t) = \frac{2C_0}{L_s}\int_0^t \varepsilon_r(t)dt \tag{3.19}$$

$$\sigma_s(t) = \frac{A_B}{A_s}E_B\varepsilon_t(t) \tag{3.20}$$

3.1.3 Confined SHPB experiments

In confined SHPB experiment the sample is sandwiched between the IB and OB and also constrained by a lateral jacket/chamber, which prevents or reduces sample's radial deformation during compression, depending on the material properties of the jacket. Confined SHPB experiments have been used to study for example the mechanical properties of ceramics [82] and of soft soil [83]. When the compressive pulse travelling along the input bar reaches the sample - bar interface, a load is transmitted to the sample. In order to ensure confinement, the axial stresses in the sample must be lower than the yield strength of the jacket material. If the circumferential strain in the jacket (ε_θ) is significantly lower than the longitudinal sample strain (ε_x), it is possible to assume that the sample is under one dimensional strain and bi-axial stress states [83]. The components of stress and strain tensors developed in the confined sample during SHPB compression are shown in Fig. 3.4.

With reference to a Cartesian system, they can be summarised as:

$$\sigma_1 = \sigma_x; \sigma_2 = \sigma_3 = \sigma_r; \varepsilon_1 = \varepsilon_x; \varepsilon_2 = \varepsilon_3 = 0 \tag{3.21}$$

Analysis derived from thick-walled cylinder under internal pressure loading theory can be used to determine the radial component of stress σ_r as a function of the measured hoop strain, geometry and elastic modulus of the confining jacket, as reported in section 1.3.2. The pressure developed in the sample can be calculated from the principal stress components as:

$$P = \frac{\sigma_x + 2\sigma_r}{3} \tag{3.22}$$

3.1.4 Practical aspects and possible sources of error in a SHPB system

According to Gray III [79] specific conditions need to be satisfied to validate SHPB tests: the stress waves must propagate in the bars uniaxially; the surfaces of the bars in contact with the specimen must remain flat and parallel at all times; the specimen has to reach dynamic stress equilibrium in a short time interval compared to the length of the loading pulse; the volume of the specimen must remain constant; and friction and inertia must be negligible [79]. To achieve all these conditions the bars need to be homogeneous, isotropic and their material must remain in the linear elastic state under loading; the length of the specimen must be relatively small in order to reach equilibrium quickly; and Gray III suggested that a sample length to diameter ratio between 0.5 and 1.0 to minimise both friction and inertia effects [79]. These guidelines are relevant to metal samples in particular, but are generally useful to bear in mind.

3.1.4.1 Sample's stress-state

In a compression SHPB experiment, when the incident pulse reaches the end of the IB, the specimen is subjected to a compressive load. This compressive wave travels through the specimen until it reaches the OB surface. Then, part of this wave is transmitted to

the OB and part is reflected into the sample. For solid specimen the reverberation of the loading wave within the sample continues until the stress within the specimen has reached that of the bars [84]. Once this state is reached the sample is said to be in stress equilibrium. The time necessary to reach stress equilibrium is influenced by the length and sound speed of the specimen and by the mechanical impedance mismatch between the bars and the sample materials. In a sample of initial length L_0 and sound speed C_0 the time necessary for the compression wave to travel through the sample (specimen characteristic time [84]) is $t_0 = L_0/C_0$. It is generally accepted that the time necessary for the sample to reach a stress equilibrium state is approximately 3 times the specimen characteristic time [81].

The amount of reflection and transmission of the wave between the sample and the bars depends on the specific mechanical impedance, z, of the bars' and sample's materials. z is defined as:

$$z = C\rho \tag{3.23}$$

where C is the elastic wave speed and ρ is the density of the material. Assuming force continuity at the sample-bar interfaces, it is possible to determine the reflection and transmission coefficients [85], and Meyers has developed a method by which the number of reverberations necessary to reach a stress equilibrium state can be calculated by summation of subsequent reflection and transmission coefficients [85].

In practical terms stress equilibrium can be verified comparing the bars' stress history at the two sample-bar interfaces. The *back* stress (σ_2, at the sample-OB interface) is calculated using the transmitted strain on the OB and is generally referred to as one-wave analysis. Two-waves analysis refers to the use of the incident and reflected strain pulses to determine the *front* stress (σ_1, at the IB-sample interface). *Front* stress is usually associated with large oscillations due to the superimposition of the geometrical dispersion effects in the incident and reflected signals measured at the IB strain gauge, while the *back* stress signal is generally smooth because the high frequency components of the travelling wave have been largely dumped by the sample [80] before they reach the OB gauge. If the sample has reached stress equilibrium, the *front* stress will oscillate about the *back*

stress. Quantitative approaches can be used to measure the time necessary to reach stress equilibrium, in which for example the difference

$$\Delta\sigma(t) = \sigma_1(t) - \sigma_2(t) \tag{3.24}$$

between *front* and *back* stresses is compared to the experimental error associated with the deviation υ_σ [86]. The time to reach equilibrium t_{eq} is hence determined imposing the condition $\Delta\sigma(t_{eq}) \leq \upsilon_\sigma$.

3.1.4.2 Wave dispersion

The equations used in SHPB theory are based on the solution of 1D wave propagation theory, which does not take into account dispersion effects due to the finite diameter nature of the bars. The propagation of a sinusoidal stress wave through a rod of finite diameter was first described by Pochammer and Chree [87] who proposed a three-dimensional (3D) analysis in the form of a frequency equation. Bancroft [88] later applied this theory to study dispersion effects in SHPBs and demonstrated that pressure bars predominantly vibrate in one fundamental mode. In a SHPB arrangement dispersion occurs as the result of the bar's phase velocity dependence on frequency, with the high frequency harmonic waves (short wavelengths) traveling slower than the low frequency harmonic waves (long wavelengths) [81]. The effect is visible on the signal recorded by the strain gauges mounted on the bar: the oscillations propagating through the bar change relative position and amplitude along the bar, so that the high frequency oscillations will be superimposed on the main rectangular pulse [81]. In order to evaluate dispersion in the SHPB system used in the cell pressurisation experiments the method proposed by Li *et al.* [89] was followed. The calculation aimed to evaluate the effects of dispersion on the input pulse function traveling from the strain gauge position to the bar-sample interface or to the bar free end. Briefly, an input pulse $y(t)$ with duration of 80 μs was selected from a typical SHPB experiment. As described by Gama *et al.* [81] a discrete time signal with time interval Δt

can be expressed in terms of a Fourier series as:

$$y(n\Delta t) = \frac{A_0}{2} + \sum_{k=1,2,...}^{N} [A_k cos(k\omega_0 n\Delta t) + B_k sin(k\omega_0 n\Delta t)] \tag{3.25}$$

where N equal half the number of the signal data points, $\omega_0 = 2\pi/\mathrm{T}$ is the radial frequency, T is the length of the time window chosen for the Fourier analysis and the Fourier constants A_0, A_k and B_k are calculated as

$$A_0 = \frac{2}{T} + \sum_{n=1,2,...}^{2N} [y(n\Delta t)\Delta t] \tag{3.26}$$

$$A_k = \frac{2}{T} + \sum_{n=1,2,...}^{2N} [y(n\Delta t)cos(k\omega_0 n\Delta t)\Delta t] \tag{3.27}$$

$$B_k = \frac{2}{T} + \sum_{n=1,2,...}^{2N} [y(n\Delta t)sin(k\omega_0 n\Delta t)\Delta t] \tag{3.28}$$

Each frequency component will travel with a different phase velocity C_k which can be calculated numerically solving the system of equations

$$C_k = \frac{kw_0\Lambda_k}{2\pi} \tag{3.29}$$

$$\frac{C_k}{C_0} = A + \frac{B}{C(\frac{r}{\Lambda_k})^4 + D(\frac{r}{\Lambda_k})^3 + E(\frac{r}{\Lambda_k})^2 + F(\frac{r}{\Lambda_k})^{1.5} + 1} \tag{3.30}$$

where C_0 is the elastic wave velocity, C_k is the wave speed of the k-th component, r is the radius of the pressure bar and Λ_k is the wave length of the k-th component. The coefficients A, B, C, D, E and F are nonlinear fitting parameters: Bancroft [88] calculated them for a range of Poisson's ratio from 0.10 to 0.40 with an increment of 0.05. Gong *et al.* [90] derived the parameters values for the Poisson's ratio missing from Bancroft's table using an interpolation method. In the analysis performed here, Gong's values of the fitting parameters for the two different bar materials were used as shown in Table 3.1 In the case of no dispersion, the whole pulse would travel a distance Δx along the bar at the wave velocity C_0 in a time t = $\Delta\mathrm{x}/\mathrm{C}_0$. However, the different frequency components kw_0

Bar Material	Poisson's Ratio	A	B	C	D	E	F
Inconel 718	0.29	0.57594	0.42555	21.3260	19.2240	-7.3258	2.4713
Ti6Al4V	0.34	0.56983	0.43132	15.7410	19.7140	-5.4671	2.0717

Table 3.1: **Wave dispersion fitting parameters** Nonlinear fitting parameters for dispersion wave analysis as obtained by Gong et al [90] via interpolation of Bancroft's data [88]

travel distance Δx along the bar at the corresponding velocity C_k in a time t = Δx/C_k. The phase angle difference between the k-th component and the component wave traveling with no dispersion equals:

$$\Phi_k = kw_0[(\Delta x/C_k) - (\Delta x/C_0)] \tag{3.31}$$

After the pulse travels a distance Δx along the bar, the pulse at the new position x can be reconstructed using a transformation equation within the Fourier series

$$Y(n\Delta t) = \frac{A_0}{2} + \sum_{k=1,2,...}^{N} [A_k cos(k\omega_0 n\Delta t - \Phi) + B_k sin(k\omega_0 n\Delta t - \Phi)] \tag{3.32}$$

The SHPB system used is characterized by small diameter bars and a short distance between the strain gauge and the bar/sample interface. This arrangement resulted in a low level of dispersion, as shown in Fig. 3.5 where the incident pulse from a typical experiment with Inconel bar was dispersed forward and backward to represent the original trapezoidal pulse at the free surface of the input bar and the fully dispersed signal at the IB-specimen interface. Although minimal effects were associated with dispersion, it was still implemented in the data analysis software in order to provide better wave alignment.

3.1.4.3 Bars calibration

To analyze the data from a Hopkinson bar experiment, the system must be calibrated prior to testing. Calibration of the Hopkinson bar setup is obtained by comparing the measured amplitude of the incident wave pulse with the theoretical constant stress of a rectangular pulse generated by the impact of the striker bar at a known velocity for each bar separately, *Bars apart* [80]. A dynamic calibration of the strain gauges, as developed

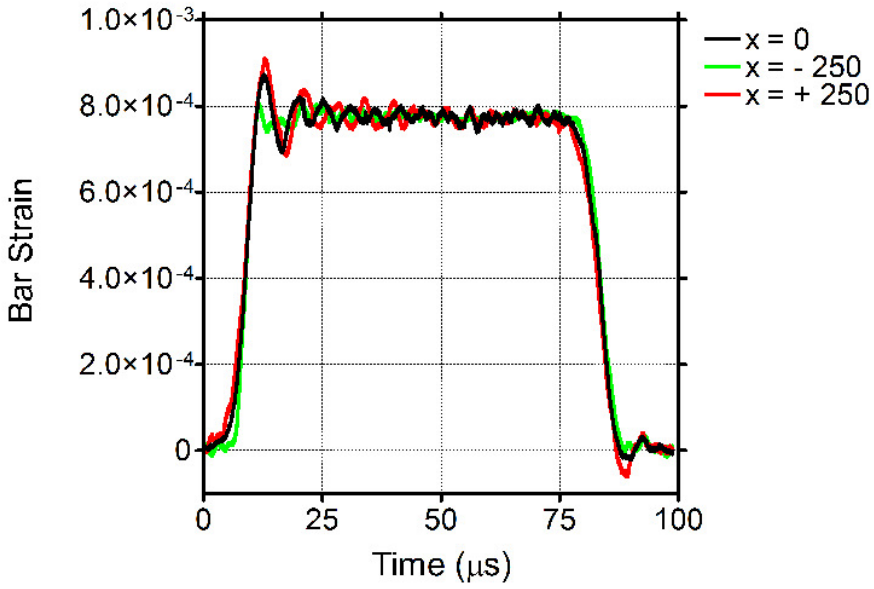

Figure 3.5: **Dispersion correction influence on a typical SHPB pulse** In black the incident pulse measured at the strain gauge on the Inconel 718 input bar for a compressive experiment with impact velocity of 6.2 ms^{-1}. In green and red respectively the pulse back and forward dispersed by 250 mm in a 12.7 mm diameter bar with $\omega_0 = 63582\ s^{-1}$, $C_0 = 5020\ ms^{-1}$ and Poisson's ratio = 0.29

at the Cavendish laboratory, was performed to determine calibration parameters for the input and output bars. Calibration of the SHPB system was performed each time the set up was assembled or modified such as when the strain gauges were changed.

When the striker bar impacts the input bar the pulse developed at the interface is initially rectangular, with a constant value of force $\overline{F}$ and duration $t_L = 2L/C_0$, where L is the striker bar length and C_0 the sound speed of the bar material, we obtain:

$$v_0 t_L = \frac{Z_s + Z_b}{Z_s Z_b} \overline{F} t_L \tag{3.33}$$

where Z_s and Z_b are, respectively, the striker impedance and the bar impedance. Assuming that momentum is conserved, the impulse $\overline{F} t_L$ is conserved along the bar so that the force experienced at the gauge is the same as the one experienced at the interface. Let's consider the definition of impedance

$$Z_s = A_s c_s \rho_s \tag{3.34}$$

where A_s is the striker surface area, ρ_s the is striker density. Considering that c_s=2L/t_L, it can be shown that by substitution of these term in Eq. (3.34) the impedance can be expressed as Z_s = m/t_L, which when substituted in Eq. (3.33) shows that the average force measured at the gauge is:

$$\overline{F} = \frac{2mv_0}{2m/Z_b + t_L} \tag{3.35}$$

The contact duration t_L can be found equating the impulse recorded at the gauge, $\int V(t)dt$, to the predicted initial contact pulse, $\overline{V}t_L$, thus obtaining

$$t_L = \int \frac{V(t)}{\overline{V}} dt \tag{3.36}$$

where $\overline{V}$ is the average plateau height of the measured strain gauge signal V(t). This calculation is valid assuming that the Pochammer-Chree oscillations associated with wave dispersion as measured at the strain gauge location are about an average of the amplitude of the initial signal. Eq. (3.36) can be substituted in Eq. (3.35) to obtain an expression for $\overline{F}$. The force, f(t), developed in the bar when impacted by the striker can then be calibrated against the voltage, V, recorded from the bar strain gauges as:

$$F = kV(1 + bV) \tag{3.37}$$

where k and b are two parameters obtained by a linear fit of $\overline{F}/\overline{V}$ versus $\overline{V}$ for a range of impact velocities.

3.1.4.4 Sample inertia and friction

A possible source of error in the stress-strain curve is due to the inertial restraints by axial and radial particle acceleration in the specimen. As discussed by Gorham [91], the force required to accelerate a material increases with an increase of the rate of deformation. The magnitude of the inertial contribution hence depends on the strain rate, but also on the density and geometry of the specimen. Based on Gorham approach, Ramesh calculated

the relative error in the sample flow stress due to inertia as [84]:

$$\frac{\sigma_{s,2}-\sigma_y}{\sigma_y}=\frac{\rho d^2}{\sigma_y}\left[\frac{1}{64}+\frac{1}{6}\left(\frac{L_0}{D_0}\right)^2\right]\dot{\varepsilon}^2 \tag{3.38}$$

where $\sigma_{s,2}$ is the stress measured from classical SHPB theory, σ_y is the actual yield stress of the material, ρ is the material density and d the instantaneous diameter of the sample. The value of inertial contribution calculated for the experiments described in this chapter is negligible.

Finally the stress in the sample can be inaccurately measured as a result of frictional effects between the bars and the specimen. Friction depends on the smoothness of the end surfaces, the bar and specimen materials, the lubricant used, the impact velocity and temperature [84]. In the SHPB system used for the cell pressurisation experiments, it was unlikely that frictional forces could develop at the interface between the bar and the liquid sample, while friction could occur between the bar and the O-rings inserted in the confinement chamber. As shown later in the chapter in Fig. 3.20, experiments performed to compare the strain gauges signals with or without the chamber mounted on the IB and OB showed that there was no influence due to friction between the O-rings and the bars in the output signal.

3.1.4.5 Bar material properties

Accurately determining the material properties of the bars used in the SHPB experiments can help minimise the error in the values of stress and strain calculated from a compression test. In this study the length and diameter of each bar were measured with calipers so that dimensions could be obtained with errors respectively of 5 mm and 0.1 mm, while the bar mass was measured with a balance with error lower than 0.1 g. Density was then calculated as the ratio of measured weight over measured volume. Bar wave velocity was measured firing the projectile into the free end of the bar and measuring the time necessary for the compressive pulse to travel multiple distances of the strain gauge - bar free end which returned an error lower than 0.1% of the measured velocity. Finally, the longitudinal elastic modulus was calculated as the product of the bar density times the

bar wave velocity squared. Overall, the contribution of the errors in the measurement of the bar material properties to the final values of calculated pressure was lower than 2%.

3.1.5 SHPB for liquid samples

The first fluid Hopkinson bars experiment was reported by Kenner in 1980 [92]. In these experiments a vertical set up was composed of a striker bullet, a single incident bar and a long fluid column held in a rigid tube sealed with a rubber O-ring. The pressure generated within the liquid was measured by piezoelectric pressure transducers at two different locations and used to calculate the propagation velocity, the liquid bulk modulus and the attenuation coefficient. Later studies by Ahrstrom *et al.* [93] focused on the determination of the dilatation-pressure relationship of lubricants using a modified SHPB system up to 2 GPa. The set up was composed of a typical SHPB compressive system to which two pistons and a container were added to confine and load the liquid specimens. The authors reported good repeatability and limited fluid leakage for their modified setup. Ogawa [94] developed a through bar SHPB system to investigate the dynamic behavior of fluids under high rates of shear. In this paper the author explained the mathematical treatment of the SHPB strain gauges data in order to obtain a measure of shear strain and found a relation between the viscosity and shear rate for a high viscous silicon oil. Finally Lim *et al.* [95] developed a modified SHPB system to evaluate the dynamic squeeze flow behavior of viscous Newtonian fluids at high shear stresses and discussed the conditions under which classic Hopkinson bar data analysis is applicable for fluid specimens. These can be summarised as:

- The amplitude of the transmitted signal must be clearly distinguishable from the background noise
- Fluid flow must be stable and laminar
- A stress equilibrium state must be achieved in the fluid specimen

The first point, concerning signal to noise ratio, can be addressed by observing the strain gauges signals for a SHPB compression experiment on a 800 μl water sample,

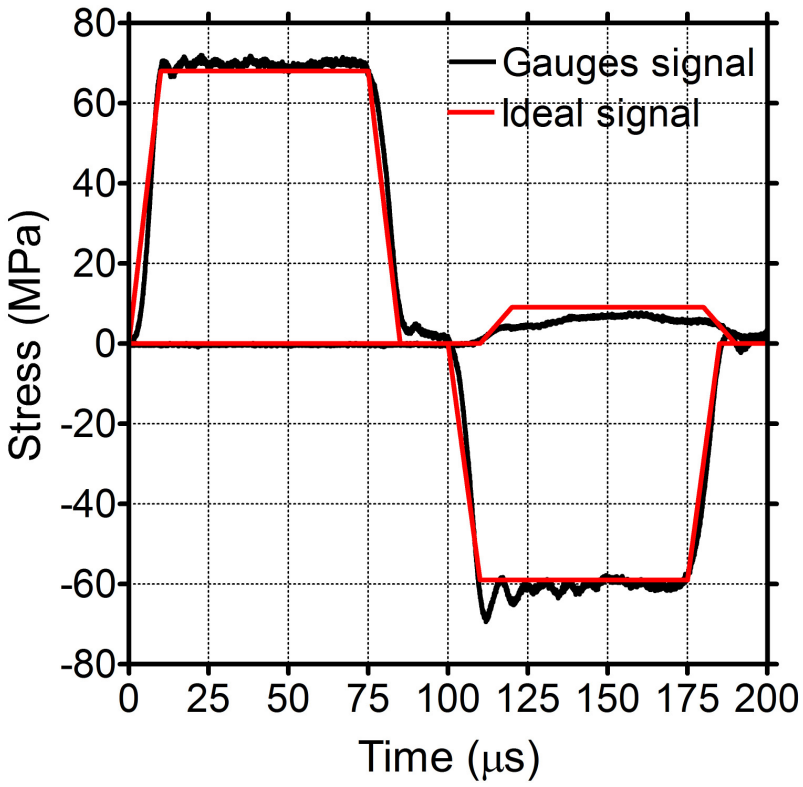

Figure 3.6: **Typical SHPB signal from compression experiments of water** In black the stress calculated from the input and output bar strain gauges signals and in red the ideal stress calculated according to elastic wave theory

corresponding to a cylinder with area of 126.7 mm^2 and thickness of approximately 6.3 mm. As shown in Fig. 3.6, the transmitted signal on the output bar shows the typical trapezoidal pulse shape of a SHPB test and the amplitude of the signal is comparable with the expected values of stress as calculated from elastic wave theory. Moreover, if we compute a discrete Fourier transformation of the ideal and real signals it's possible to notice that they both return a main peak in the low frequencies which corresponds to the actual trapezoidal shaped signal, while an additional peak at high frequencies appears only in the real signal, which corresponds to the noise from the acquisition system, associated with the sampling frequency, as shown in Fig. 3.7. In order to give a quantitative estimate of the fulfillment of the first SHPB condition, it is possible to calculate the signal to noise ratio (SNR (dB)) defined as:

$$SNR(dB) = 20Log\frac{A_s}{A_n} \tag{3.39}$$

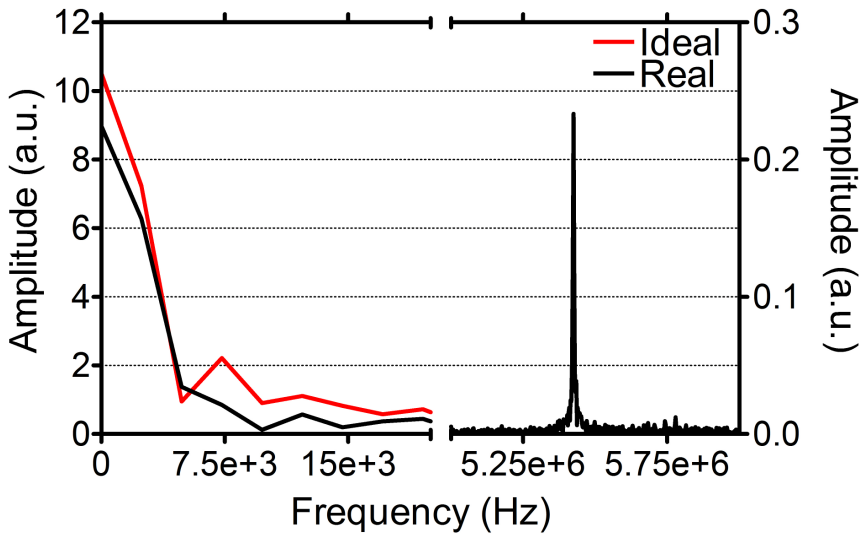

Figure 3.7: **Fourier transform of a real and ideal SHPB output signals** A discrete Fourier transform of a recorded output bar signal from the compression of 800 μl of water with impact velocity of 3.4 ms^{-1}, and the equivalent ideal output bar signal calculated with elastic wave theory were computed with a fast Fourier transform algorithm. Only two portions of the frequency spectra (0-22.5 kHz and 5-6 MHz) where features were present were plotted.

where A_s and A_n are respectively the amplitude of the signal and of the noise. In the case of the lowest output pressure achieved in the SHPB pressurisation experiments the value of SNR (dB) $\approx$ 30. Hence, the signal was easily distinguishable from the noise and no additional filtering was required.

The second condition requires the fluid flow to be stable and laminar. As discussed by Lim *et al.* [95] it is possible to calculate the maximum Reynolds number Re for the compression experiments as

$$Re_{max} = \frac{\rho D \nu_{max}}{\mu} \tag{3.40}$$

where ρ is the fluid density, D is the hydraulic diameter, ν_{max} is the maximum velocity developed in the liquid sample and μ is the dynamic viscosity of the fluid. In the SHPB pressurisation experiments the maximum bar particle velocity was 5 m s^{-1} which corresponds to a maximum radial flow velocity V_r, calculated at the middle of the specimen thickness, of 4.2 m s^{-1}. Thus the maximum fluid velocity was the one developed in the axial direction and the maximum Reynolds number for the cell pressurisation experiments was 63.3. The condition of laminar and stable flow for a Poiseulle flow between parallel

plates is Re <2000. In the experiments performed with the SHPB system it was estimated a maximum value of Re which was two orders of magnitude below the laminar flow limit, hence it was possible to conclude that the pressure-induced flow in the SHPB system was laminar. However, high speed photography of the SHPB pressurisation experiments showed that after the first 800 μs cavities appeared within the liquid specimen indicating that other physical phenomena could take place. These observations will be discussed in more details in the results section.

Finally, a stress equilibrium state must be achieved within short time compared to the duration of the experiment. Given the thickness L_S and the sound speed C_0 of the fluid sample it is possible to calculate the time required for the stress wave to be transmitted from the input bar-sample interface to the sample-output bar interface as

$$\tau_S = \frac{L_S}{C_0} \tag{3.41}$$

In the cell pressurisation experiments the maximum thickness of the sample was 6.3 mm and the sound speed was assumed to be equal to the sound speed of water at ambient temperature ($\approx$ 1500 m s^{-1}). This corresponds to a transit time in the order of 4.0 μs which is very small compared to the duration of the experiment ($\approx$ 100 μs). From this estimate, even considering that a π number of reverberations occurred, the sample would have been in stress equilibrium for $\approx$ 85% of the duration of the compressive experiment. However, a more rigorous approach was used to evaluate sample stress equilibrium: the incident,σ_I, reflected, σ_R, and transmitted, σ_T, stress signals measured at the strain gauges were shifted in time and corrected for wave dispersion in order to evaluate the signals at the specimen-bars interfaces. For bars and specimen of equal surface area ,the adimensional parameter R, defined as

$$R = \frac{2(\sigma_I + \sigma_R - \sigma_T)}{\sigma_I + \sigma_R + \sigma_T} \tag{3.42}$$

gives a measure of the stress difference between the signal at the two interfaces normalised by the average stress. At equilibrium the value of R tends to 0. However, taking in consid-

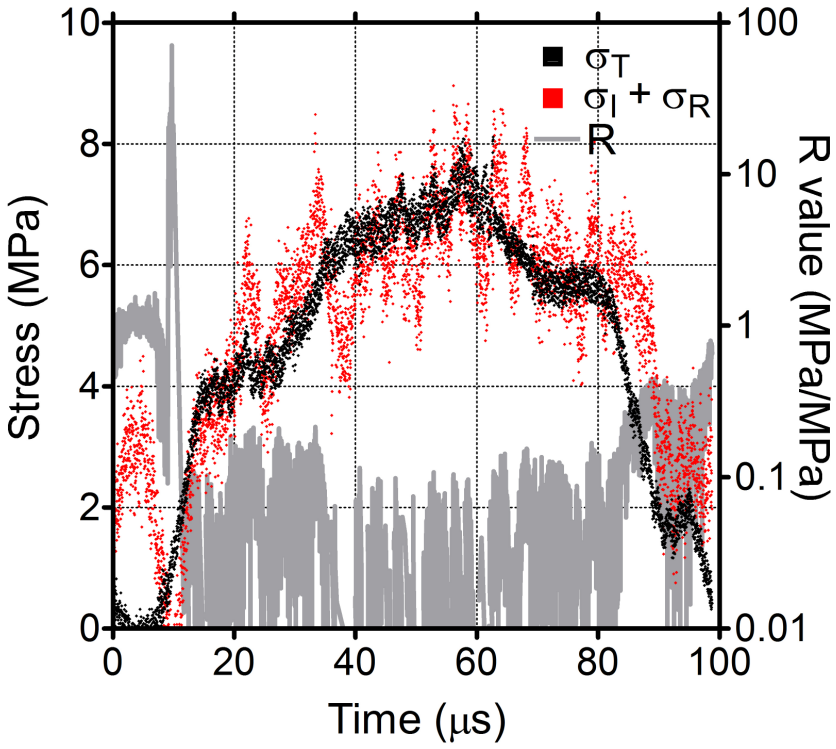

Figure 3.8: **Analysis of stress equilibrium for SHPB compression of water** In black and red the specimen stress calculated respectively at the OB-specimen and at the IB-specimen interfaces using 1-wave and 2-waves analysis for a compressive experiment on a 800 μl water specimen with impact velocity of 3.4 m s^{-1}. In gray, the values of the adimesional parameter R, for the entire duration of the compressive pulse

eration experimental error, it was accepted that the sample was in equilibrium for values of R <1. As shown in Fig. 3.8, after the first 10 μs, the stress measured at the IB-sample interface (σ_I+σ_R) and at the sample-OB interface (σ_T) were in close agreement, indicating that the specimen had reached stress equilibrium. Moreover, to give a quantitative measure of the difference between the stresses developed at the two extremities of the sample it was possible to calculate the value of R which for the experiment presented here was lower than 1 after 11 μs which represents $\approx$ 10% of the entire duration of the compression wave. It was hence concluded that all the conditions required to perform SHPB experiments on liquid samples were fulfilled.

3.2 The modified SHPB system: confinement chamber designs

In order to develop a confinement system for the SHPB in which live biological samples could be used a step-by-step development process was undertaken. Focus was placed on specifying appropriate materials, reducing manufacturing time and cost and conducting prototype testing. Firstly, the biocompatibility of the material, the requirement of sterilisation and the ability to see the specimen during the compression experiment were taken into account. This limited the choice of material to two main candidates: polycarbonate (PC) and polymethyl methacrylate (PMMA). Both materials are known for their biocompatibility, PC being used in several medical devices in contact with body fluids while PMMA is used directly in contact with bone in implants. They have similar compressive strength and rigidity and both are transparent. However, PMMA has low fracture toughness, it is more brittle at ambient temperature compared to polycarbonate. Polycarbonate can be sterilized by irradiation and steam autoclaving or disinfected with common clinical disinfectants, such as isopropyl alcohol. For these reasons polycarbonate was chosen as the main material of the confinement chamber.

The dynamic stresses that were going to be developed during experiments were taken into account into the design. The confinement chamber had to be able to contain liquid samples when high and dynamic internal pressures were generated. The highest pressure in the chamber, estimated from elastic wave theory, where the bars would not be damaged, was of approximately 40 MPa. The inner size of the confinement chamber was fixed by the bar diameter to 12.7 mm, so only the outer diameter could be varied. The ratio of the outer to inner diameters required to resist the maximum radial stress without yielding and was calculated using:

$$\sigma_y \geq P_{max} \frac{(b/a)^2 + 1}{(b/a)^2 - 1} \tag{3.43}$$

where σ_y was the yield strength of polycarbonate, assumed to be 70 MPa for this calculation, P_{max} was the maximum expected pressure developed within the chamber, and b/a was the outer/inner radial ratio. The calculation indicated a ratio higher than 1.92

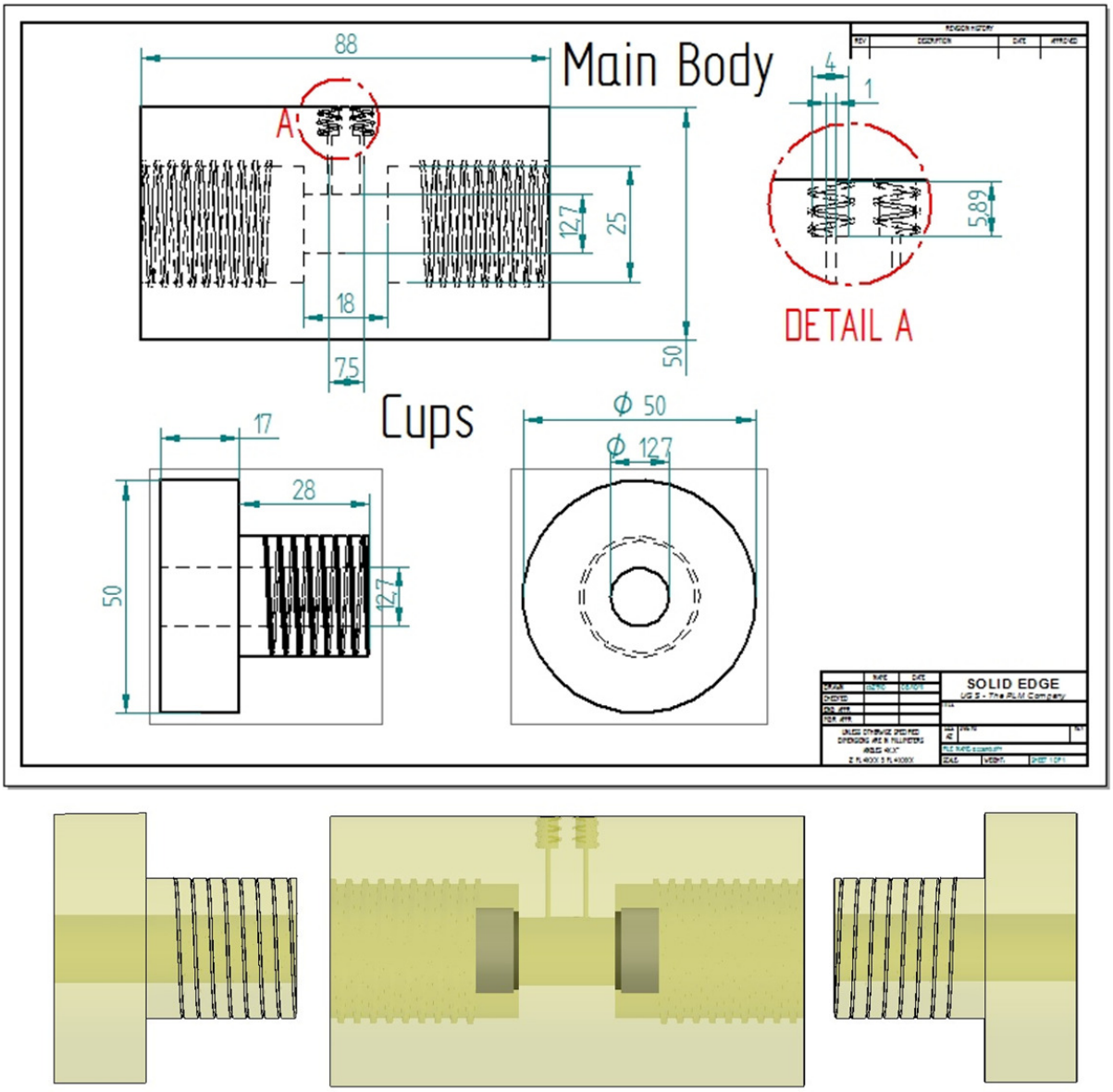

Figure 3.9: **Confinement Chamber 1.** The main body, in polycarbonate, contains the liquid sample inserted with a syringe through the counter bored holes. The lateral screw cups keep the system in place during the test.

to prevent plastic deformation.

Another important aspect of the design was to achieve good specimen sealing without affecting bars movement during the experiment. The use of O-rings seemed the most simple and cost-effective method. Different O-ring materials were considered such as nitrile, neoprene and silicone, but only silicone was biocompatible, as discussed in the next chapter.

Three different chamber prototypes were designed and tested. As shown in Fig. 3.9, the first chamber (Chamber 1) used three main parts: the body being a hollow cylinder with a 50.0 mm outer diameter, a 12.7 mm inner diameter, and 88.0 mm long. Two tapped holes, 25.0 mm in diameter and 35.0 mm in length, were drilled into the lateral surfaces of the cylinder. These holes allowed the insertion of an O-ring into each side of the chamber. The O-ring was kept in place by a metal ring, pressed by lateral cups screwed into the body. Each chamber piece could be easily cleaned and mounted on the SHPB system. The disadvantages included the weight of the chamber on the bars which caused misalignment of the IB with the SB. Also, because the O-rings were not inserted in the chamber, the loss of liquid during the experiment was significant, more then 30% of the initial volume.

A second chamber design focused on the reduction of chamber weight and included the insertion of inner O-rings to reduce loss of sample. Chamber 2, as shown in Fig. 3.10, consists of two concentric cylinders, an inner one containing the liquid and an outer one holding the sample chamber in place. As in the design for Chamber 1, two lateral cups keep all the elements together. In the outer cylinder a window was cut to allow the use of high speed photography. In order to minimise the risk of fatigue failure and of liquid loss, one counter bored hole in the outer cylinder was connected to two internal 1 mm diameter holes in the inner cylinder. An extra hole was drilled in the outer chamber to allow a plastic screw to hold the inner chamber in place and the small-diameter inner holes to be aligned. O-ring grooves were added in the inner cylinder to accommodate two O-rings which seal the chamber when mounted on the bars. However, during the insertion of the liquid and during the tests the outer components of the chamber misaligned allowing the liquid to leak around the inner chamber.

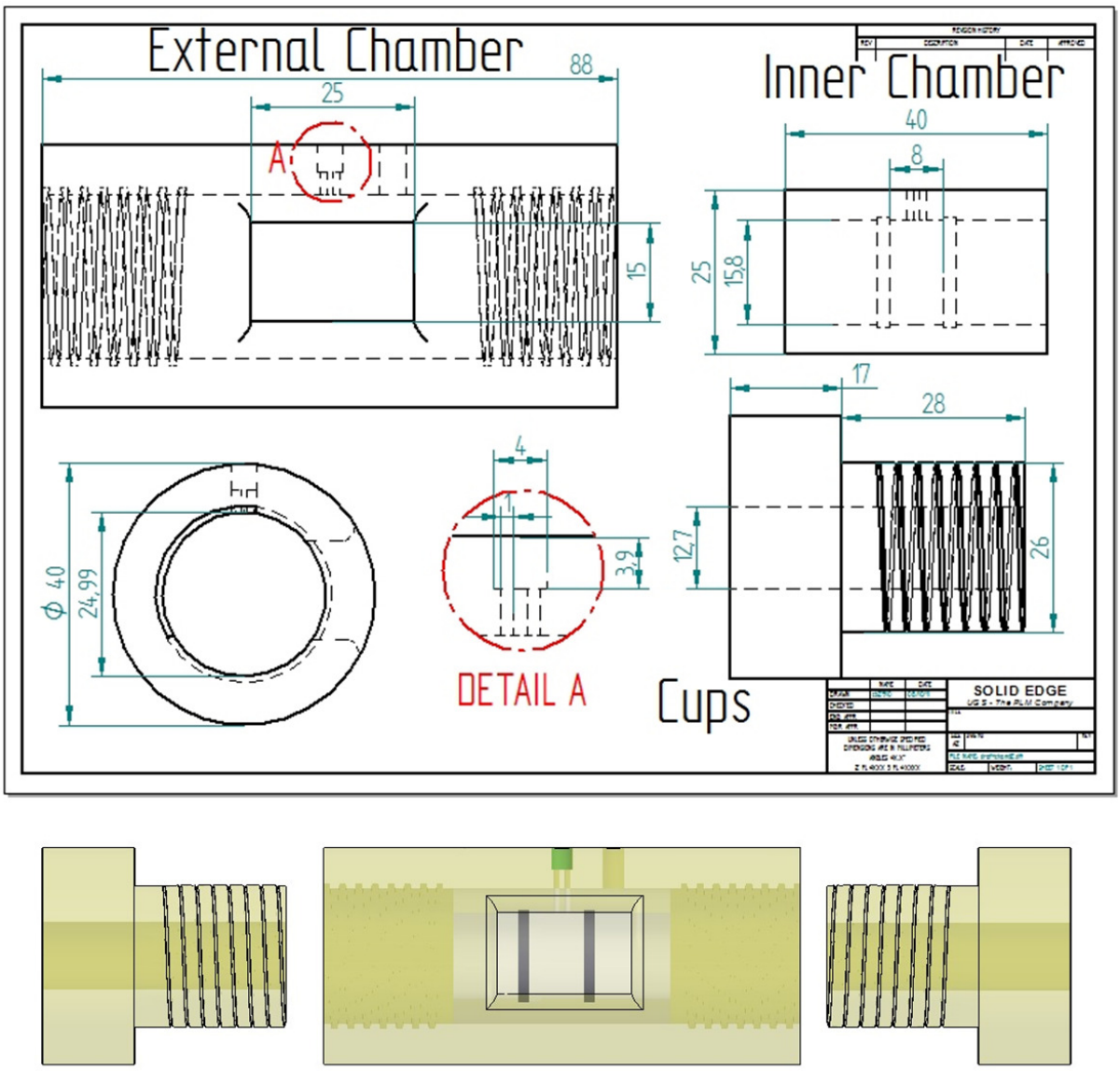

Figure 3.10: **Confinement Chamber 2.** Two concentric cylinders constitute the central part of the chamber, the inner one contains the liquid while the outer one holds the chamber in place using the lateral screw cups. O-ring grooves were added to the inner cylinder to prevent leakage during the bar movement.

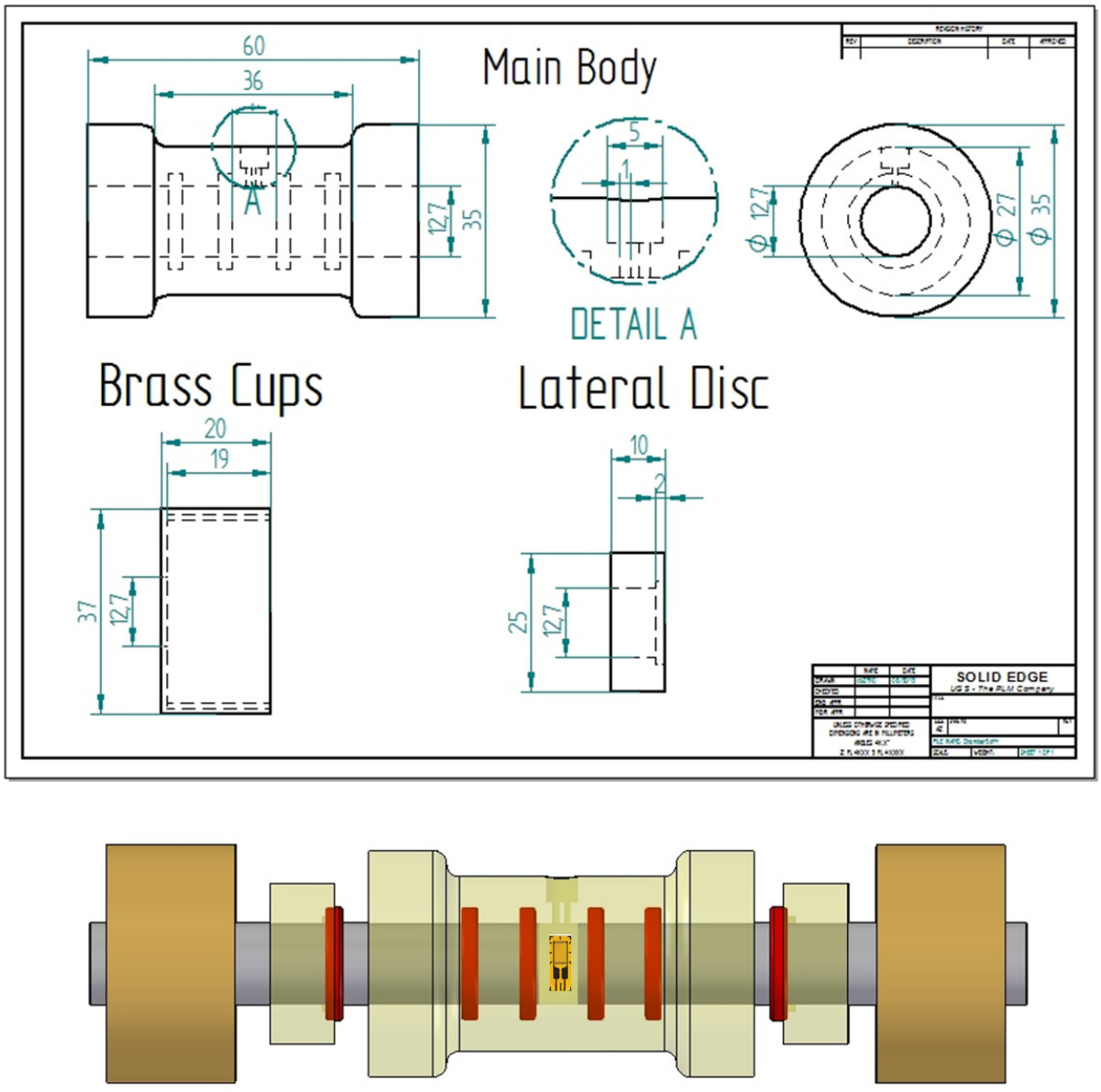

Figure 3.11: **Confinement Chamber 3.** The chamber is composed of three parts: a main body in polycarbonate (center object) with bore holes where liquid is inserted using a syringe; two polycarbonate discs with O-ring seals; and two brass screw caps that hold the components together and align the chamber on the bars.

The final design, Chamber 3 shown in Fig. 3.11, was composed of five main parts: the body in polycarbonate with one counter bored hole that connected two 1 mm diameter holes where liquid was inserted using a syringe from the outer surface of the chamber; two polycarbonate discs with O-ring seals; and two brass screw caps that hold the components together and aligned the chamber on the SHPB. In the main body inner O-rings were inserted as in the designs of Chambers 2 to prevent leakage of liquid. Also, as the wall of the cylinder were thinner compared to the previous designs, a strain gauge could be applied on the outer surface to measure the hoop strain and allow the inner radial stress developed during compression experiments to be measured.

3.3 Materials & methods

3.3.1 SHPB apparatus

Two SHPB systems were used for the cell pressurisation experiments: initial experiments were performed with the SHPB at the Cavendish laboratory, University of Cambridge, while the main experiments were performed with the SHPB developed at the Center for Blast Injury Studies at Imperial College London. The two systems are similar so for brevity only the Imperial College system will be described in detail. The SHPB system was composed of a one-stage gas gun with a 150 cm, 12.8 mm bore barrel, three 500 $\pm$ 1 mm in length and 12.7 $\pm$ 0.1 mm in diameter bars and 12.7 $\pm$ 0.1 mm in diameter striker bars of different lengths. All the bars were precision machined and centerless ground for a high degree of alignment. The whole system was mounted on a 4 m long steel frame with a central track with guide rails on which 6 carriages are slided and fixed. On each carriage a custom made V-block was secured by a screw. Each bar was supported by two V-blocks and secured with plastic cable-tie straps; the edges of the V-block were covered with insulating tape to reduce the friction between the bars and the supports and to prevent wear. Two different bar materials have been used in the cell pressurisation experiments: Inconel Steel 718 and Ti6Al4V. The material properties of these bars are summarised in Table 3.2 for both the Imperial College and Cavendish laboratories. A

Laboratory	**Material**	**Density** (Kg/m^3)	**Wave velocity** (ms^{-1})	**Elastic Modulus** (GPa)
Imperial	Inconel 718	8203 ± 1	5020 ± 4	206.7 ± 0.2
Imperial	Ti6Al4V	4414 ± 1	5050 ± 5	112.6 ± 0.1
Cavendish	Inconel 718	8270 ± 1	4980 ± 4	205.0 ± 0.1

Table 3.2: **SHPB material properties** Measured properties of bars of different material used in the cell pressurisation experiments at Imperial College London and at University of Cambridge

three point velocimeter, composed by three laser beams each aligned to a photodiode at known distances, was installed on the muzzle of the gas gun, in front of the input bar. The output signal of the photodiodes was recorded by a Tektronics DPO 3014 digital oscilloscope to measure the time-of-flight of the projectile between the 3 points and thus the final velocity of the striker bar at impact with an accuracy of ± 3% of the velocity value.

3.3.1.1 Strain Gauges

The input and output bars were each instrumented with semiconductor gauges. Compared to foil gauges, semiconductor strain gauges have higher sensitivity, smaller size, higher fatigue life and lower non-linearity. The gauges were mounted on the bars by Vishay Precision Group: an epoxy adhesive was used to bond them to the bar surface taking care that the strain gauge wires were not shorted by contact with the bar. On each bar two Kulite type AFP-500-90 gauges were located halfway along the bar length and diametrically opposite to each other to remove effects of bar flexure. These gauges are non-encapsulated single element gauges with terminal leads at both ends, P-type doped, with an initial resistance of 500 Ω (R_0) and length of 2.3 mm. Their working principle is based on the piezoresistance effect: a change in applied stress induces a change in electrical resistivity. The fractional change in resistance (ΔR) of a gauge with applied strain (ε) is called the gauge factor (GF), given by equation

$$GF = \frac{\Delta R}{R_0 \varepsilon} \tag{3.44}$$

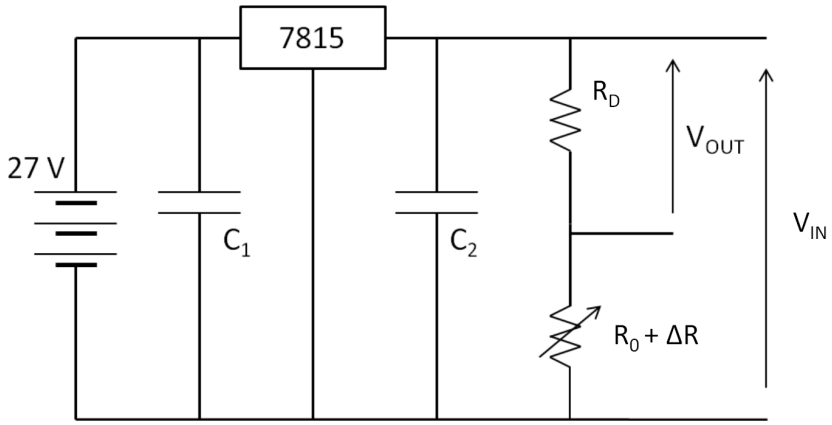

Figure 3.12: **SHPB strain gauge potential divider circuit** The circuit is supplied by three 9 V batteries in series which are connected to the LM7185 fixed voltage regulator which supplies a stable bridge voltage V_{IN} = 15 V. The change in resistance due to the straining of the strain gauge is measured with an oscilloscope on the R_D arm of the potential divider. Reproduced from [86].

which for the AFP-500-90 Kulite gauges is 140 as stated by the manufacturer.

The gauges are powered by a simple potential divider circuit shown in Fig. 3.12. Three 9 V batteries power a 7815 voltage regulator that supplies a stable 15 V bridge voltage (V_{IN}) applied across the fixed resistance R_D and the strain gauges in series. The output signal V_{OUT} is measured across R_D by an oscilloscope. The capacitors C_1 and C_2 smooth respectively the power supply voltage and the bridge voltage. For the experiments reported in this chapter strain gauge signals were recorded with a Tektronics DPO 3014 digital oscilloscope at a sampling rate of 5 MHz and with AC coupling enabled to remove the voltage offset.

3.3.2 Hoop strain measurement of the confinement chamber

One of the main advantages of Chamber 3 was that it allowed measurement of the hoop strain during the compression experiments. This could be used to validate the SHPB data and further characterise the pressure developed inside the chamber. A schematic of the quasi static experiments performed to characterise the chamber's hoop strain is presented in Fig. 3.13. Two foil strain gauges GFLA-3-350-70 (Techi Measure, Studley, Warwickshire, UK) were mounted on the outer surface of the chamber with a cyanoacrylate adhe-

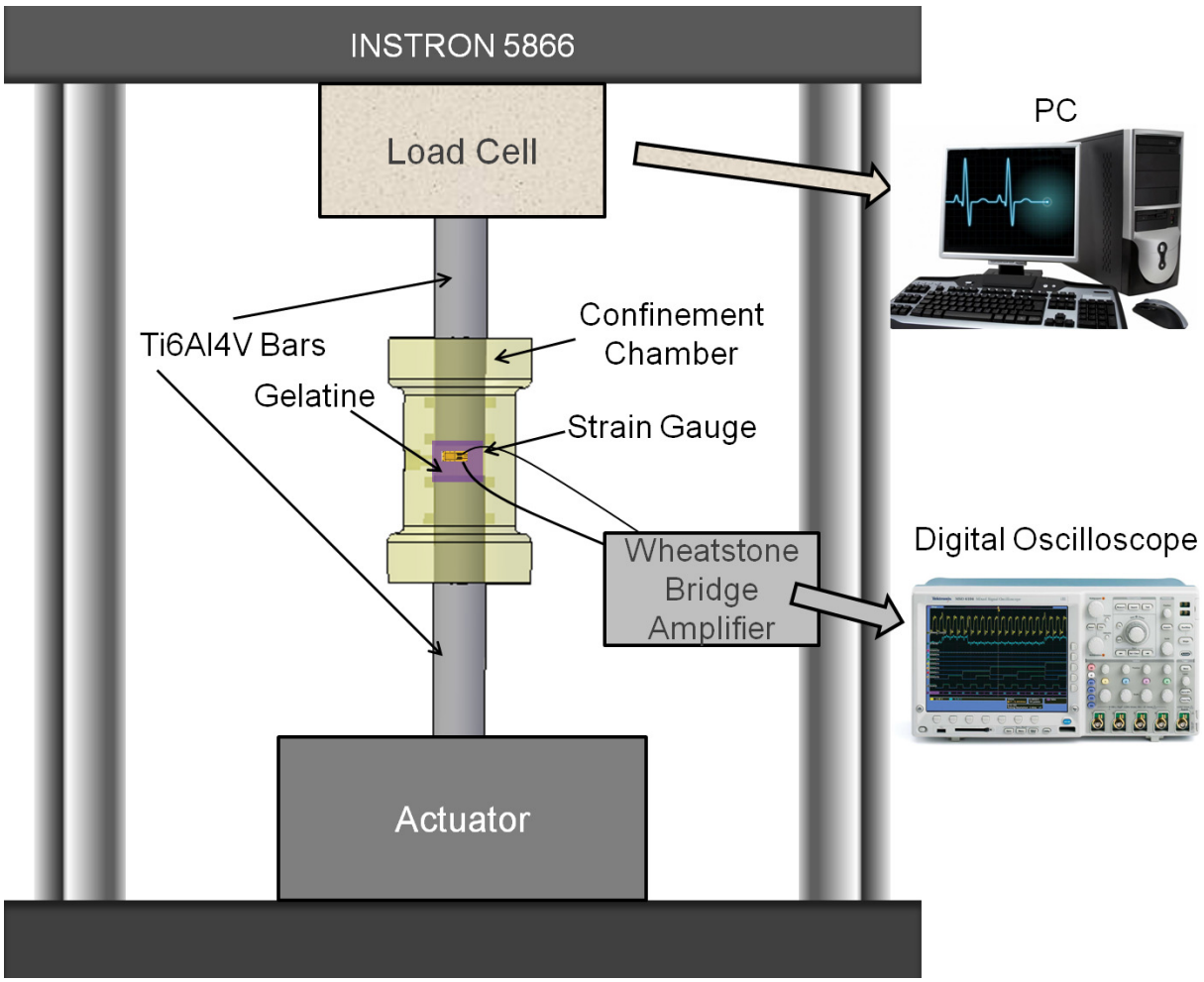

Figure 3.13: **Schematic of quasi static compression experiments to characterise chamber hoop strain** The longitudinal stress applied by the actuator to a gelatin sample contained in the confinement chamber was measured by a 50 kN load cell connected to a PC for data acquisition. The hoop strain developed during compression of the gelatin specimen was measured on the chamber surface by two foil strain gauges connected to a Wheatstone Bridge amplifier. The voltage signal was acquired with a Tektronics DPO 3014 digital oscilloscope.

sive. They were located halfway along the chamber length, diametrically opposite to each other, in order to measure the circumferential strain. The strain gauges were then coated to prevent damage while inserting liquid samples. The strain gauges were connected to a Wheatstone bridge (courtesy of Richard Curry, University of Cape Town) as two active arms. A power supply was used to provide the voltage to the bridge and the gain was set prior to each experiment. The output voltage was recorded with a Tektronics DPO 3014 digital oscilloscope. The response of the chamber to the compression of a confined sample was first assessed using gelatin in a quasi-static system. A Ti6Al4V bar of 12.7 mm in diameter and 50 mm length was inserted in one side of the confinement chamber equipped with silicone o-rings. Then, a disc of gelatin of 12.7 mm in diameter and 6.2 mm in hight was inserted in the chamber from the free end and followed by another Ti6Al4V bar. The chamber was sealed with a nylon screw and the whole assembly positioned between two plates of an INSTRON 5866 machine. Samples were compressed at a rate of 0.6 mm/min up to a load of 1.3 kN. The load was retained for few seconds and then released. The signal from the strain gauges mounted on the chamber was recorded during the whole compression experiment. This could be used to measure the chamber hoop strain and consequently the inner radial stress as explained in the Data Analysis section.

3.3.3 SHPB compression of fluid specimens: water and cell suspensions

Dynamic SHPB compression experiments of fluid specimens were performed in order to determine the pressure developed inside the chamber. Characterisation of the system was performed using water. For each experiment chamber 3 was equipped with new silicone O-rings and mounted on the input and output bar of the SHPB system instrumented with Inconel 718 bars. 800 μl of water was inserted in the chamber using a 19 gauge needle through one of the 1 mm holes at the top of the chamber. It was important to avoid any air bubble formation during loading. Once the liquid was transferred, the input and output bar were gently pushed in order to fill completely the inner chamber space with liquid and remove any air. A nylon screw was then used to seal the main chamber hole

and the pressure experiments was performed. The bars and the chamber strain gauges signals were recorded and saved for subsequent analysis, as described in the Data Analysis section. Experiments were performed varying the striker bar impact velocity in order to generate different pressures within the chamber. High speed photography was used to monitor the compression experiments with a Phantom v12.1 (Vision Research, Wayne, NJ, USA). The camera was triggered when the striker bar was launched and images were acquired at a sample rate of 10^4 frames/s.

The cell experiments were performed following the same procedure as described for water. Between each test the confinement chamber, the bars and the nylon screw used to seal the chamber were sprayed with 70% ethanol solution and allowed to dry, to prevent bacterial contamination. Experiments were performed with 800 μl cell suspension aliquots with a range of impact velocities from 3.4 - 7.8 m s^{-1}. The strains associated with the stress pulses in the bars were measured in each experiment.

3.3.4 SHPB compression of cells adherent to a solid substrate

In order to be able to perform experiment on cells grown on monolayers, the SHPB was further modified with the addition of two TI6Al4V 60 mm long bars on which a glass coverslip could be secured, using two M2 nylon screws. With the coverslips mounted, the bar inserts were slided into the confinement chamber. 400 μl of cell medium was inserted, as in previous experiments. The chamber was sealed with a nylon screw and placed on a custom stainless steel support frame as shown in Fig. 3.14 A. The inserts were aligned with the input and output bars and a compression experiment was carried out as previously described. The hoop strain of the chamber as well as the bar strain gauges signals were recorded during the experiment. The chamber was then removed from the support and disassembled using the reverse order to assembly, removing the liquid first using a syringe, then gently sliding the inserts out to recover the glass coverslips.

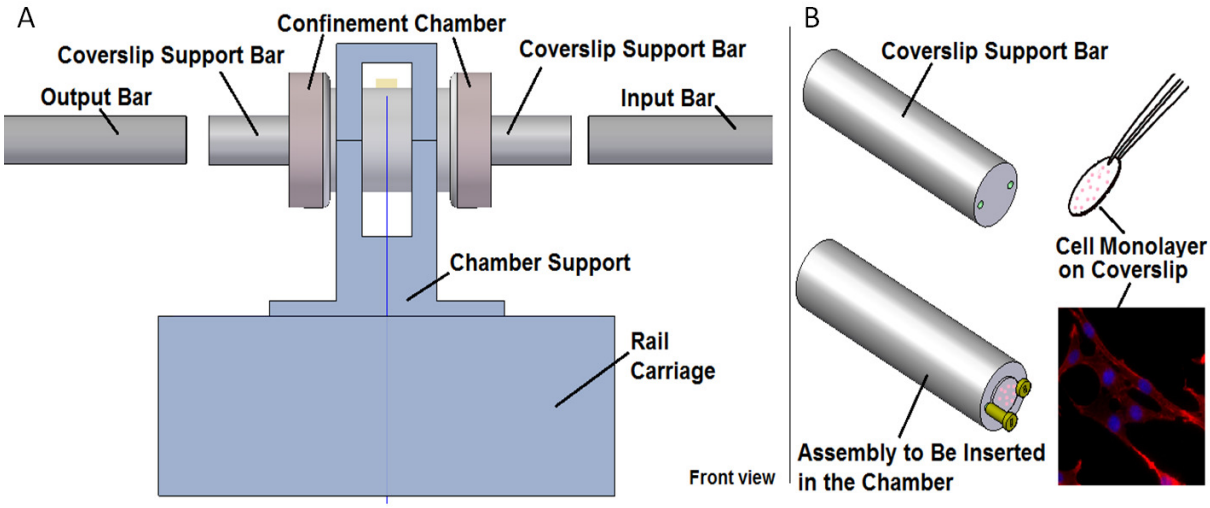

Figure 3.14: **Modified SHPB system for *in vitro* pressurisation of cells adherent to a solid substrate** Two Ti6Al4V bars of 60 mm in length and 12.7 mm in diameter with two M2 holes drilled on one of the flat surface are used to transmit the pressure pulses to glass coverslips (B). Coverslips are placed on the bar inserts using tweezers with the cell monolayer facing upwards and secured with two M2 sterile nylon screws. (A) A custom made support is secured on a rail carriage with four screws which allow alignment of the pressurisation chamber with the input and output bar.

3.4 Data analysis

Hopkinson bar data reduction software applications were developed in Matlab to calibrate the bars, calculate the wave dispersion, determine the start points of the SHPB pulses and calculate the specimen pressure-time history. The routines are listed in the Appendix. The analysis routine was developed taking in consideration ease of use by researchers, the speed of data processing and the flexibility to analyse different types of SHPB experiments. The output is saved in .xls files which can be stored for subsequent analysis.

3.4.1 SHPB calibration GUI software application

A Graphic User Interface (GUI) software application was developed in Matlab to calculate the dynamic calibration parameters for input and output bars, as shown in Fig. 3.15. The user enters the striker bar properties: diameter, mass and mechanical impedance. Then, the user enters the average time of flight of the striker bar, using the time and distance between the laser-photodiode sensors and the firing pressure used to launch the striker bar. The strain gauge signal measured from a *Bar apart* test is then loaded via the "Load

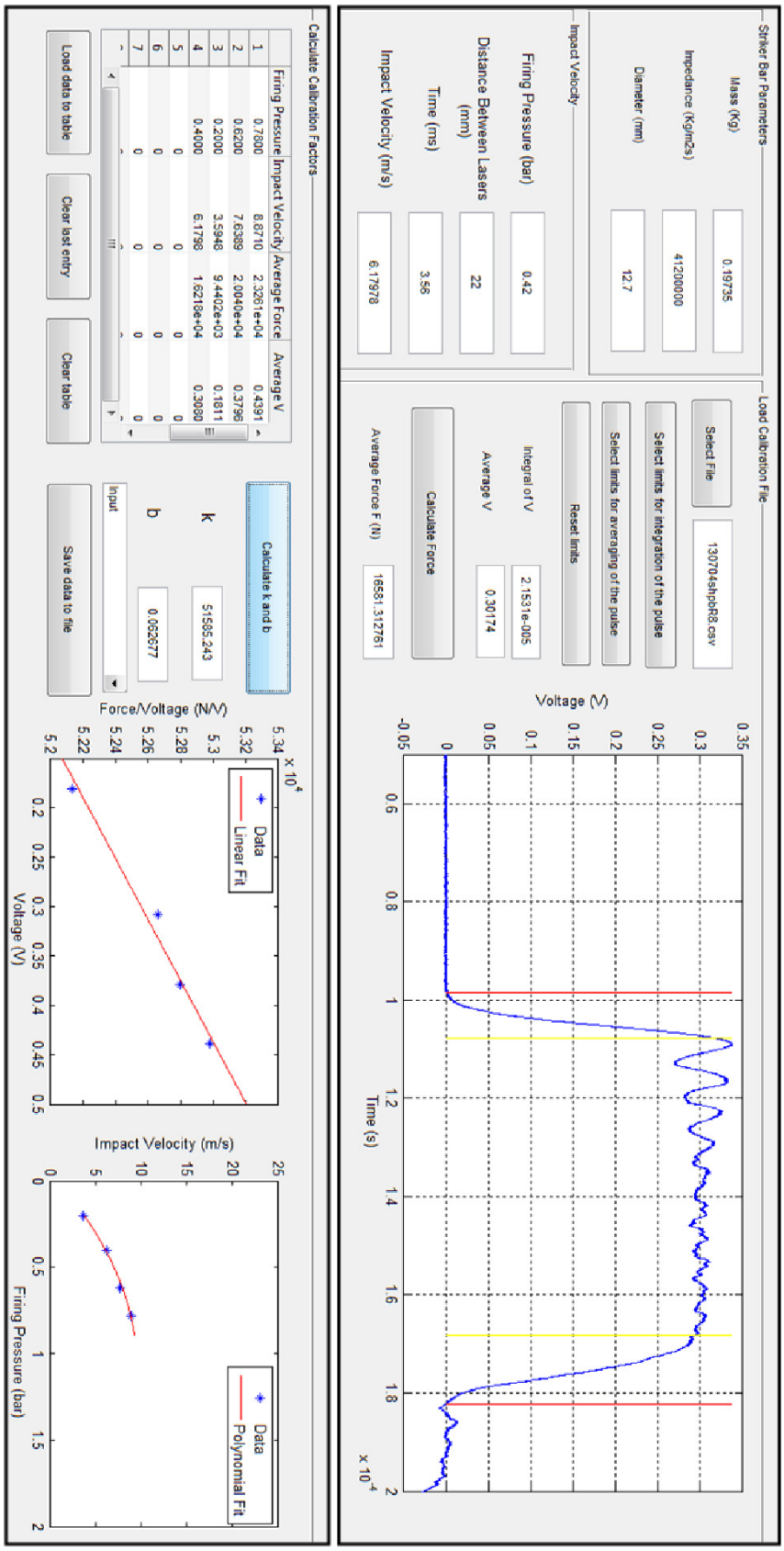

Figure 3.15: **SHPB Calibration GUI software application** Screenshot of the user interface application developed in Matlab for the calibration of each bar used in the SHPB system

Calibration File" panel and the limits for integration and averaging of the pulse must be selected by positioning a cursor on the gauge trace. Pressing the "Calculate Force" button, the impact velocity, the average force $\overline{F}$ and the measured average gauge voltage $\overline{V}$ are calculated. In the lower panel of the interface (Calculate Calibration Factors) the force and gauge voltage data can be loaded into a table and used to calculate the calibration parameters k and b as discussed in the *Calibration of the bars* section (3.1.4.3). Once the calibration parameters have been calculated, two values appear in the panel which show the linearity of fit, in the calculation of k and b and the relationship between the firing pressure and the impact velocity of the striker bar.

3.4.2 SHPB data processing GUI software application

The GUI application developed for SHPB data analysis is shown in Fig. 3.16 Sample and bar calibration parameters and general bar properties are entered. After the analysis of the first experiment, only the sample parameter need to be changed, for subsequent analysis, if the bar parameters don't change. The user is requested to load the file containing the strain gauges data by clicking the "Select File" button and selecting the file. Once the file is selected, a plot of the gauges traces appears in the dedicated image space in the "Strain Gauges Data" panel. To perform the wave dispersion correction the user must generate a file containing the values of the C_K velocities for the various frequencies used in the Fourier analysis. The calculation of these values requires a numerical solution to a system of equations, thus it may be very time consuming. However, once the C_K values have been calculated for a bar with known Poisson's ratio, they can be stored in a .xls file which can be used for all subsequent analysis, provided that the experiments use that set of bars, the striker bar and importantly the same sampling rate. Hence, the C_K values can be loaded from a .xls file. The user needs only to identify the start of the Hopkinson bar pulse by clicking the "Select start point" button and selecting the point with a cursor. The software automatically calculates the start and end points for the incident, reflected and transmitted waves as shown in Fig. 3.17. This is achieved by defining a temporal

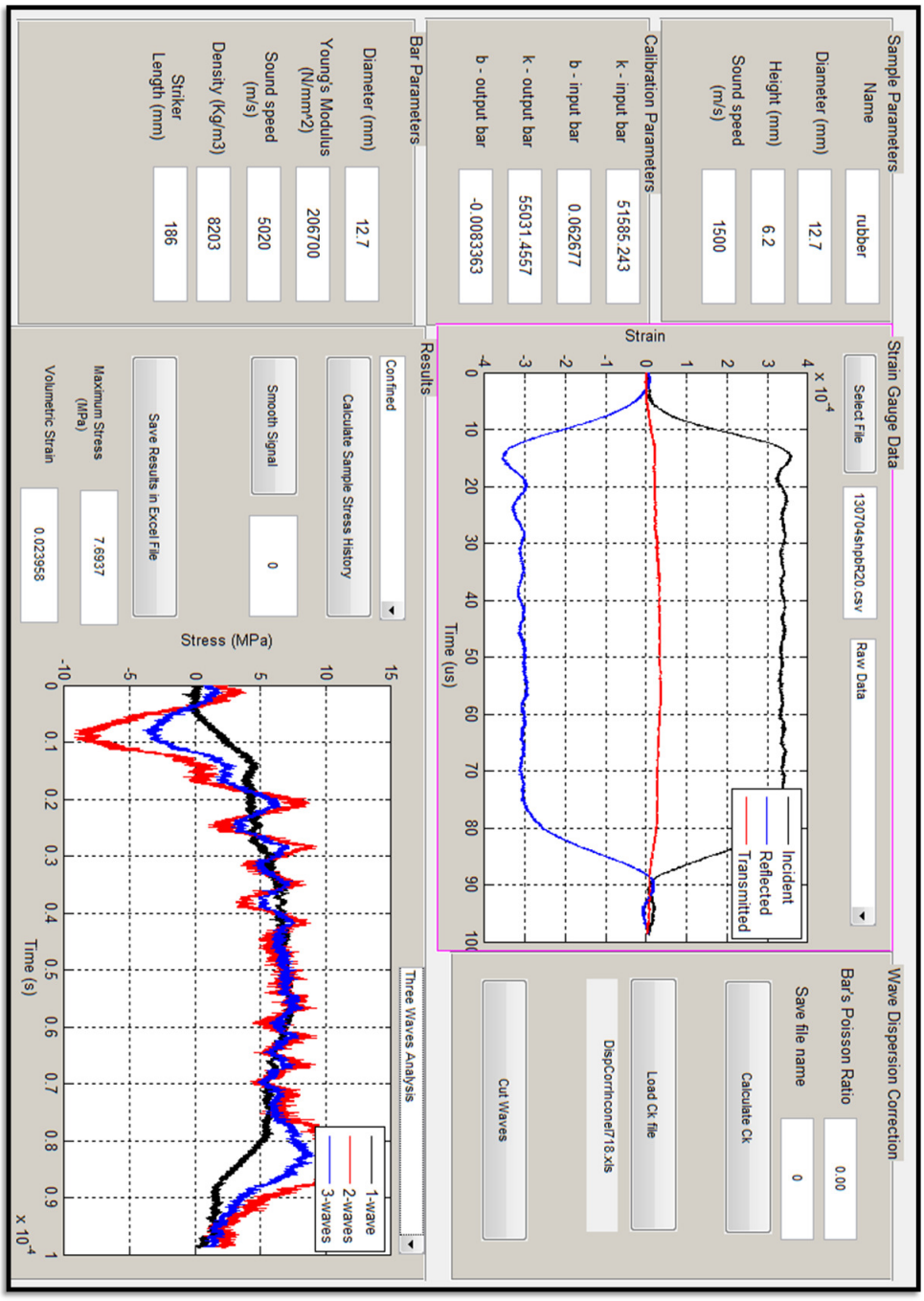

Figure 3.16: **SHPB data analysis GUI software application** Screenshot of the user interface application developed in Matlab for the automated analysis of SHPB strain gauges data.

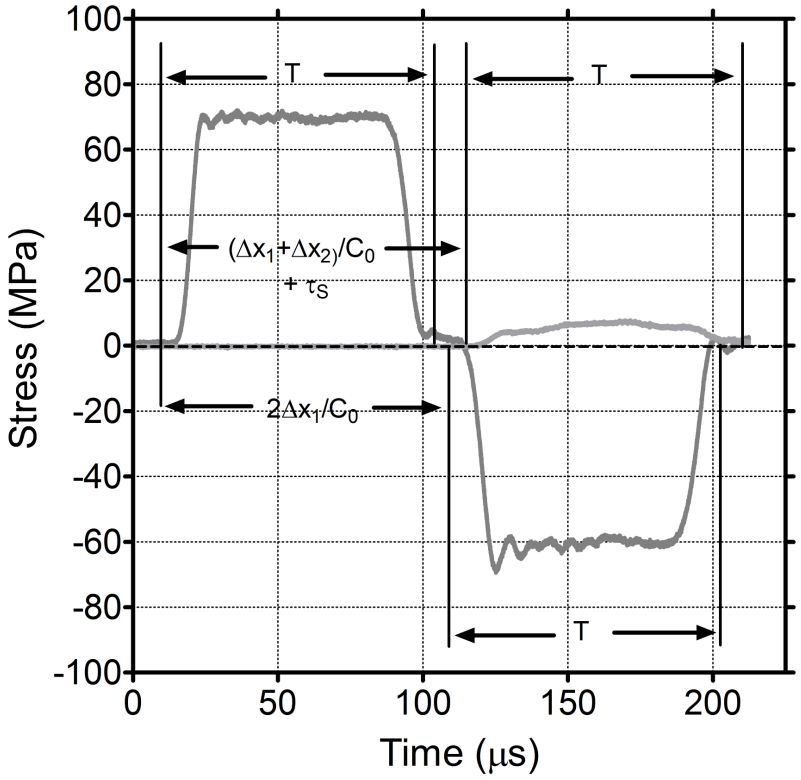

Figure 3.17: **Location of the time window used to select incident, reflected and transmitted pulses from typical SHPB strain gauges signals** The start and end point of the incident, reflected and transmitted pulses are automatically calculated using a window that is shifted in time to match the position of the pulses at the strain gauges location. Modified from [81], Fig.30, p. 245

window with period T = $4/3\tau_P$ where τ_P is the Hopkinson pulse duration calculated as

$$\tau_P = \frac{2L_P}{C_0} \tag{3.45}$$

where L_P is the length of the striker bar. The start point of the reflected wave is identified at a distance in time of $2\Delta x_1/C_0$ from the start point of the incident wave, where Δx_1 is the distance between the strain gauge and the IB-specimen interface. The start point of the transmitted wave is identified at a time from the start point of the incident wave of $(\Delta x_1 + \Delta x_2)/C_0 + \tau_S$ where Δx_2 is the distance between the specimen-OB interface and the strain gauges and $\tau_S = L_S/C_S$ where L_S is the specimen thickness and C_S the specimen sound velocity. Once the three pulses have been identified they are translated onto the same timebase and start point by $\Delta x = \Delta x_1$ for the incident (forward) and the

reflected (backward) waves and $\Delta x = \Delta x_2$ for the transmitted (backward) waves. The result of this three wave displacement is plotted in the dedicated image space in the 'Strain Gauge Data' Panel. It has been noticed that using an automated start point calculation may not give an exact wave alignment. Although the specimen transit time is taken in consideration to disperse and translate the transmitted wave, no influence of the presence of the specimen is considered for the reflected wave. A correction factor ξ has hence been added to the term that define the distance Δx_1 from the specimen-IB gauge in order to allow user correction of the waves alignment. The correction factor is varied in order to minimise the misalignment of the first Pochhammer-Chree oscillation on the incident and reflected waves. The values of ξ are chosen between 0 and $L_S/2$ which for the Inconel bar correspond to a maximum correction in wave transit time of 1.2 μs.

In the "Results" panel, the user selects the type of analysis to be performed. It's possible to choose between an "Unconfined Test", which correspond to an experiment in which the sample is free to expand radially during compression or a "Confined Test", in which the specimen radius is constant and equal to the bar radius. In terms of analysis, in the first case the instantaneous sample surface area is calculated assuming conservation of volume during axial deformation

$$A_S(t) = \frac{A_0 l(t)}{L_S} \tag{3.46}$$

where l(t) is the instantaneous sample length, while in the second case the value of surface area is kept constant.

When "Calculate stress history" is pressed, the software uses the calibration factors of the two bars to transform the voltage signals into force values and consequently into velocity, using the bar impedance. From this the velocity of the bars-specimen interfaces are calculated using either a one-, two- or three-wave method:

$$\Delta v(t) = 2v_R(t) \tag{3.47}$$

$$= 2(v_T(t) - v_I(t)) \tag{3.48}$$

$$= (v_I(t) + v_R(t) + v_T(t)) \tag{3.49}$$

From the velocity difference, the instantaneous length of the specimen is calculated as;

$$l(t+1) = l(t) + \Delta v(t)dt \tag{3.50}$$

where the first value of l(t) is set as the initial specimen length L_S and dt is the acquisition time step. The specimen strain rate, true strain and engineering strain are then computed as

$$\dot{\varepsilon(t)} = -\frac{\Delta v(t)}{l(t)} \tag{3.51}$$

$$\varepsilon(t+1) = \varepsilon(t) + \dot{\varepsilon(t)}dt \tag{3.52}$$

$$\varepsilon(t) = 1 + \frac{l(t)}{L_S} \tag{3.53}$$

Finally the true sample stress is calculated with one-, two- and three- waves method respectively as:

$$\sigma(t) = \frac{A_B E_B}{A_S(t)}\varepsilon_T \tag{3.54}$$

$$\sigma(t) = \frac{A_B E_B}{A_S(t)}(\varepsilon_I + \varepsilon_R) \tag{3.55}$$

$$\sigma(t) = \frac{A_B E_B}{2A_S(t)}(\varepsilon_I + \varepsilon_R + \varepsilon_T) \tag{3.56}$$

$$\tag{3.57}$$

where A_B is the bar surface area and E_B is the bar elastic modulus. The engineering stress is also calculated for completeness as:

$$\sigma(t) = \frac{A_B E_B}{A_S}\varepsilon_T \tag{3.58}$$

where A_S is the initial sample surface area. The user can save the results of the analysis in a .xls file by pressing the 'Save file to Excel' and choosing the directory in which to save.

3.4.3 Chamber hoop strain

The output signal of the strain gauges mounted on the chamber was used to calculate the hoop strain ε_θ of the chamber during compression of the confined specimen using the formula

$$\varepsilon_\theta = \frac{4V_{out}}{NGV_{bridge}GF} \tag{3.59}$$

where V_{out} is the output voltage recorded with the oscilloscope, N is the number of active arms (2), G is the amplifier gain (varying from 100-500), V_{bridge} is the bridge input voltage (6.4 V) and GF is the strain gauge factor (2.07 as from manufacturer). The hoop strain was then used to calculate the pressure developed within the chamber using thick-walled cylinder theory. The inner pressure P_i can be expressed as a function of the measured hoop strain assuming that it equals the chamber radial stress at the internal radius coordinate as

$$P_i = \sigma_r = \frac{1}{2R_i^2} E_C (R_o^2 - R_i^2)\varepsilon_\theta \tag{3.60}$$

where R_i and R_o are the inner and outer radii of the cylinder, respectively, and E_C is the Young's modulus of the confinement chamber's material (2.4 GPa, as supplied by manufacturer). This relation is true if the chamber deforms linearly as a function of the inner pressure. In the case of a polycarbonate chamber the condition of linear deformation might not be fulfilled due to the viscoelastic nature of the material. A quasi static calibration of the chamber was performed in order to verify the condition $Pi = k\varepsilon_\theta$. This was done calculating the inner pressure using the INSTRON 5866 machine load cell;

$$P_{i2} = \frac{Load(t)}{A_S(t)} \tag{3.61}$$

where $A_S(t)$ is the instantaneous specimen surface area calculated assuming conservation of the specimen volume. The inner pressure was calculated using Eq. 3.60. The deviation of the values of inner pressure calculated with the two different method was expressed as

a function of the hoop strain as

$$\varsigma(\varepsilon_\theta) = \frac{P_{i2}(\varepsilon_\theta) - P_i(\varepsilon_\theta)}{P_i(\varepsilon_\theta)} \tag{3.62}$$

In the dynamic SHPB experiments the inner pressure was hence calculated using Eq. 3.59 and 3.60 and used to compute the pressure generated inside the chamber, as described in the next section.

3.4.4 Pressure developed inside the chamber

In order to accurately measure the pressure within the chamber during the SHPB experiments, the values of pressure calculated from SHPB analysis and the one calculated from the chamber hoop strain were used to obtain a final average pressure value. Specifically this was obtained as:

$$P_{AVG}(t) = \frac{\sigma_x + 2\sigma_r}{3} \tag{3.63}$$

where σ_x is the longitudinal stress calculated with the one-wave analysis of SHPB data, whereas σ_r is the stress measured from the chamber hoop strain. Moreover, the pressurisation impulse, defined as

$$I_P = \sum_{t=0}^{N} P_{AVG}(t)\Delta t \tag{3.64}$$

where N is the length of the entire pressure event and Δt is the acquisition time step, was calculated for each experiment.

3.5 Results

3.5.1 SHPB calibration

Each bar was individually calibrated using the Bars Apart method. The impact velocity, striker bar parameters and output voltage were recorded for each calibration experiment. In Fig. 3.18 the results for the calibration of the input bar for the Inconel 718 and Ti6Al4V systems at Imperial College London are shown. The impact velocity of the striker bar was

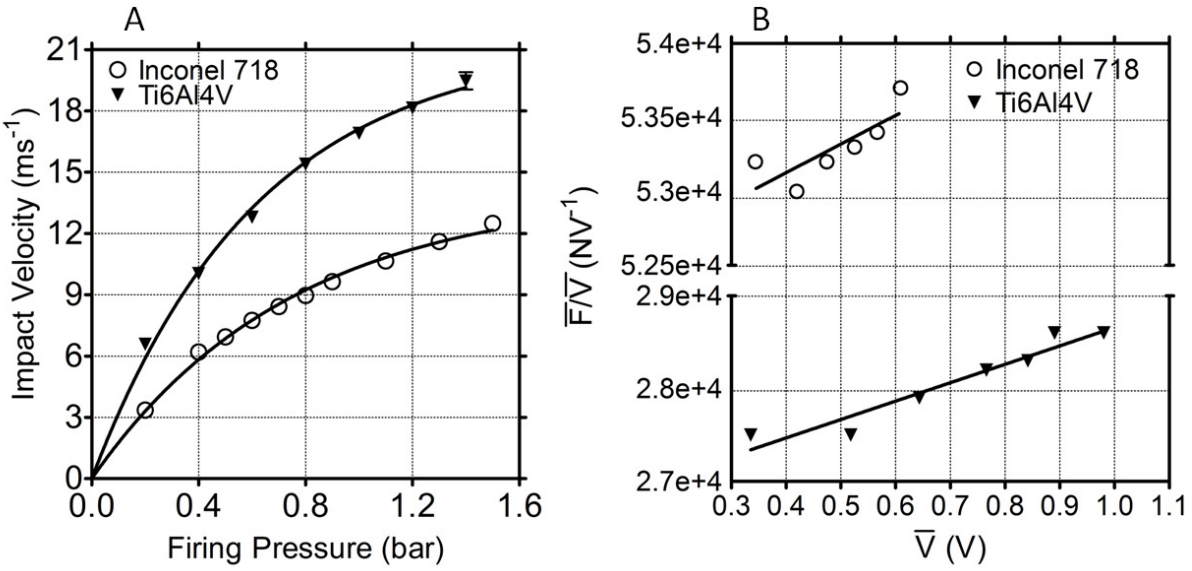

Figure 3.18: **Comparison of Ti6Al4V and Inconel 718 bars calibration.** In the left, plot of the impact velocity versus firing pressure for Ti6Al4V and Inconel 718 striker bars respectively of 210 mm and 186 mm length. Each data point represents the average of three independent measurements. In the right, average force and voltage calculated using the Calibration application for different impact velocities for the two bar materials. A linear fit is applied to the data in order to calculate the calibration parameters k and b for each bar.

Laboratory	**Bar Material**	**Date**	$\mathbf{k}_{in}$	$\mathbf{b}_{in}$	$\mathbf{k}_{out}$	$\mathbf{k}_{out}$
Imperial	Inconel 718	14/11/12	54158	-0.0200	52418	0.0353
		5/6/13	51585	0.0627	55031	-0.0083
	Ti6Al4V	14/11/12	26654	0.0756	25392	0.22351
Cavendish	Inconel 718	10/08/2010	57858	-0.0503	52832	0.05145
		07/05/2011	58962	-0.0945	53734	-0.0765
		01/06/2012	58744	-0.2158	55933	-0.0982

Table 3.3: **Calibration parameters** Values of calibration parameters calculated for different bar materials and different SHPB systems

plotted against the gas gun firing pressure: a high degree of repeatability was observed in the impact velocity for experiments performed with the same firing pressure. The experiments at lower firing pressure demonstrated the highest variability (± 3.4% of the velocity measurement). In Table 3.3 the calibration parameters for all the bar materials used are reported.

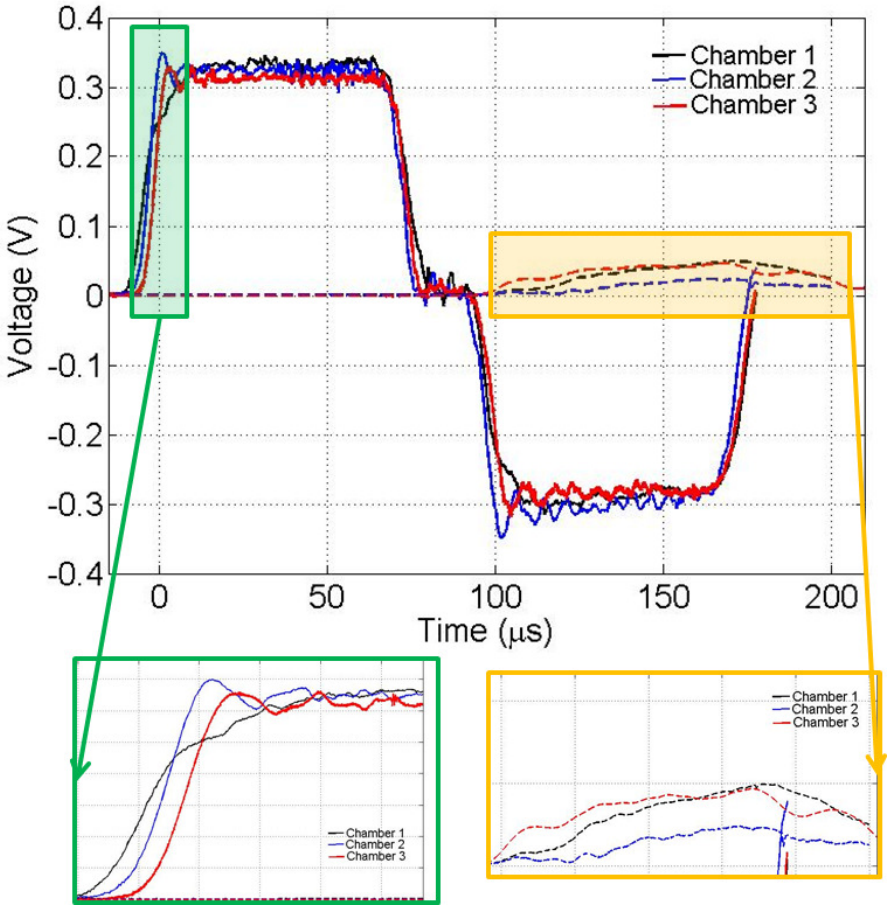

Figure 3.19: **Comparison of strain gauges signals obtained from compression of water using different confinement chambers.** 1 ml of water was compressed using the three confinement chamber prototypes with an impact velocity of 3.4 ms^{-1}. In green the rise of the incident pulse is highlighted, while in yellow the zoom of the signals transmitted on the output bar.

3.5.2 Comparison of the performance of the different confinement chambers

Here a comparison of the performance of the three different chambers is presented. In Fig. 3.19 the results of compression experiments performed on 1 ml of water samples and impact velocity of 3.4 m s^{-1} using the three different chambers. The gauge signals obtained for experiments performed with chamber 1 showed a very slow rise and no Pochammer Chree oscillations for the input bar, (as highlighted in the lower left zoom of Fig. 3.19) due to misalignment of the SB and IB at impact, caused by the weight of the chamber. The signals obtained from gauges on the input bar for experiments performed with chambers 2 and 3 showed equal rise time and Pochammer Chree oscillations, indicative of good SB

and IB alignment. However, the output signal for chamber 2 was significantly lower than for chamber 3. This was due to loss of water caused by the relative movement of the inner and outer cylinders, which corresponded to misalignment of the fluid channel used to load the liquid samples. The design of the third chamber was focused on preventing sample loss. This was achieved with a one main central cylinder piece with double inner O-rings. As shown in the right zoom in Fig. 3.19 the output signal correspondent to experiments performed with chamber 3 shows a clear initial rise followed by a quasi-flat plateau. This suggested that a high pressure existed inside the chamber along with no significant liquid loss. Hence, chamber 3 was chosen for the cell pressurisation experiments and a full characterisation of the confinement system was performed only for this chamber design. In order to evaluate the effects of the confinement chamber on the gauges signal due to possible friction effects a Bar together experiment was performed with and without the chamber mounted on the input and output bar. As shown in Fig. 3.20 the rise time for the input and output signals was unaffected by the presence of the chamber. The only noticeable difference was the amplitude of the Pochammer Chree oscillations on the output bar signal which was larger for the experiments performed without the chamber. This, however, lies within experimental error.

3.5.3 Quasi-static characterisation of the confinement chamber

The confinement chamber was tested under quasi-static conditions in order to evaluate the hoop strain and the inner pressure developed during compression. In Fig. 3.21 A the inner pressure P_i as measured from the load cell of the INSTRON 5866 machine versus the hoop strain measured on the outer surface of the chamber are plotted for three independent experiments. It is evident that P_i is linearly proportional to ε_θ for values of hoop strain higher than $5\text{x}10^{-4}$ and the maximum standard deviation for values of pressure in the linear portion of the curve is 0.36 MPa. In Fig. 3.21 B the deviation coefficient ς is plotted versus the hoop strain for the same three experiments. The curves show that for strain higher than 0.0005 the inner pressure measured using the hoop strain data is in agreement with the values of pressure measured from the load cells. These

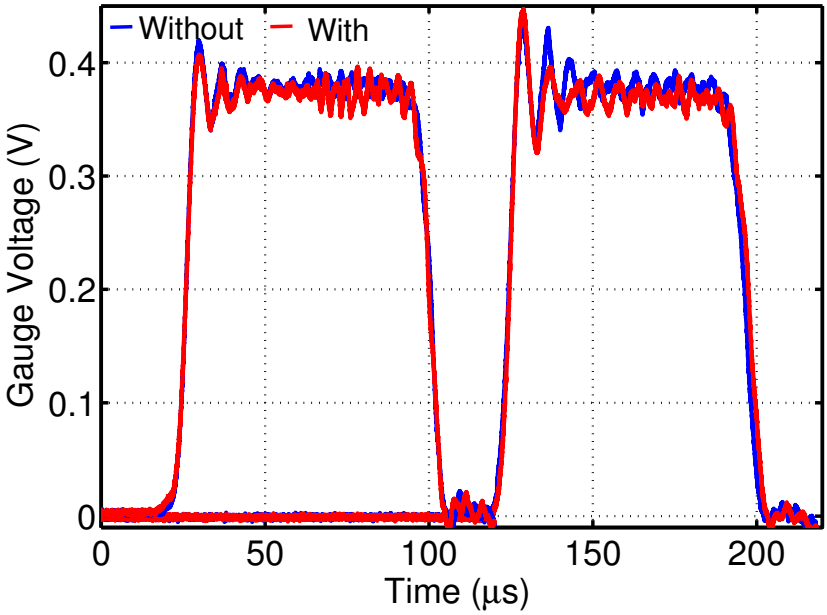

Figure 3.20: **Comparison of strain gauges signal for Bar together experiments with or without the confinement chamber 3** The striker bar was fired towards the input bar with impact velocity of 6.2 ms^{-1}. The input and output strain gauges signals were recorded for the same experiment performed with or without the confinement chamber mounted on the bars. No significant differences were observed between the two tests.

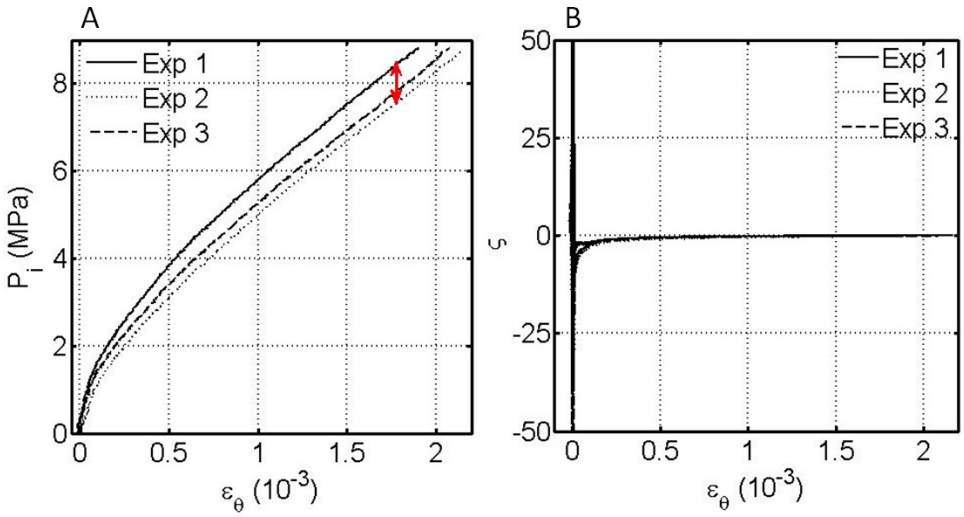

Figure 3.21: **Characterisation of the chamber hoop strain and inner pressure during quasi-static compression experiments.** A, the pressure calculated from the Instron load cell data versus the hoop strain measured by the strain gauges mounted on the chamber during the compression of 6.2 mm thick and 12.7 mm diameter gel discs. The red double arrow indicates the larger variability between three independent experiments. B, the deviation of the values of inner pressure calculated with the two different method (from Instron load cell data and from the confinement chamber hoop strain data) as a function of the hoop strain.

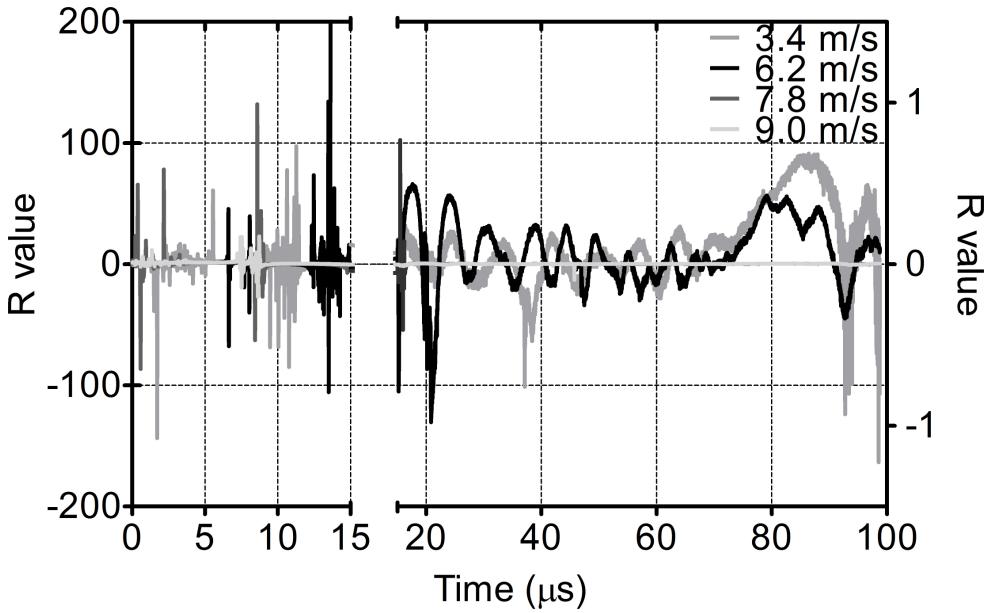

Figure 3.22: **Stress equilibrium in compression of water experiments for different impact velocities.** R values for compression of 800 μl water samples for impact velocities varying from 3.4 to 9.0 ms^{-1}. Values of R in the time interval 0 to 15 μs are plotted on the left axes (range -200,200) while values of R after 15 μs are plotted on the right axes (range -1.5,1.5).

results demonstrate that the hoop strain of the chamber can be used as a measure of the pressure developed inside the chamber during compression experiments.

3.5.4 Characterisation of the modified SHPB system: liquid samples

3.5.4.1 Stress equilibrium

One of the conditions that validate SHPB analysis is that the specimen reaches a state of stress equilibrium in a time significantly lower compared to the total duration of the compression experiment. In Fig. 3.22 the average value of R calculated for experiments with different impact velocities, each in triplicate, was plotted versus time. The oscillations in the values of the adimensional parameter R were very large in the first 15 μs of the compression experiments for all the different impact velocities, but after 15 μs the values of R were lower than |1|, confirming that the specimen had reached stress equilibrium. Thus, one-wave SHPB analysis was validated for compression experiments performed with the

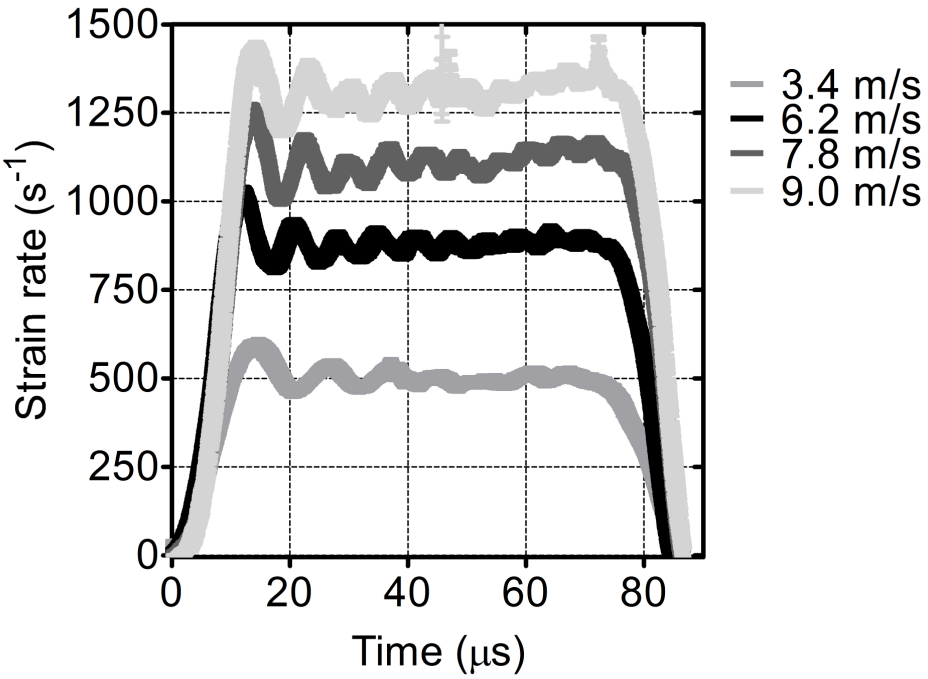

Figure 3.23: **Strain rate calculated from water compression experiments at different impact velocities.** Each line represents the average ± standard error of three independent experiments. Data were acquired at 5 MHz.

confinement Chamber 3 on liquid samples of 800 μl in volume.

3.5.4.2 Chamber inner pressure from SHPB data

In order to characterise the performance of the SHPB system modified with a confinement chamber, compression experiments were performed on 800 μl water specimens. Different firing pressures (0.2, 0,4, 0.6 and 0.8 bar), which correspond to impact velocities of 3.4, 6.2, 7.8 and 9.0 m s^{-1} were used to launch the striker bar towards the input bar and generate compression waves. Experiments were repeated 3 times to verify repeatability. As shown in Fig. 3.23, varying the impact velocity it was possible to achieve strain rates in the range of 500-1300 s^{-1}. Moreover, the average strain rate from each experiment remained constant for the duration of the compressive pulse. The pressure developed inside the chamber during SHPB compression experiments was calculated using the data collected from the strain gauges mounted on the bars. As explained in the Data Analysis section, a time window of the duration of 4/3 of the compressive pulse length was used to cut the gauges signals. The R values for all experiments confirmed that stress equilib-

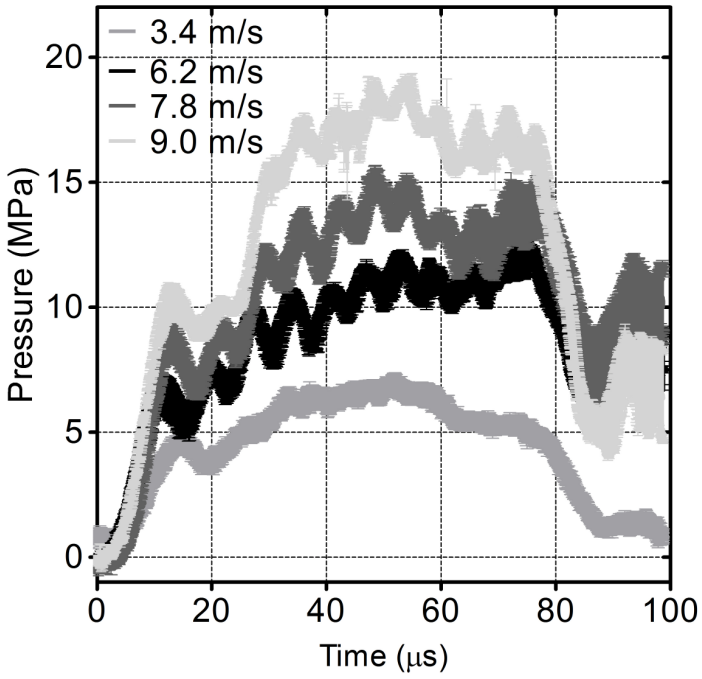

Figure 3.24: **Single pulse pressure developed inside the chamber in SHPB water compression** The pressure developed inside the confinement chamber as calculated with 1-wave analysis using the first incident, reflected and transmitted pulses calculated from the bar strain gauges data for SHPB compression of 800 μl of water at different impact velocities. Each line represents the average ± standard error of three independent experiments. Data were acquired at 5 MHz.

rium was reached within a short time, compared to the duration of the compressive pulse. One-wave analysis was used to calculate the pressure developed inside the chamber. In Fig. 3.24 the values of pressure calculated for experiments performed varying the impact velocity are presented. Increasing the impact velocity, higher pressures could be achieved within the chamber with the same duration but different plateau pressures. A high degree of repeatability was observed: the standard error was calculated from three independent experiments and plotted on the graph as error bars for each data point, demonstrating that no significant overlap of the pulses generated with different impact velocities was observed.

Repeated experiments at the highest impact velocity lead to failure of the chamber initiating around the hole used to insert the liquid. Hence, further characterisation and cell pressurisation experiments were performed with impact velocities up to a maximum of 7.8 m s^{-1}, to avoid damaging the chamber.

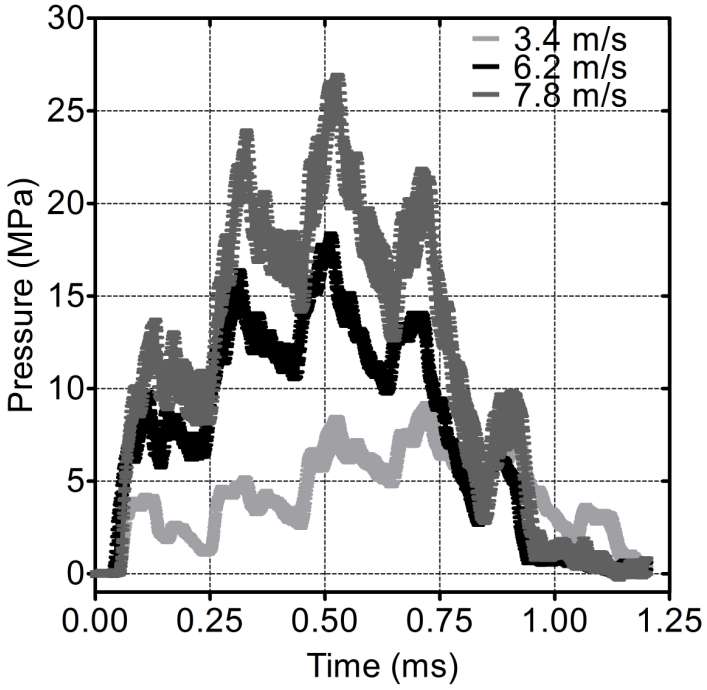

Figure 3.25: **Confinement chamber inner pressure calculated from hoop strain measurements** Inner pressure was calculated using thick walled cylinder theory from the measurement of hoop strain of the confinement chamber during SHPB compression of 800 μl of water at different impact velocities. Each line represents the average $\pm$ standard error of three independent experiments. Data were acquired at 5 MHz, but for image clarity data were plotted every 10 μs.

3.5.4.3 Chamber inner pressure from hoop strain measurements

The pressure developed within the chamber varying the impact velocity of the striker bar was evaluated using the measurement of the hoop strain of the chamber. As shown in Fig. 3.25 varying the impact velocity different levels of inner pressures were developed, with the lower velocity corresponding to the lowest pressure. A high degree of repeatability was observed between subsequent experiments with the same impact velocity. However, the total duration of the pressure event recorded from hoop strain data was significantly longer than one single SHPB pulse ($\approx 80\mu$s). These results suggested that multiple SHPB pulses were transferred through the sample and hence that the SHPB analysis had to be extended to 5 subsequent incident pressure pulses.

3.5.4.4 SHPB versus hoop strain measurement of the chamber's inner pressure

A comparison between inner pressure calculated using the hoop strain measurement and the SHPB strain gauges data extended to multiple subsequent pulses is presented in Fig. 3.26 for an experiment performed with firing pressure of 6.2 ms^{-1}. The results show that the two different methods provide comparable values of inner pressure: they both show five subsequent pressure pulses, each of the duration of approximately 200 μs with increasing peak pressure up to the third peak for the hoop data and fourth for the SHPB data. However, it is evident that the values of pressure calculated from the SHPB gauges data are more noisy and slightly higher in modulus compared to that obtained from the hoop strain data. The SHPB data suggest that the pressure inside the chamber drops almost to 0 MPa after each pulse, while the data from the hoop strain measurement suggest that the pressure after each pulse is hold and the next pulse adds on top of the previous one up to the fourth pulse after which the inner pressure drops almost to 0 MPa and then the last pressure pulse is loaded. In general, the two techniques provide repeatable measurements of the pressure developed inside the chamber and both were used to determine the average values of pressure, impulse and peak pressure in the experiments.

3.5.4.5 Average pressure developed in the chamber

The average pressure developed in the chamber for SHPB compression experiment performed with different impact velocities of the striker bar was calculated averaging the values of pressure obtained from the SHPB gauge data and from chamber hoop strain data. As shown in Fig.3.27 increasing the impact velocity provided higher pressure in the chamber. Experiments performed at the lowest impact velocity showed six subsequent pulses, while the other two impact velocities were associated with five cleat pulses. Moreover, the shape of the pulses was trapezoidal for experiments with impact velocity 3.4 m s^{-1} while was triangular for experiments at higher impact velocity. The pressurisation impulse as well as the peak pressure were calculated for each experiment. Results are presented in Fig.3.28 where the average values from three independent experiments are

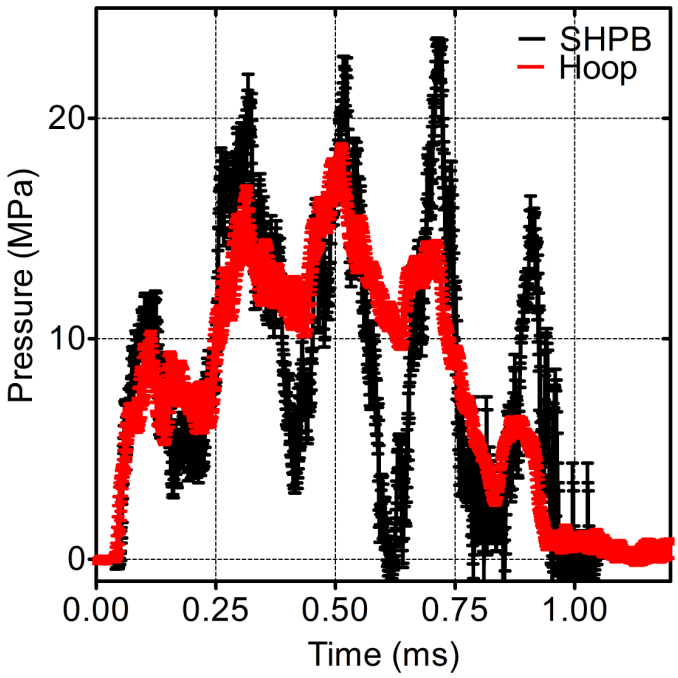

Figure 3.26: **Comparison of chamber inner pressure calculated from SHPB strain gauges data and chamber hoop strain data** Each line represents the average ± standard error of three independent SHPB water compression experiments with impact velocity of 3.4 ms^{-1}. Data were acquired at 5 MHz, but for image clarity data were plotted every 10 μs.

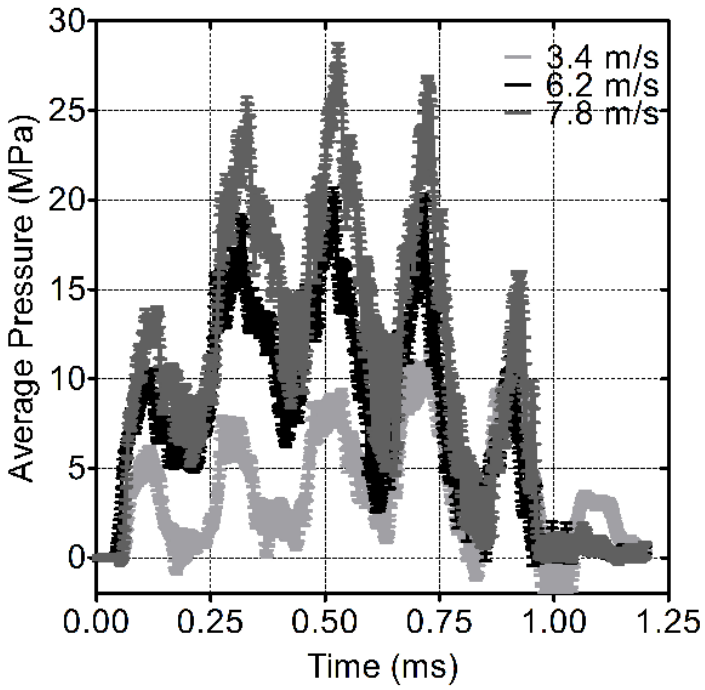

Figure 3.27: **Average confinement chamber inner pressure in SHPB water compression experiments with different impact velocities.** The average pressure developed inside the chamber during SHPB water compression was obtained using the values of pressure calculated from 1-wave SHPB analysis and from hoop strain measurements for each time point. Each line represents the average ± standard error of three independent experiments. Data were acquired at 5 MHz, but for image clarity data were plotted every 10 μs.

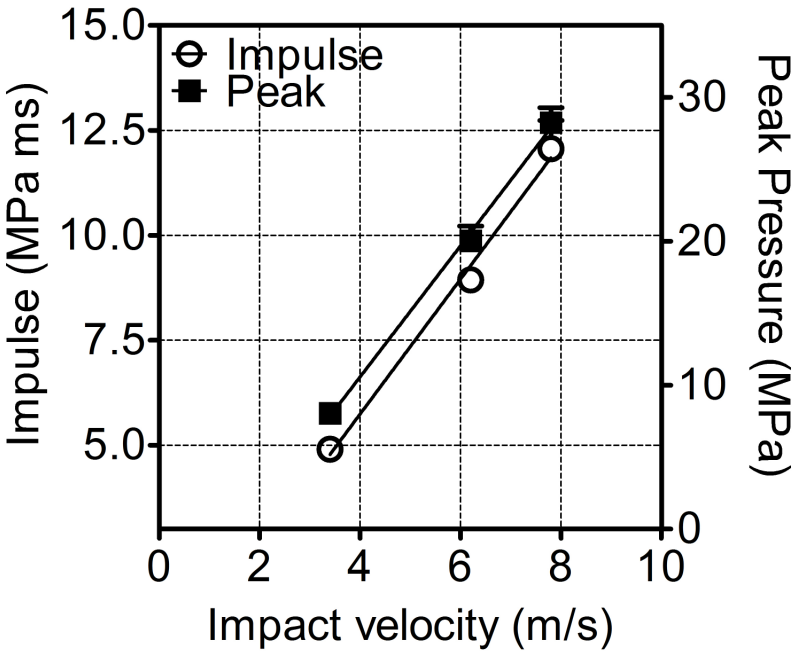

Figure 3.28: **Impulse and peak pressure in SHPB water compression experiments.**

plotted as a function of the impact velocity. A linear fit indicates that both impulse and peak pressure are linearly correlated to the impact velocity.

3.5.4.6 High Speed Photography

The SHPB compression experiments of liquid samples were monitored with high speed photography. In Fig. 3.29 and 3.30 a series of frames from experiments performed with impact velocities of respectively 3.4 and 7.8 ms^{-1}. The first line of frames shows the relative movement of the input and output bar, correspondent to the subsequent pressure pulses generated in the fluid sample. These first 9 images show no turbulence, hence confirming that the condition of laminar flow as calculated in the "SHPB for liquid samples" section was respected. However, in the frame correspondent to the 900 μs time point for the experiments performed at the highest impact velocity it is possible to notice a front of bubbles forming in proximity of the input bar surface. These becomes more clearly visible in the subsequent frame, where a similar front appears near the output bar surface. In the second line of Fig. 3.30 it is evident that the two fronts progress towards each other and meet approximately at the middle length of the liquid sample. A similar phenomenon

occurs in the experiments performed at the lowest impact velocity but significantly delayed. The first appearance of a front of air bubbles in this experiment corresponds to the frame at the 1.8 ms time point. Moreover, the front seems to originate first next to the output bar surface, while only a small turbulence is evident near the input bar surface. Finally in both experiments we can see that a series of small cavities randomly form and collapse within the liquid volume, for a duration of approximately 30 ms. These results suggest that complex phenomena such as cavitation take place in the fluid sample after the series of pressure pulses have died out.

3.5.5 Characterisation of the modified SHPB system: coverslip samples

The SHPB system with short bars used to mount coverslips was characterised first by performing a comparison of strain gauges data obtained from Bar together experiments performed with and without the inserts present. Typical results are shown in Fig. 3.31. It is immediately obvious that the output signal in the experiments performed with the bar inserts is time shifted by approximately 25 μs which corresponds to the time it takes to the compressive pulse to travel 120 mm of extra bar length, no other significant differences were observed in the input signal, as expected. Analysing more in detail the output signals from the two experiments other differences become evident: although the amplitude of the signals are comparable within experimental error, the amplitude of the Pochammer Chree oscillations in the experiment with inserts is significantly reduced. Moreover, the duration of the output pulses are not the same: the arrows in Fig. 3.31 highlight the duration of the pulses which was reduced in the case of the experiments with inserts by approximately 10%. Finally, several spikes are present in the signals from experiments with inserts which suggest that the alignment of the inserts with the bar was not optimal; however, they could be due to multiple reflections occuring within the bar inserts after the first stress pulse. All these considerations suggest that a simple SHPB data analysis might not be very accurate when inserts are added. Hence, only the data obtained from the hoop strain of the chamber were used to calculate the pressure developed during the

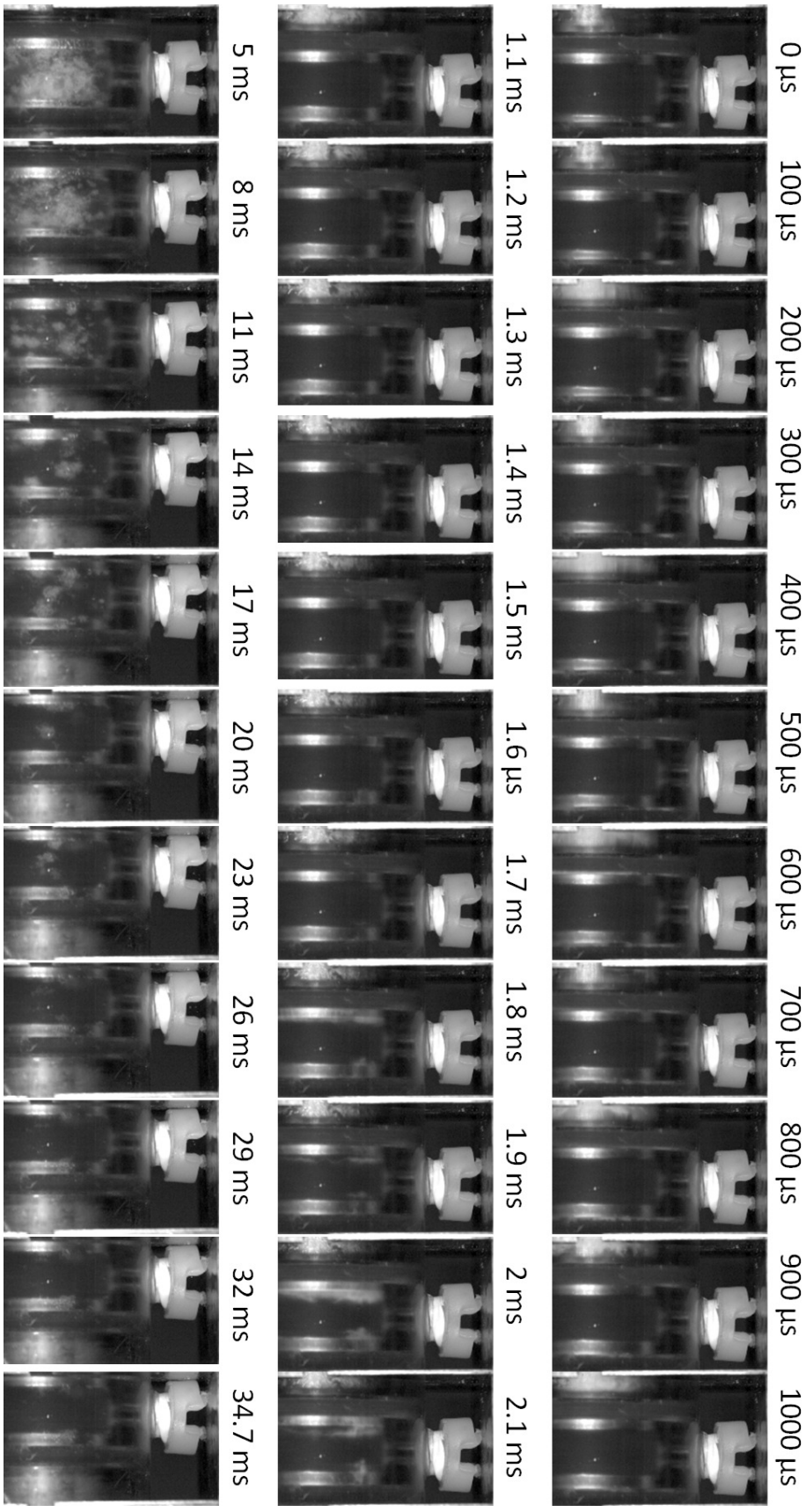

Figure 3.29: **Sequence of high speed photography images acquired during a SHPB water compression experiment with impact velocity of 3.4 ms^{-1}** Images were acquired with a Phantom v12.1 camera at a frame rate of 10^4 frames/s.

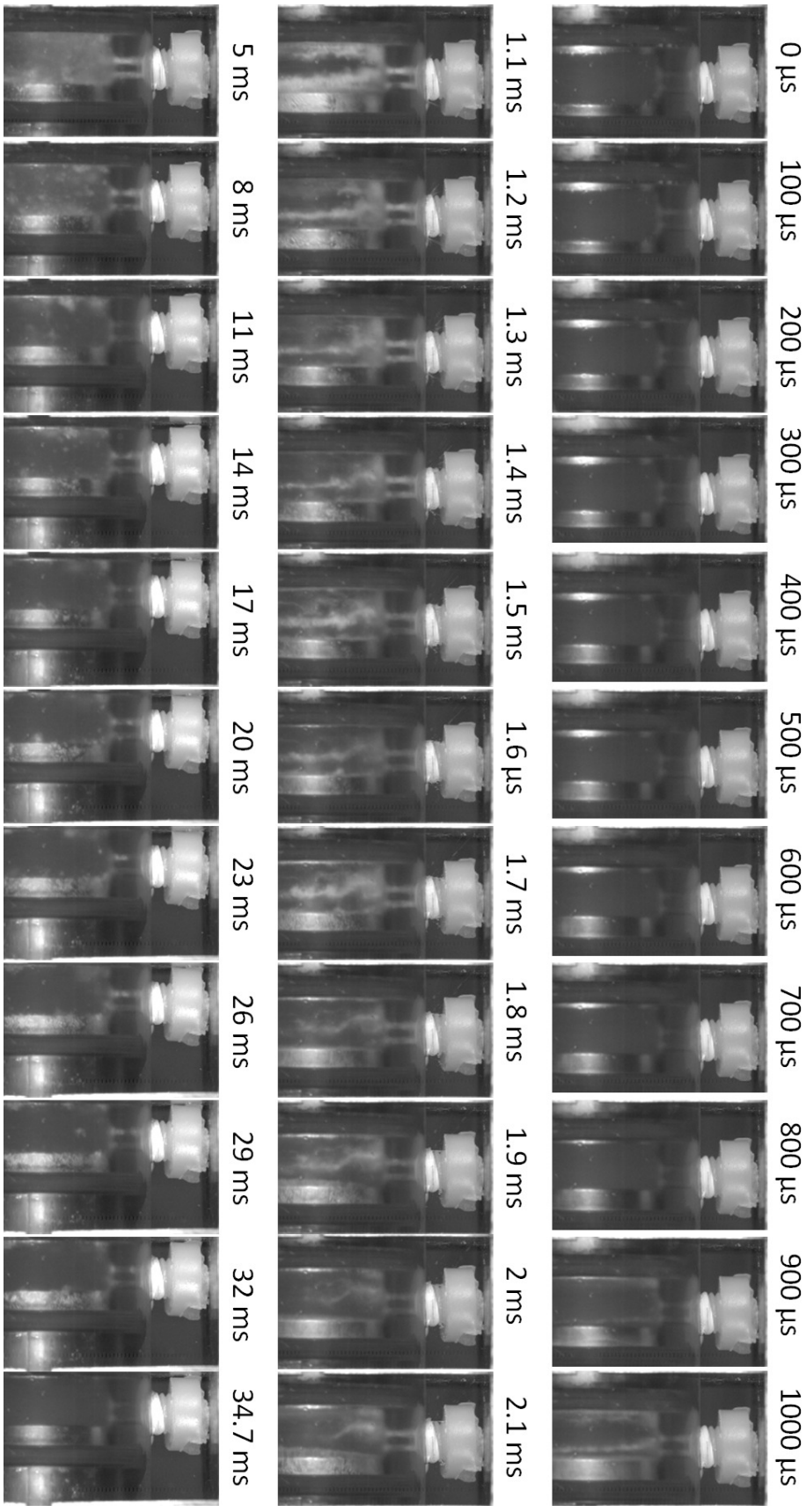

Figure 3.30: **Sequence of high speed photography images acquired during a SHPB water compression experiment with impact velocity of 7.8 ms^{-1}** Images were acquired with a Phantom v12.1 camera at a frame rate of 10^4 frames/s.

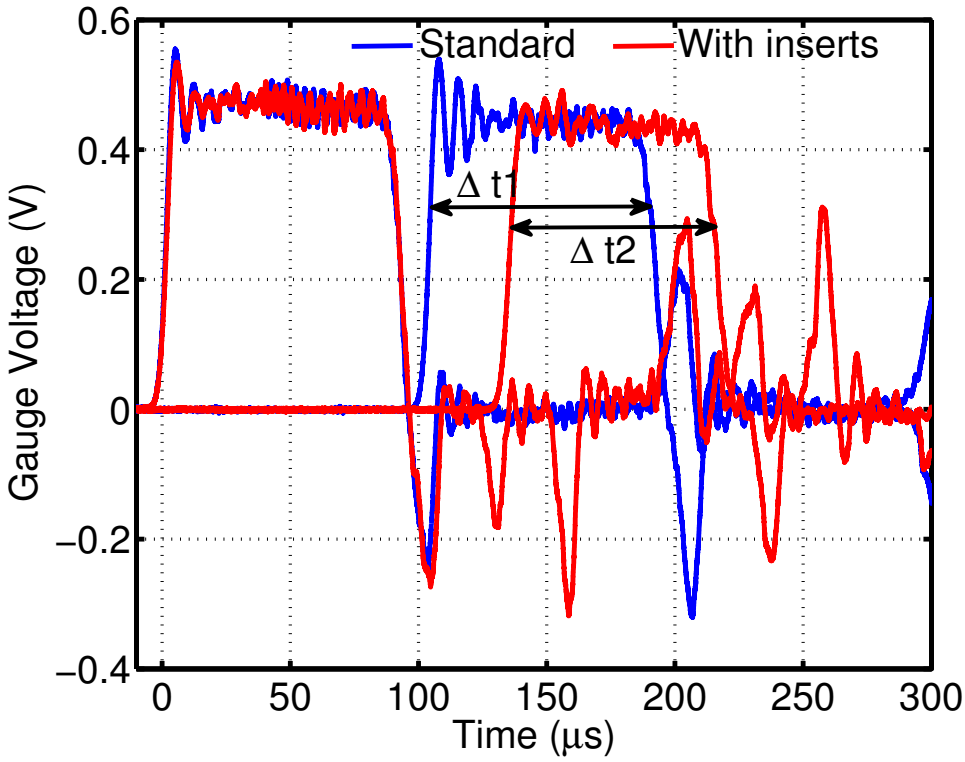

Figure 3.31: **Comparison of SHPB strain gauges signal from experiments performed with or without extra bar inserts** Results from 'Bars together' experiments performed with the SHPB system instrumented with Ti6Al4V bars, with or without the extra 60 mm long bar inserts at the impact velocity of 12.8 ms^{-1}. Data were acquired at 5 MHz.

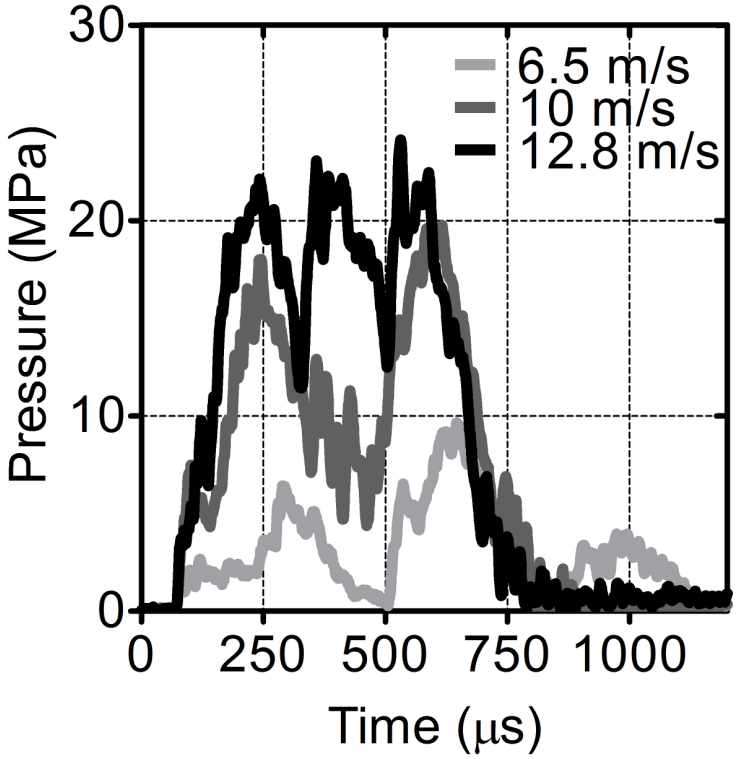

Figure 3.32: **Confinement chamber inner pressure developed during pressurisation of coverslip samples** 8 mm in diameter glass coverslips were mounted and secured on the bar inserts. Once the bar inserts were slided inside the confinement chamber 400 μl of cell medium was transferred inside the chamber, which was then sealed with the nylon screw. SHPB compressive experiments were carried out with impact velocities varying from 6.5 to 12.8 ms^{-1}. The hoop strain of the chamber was recorded and used to calculated the pressure developed inside the chamber. Data were acquired at 5 MHz.

compression experiments.

The results for experiments performed varying the firing pressure are presented in Fig. 3.32. In nine experiments it was possible to recover the intact glass coverslips in all experiments except one at the highest impact velocity. Although an increase in pressure was observed upon increasing the impact velocity, the shape of the pressure traces significantly changed varying the impact velocity. Preliminary analysis of biological samples subjected to the lowest pressure developed with this setup showed that very low cell viability was detectable post compression, indicating that most of the cells had died following the experiments, as will be discussed in the next chapter. No further characterisation of the system was performed and alternative experiments were conducted to study the effects of pressurisation on cell monolayers, as described in Chapter 5.

3.5.6 Pressurisation of live biological samples: cells in suspension

The pressure history, impulse and peak pressure for all the pressurisation experiments performed on cells in suspension were summarised in Fig. 3.33 and Table 3.4. Experiments were performed with different cell types, varying the cell concentration and the striker bar impact velocity. The pressure of each experiment was calculated using 1-wave SHPB analysis as it was not possible to have the strain gauges mounted on the surface of the chamber to measure the hoop strain for sterilisation reasons. Stress equilibrium was achieved within 20 μs of the first pressure pulse. Pressure traces from independent experiments with varying impact velocity were generally comparable, as well as the calculated impulse and peak pressure, with the peak pressure being the parameter with larger variability.

The effects of the cell pressurisation event on the different cell types will be presented in Chapter 4.

3.6 Discussion

The effects of blast waves on biological samples at the cellular level have not been fully characterized. In literature different systems have been proposed to study tertiary blast injuries effects on cell cultures, mimicking shearing of tissues or cell monolayers, by stretching samples below levels known to cause cellular structural failure [22, 39, 40]. Few experimental models are described in literature to study primary blast waves effects among which extracorporeal shock wave systems (ESW) [47, 50], laser-driven shock waves systems [56, 57] or modified shock tubes [53]. The pressure stimulus generated by these systems are in the order of MPa for peak pressures and of few μs in duration. In most of the cases multiple exposures were necessary to damage the biological samples. In the case of a blast event, primary effects may occur in relation to a single or few pressure rises, and the duration of the stimulus can vary from hundreds of μs to few ms [10]. Only one paper was found in which a modified SHPB setup was used to subject cells to

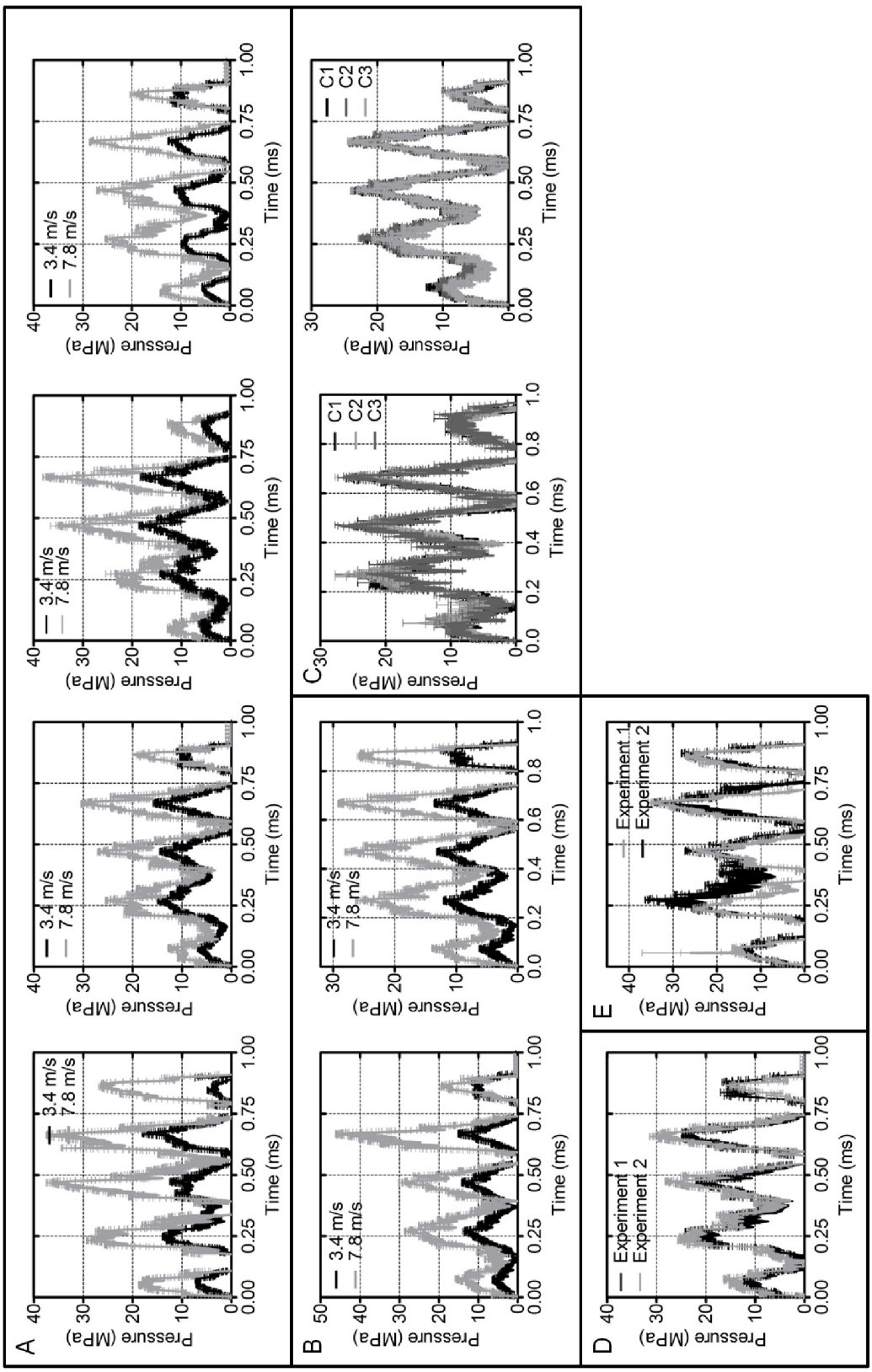

Figure 3.33: **Summary of pressure history in cell pressurisation experiments** 1-wave SHPB analysis results for cell pressurisation experiments performed on (A) mesenchymal stem cells at different impact velocities (B) PLB985 cells at different impact velocities (C) PLB985 cells with varying initial cell concentration (D) bone marrow cells suspensions with impact velocity of 6.2 ms^{-1} (E) mesenchymal stem cells with impact velocity of 6.2 ms^{-1} for cell migration studies

Panel	**Exp.**	**# of samples**	**Conc.**	**Impact velocity**	**Impulse**	**Peak pressure**
			cells ml^{-1}	m s^{-1}	MPa ms	MPa
A	1	4	10^6	3.4	4.38 ± 0.20	17.31 ± 1.20
A	1	4	10^6	7.8	11.84 ± 0.71	40.22 ± 2.45
A	2	5	10^6	3.4	5.22 ± 0.11	16.03 ± 0.36
A	2	5	10^6	7.8	9.56 ± 0.34	30.49 ± 0.74
A	3	4	10^6	3.4	5.62 ± 0.52	17.65 ± 1.81
A	3	4	10^6	7.8	11.17 ± 0.52	36.95 ± 3.46
A	4	5	10^6	3.4	4.13 ± 0.33	12.67 ± 0.36
A	4	4	10^6	7.8	11.17 ± 0.52	28.79 ± 0.25
B	1	4	10^6	3.4	5.56 ± 0.45	14.97 ± 0.44
B	1	5	10^6	7.8	11.71 ± 0.69	38.46 ± 9.69
B	2	4	10^6	3.4	5.28 ± 0.29	13.50 ± 0.26
B	2	4	10^6	7.8	12.24 ± 0.10	29.33 ± 0.43
C	1	3	10^6	6.2	9.47 ± 0.06	26.93 ± 0.84
C	1	3	4 x 10^6	6.2	9.87 ± 0.20	26.78 ± 1.00
C	1	3	8 x 10^6	6.2	9.40 ± 0.13	27.34 ± 0.87
C	2	3	10^6	6.2	8.89 ± 0.38	24.08 ± 0.80
C	2	3	4 x 10^6	6.2	9.38 ± 0.16	23.75 ± 0.16
C	2	3	8 x 10^6	6.2	8.67 ± 0.14	23.98 ± 0.56
D	1	3	10^7	6.2	8.90 ± 0.86	26.63 ± 1.38
D	2	3	10^7	6.2	9.90 ± 0.98	28.72 ± 3.82
E	1	3	10^6	6.2	10.90 ± 0.38	33.99 ± 4.92
E	2	3	10^6	6.2	12.11 ± 1.52	35.35 ± 1.06

Table 3.4: Summary of calculated impulse and peak pressure

high pressure waves [63]. In their study they used a SHPB system with 6 m long bars to generate a 2 MPa pressure pulse of the duration of 0.7 ms on neuronal cells grown on a glass slide. However, very little characterisation of the system was presented and no relation between the pressurisation parameters and the cellular damage observed were reported. Here, a modified split-Hopkinson pressure bar setup has been designed to test live biological samples under compressive loading conditions. Three different chamber designs were constructed and tested to study live biological samples under compression in liquid environment. Chamber 3 has been chosen as the best design since it prevented misalignment of the bars during the experiments, allowed the recovery of the samples, and also allowed the chamber hoop strain measurement during compression.

Experiments performed with water suggested that the classical Hopkinson bar theory could be used to calculate the pressure developed inside the chamber during the experiments, since equilibrium was reached in a short time compared to the duration of the pressurisation event. Measurement of the chamber hoop strain during SHPB compression of water indicated that the duration of the entire pressure stimulus was of approximately 1 ms, hence SHPB analysis was expanded to multiple consecutive pressure pulses. The magnitude and duration of the impulsive overpressure in the confinement chamber could be successfully controlled. Pressure history, impulse and peak pressure were calculated for all the cell pressurisation experiments performed.

Chapter 4

Pressure-induced damage in live biological samples

4.1 Introduction

The use of Improvised Explosive Devices (IED) in the recent conflicts in Afghanistan and Iraq have resulted in severely injured casualties with complex musculoskeletal injuries [14]. As described in the first chapter, blast injuries can be classified with respect to the physical mechanism that causes the injury. This chapter will focus exclusively on primary blast injuries. Primary injuries are a result of the initial blast overpressure that transmits forces producing violent differential acceleration to the human body causing direct tissue damage. Primary blast injuries affecting the musculossketal system include compartment syndrome [4] and traumatic amputations [4]. Compartment syndrome is a serious condition that involves increased pressure in a muscle compartment which can lead to muscle and nerve damage. There are reported cases of patients subjected to explosions who develop delayed compartment syndrome in apparently uninjured extremities [96]. Further studies of the effects of blast overpressure on live tissues and blast-induced release of inflammatory mediators [4], for example, may help better understand the etiology of this syndrome.

Blast-induced musculoskeletal injuries are also aggravated by the longer term complica-

tions known as heterotopic ossification (HO), an aberrant bone formation near the wound site [26,97]. It has been hypothesized for HO that bone progenitor cells, such as mesenchymal stem cells (MSCs) are adversely affected in blast-trauma resulting in inappropriate wound-healing and repair processes [26, 28, 29]. However, the cellular and molecular processes related to the growth of the ectopic bone following blast trauma remain unclear [97]. Improving treatments for HO requires a better understanding of cellular and molecular changes that occur in biological samples subjected to overpressure.

In this chapter the effects of high intensity pressure waves (HIPWs) on live biological samples were investigated. The research focused on the acute and short term effects of HIPWs on cells in suspension generated using the Split Hopkinson Pressure Bar (SHPB) system described in the previous chapter. First, the biocompatibility of the confinement chamber was assessed with different cell types. Initial HIPWs experiments were performed using human PLB985 cells because this cell line is simple to culture and proliferates rapidly. Subsequent experiments were performed using murine bone marrow cell suspensions, which contain a mixture of cells with different sizes and granularity. Similar studies were also performed on mesenchymal stem cells (MSCs) because of their potential role in damage and repair injury processes in blast injury. Specifically, cell damage was determined by measuring cell viability, cell lysis and cell metabolic activity. Functional changes in cells subjected to HIPWs were analysed by measuring cell proliferation, migration and differentiation. Comparative studies were also conducted on the effects of the medium in which cells were maintained following exposure to HIPWs. Finally, similar studies of the effects of HIPWs on adherent cells were also carried out.

4.1.1 Bone marrow and its role in blast injuries

Bone marrow, also called myeloid tissue, is a soft, gelatinous tissue that fills the central cavities of bones. It is composed of two different types of tissues called the red marrow and the yellow marrow. The red marrow is a highly vascular fibrous tissue containing mainly hematopoietic cells. In adult humans it is found mainly in the epiphyseal ends of long bones. The yellow marrow is a less vascularised tissue composed primarily of fat cells

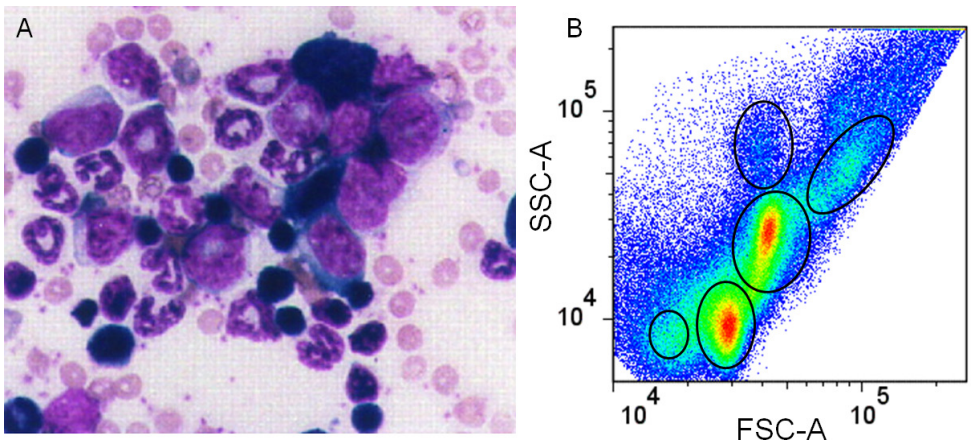

Figure 4.1: **Bone Marrow Cell Populations** A, Murine bone marrow isolates. Image reproduced from [98]. Copyright (1997) National Academy of Sciences, U.S.A. B, flow cytometry FSC-SSC dot plot showing the numerous bone marrow cell populations which can be identified because they show different size (FSC axes) and different granularity (SSC axes), as explained later on in section 1.2.7

which can be found in the medullary cavity of long bones. The main function of the bone marrow is hematopoiesis, the production of blood cellular components from hematopoietic progenitor cells which can differentiate into various blood cells such as erythrocytes, granulocytes, monocytes, and platelets. The bone marrow also plays an important role in the immune defense system, through the production of lymphocytes. As shown in Fig. 4.1 A and B, the bone marrow is characterised by a variety of cell types with different sizes and degrees of granularity. It can be hypothesised that different cell types would be dissimilarly affected by a pressure wave, such as the one experienced in blast injuries.

It has been shown that trauma and hemorrhagic shock can induce bone marrow suppression and release of hematopoietic progenitor cells into the peripheral blood [99]. Moreover, animal studies indicated that trauma-induced mobilization of bone marrow cells to the site of injury was necessary for successful wound healing processes [99]. In the context of blast injuries, bone marrow has been implicated in relation with the acute phase sequestration of plasma iron, related to activation of hemopoiesis and leukocyte maturation, as well as bone marrow embolism in which hemopoietic cells and fat droplets have been reported to occlude a pulmonary artery [17]. Moreover, it has been hypothesised that there is a systemic response to blast-induced lung injury that involves systemic release of neutrophils from the bone marrow and production of inflammatory cytokines which

contributes to hypotension and bradycardia [17]. However, the authors conclude that it is still not clear whether these are shock-induced pathological features or enhanced responses to extremely traumatic injuries.

4.1.2 Mesenchymal stem cells and their role in blast trauma

MSCs are a heterogeneous population of self-renewing and multipotent stem cells that can differentiate into a variety of cell types [100]. They usually reside in the bone marrow but they have been found also in muscle tissue, adipose tissue, epidermal tissue, and around blood vessels [101]. MSCs have been shown to differentiate into osteocytes, chondrocytes, myocytes, adipocytes, fibroblasts, epithelial cells and neurons [102]. MSC cultures display a rather homogeneous population of fibroblast-like cells, characterized morphologically by a rounded cell body with a few cell processes that are long and thin. Properties of cultured MSCs include: adherence to plastic in culture; expression of markers including CD105, CD73, Sca-1, CD90; lack of expression of other markers such as CD45, CD34, CD11b, and CD31 [103, 104]; and the ability to differentiate into bone, cartilage and fat. MSCs are also characterized by an extended cytokine expression profile, which include interleukines, chemokines and growth factors [102].

MSCs constitute a functional component of the hematopoietic stem cell (HSC) niche that support hematopoiesis, regulating the quiescence and proliferation of HSC [100]. Also, MSCs have immunosuppressive properties, demonstrated *in vitro* and *in vivo* by their ability to mediate anti-proliferation of T-cells, and have immunomodulatory properties, that regulate the maturation of dendritic cells and inhibiting natural killer cells *in vitro* [100, 105].

In addition, MSCs have been shown to be mobilised into the bloodstream following injury/trauma, and to migrate to the sites of injury and participate in repair processes [106]. It is believed that once in the circulation, MSCs are homed to the damaged tissue through processes involving adhesion molecules, chemokine receptors and integrins [107]. Finally, when MSCs have reached the zone of injury they transmigrate across the endothelium and start the repair process by proliferating and differentiating into mature functional

tissue [108]. It has been proposed that MSCs can also contribute to tissue regeneration by modulating the local environment of the injured tissue [106]. For example, Davis et al. [109] collected muscle biopsies from wounded patients. They isolated MSCs from the wounded tissues and observed an increase in the number of progenitor cells with osteogenic potential in the tissue extracted from patients that later developed HO. Moreover, Potter et al. [26] showed that wound effluent collected from patients with early stages of HO was highly osteogenic. Specifically, *in vitro* cultured MSCs in the presence of this effluent show accelerated rates of differentiation into osteroblasts.

All these findings suggest that MSCs may play an important role in the processes affecting the damage and repair of tissues subjected to blast injuries.

4.2 Materials & methods

4.2.1 Cell culture

Cell culture refers to the process by which cells are grown under controlled conditions. In the following sections the protocols used for harvesting and culturing cells used in the HIPW experiments are described.

4.2.1.1 PLB985 cells

PLB985 is a human diploid cell line established from the peripheral blood of a patient with acute nonlymphocytic leukemia. PLB985 cells were a kind gift from Dr. James Pease, Imperial College London. These cells were cultured using standard culture conditions (37 °C and 5% CO_2) in Roswell Park Memorial Institute medium (RPMI, Life Technologies), containing 10% (v/v) foetal bovine serum (FBS, Life Technologies) and 1% (v/v) penicillin-streptomycin (Pen-Strep, Invitrogen). Cells were passaged twice a week and, prior to the high pressure experimentsm, cells were resuspended in RPMI medium containing 0.1% (w/v) Bovine Serum Albumin (BSA, Sigma Aldrich) and 1% (v/v) Pen-Strep and then aliquoted (800 μl) into microfuge tubes.

4.2.1.2 Bone marrow

Bone marrow was flushed from the femurs and tibiae of Balb/c mice with Dulbecco's Modified Eagle Medium (DMEM, Life Technologies) containing 10% (v$\check{}$) FBS and 1% (v$\check{}$) Pen-Strep. Red blood cells were lysed resuspending the cell mixture in 0.2% (w/v) and 1.6 % (w/v) hypotonic solutions of sodium chloride. The remaining viable cells were washed and resuspended in fresh DMEM containing 1% (v/v) FBS and 1% (v/v) Pen-Strep at a concentration of 10^7 cells/ml and aliquoted in sterile microfuge tubes.

4.2.1.3 Mesenchymal stem cells

Murine MSCs were obtained from the femurs, tibiae and iliac bones of Balb/c mice. Bones were digested in Phosphate Buffer Solution (PBS) with 2% (v/v) FBS, Collagenase I (2.5 mg/mL, Sigma Aldrich), Collagenase II (0.7 mg/mL, Sigma Aldrich) and Dispase I (1 U/mL, BD Bioscience). Cells were then seeded in tissue culture flasks and expanded to near-confluency (70%-90%) under standard culture conditions (37°C and 5% CO_2) in DMEM containing 20% (v/v) FBS, 1% (v/v) Pen-Strep, basic fibroblast growth factor (bFGF, 5 ng/ml, Peprotech) and heparin (1 U/mL, Sigma Aldrich). After one week in culture MSCs were detached from the culture flasks using 0.05% (v/v) trypsin with EDTA solution (Invitrogen) and replated in fresh medium (first passage) using the standard culture conditions just described. Cells were typically passaged every 7 days. Cells used in the high pressure experiments were at passage three. On the day of the experiments cells were detached from culture flasks as just described, resuspended in DMEM containing 1% (v/v) FBS and 1% (v/v) Pen-Strep at a concentration of 10^6 cells/ml and aliquoted into microfuge tubes.

4.2.1.4 Neutrophils

Neutrophils were isolated from the bone marrow of Balb/c mice. Briefly, femurs and tibiae of Balb/c mice were dissected, and the marrow was flushed with RPMI medium containing 0.1% (v$\check{}$) BSA. Red blood cells were lysed resuspending the cell mixture in 0.2% (w$\check{}$) and 1.6 % (w/v) hypotonic solutions of sodium chloride. The remaining cells were centrifuged

at 745 g for 6 min. Cells were layered on a three-step Percoll (Amersham Bioscience) gradient (72%, 64%, and 52%) and centrifuged at 1500 g for 30 min. Neutrophils were extracted from the layer between the 64% and 72% Percoll layers and washed once with PBS before being suspended in RPMI medium containing 10% FBS at a concentration of 10^7 cells/ml.

4.2.2 Chamber biocompatibility

To assess the effects of the materials used in the confinement chamber on MSCs, nitrile, neoprene and silicone O-ring conditioned media were generated by placing one O-ring per material in 1 ml of DMEM medium containing 1% (v/v) FBS and 1% (v/v) Pen-Strep. After 15 min the O-ring was removed and 100 μl of each medium were transferred to 3 wells in a 96-well plate containing 10^4 MSCs/well. 100 μl of DMEM medium were added as control. Cell metabolic activity was analysed with a MTS assay, as explained in section 4.2.6.1, when the media were added, and then after 6 h and after 24 h.
The toxicity of the O-ring material on neutrophils was also assessed with flow cytometry, using an Annexin V/PI assay, as described in section 4.2.8.1.
Finally, the biocompatibility of the chamber was investigated inserting PLB985 and MSCs cell suspensions (10^6 cells/ml) into the chamber. Samples were recovered after 5 minutes and analysed with cell viability, cell lysis and cell metabolic activity assays, described in sections 4.2.4, 4.2.6.1 and 4.2.5 respectively. Results were compared to control samples that were not inserted into the chamber.

4.2.3 SHPB cell pressurisation experiments

Initial cell pressurisation experiments were performed using the SHPB system at the Cavendish laboratory, University of Cambridge. However, most of the experiments presented in this chapter were performed with the SHPB system developed at the Royal British Legion Centre for Blast Injuries Studies at Imperial College London. The main difference between the experiments performed at the two institutions was the transport time between the biology laboratory and the SHPB laboratory which was approximately

5 min at Imperial College London and 2.5 h for the University of Cambridge. In Table 4.1 a summary of the experiments performed at the Imperial College London and at the University of Cambridge laboratories.

Table 4.1: Summary of HIPW experiments performed on cells in suspension at Imperial College London and University of Cambridge

Experiment description	**Cell type**	**Number of samples**	**Repeats**	**Laboratory**
Preliminary studies	MSCs	5	20	Cambridge
System biocompatibility	MSCs	3	3	Cambridge
System biocompatibility	PLB985 & MSCs	5	3	Imperial
Effects of HIPW on cell suspensions of different initial concentrations	PLB985	3	3	Imperial
Effects of different HIPW on cell suspensions	PLB985	5	3	Imperial
Effects of HIPW on mixed cell populations	Bone Marrow	3	2	Imperial
Effects of different HIPW on cell suspensions	MSCs	5	4	Imperial
MSCs Migration Study	MSCs	3	2	Imperial
Neutrophils Migration Study	MSCs	3	2	Cambridge

4.2.3.1 Cells in suspension

A schematic of the experimental procedure used in High Intensity Pressure Wave (HIPW) experiments on cells in suspension is presented in Fig. 4.2. Prior to each HIPW experiment cells were cultured and suspended in a liquid medium as described in section 4.2.1. The SHPB bars were cleaned with 70% (v/v) ethanol and allowed to dry. The sterile chamber was placed onto the bars, rinsed twice with PBS and the sample was then loaded with a 21 gauge needle syringe. Different striker impact velocities were used for generating increasing levels of pressures in the cell suspension as described in the previous chapter. After each HIPW experiment, samples were recovered with a syringe, transferred to a new sterile microfuge tube and transported back to the biology laboratory to perform the biological assays decribed in this chapter.

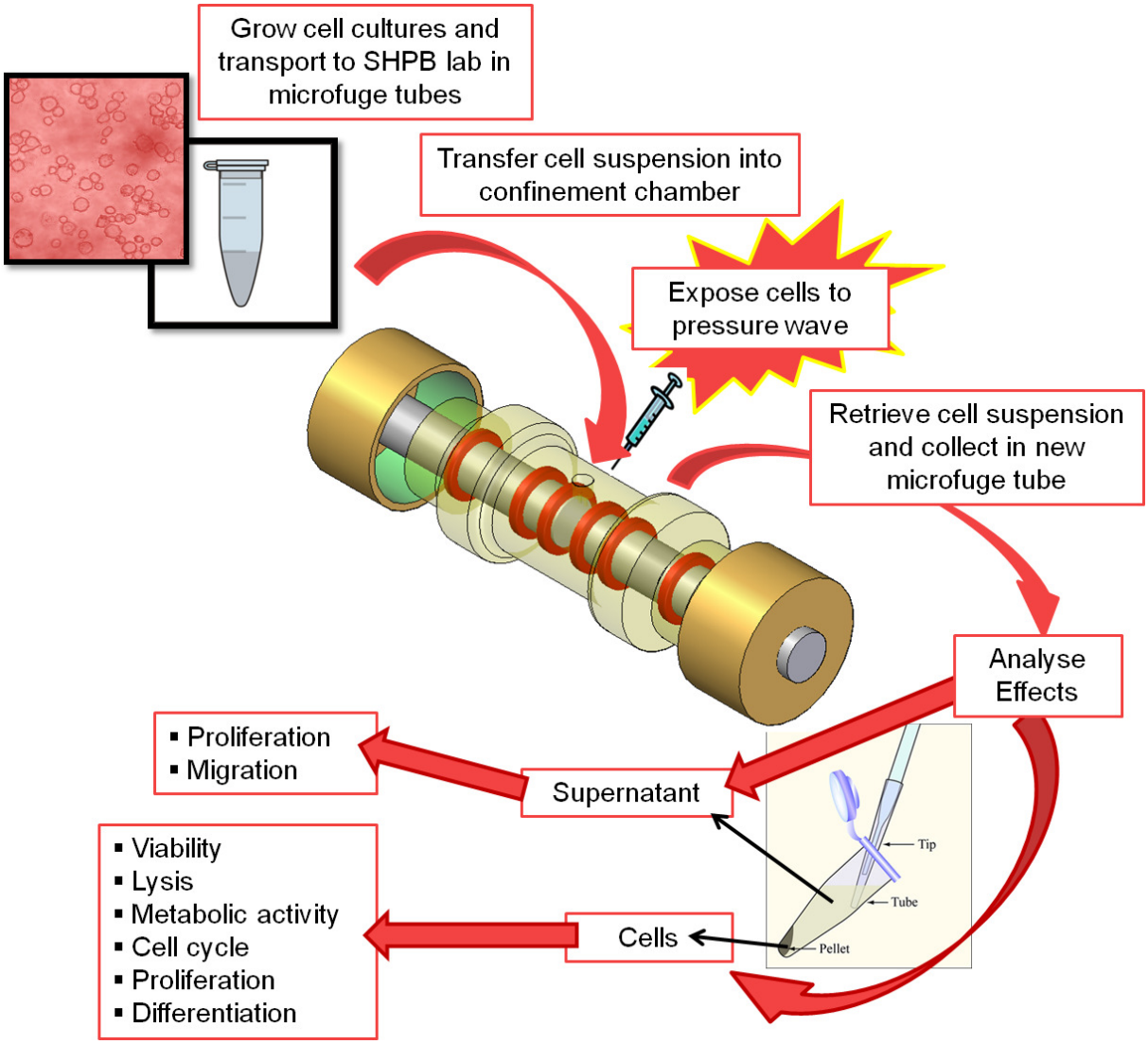

Figure 4.2: Schematic of HIPW experiments on cells in suspension

4.2.3.2 Cell monolayers

The day before the HIPWs experiments a 100 μl drop of cell suspension containing 10^4 cells (MSCs) was spread on a 8-mm diameter glass coverslip and placed in a 24 well plate (16 samples in total). Cells were allowed to adhere for 3 h before 500 μl of complete DMEM culture medium were added to each well. On the day of the experiments, each coverslip was gently lifted from the well, and transferred with tweezers to the surface of one Ti bar insert where it was secured with two M2 nylon screws, as previously described in section 3.3.4. For each HIPW experiment two bar inserts were gently inserted in the chamber which was then filled with DMEM medium with 1% (v/v) FBS and sealed with the nylon screw (please refer to Fig. 3.14). The entire assembly was mounted in the SHPB system, the HIPW experiment was carried out as decribed in section 3.3.4. The entire assembly was then returned to the microsafety cabinet where it was disassembled by first removing the liquid medium. The bar inserts were then removed in order to recover the coverslips, each of which were transferred into a well in a new 24-well plate and covered with fresh DMEM medium (400 μl) for subsequent analysis.

4.2.4 Cell viability

Live cells possess intact cell membranes that exclude certain dyes compared to dead cells. In general, a cell suspension is simply mixed with the dye and then visually examined to determine whether cells take up or exclude the dye. In these experiments 40 μl of cell suspension were stained with 40 μl of 0.4% (v$\check{}$) Trypan Blue solution (Sigma Aldrich) and then diluted, if necessary, with fresh medium. One aliquot (10 μl) per sample was transferred to a counting slide which was then analysed with a microscope: counts of viable (clear cytoplasm) and non viable (blue cytoplasm) cells were performed on four separate quadrants of the slide. and the means per sample were recorded. Each quadrant corresponds to a volume of 10 μl and the concentration of each cell suspension (cells/ml) was obtained by averaging the counts from each of the four quandrants.

4.2.5 Cell lysis

Lysis refers to the dissolution or destruction of cells. When cell integrity is compromised (e.g. the plasma membrane is disrupted), the contents of the cells will be released into the medium in which they are suspended. The measurement of the release of cytoplasmatic lactate dehydrogenase (LDH) enzyme in the medium can hence be used as a measure of cell lysis. LDH activity was measured from cells exposed to HIPW using the LDH-Cytotoxicity Assay Kit II (Abcam). The recovered samples were centrifuged at 160 g for 5 min and the supernatant collected. Three aliquots (10 μl) of supernatant per sample were added to 50 μl of fresh medium. Three 10-μl aliquots of the diluted supernatant per sample were each placed in a wells of a 96-well plate with 100 μl of the LDH assay kit mixture. The plate was then incubated 30 min at room temperature in the dark. Optical density at 450 nm was measured with a Sunrise^{TM} plate reader. In addition controls for each experiment were obtained by measuring three 10-μl aliquots of fresh medium (Background),three 10-μl aliquots of supernatant from cell samples lysed with the lysing buffer provided with the LDH kit (High) and incubated with 100 μl of the LDH assay kit mixture as just described. Cell lysis was expressed as a percentage of the maximum release of LDH obtained from complete lysis of the cell population corrected by the background LDH level in the fresh medium as:

$$LDH\,Release(\%) = \frac{Test\,Sample - Background\,Control}{High\,Control - Background\,Control} \tag{4.1}$$

4.2.6 Cell metabolic activity

The ability of cells to demonstrate metabolic activity in samples subjected to HIPW was studied using a colorimetric CellTiter 96^{R} Aqueous Non-Radioactive Cell Proliferation Assay kit (MTS) (Promega). This is a colorimetric assay in which MTS (3-(4,5-dimethylthiazol-2-yl)-5-(3-carboxymethoxyphenyl)-2-(4-sulfophenyl)-2H-tetrazolium) is bioreduced by viable cells into a formazan product that is soluble in the cell culture medium. The amount of formazan produced is proportional to the number of live cells in the sample.

4.2.6.1 Cells in suspension

To investigate the effects of HIPW of different intensities on cells (PLB985 and MSCs), three aliquots (10 μl) per sample of recovered cell suspension were suspended in 100 μl of fresh culture medium in a 96-well plate. One aliquot (20 μl) of MTS reagent was added to each well and the plate was incubated at 37 °C and 5% CO_2. Fresh medium (20 μl) was also placed in three separate wells of the plate as a background control. After 3 hours the plate was briefly centrifuged (690 g for 2 minutes) to eliminate air bubbles. The absorbance of each sample was measured at 490 nm with a Sunrise^{TM} plate reader.

4.2.6.2 Cell monolayers

To investigate the effects of HIPW on MSCs monolayers, 40 μl of MTS reagent were added to each well of the 24-well plate where the coverslips were positioned and covered with 400 μl of DMEM medium containing 1% (v/v) FBS and 1% (v/v) Pen-Strep. Fresh medium (500 μl) was also placed in three separate wells of the plate as a background control. After 3 hours, 100 μl of medium were collected from each well and transferred to a 96-well plate. The plate was briefly centrifuged (690 g for 2 minutes) to eliminate air bubbles and the absorbance of each sample was then measured at 490 nm with a Sunrise^{TM} plate reader.

4.2.7 Cell proliferation

The term cell proliferation refers to the increase in cell number in a culture due to cell division. Here, cell proliferation was studied by monitoring the metabolic activity of samples at different time points using the MTS assay described in the previous section. To investigate the effects of HIPW on cells, three aliquots of recovered viable cells ($5x10^3$) from each experiment were suspended in 100 μl of fresh DMEM medium containing 1 % (v/v) FBS, placed in wells of 96-well plates (one plate for each time point, 0 h, 24 h, 48 h and 72 h) and allowed to grow for up to 72 hours. At each time point, 20 μl of MTS reagent were added to each well and the plate was incubated at 37 °C and 5% CO_2 for 3 h and absorbance was measured at 490 nm with a SunriseTM plate reader.

Supernatants from cell cultures subjected to HIPW on cells were collected to study their

effects upon cell proliferation of MSCs. Triplicate aliquots of $5x10^3$ MSCs were placed in a 96-well plate and cultured in DMEM medium containing 1% (v/v) FBS. After 10 h the medium was replaced with the harvested supernatants from HIPW experiments obtained by centrifuging the recovered samples at 160 g for 5 min and decanting the supernatant. Metabolic activity was measured with the MTS assay as described in the previous section. Average background, obtained from wells filled with fresh DMEM medium containing 1% (v/v) FBS, was subtracted from all the test samples values and the metabolic activity was expressed as the average absorbance value normalised against the absorbance value at time point 0 h for each HIPW carried out.

4.2.8 Flow cytometry

Flow cytometry is a technique that allows a multiparametric analysis of physical and chemical properties of cells as they are moving in a fluid stream and passing by an electronic detection apparatus [110]. Applications of this technology, used both in basic research and clinical laboratories, include immunophenotyping and cell counting. Immunophenotyping refers to the analysis of heterogeneous populations of cells to identify the specific lineage of single cells through the use of antibodies that detect antigens or markers on the cell. These markers are functional proteins involved in cell communication, adhesion, or metabolism and can be expressed on the cell surface, in the cytoplasm or the nucleus of the cells. Some antigens are found only on one type of cell, whereas, most commonly, a marker is expressed by various cell types. Therefore, multiple markers are used to identify a specific cell population, which requires the use of multiple antibodies conjugated with different fluorochromes (polychromatic flow cytometry) [111].

In a typical flow cytometry experiment, cells are suspended in a liquid medium and stained with a cocktail of antibodies before being analysed with the flow cytometer. As shown in Fig. 4.3, cells individually pass through a focused light source, generally a laser beam, using a hydrodynamic focusing system. A cell suspension is injected in the center of a sheath fluid which, in combination with the narrowing of the central chamber, drags the central fluid generating a single stream of cells that then passes through the light source

focused at a very small region. As cells pass through the laser beam, they scatter light and, if the samples are labeled with fluorochrome-conjugated antibodies, they emit a fluorescent signal. In this system, light scattered in different directions is used to obtain

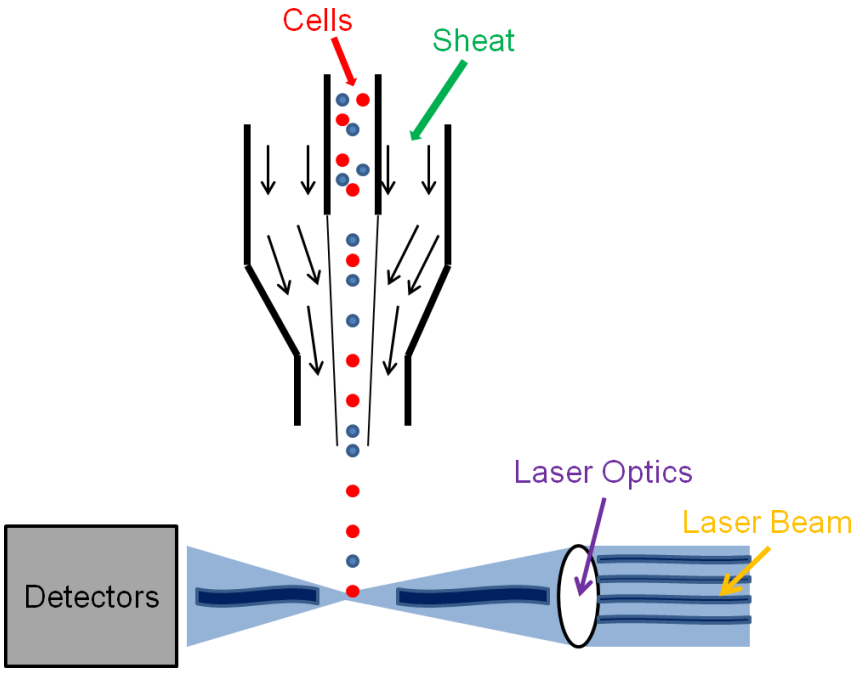

Figure 4.3: **Flow cytometry** A schematic of hydrodynamic focusing of cell suspension in a flow cytometer. The cell suspension is injected in the center of a sheath fluid which, in combination with the narrowing of the central chamber, drags the central fluid generating a single stream of cells that pass through a focused laser beam.

information about different physical properties of the cells. Light that is scattered in the forward direction, up to 20° deflection from the laser beam axis, is directed to the forward scatter channel (FSC) and gives information about particle size. Light scattered at approximately 90° from the excitation line is detected by the side scatter channel (SSC) and provides information about the granular content within cells. Different filters are used to separate fluorescence (FL-) channels to detect the emitted light.

In single stain experiments, isotype controls are used as a negative control designed to measure the level of non-specific background signal caused by primary antibodies when they bind to Fc receptors present on the cell surface. For each marker antibody used in an experiment to evaluate the expression of the antigen on the cell surface, the correspondent isotype control should also be included.

In polychromatic experiments, the emission spectra of a fluorochrome-conjugated anti-

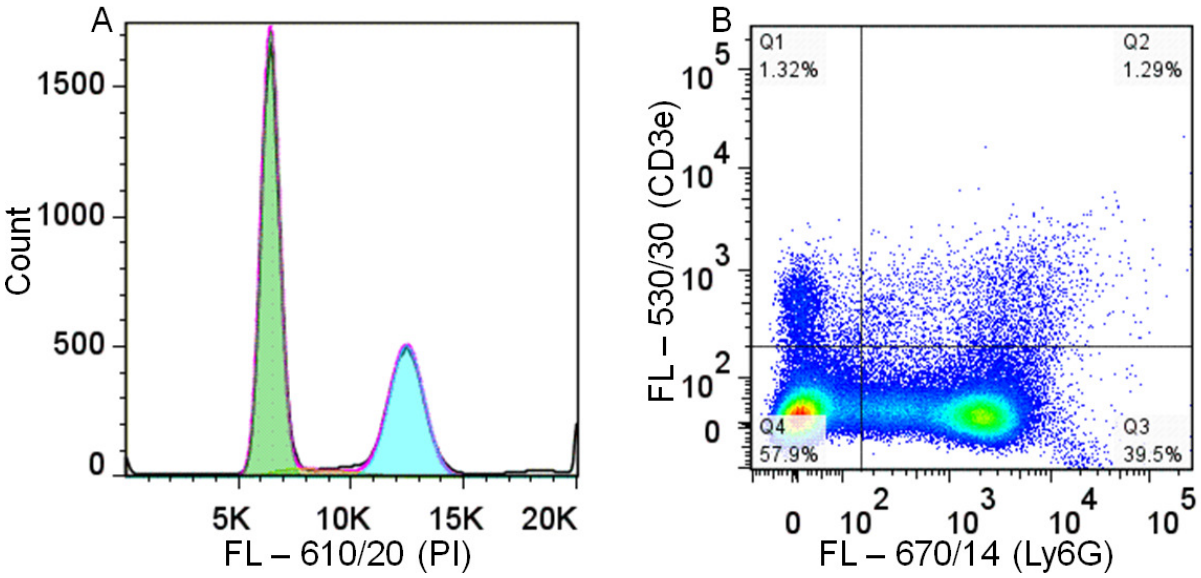

Figure 4.4: **Examples of flow cytometry data analysis** A, data are plotted in a histogram to identify the number of cells that express the marker PI. B, a dot plot showing different cell populations based on their expression of the markers CD3e and Ly6G

body spills over into the other fluorochrome detectors. Therefore, there is a need to compensate for each single staining fluorochrome-conjugated antibody, by mathematically eliminating its contribution from the signal measured in the detectors not assigned to that fluorochrome [111]. This process is carried out by preparing several cell suspensions individually labeled with one fluorochrome-conjugated antibody (Compensation Controls). These controls are run through the flow cytometer to obtain the emission spectra measured at the different fluorochrome detectors used in the polychromatic experiment. These spectra are then used by the analysis software to calculate the compensation matrix [112]. The data generated by flow-cytometers can be plotted in histograms (single parameter) or in dot plots (two or three dimensional parameters), as shown in Fig. 4.4. Each dot on the dot plot represents a cell, and each cell has associated with it values of the scatter and fluorescence data. Different regions can be sequentially identified in the dot plots, based on fluorescence intensity, by creating a series of subset extractions, called 'gates'. In order to distinguish if the recorded events do or do not express a certain surface marker (positive and negative cells) fluorescence minus one (FMO) controls can be used. These controls reveal the maximum fluorescence expected for the group of stained cells in a given channel when the fluorochrome-conjugated antibody reagent associated with that

detector is omitted from the stain. This helps identify the upper boundary of the negative cells gate for the specific fluorescent channel.

In the context of this research, flow cytometry was employed to study the cytotoxicity of the O-rings used to seal the confinement chamber on neutrophils, using an Annexin V/PI assay. The technique was also used to distinguish different cell populations within the bone marrow based upon their cell surface markers, to characterise the phenotype of cultured MSCs, and to study the cell cycle of MSCs subjected to high pressure waves. Finally, flow cytometry was used to count cells in neutrophils migration experiments. All the experiments were performed with a LSR Fortessa (Becton Dickinson) flow cytometer. Data were acquired using the built-in FACSDiva acquisition software and analysed with Flow-Jo (TreeStar Inc.) flow cytometry analysis software.

4.2.8.1 Annexin V/PI

As discusses in chapter 2, cell injury and death can be caused by chemical agents (citotoxicity). When the damage is irreversible, cells will die either by apoptosis or necrosis. The initial phase of apoptosis is manifested in cells by externalization of the phosphatidylserine (PS) complex on the outer surface of the cell membrane. In later stages of apoptosis and in necrotic cells, the membrane ruptures and allows internalisation of large dyes. Annexin V/PI staining is a method used to detect the externalization of PS in apoptotic cells using recombinant Annexin V conjugated to green-fluorescent FITC dye and dead cells using propidium iodide (PI) which binds to DNA. After staining with both probes, early apoptotic cells show green fluorescence, dead cells show red and green fluorescence, while live cells show little or no fluorescence.

To assess the citotoxicity of O-ring conditioned media (produced as described in section 4.2.2) on neutrophils, the FITC Annexin V/ Dead Cell Apoptosis Kit (Molecular Probes^R,Life Technologies) was used according to manufacturer. Aliquots of 10^6/ml neutrophils, incubated for 24 h in the O-ring conditioned media, were washed once with PBS and then resuspended in 100 μl of Annexin Binding Buffer (1X) (diluted from 5X stock solution in sterile water, Life Technologies). 7 μl of Annexin V-FITC were added to each

aliquot and the samples were incubate at room temperature for 15 min in the dark. 10 μl of PI (100 microgram/ml - diluted from stock solution at 2 mg/mL in sterile water, Life Technologies) were then added to each aliquot and the samples were incubate for 5 min at room temperature in the dark. Finally, 400 μl of Annexin Binding Buffer were added to each sample. The tubes containing the samples were kept on ice and analysed with a flow cytometer within one hour. Data were analysed creating first a gate in the FSC-SSC space to identify the neutrophils cell population and then identifying 3 regions in the FITC-PI space correspondent to live cells (negative for both FITC and PI staining), early apoptotic cells (positive only for FITC staining), dead cells (positive for both FITC and PI staining).

4.2.8.2 Bone marrow immunophenotype

Aliquots (10^6 cells/ml) of HIPW-exposed murine bone marrow cells (obtained as described in section 4.) were suspended in a 96-well v-bottom plate using 100 μl of FACS buffer (3.0% (v/v) FBS in PBS) per well. 10% (v/v) of mouse serum was added to each well to block unspecific cell surface receptors. Samples were incubated for 20 min at 4 °C in the dark. Cells were washed twice with 200 μl of FACS buffer and then suspended in FACS buffer (100 μl for compensation controls and FMO controls, 50 μl for samples) to which the monoclonal fluorochrome-conjugated antibodies were added, as reported in Table 4.2. Incubations were all carried out for 20 min at 4 °C in the dark.

Cells were washed three times with 200 μl of FACS buffer, then resuspended in 200 μl of FACS buffer and analysed within 1 h of the buffer addition. Data were analysed in order to evaluate the percentage of different cell population within the total bone marrow. As shown in Fig. 4.5, a gate was applied to identify live cells in the FSC - SSC space. Then each cell population was identified by its expression or lack of expression of one or more surface markers.

	Fluorescence channels				
	450/50	582/15	780/60	530/30	670/14
Compensation controls					
Tube 1	Lin-PB (10 μl)				
Tube 2		Ly6G-PE (0.5 μl)			
Tube 3			Ly6G-PECy7 (0.5 μl)		
Tube 4				Ly6G-FITC (0.5 μl)	
Tube 5					Ly6G-APC (0.5 μl)
FMO controls					
Tube 6		Lin-PB (10 μl)	Lin-PB (10 μl)	Lin-PB (10 μl)	Lin-PB (10 μl)
Tube 7	Ckit-PE (2 μl)		Ckit-PE (2 μl)	Ckit-PE (2 μl)	Ckit-PE (2 μl)
Tube 8	Sca1-PECy7 (1 μl)	Sca1-PECy7 (1 μl)		Sca1-PECy7 (1 μl)	Sca1-PECy7 (1 μl)
Tube 9	CD45RB-FITC (2 μl)	CD45RB-FITC (2 μl)	CD45RB-FITC (2 μl)		CD45RB-FITC (2 μl)
Tube 10	Ly6G-APC (0.5 μl)	Ly6G-APC (0.5 μl)	Ly6G-APC (0.5 μl)	Ly6G-APC (0.5 μl)	
Samples					
Stain 1		CD115-PE (1 μl)		CD45RB-FITC (1 μl)	
Stain 2				CD3e-FITC (1 μl)	Ly6G-APC (0.25 μl)
Stain 3	Lin-PB (5 μl)	Ckit-PE (1 μl)	Sca1-PECy7 (1 μl)		
Stain 4	Lin-PB (5 μl)		Sca1-PECy7 (1 μl)		PDGFRα-APC (1 μl)

Table 4.2: **Bone Marrow multicolor staining setup**

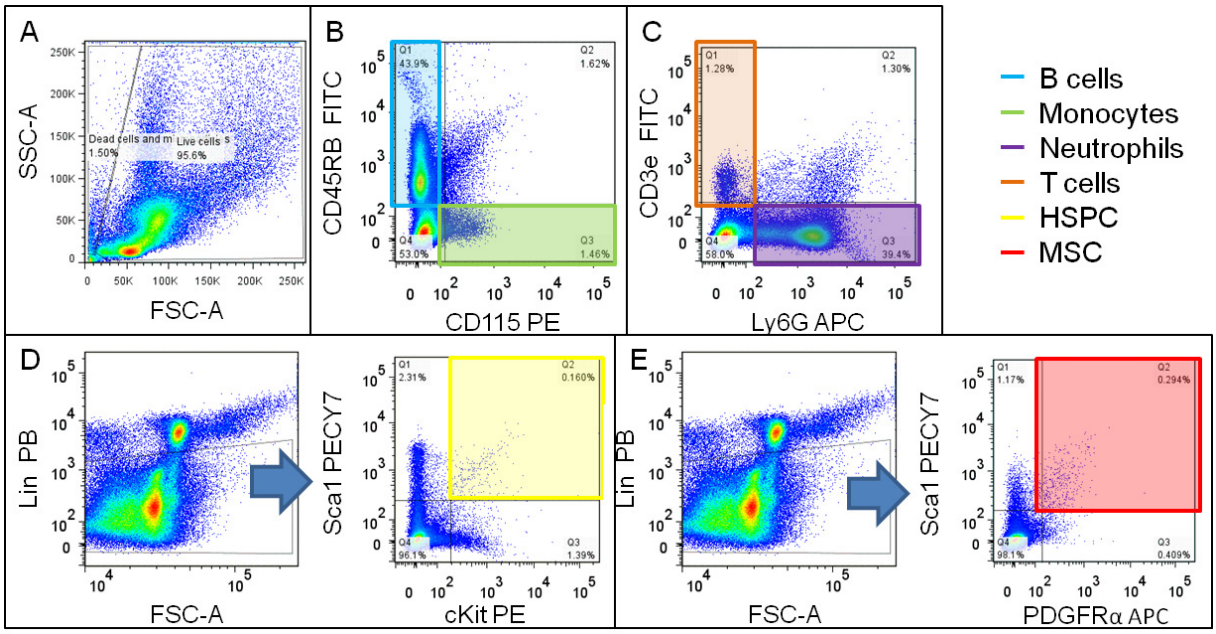

Figure 4.5: **Flow cytometry analysis of Bone Marrow cells** Four different stains were used to identify six different cell types within the bone marrow. (A) A 'viable cells' gate is created on the FSC-SSC plot; (B) Stain 1: two gates are created to identify cells positive for CD45RB or CD115 which correspond respectively to B cells and Monocytes; (C) Stain 2: two gates are created to identify cells positive for CD3e or Ly6G which correspond respectively to T cells and Neutrophils; (D) Stain 3: first a gate is created to identify Lin negative cells, then a quadrant gate is applied in the PE - PECY7 space to identify cells simultaneously positive for Ckit and Sca1, which corresponds to HSPCs; (E) Stain 4: first a gate is created to identify Lin negative cells, then a quadrant gate is applied in the APC - PECY7 space to identify cells simultaneously positive for PDGFRα and Sca1, which corresponds to MSCs

4.2.8.3 MSCs immunophenotype

Aliquots (5x10^5 cells) of passage 3 MSCs were washed in PBS and then resuspended in a 96-well v-bottom plate using 100 μl of FACS buffer (3.0% (v/v) FBS in PBS) per well. 10% (v/v) of mouse serum was added to each well to block unspecific cell surface receptors. Samples were incubated for 20 min at 4 °C in the dark and then washed twice with 200 μl of FACS buffer. Cells were resuspended in 50 μl of FACS buffer per well to which a single antibody (conjugated to the surface marker or the isotype control) was added, as described in Table 4.3. Samples were incubated for 20 min at 4 °C in the dark and then washed three times. Each sample was resuspended in 200 μl of FACS buffer and analysed within 1 hour with the flow cytometer acquiring 200,000 events per sample. MSCs are characterized by the expression of specific phenotypic markers on the cell surface and the lack of expression of others. To qualitatively determine the expression of a surface marker, data were analysed comparing the hystogram representing the fluorescence emission for each surface marker-conjugated antibody with the correspondent isotype control.

Table 4.3: **Phenotypic surface markers for murine MSCs** Antibodies, and correspondent isotypes, used to determine the expression of specific surface markers on the cell surface of MSCs [103]

Marker Name	Isotype	Expression in MSCs
CD45-PE (BD)	Rat IgG_{2b}, κ	Negative
CD31-PE (BD)	Rat IgG_{2a}, κ	Negative
CD11b-FITC (BD)	Rat IgG_{2b}, κ	Negative
CD34-FITC (BD)	Mouse IgG_1, κ	Negative
CD73-PE (BD)	Rat IgG_{2a}, κ	Positive
CD105-PE (eBioscience)	Rat IgG_{2a}, κ	Positive
Sca-1-PE (BD)	Rat IgG_{2a}, κ	Positive
CD90-FITC (BD)	Mouse IgG_1, κ	Positive

4.2.8.4 Cell cycle

The life span of a cell from the time it is created by the division of its parent cell to the time of its own division is called the cell cycle. The cell cycle is divided into four main subsequent periods:

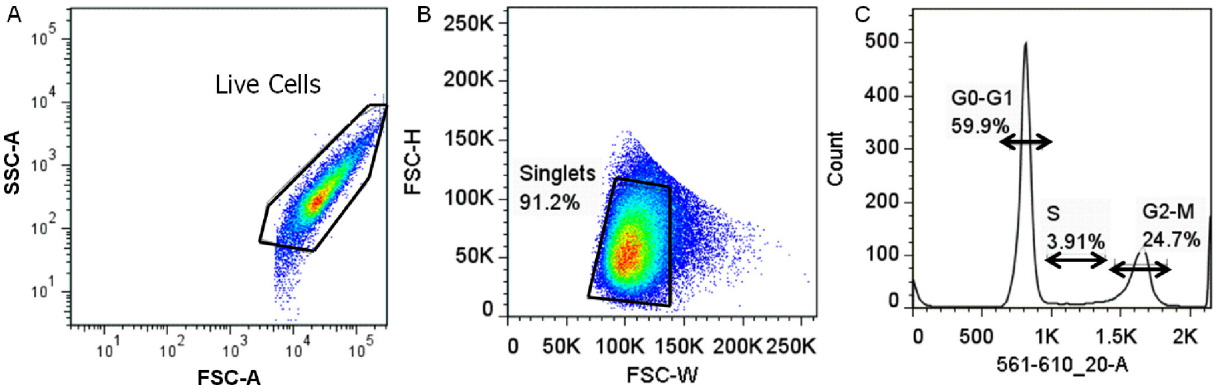

Figure 4.6: **Cell cycle data analysis** (A) Live cells are identified in the FSC - SSC space. (B) Single cells are identified having comparable width and height in the FSC-H - FSC-W space. (C) Three gates are created on the PI histogram to identify cells in the different phases: cells in the G_2/M phase have double the DNA compared to cells in G_0/G_1 phase hence the intensity measured on the PI channel for those cells is approximately twice that of G_0/G_1 cells.

- first gap (G_1 phase) during which the cell grows in size and produces a number of enzymes required for DNA replication
- synthesis (S phase) during which DNA replicates
- second gap (G_2 phase) during which the cell continues to grow and prepare for mitosis, mainly by producing microtubules
- mitosis (M phase) during which the cell undergoes the structural changes necessary for dividing and then ultimately divides

Depending on the suitability of the conditions for division there will be a higher or lower percentage of cells in the G_1 phase within the total population. To study the cell cycle, cells are labeled with a DNA dye to quantify the amount of DNA per cell and estimate what proportion of cells are in a specific phase at the time of staining. In experiments undertaken here, cells were labeled with propidium iodide (PI). Specifically, cells were collected in suspension either immediately after the pressure experiments, or at the 24 h time point following detachment from the cell culture plates using trypsin (as described in section 1.2.2). The suspension was then centrifuged (690 *g* for 5 minutes at 4 °C), the supernatant was discarded, and the cells were resuspended in PBS (1 ml). Absolute ethanol (to a final concentration of 70% in volume) was added to the each sample while

vortexing the suspension at half speed to prevent clustering of the cells during fixation. The cells were incubated on ice for 15 min, then washed twice with 1 ml of PBS. Samples were stained by adding 500 μl of a PI solution (50 μg/ml PI, 0.1 mg/ml RNase A, 0.05% Tritin X-100 in PBS) and incubating at 37 °C and 5% CO_2 for 40 minutes. After incubation cells were washed once and resuspended in 300 mul of PBS containing 1% FBS and analysed with flow cytometry, acquiring 10,000 events per sample. Data analysis was performed as shown in Fig. 4.6. First a population of live cells was identified in the FSC - SSC plot. A singlets' gate was then created, removing debris and doublets, for cells with comparable hight and width (FSC-H, FSC-W space). Finally, subgroup of the singlets' population were identified as the G_0/G_1, S and G_2/M phases selecting the portion of spectra correspondent to the emission peaks. The percentage of each population was recorded for all samples. Results presented as the average and standard error of three different samples per condition for two independent experiments.

4.2.9 MSCs differentiation potential

4.2.9.1 *In vitro* differentiation

MSCs are stromal cells that are capable of differentiating into mesenchymal tissues such as bone, fat and cartilage. *In vitro* differentiation was studied by culturing confluent MSCs in 6-well tissue culture plates in osteogenic medium (DMEM containing 10% (v/v) FBS, 1% (v/v) Pen-Strep, 10mM β-glycerol phosphate, 82 μg/ml ascorbic acid and 10nM dexamethasone) or adipogenic medium (DMEM containing 10% (v/v) FBS, 1% (v/v) Pen-Strep, 0.5 μM dexamethasone, 0.5 μM isobutyl-methylxanthyne and 50 μM Indomethacin). Media were changed every 3 days. After 3 weeks, the medium was removed from each well, the cell monolayers were gently washed with 2 ml of PBS and then cells were fixed adding 2mL 10% formalin. After 30 min of incubation at room temperature, the formalin was removed and cells in each well were gently rinsed with 2 mL destilled water. To detect osteoblastic differentiation, 2 mL of Alizarin Red S staining solution (Sigma-Aldrich) were added to each well. Samples were incubate at room temperature in the dark for 45 min, the staining solution was then removed and the cell monolayer was washed four times with

2 ml of distilled water. To investigate adipogenic differentiation, 2 mL of 60% isopropanol were added to each well and let sit for 5 minutes. The isopropanol was then removed and 2 mL of Oil Red O working solution (Fisher, M312512) were added to each well. After incubation for 5 minutes at room temperature, the Oil Red O solution was removed and each well rinsed with destilled water until the water rinsed off clear. MSC-derived osteoblasts, with extracellular calcium deposits, appeared bright orange-red, under light microscopy. Lipids in MSC-derived adipo cells appeared red, under light microscopy.

4.2.9.2 Early detection of osteogenic differentiation

When MSCs are cultured in osteogenic media they express intracellular markers that are typically expressed by osteoblasts, which are the cells responsible for bone formation *in vivo* . Osteogenic differentiation in MSCs, cultured between 5 to 14 days in osteogenic medium, is characterised by the transcription and protein expression of alkaline phosphatase (ALP) [113]. MSCs were seeded in 96-well plates, in triplicates, at a density of 10^4 cells/well and left overnight to adhere. The following day the media was replaced either with DMEM medium + 10% (v/v) FBS and 1% (v/v) Pen-Strep or osteogenic medium (as described in the previous section). Media was changed at day 2 and 4 and osteogenic differentiation of MSCs was quantified using the LabAssay^{TM} ALP Kit (Wako pure chemical, Japan) at day 7. Briefly, MSCs were washed twice with PBS, then 20 μl of NP-40 protein lysis buffer (0.5% (v/v) Nonidet P-40, 20 mM Tris base, 150 mM NaCl adjusted to pH 7.8) were added to each well. 100 μl of ALP working solution (prepared according to the manufacturer, Wako pure chemical) were then added to each well and the plate was incubated at 37 °C and 5% CO_2 for 15 min. Finally 80 μl of stop solution were added to each well and ALP activity was optically measured at 405 nm in a Sunrise^{TM} plate reader. ALP activity was measured based upon a standard curve for the conversion of p-nitrophenyl phosphate to p-nitrophenol. One unit of ALP activity is defined as the release of 1 nmol p-Nitrophenol per minute.

4.2.10 Cell migration

4.2.10.1 MSCs

MSCs were seeded in a 24-well plate at a density of 10^4 cells/insert, in triplicates, on 8 μm pore transwell membranes (VWR International Ltd, Lutterworth, Leicestershire, UK) in 1% (v/v) FBS medium (upper compartment). The lower compartment contained 500 μl either of 1% (v/v) FBS medium (negative control), 10% (v/v) FBS medium (positive control) or supernatant collected from the HIPW experiments. Cell cultures were incubated at 37 °C and 5% CO_2 for 24 h. The next day, transwell membrane insertes were removed from the wells, washed with PBS and the upper chamber was wiped thoroughly with cotton wool in order to remove MSCs which did not migrate. The membranes were fixed using 500 μl of paraformaldehyde (4% (v/v) in PBS) for 20 min at room temperature, washed with PBS and stained with 1% (w/v) crystal violet solution (Sigma-Aldrich) for 30 min. Transwell membrane inserts were left to dry and observed under a light microscope. Migrated MSCs were counted in 8 fields of view (40X magnification).

4.2.10.2 Neutrophils

Supernatant media HIPW experiments were tested in chemotaxis assays using ChemoTx chambers with a 3-μm pore filter (NeuroProbe, Gaithersburg, MD). Lower chambers were filled with 200 μl of different conditioned medium, including RPMI + 1% BSA (negative control), RPMI + 1% BSA and CXCL1 (KC, 30 ng/ml), RPMI + 1% BSA and CXCL1 (SDF-1, 30 ng/ml) and the supernatant collected from the HIPW experiments. Where indicated, neutrophils were pre-treated with SB265610 (100 nM) or AMD3100(126 nM) for 30 minutes, which are respectively the inhibitors for receptors CXCR2 and CXCR4. Migration of 2.5 x 10^4 neutrophils to the lower chamber was quantified labelling cells migrated to the lower chamber with Ly6G and analysing samples with flow cytometry. For each sample events were acquired for 10 seconds with high flow speed.

4.2.11 Statistical analysis

Each experiment was performed with either three samples (N=3) or five sample (N=5) for each condition as specified in the correspondent figure. Experiments were repeated two, three or four times (E = 2,3,4), as reported in each figure. When only two conditions were present in the experiment, data were analysed with a two-tailed unpaired t test to determine the significance difference between treated and untreated groups. A p value <0.05 was considered to be statistically significant. For experiments where multiple conditions were to be compared, data were analysed with a non parametric one-way analysis of variance (ANOVA) followed by Tukey's comparison test.

4.3 Results

4.3.1 Chamber biocompatibility

Part of the design process of the confinement chamber focused on the research of biocompatible materials that would not affect the live biological samples used in the HIPWs experiments. Once inserted in the chamber, cells in suspension were in contact with the main body of the chamber, made of polycarbonate, the SHPB bar surfaces, made of Inconel 718 steel, and the O-rings. Particular attention was focused on the material of the O-rings used to seal the chamber. As shown in Fig. 4.7, the metabolic activity (expressed as normalised OD) of MSCs cultured in media previously conditioned by different O-rings materials drastically decreased after just 6 hours in the case of nitrile and neoprene compared to control, while no significant differences were observed between the silicone conditioned medium and the control at any time point. Moreover, the effects of O-ring conditioned media on neutrophils were investigated with flow cytometry. Annexin V-PI staining of cells incubated 24 hours in the different conditioned media showed that neutrophils cultured in the nitrile medium were either early apoptotic (stained positive for Annexin V, but not for PI) or late apoptotic/necrotic (stained positive for both Annexin V and PI) while all the other media did not have any effects on neutrophils, Fig. 4.8. In general, results showed that nitrile O-rings were cytotoxic to different cell types while

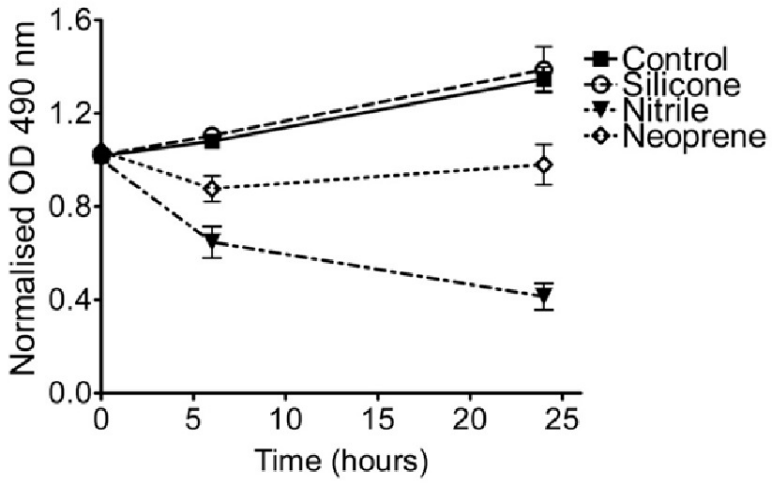

Figure 4.7: **Cytotoxicity of the O-ring materials on MSCs** Metabolic activity, expressed as normalised optical density at 490 nm, of MSCs grown in different conditioned media up to 24 hours. (N = 3, E = 2)

medium conditioned with silicone O-rings did not have cytotoxic effects on MSCs or on neutrophils.

In order to ensure sterility, the chambers were soaked in 70% ethanol for 12 h before the experiments. Just prior to each experiment the chamber was removed from the ethanol bath, allowed to dry in a microsafety cabinet, mounted on the SHPB bars and rinsed twice with sterile PBS. To assess the biocompatibility of the confinement chamber, a comparison of viability, cytotoxicity and metabolic activity between control samples and samples inserted and recovered from the chamber (sham) was performed with two different cell types (PLB985 and MSCs). As shown in Fig. 4.9-A, no significant difference (t-test) was observed between control and sham samples in the numbers of viable cells observed(left), LDH release corresponding with cytotoxicity (centre) or metabolic activity (right). Sham samples were cultured in fresh medium and displayed no significant morphological differences when compared with control populations after 24 h incubation, as shown in Fig. 4.9-B.

4.3.2 PLB985 cells

The effects of HIPW on the viability and cytotoxicity of PLB985 cell suspensions were investigated. Different initial concentrations (10^6, $4x10^6$ and $8x10^6$ cells/ml) were sub-

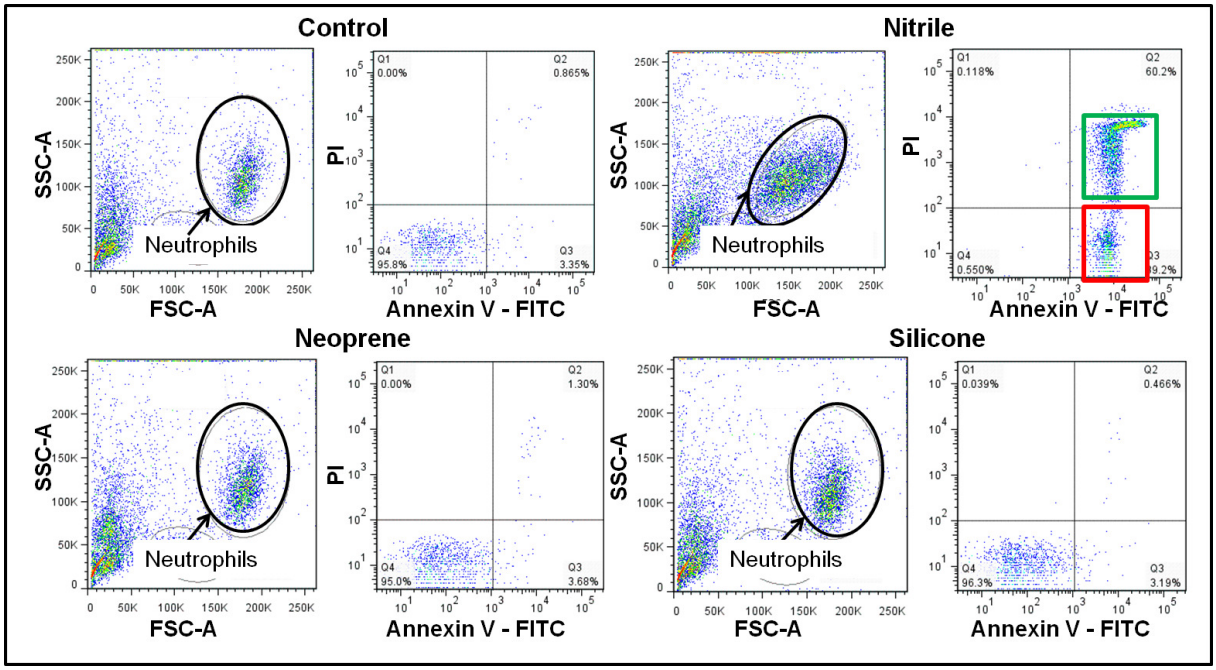

Figure 4.8: **Cytotoxicity of the O-ring materials on neutrophils** Flow cytometry analysis of neutrophils cultured in different O-rings conditioned media. The neutrophils population is gated in the FSC-SSC plot. The Annexin V-PI space is then divided in 4 quadrants. Events in the lower right quadrant correspond to cells positive for Annexin V (early apoptotic), while events in the top left quadrant are cells positive for Annexin V and PI (late apoptotic/necrotic). Apoptotic and necrotic cells observed for nitrile conditioned medium are identified in using the green and red boxes.

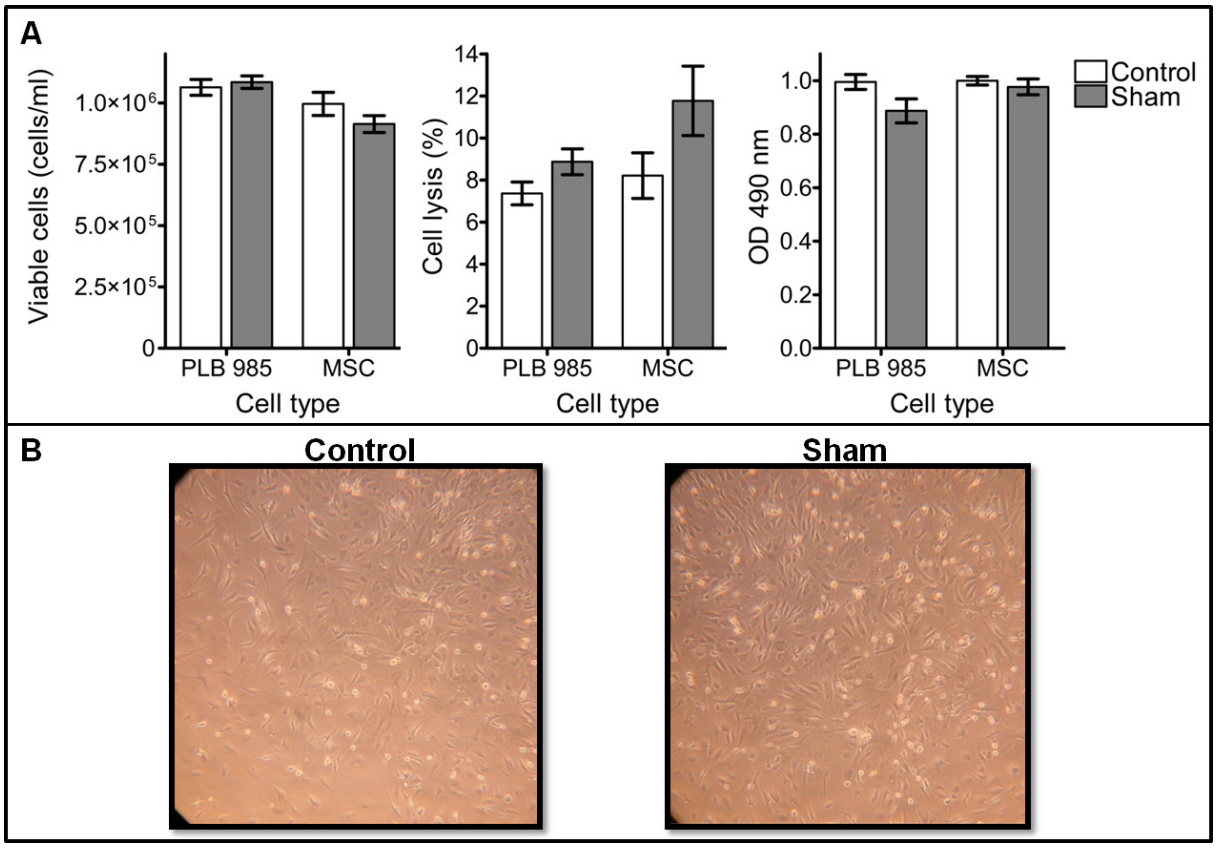

Figure 4.9: **Biocompatibility of the confinement chamber** (A) Viable cell count, percentage of LDH release in suspension and metabolic activity (OD 490 nm) for control and sham samples for two different cell populations (PLB985 and MSCs). No significant differences were observed in any of the assays. (B) Light microscopy images (10x) of MSCs control and sham samples cultured for 24 h in DMEM culture medium. Experiments were performed with N = 3, E = 3. Mean values were analysed with unpaired t test.

jected to medium HIPW (Impulse = 9.28 ± 0.43 MPa ms, Peak Pressure = 25.48 ± 1.7 MPa, values expressed as average and standard deviation of 2 experiments, 3 repeats for each concentration per experiment). As shown in Fig. 4.10-A (left) approximately 30% of cells were damaged due to the HIPW. Elevated levels of LDH in the supernatant of the samples subjected to a medium HIPW compared to sham samples suggested that cell damage was associated with cell lysis. No differences were observed between samples with different initial concentrations. This result suggested that the process by which cells were damaged was not affected by differences in cell to cell interactions during the pressure wave event. PLB985 cells at a density of 10^6 cells/ml were subjected to HIPW of different intensities (Low P: Impulse = 5.42 ± 0.45 MPa ms, Peak Pressure = 14.23 ± 1.04 MPa; High P: Impulse = 11.98 ± 0.69 MPa ms, Peak Pressure = 33.90 ± 6.46 MPa, values expressed as average and standard deviation of 2 experiments, 4 repeats for each HIPW condition per experiment). The decrease in cell viability and the amount of LDH release in medium of samples subjected to HIPW was proportional to the magnitude of the peak pressure and pressure impulse generated within the chamber as shown in Fig 4.10-B.

4.3.3 Bone marrow

Murine bone marrow cell suspensions were subjected to HIPW. As shown in Fig. 4.11 A, samples exposed to HIPW of high magnitude (Impulse = 9.4 ± 0.98 MPa ms, Peak pressure = 27.68 ± 3.82 MPa, values expressed as average and standard deviation of 2 experiments, 3 repeats for each experiment) showed a 39.3 ± 10.7% reduction in the total number of viable cells compared to sham samples. Different cell populations within the bone marrow with different sizes and levels of granularity (an example is shown in Fig. 4.11-B) were selected to compare how levels of damage might differ between cell types subjected to the same pressure conditions. Flow cytometry analysis of the recovered samples showed that the different cell types were equally susceptible to the HIPW generated with the SHPB system. The percentage difference between sham and samples exposed to HIPW for each cell population was comparable to the percentage difference of the total bone marrow, 39.8 ± 7.9%, except for MSCs and HSPCs which

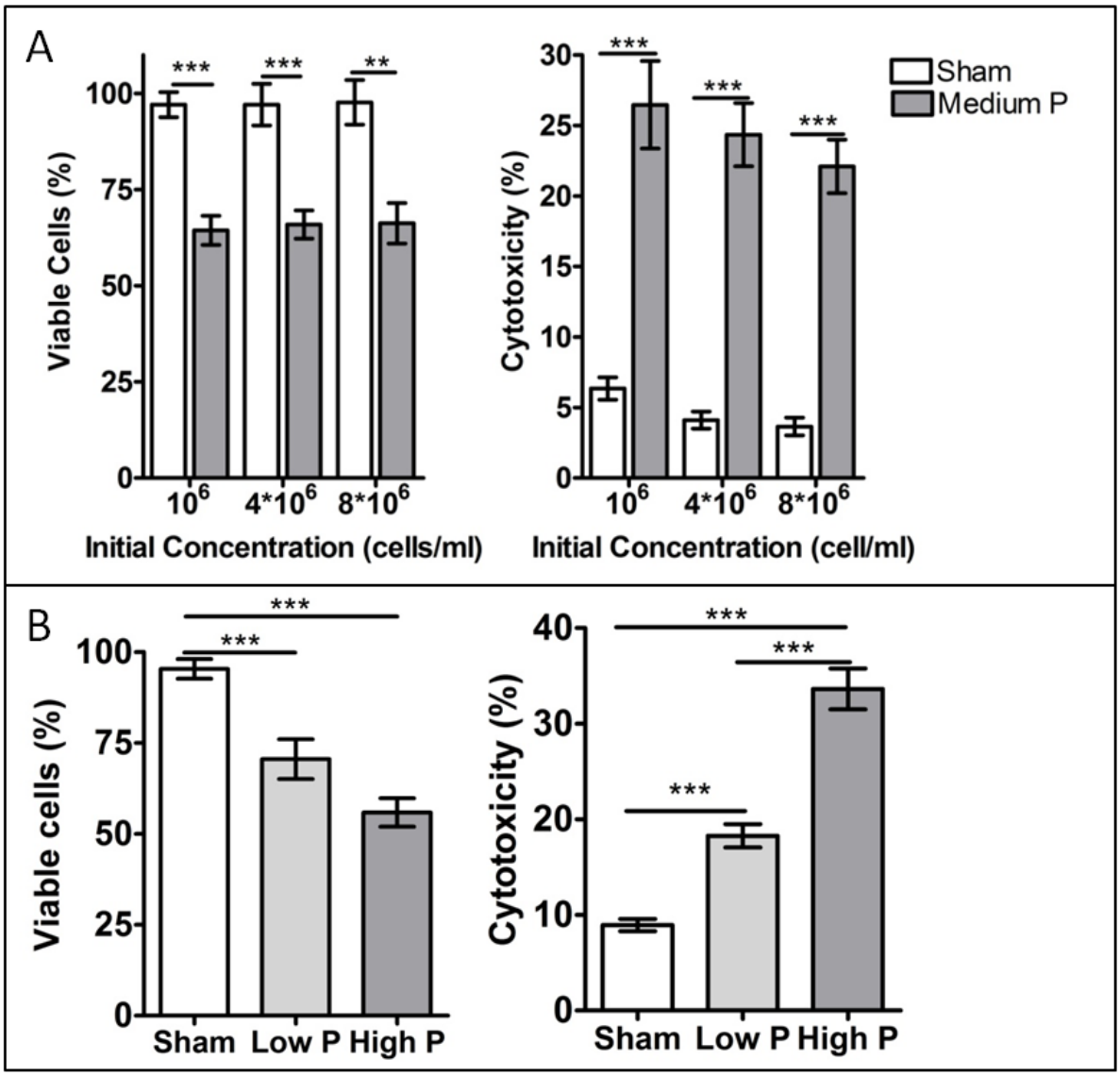

Figure 4.10: **Effects of HIPWs on the viability of PLB985 cells** (A, left), viable cell count of sham and HIPW exposed cell populations expressed as a percentage of the initial cell number. (A, right), percentage of LDH released by sham and HIPW exposed samples. All experiments performed in triplicate to N = 3. Mean values were analysed using an unpaired two-tailed t-test (*=p<0.5, ** = p<0.01, *** = p<0.001). (B, left), viable cell count of sham and HIPW exposed cell populations expressed as a percentage of the initial cell number. (B, right), percentage of LDH released by sham and HIPW exposed samples. All experiments performed in triplicate (E = 3) to N = 5. Mean values were analysed using one way ANOVA with Tukey post hoc test.

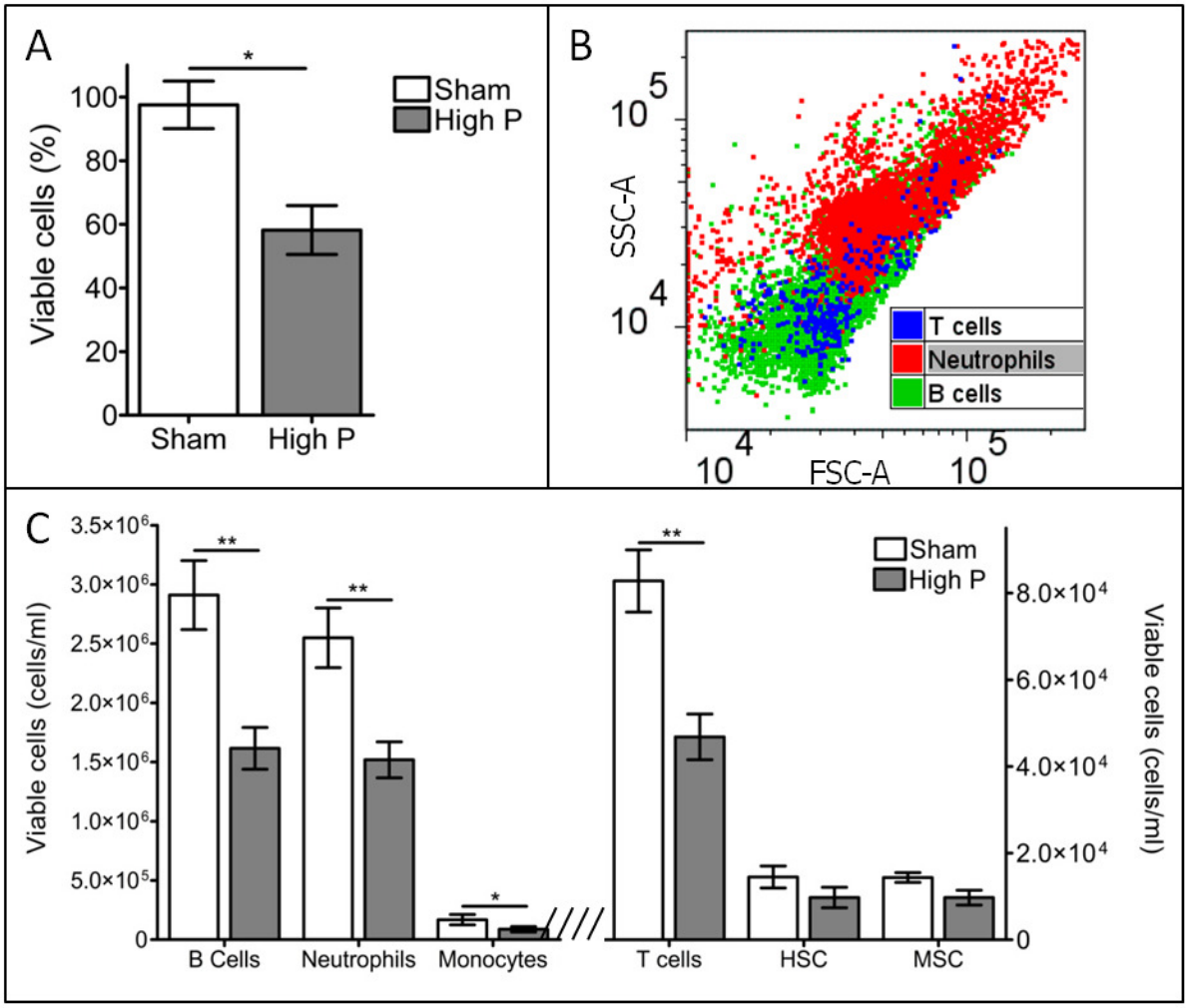

Figure 4.11: **Effect of HIPWs on the viability of bone marrow cells in suspension** (A) Count of viable cells for sham and HIPW exposed samples expressed as a percentage of the initial cell number. (B) Representative flow cytometry plot depicting three different gated population in the FSC - SSC space. For each samples 200,000 events were acquired. (C) The total number of viable cells per aliquot (500 μl) of recovered cell suspensions are shown for sham and bone marrow samples exposed to HIPW. Each experiment was performed twice (E = 2) with three samples per condition N = 3. Mean values were analysed using an unpaired two-tailed t-test (*=p<0.5, ** = p<0.01, *** = p<0.001).

appeared slightly more resistant to damage (B cells 44.5 ± 11.7%, Neutrophils 40.4 ± 11.5%, T cells 43.5 ± 6.7%, HSPCs 32.7 ± 16.3% and MSC 32.3 ± 11.9%).

4.3.4 MSCs in suspension

4.3.4.1 Characterisation

The cell surface markers of murine MSC were identified using flow cytometry. In Fig.4.12-A the results show that cells cultured for three weeks retained the typical MSC markers profile, positive for Sca-1, CD73, CD90 and CD105 surface markers and negative for CD45, CD34, CD11b, and CD31. Moreover, MSCs were successfully differentiated into adipocytes and osteocytes as shown in Fig.4.12 C and D.

4.3.4.2 Acute effects of HIPWs

The effects of HIPWs on MSCs were investigated using two different intensities (Low P: Impulse = 4.84 ± 0.70 MPa ms, Peak Pressure = 15.92 ± 2.27 MPa; High P: Impulse = 10.62 ± 1.07 MPa ms, Peak Pressure = 34.11 ± 5.38 MPa, values expressed as average and standard deviation of 4 experiments, 5 repeats for each experiment). As previously shown for PLB985 cells, the viability of MSCs decreased as a function of the pressure wave intensity. Fig. 4.13-A shows the results of the cell count assay for four independent experiments. In this assay, cells that are not able to exclude the the trypan blue dye are damaged (non-viable). The concentration of live (viable) cells was reduced in samples subjected to either Low P and High P conditions compared to sham. The concentration of non-viable cells was elevated in experiments 1 and 2 compared to experiments 3 and 4, for each condition studied. The differences observed between experiments 1 and 2 compared to 3 and 4 are probably due to environmental factors (e.g. outside temperature) and the time required to complete the experiments which was larger for the two earlier experiments due to the limited number of confinement chambers available. The decrease in viability for Low P and High P samples, expressed as the percentage difference in viable cells compared to Sham for each experiment is shown in Table 4.4. An average decrease in viability of 36.6% ± 1.6% and 50.7% ± 3.1%, respectively, for the Low P and High P samples was

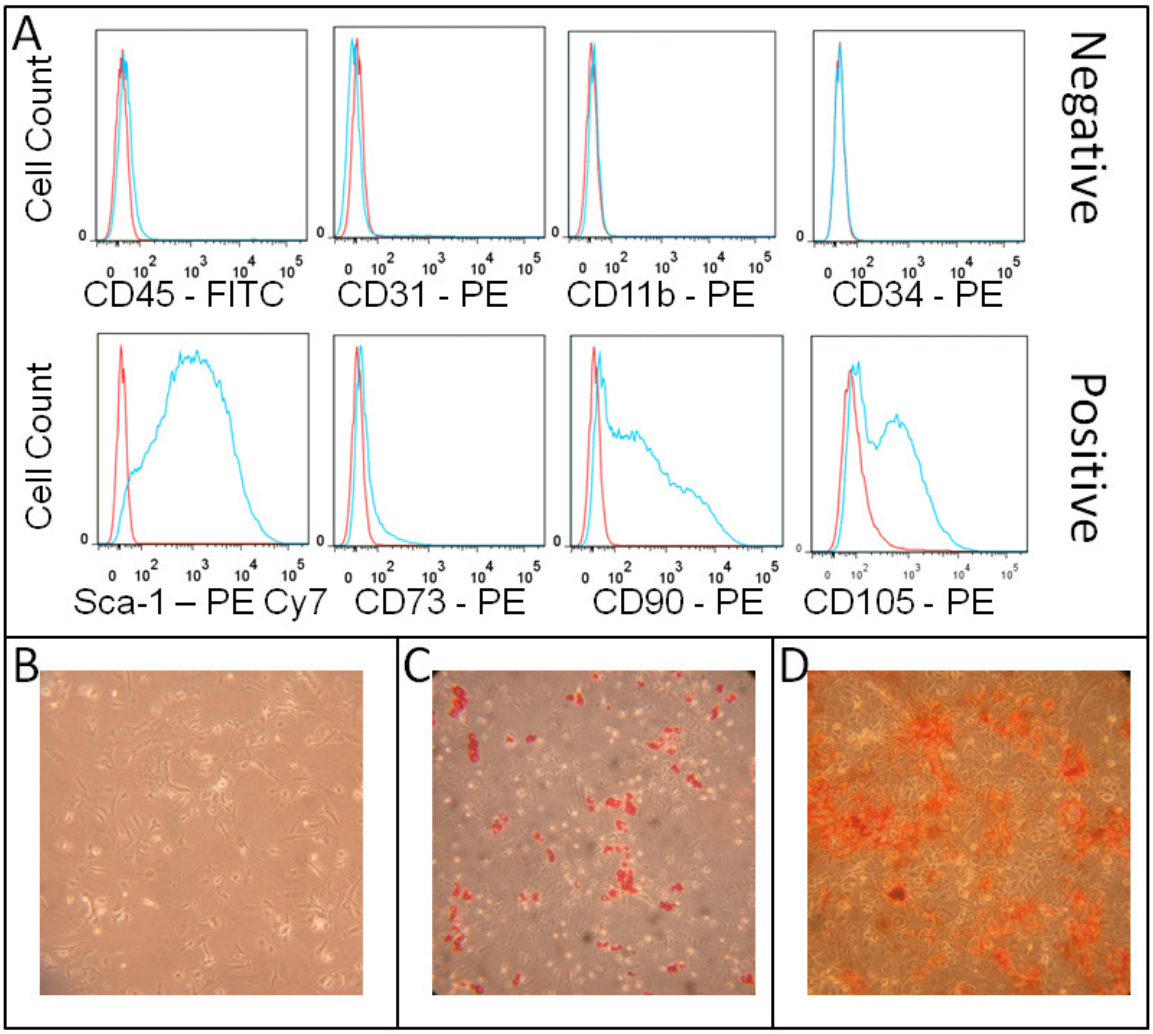

Figure 4.12: **Murine MSC characterisation** (A) Cell surface markers investigated using flow cytometry. Each plot shows the isotype control (red line) and the expression of the cell surface marker (blue line) on MSCs cultured for 3 weeks in standard conditions. (B, C and D) Light microscopy images (10x) of MSCs. Panel B shows MSCs in normal culture medium. Panel C shows MSCs that differentiated as adipocytes, indicated by the staining of lipid droplets with Oil red S. Panel C shows MSCs differentiated as osteocytes indicated by the staining of calcium deposits with Alzarin Red.

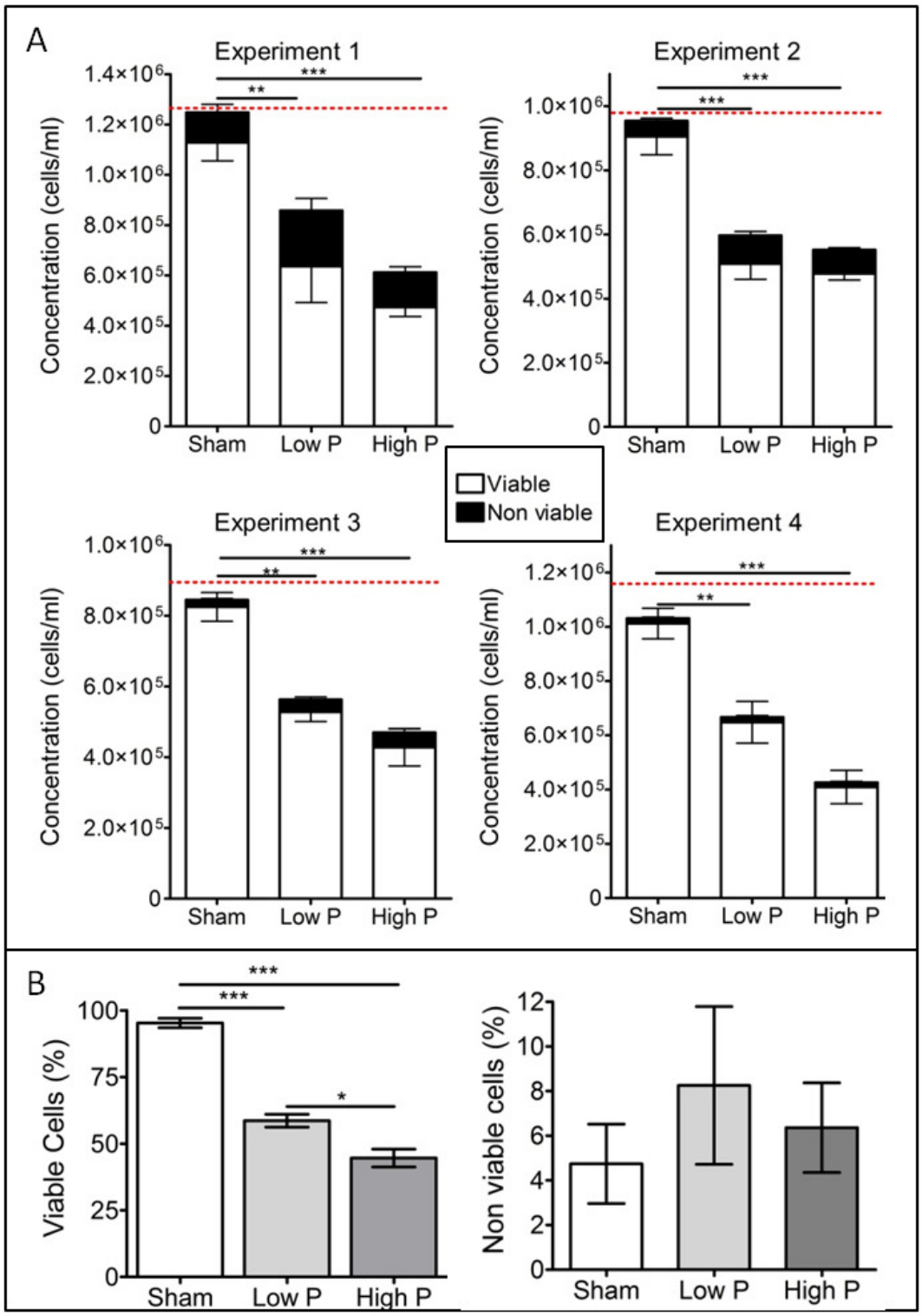

Figure 4.13: **Cell counts of MSCs samples exposed to HIPWs** (A) Cell count results expressed as cell concentration (cells/ml) for viable cells (white) and non-viable cells (black). The red dotted line indicates the initial concentration of cells for each experiment. (B) Percentage of viable and non-viable cells shown as the average of the four independent experiments relative to the initial concentration. Each experiment was performed four times (E = 4) with five samples per condition N = 5. Mean values were analysed using one way ANOVA with Tukey post hoc test (*=$p<0.5$, ** = $p<0.01$, *** = $p<0.001$).

Experiment	1	2	3	4
Low P	35.1 ± 3.2	41.5 ± 5.1	35.3 ± 7.5	34.6 ± 9.8
High P	47.0 ± 6.2	44.8 ± 2.1	58.5 ± 6.0	52.3 ± 3.0

Table 4.4: **Decrease in cell viability** From each experiment the decrease in cell viability due to Low P or High P HIPWs was expressed as the average percentage difference between Sham and the test samples. Results are expressed as average of 5 samples ± standard error for each experiment

observed. Averaging the viability data from the four independent experiments showed that the average decrease in viability was still statistically significant (Fig. 4.13-B), while no significant differences were observed in the average percentage of non-viable cells. These results suggest that damage caused by HIPW on cells in suspension was associated with complete cell desruption which corresponded to the decrease in viable cells concentration observed in all the four experiments. In comparison, no correlation was observed between HIPW and the concentrations of non-viable cells observed.

Cell disruption (lysis) was investigated by measuring the level of LDH released into the medium of samples exposed to HIPW. LDH release was expressed as percentage of the total content of LDH for one aliquot of MSCs at the initial cell concentration for each experiment. The average results for experiments 1 and 2 are presented (experiments 3 and 4 were excluded as the assay did not work, due to degradation of the reagents). In experiments 1 and 2, a low level of citotoxicity was observed for sham samples, possibly due to the fact that MSCs are adherent cells and can hence be under stress when in suspension. However, a statistically significant increase in LDH level was found in the medium of Low P and High P samples compared to sham, as shown in Fig.4.14-A. These results reinforced the hypothesis that the decrease in cell viability measured with the cell count method was associated with cell lysis due to the pressure events, and that cell lysis was dependent on the level of pressure generated within the confinement chamber.

Finally, the viability of the recovered samples was also assessed using the MTS assay which measures levels of metabolic activity. As shown in Fig. 4.14 B, there was a reduction in metabolic activity in Low P and High P samples compared to sham samples. The reduction in viability measured with the MTS assay, Table 4.5, agreed within error with values measured with the cell count method (Fig. 4.13). Taken together, these results

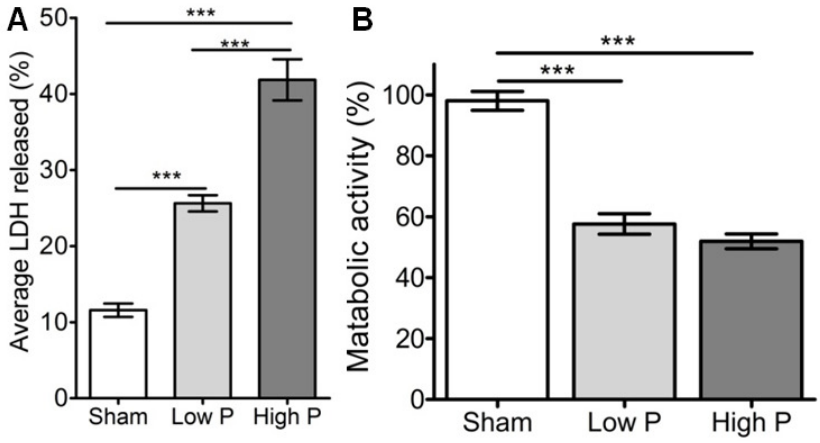

Figure 4.14: **Cell lysis and metabolic activity of MSCs samples exposed to HIPWs** (A) Cell lysis expressed as percentage of LDH released into the medium compared to LDH present in the total cell lysate for HIPWs-exposed and sham MSCs samples. Values represent the average of two independent experiments, each performed with N = 5. (B) Cell metabolic activity expressed as the percentage optical density of test samples using the MTS assays, compared to control samples. Values represent the average of four independent experiments (E = 4), each performed with N = 5. Mean values were analysed using one way ANOVA with Tukey post hoc test (*** = $p<0.001$).

Experiment	1	2	3	4
Low P	53.7 ± 7.5	42.1 ± 6.5	34.8 ± 7.0	31.0 ± 5.8
High P	58.2 ± 6.0	44.4 ± 5.3	40.2 ± 4.4	41.6 ± 3.3

Table 4.5: **Decrease in cellular metabolic activity for MSCs subjected to HIPWs of two different intensities**

suggest that cells with intact membranes which excluded trypan blue were viable cells which were metabolically active.

4.3.4.3 Short term effects

In order to investigate short term effects on cells due to HIPW, the metabolic activity of recovered samples for up to 72 h was analysed with a MTS assay. As shown in Fig. 4.15-A the results for the four different experiments were not highly consistent. In experiments 1, 3 and 4 at the 24 h time point a rapid increase in metabolic activity was observed for most of the samples, while in experiment 2 the metabolic activity remained unchanged compared to the starting point. Moreover, it appeared that in experiment 3, after the initial increase in metabolic activity (at 24 h), a steady state level of metabolic activity was attained at 48 h, followed by a dying phase (associated with a decrease in metabolic

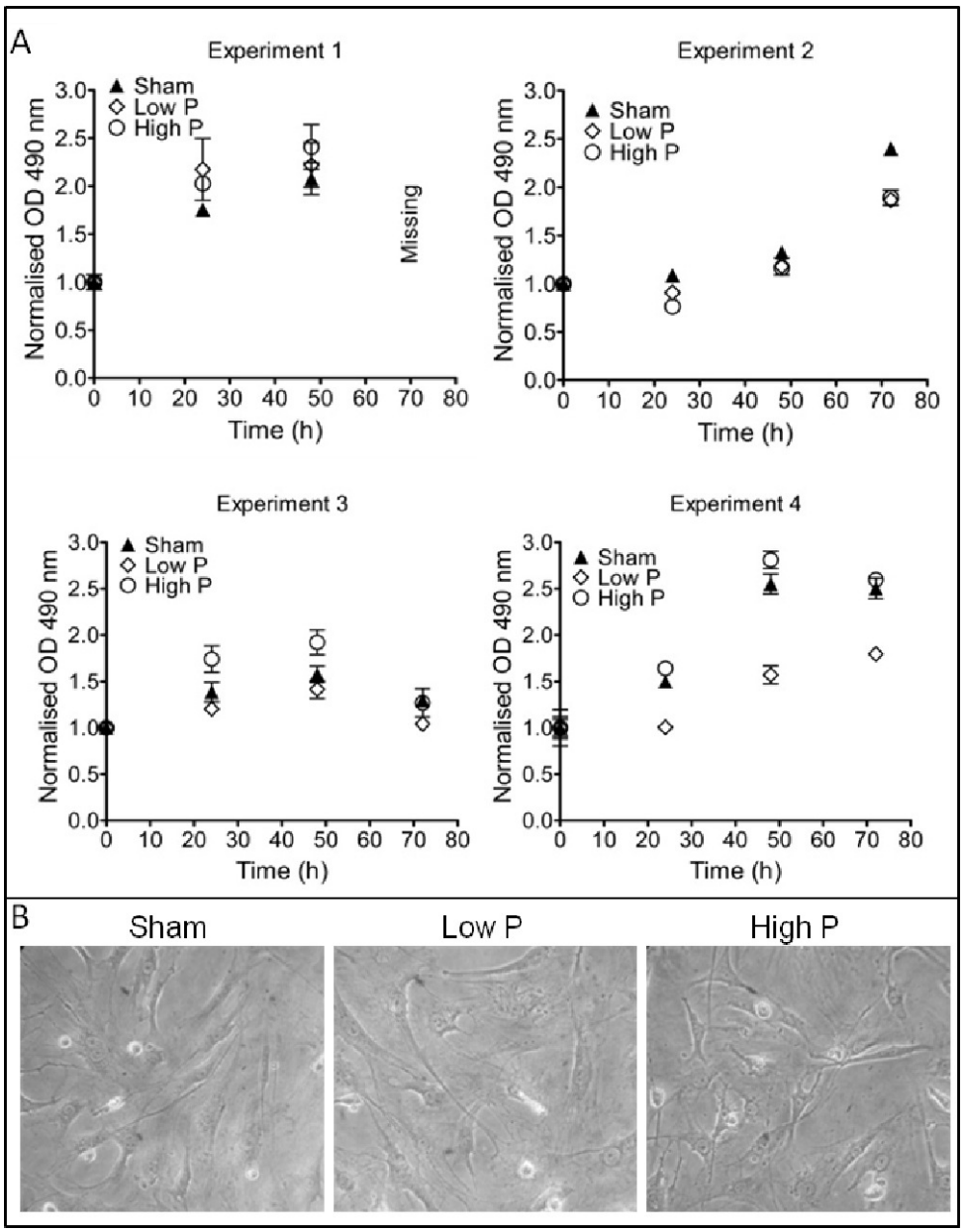

Figure 4.15: **Metabolic activity of MSCs subjected to HIPW of two different intensities** (A) The metabolic activity of cells subjected or not to HIPWs cultured in DMEM culture medium was analysed with MTS assay at four different time points (0 h 24 h, 48 h and 72 h). OD values at each time point were normalised by using the OD values at the 0 h time point in order to exclude any plating error. Each experiment was performed four times (E = 4) with three samples per condition N = 3. (B) Light microscopy images of sham, Low P and High P MSCs in culture 24 h after the HIPWs experiments.

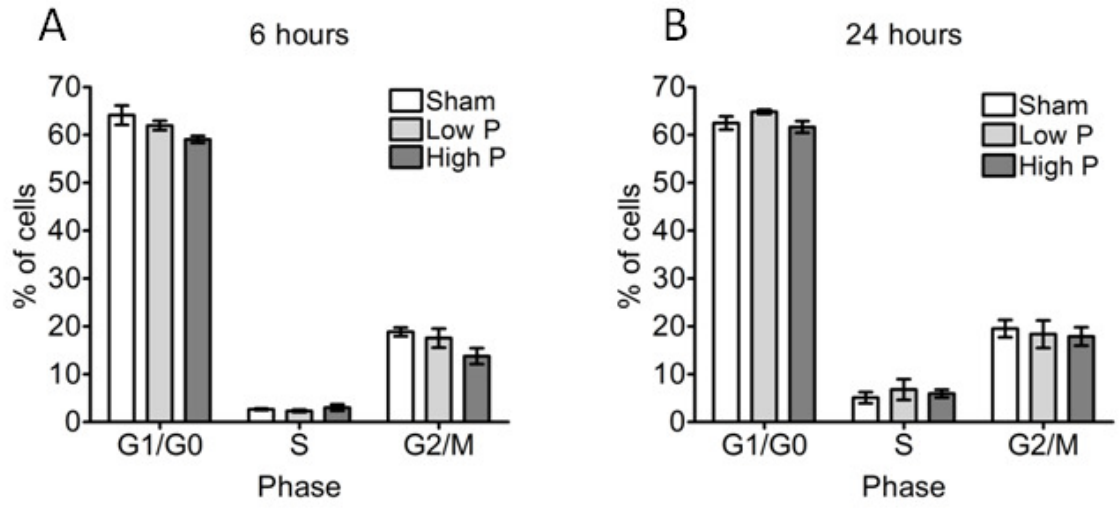

Figure 4.16: **Cell cycle analysis of MSCs subjected to HIPWs** The percentage of cells in the G_0/G_1, S or G_2/M phases of the cell cycle was determined using flow cytometry, 6 h and 24 h after the HIPWs experiments. Experiments were performed in duplicates E = 2, with N = 3. Mean values were analysed using one way ANOVA with Tukey post hoc test.

activity). In the other experiments, the levels of metabolic activity continued to grow up to 48 h after which the dying phase appeared. Comparing average values at each time point for the three different conditions suggested that there was no significant difference in metabolic activity in samples subjected to HIPW compared to sham samples.

To further confirm these results the cell cycle of samples recovered post HIPWs was studied for experiments 3 and 4 with flow cytometry. Results, shown in Fig. 4.16 showed that the majority of the cells were either in G_0 or G_1 phases for all the different samples 6 h and 24 h after HIPW exposure. Statistical analysis (one-way ANOVA) showed no difference between sham, Low P and High P samples for the three different cell cycle phases. These results also indicated that the ability of cells surviving HIPW exposure was not significantly affected.

The ability of cells subjected to HIPW to differentiate into osteoblasts was also investigated. ALP assay showed that sham cells and cells subjected to Low P and High P HIPWs produced equivalent amounts of ALP after one week in osteogenic differentiation medium as shown in Fig. 4.17-A. Moreover calcium deposits were visible after three week in culture for all the three different samples. These results indicate that cell differentiation does not appeared to be impaired nor stimulated in cells in suspension subjected to

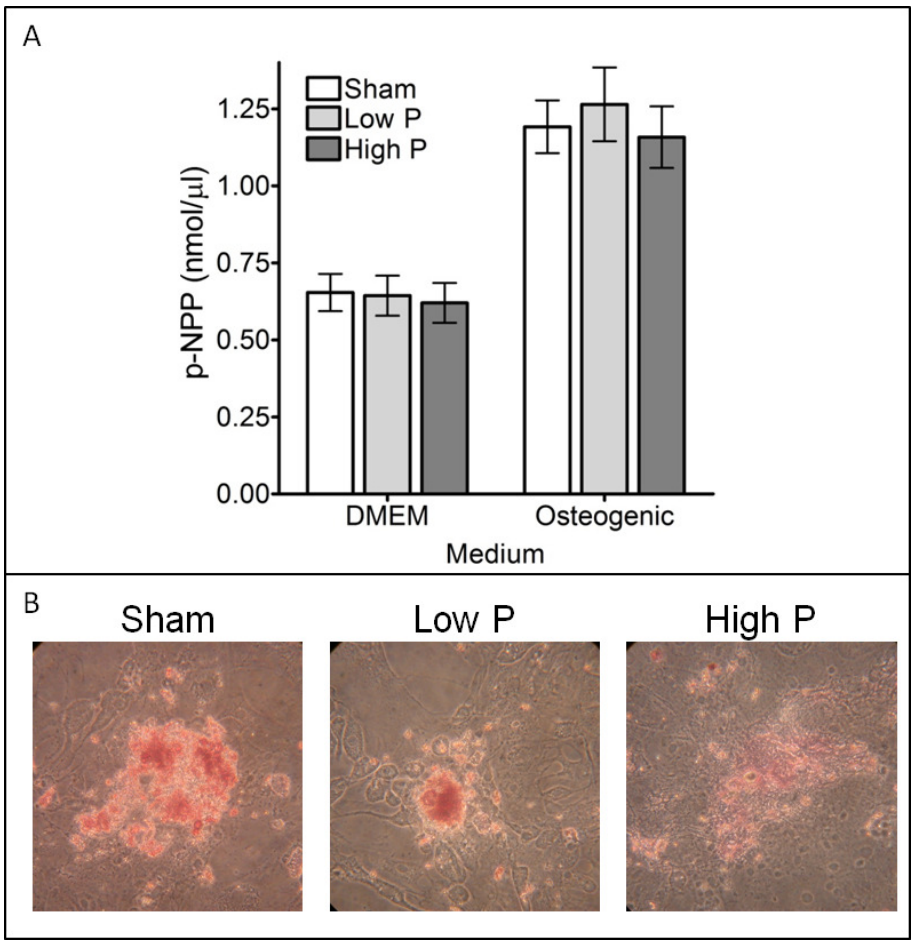

Figure 4.17: **Osteoblastic differentiation of MSCs after HIPW exposure** (A) MSCs osteoblastic differentiation was assessed with an ALP assay and expressed as concentration of *p*-Nitrophenol per well. Samples cultured in osteogenic medium were compared to samples cultured in normal DMEM medium. Experiments were performed in duplicates E = 2, with N = 3. (B) Alizarin Red stain of HIPW-exposed and sham MSCs cultured in osteogenic medium for 21 days. Calcium deposit stain red, indicative of osteoblastic differentiation.

HIPWs.

4.3.4.4 Effects of HIPWs conditioned media

The influence of the supernatant collected from HIPWs experiments on MSCs on the metabolic activity and migration of healthy cells was investigated. The results for the metabolic activity of MSCs when cultured in different HIPW-conditioned media are shown in Fig. 4.18. The data shown in panel A indicate that experiments 2 and 3 showed almost no changes over time in metabolic activity for all the samples which would suggest that all the media had toxic effects on the cells. Changes in values of metabolic activity over time were observed in experiments 1 and 4 for samples cultured in HIPW conditioned medium compared to samples cultured in sham medium and freeze/thaw medium. As we can see from Fig. 4.18 B, at 0 h 24 h time points, in experiments 1 and 4 the metabolic activity of MSCs cultured in Low P, High P and Freeze/Thaw conditioned media was lower than sham samples. These results suggested that the medium collected from samples subjected to HIPW had an initial toxic effect on healthy cells. At 48 h, however, the metabolic activity of Low P and High P was significantly increased and reached values comparable to the one of sham samples, while Freeze/Thaw samples still showed lower values. Finally, at 72 h the values of metabolic activity remained constant. Overall it is not possible to draw significant conclusions from these experiments due to the contradictory results obtained.

The effects of HIPW-conditioned medium on cell migration were also investigated. Two sets of experiments were performed using conditioned medium obtained from HIPW experiments on MSCs performed at Cambridge University and stored at -20°C for less than a week. Neutrophils migration was expressed as a percentage of cells that migrated towards the conditioned media, compared to the total number of cells that migrated towards the positive attractant for each experiment (KC or SDF-1). Results showed that neutrophils migration towards High P conditioned medium was comparable to that of positive attractant KC (30 ng/ml) and was significantly higher than negative controls (Fig.4.19-A): RPMI medium; DMEM medium (in which cells were suspended for HIPW

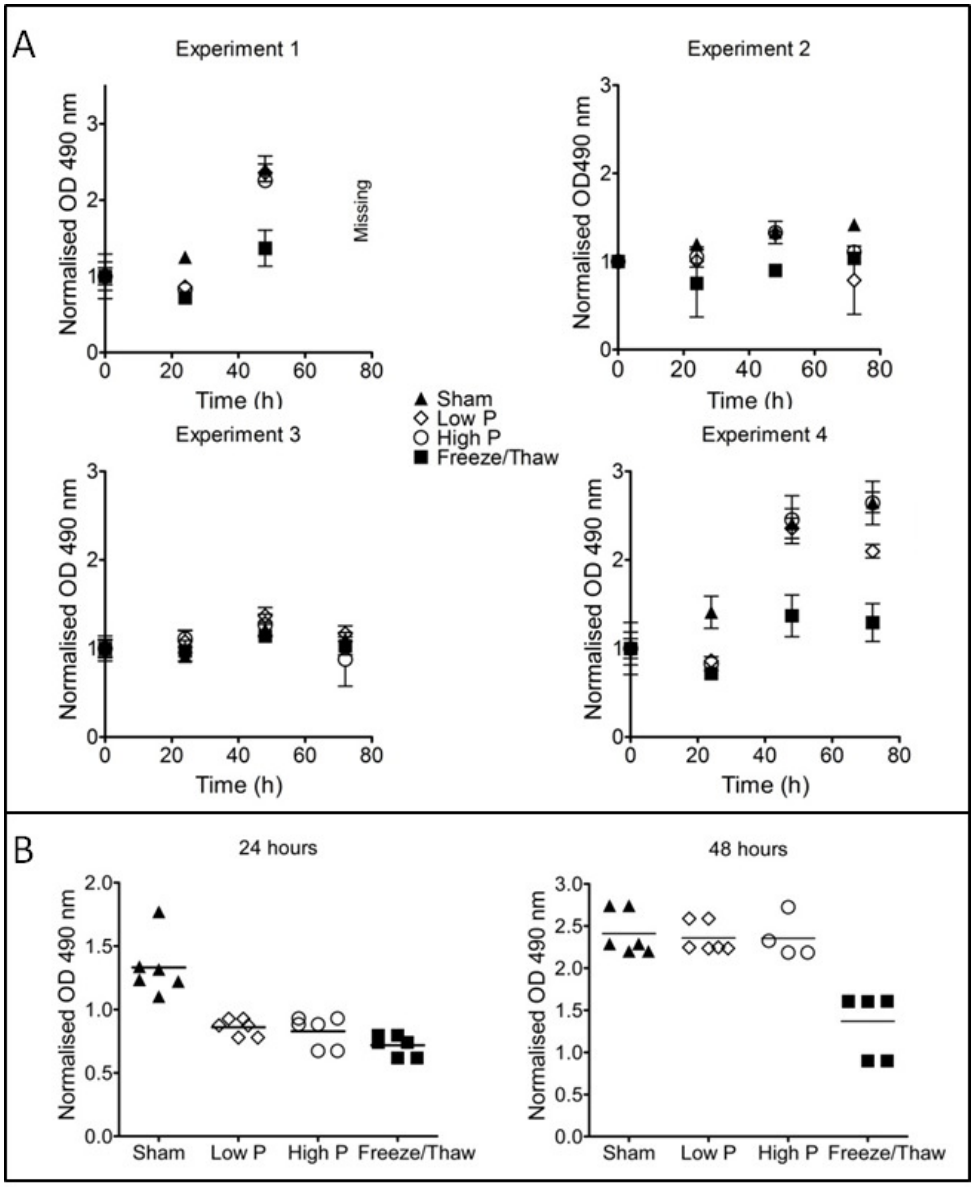

Figure 4.18: **Effects of HIPWs conditioned medium on the metabolic activity of MSCs**(A) The metabolic activity of cells cultured in sham, HIPWs or Freeze/Thaw conditioned media was analysed with MTS assay at four different time points (0 h 24 h, 48 h and 72 h). OD values at each time point were normalised by OD values at the 0 h time point in order to exclude any plating error. (B) Average metabolic activity at 24 h and 48 h for experiments 1 and 4 (E = 2, N=3 for each experiment).

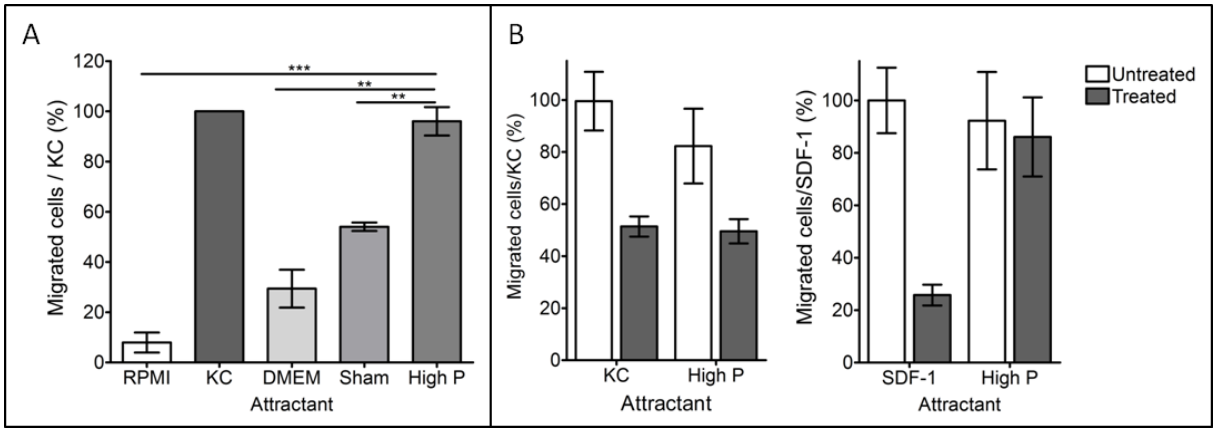

Figure 4.19: **Neutrophil migration towards HIPW-conditioned media**(A) Percentage of neutrophil migration (expressed as the percentage ratio of the test sample over the positive control KC) towards different attractant media. Values are the average of two experiments (E = 2) each performed with N=3 samples (** = $p<0.01$, *** = $p<0.001$). Mean values were analysed using one way ANOVA with Tukey post hoc test. (B) Percentage of neutrophil migration towards High P-conditioned medium compared to the positive attractants KC and SDF-1. A comparison of untreated cells with cells pre-treated with SB265610 (left) and AMD100 (right) to block respectively CXCR2 and CXCR4 receptors is shown.

experiments); and sham medium. In order to understand which factors in the HIPW-conditioned medium were driving the migration, comparative chemotaxis experiments were performed with inhibitory compounds SB265610 and AMD100. These compounds are known to act on receptors CXCR2 and CXCR4, respectively. As shown in Fig.4.19-B, neutrophil migration towards the HIPW-conditioned medium was partially reduced for cells treated with SB265610 (left), while no significant differences were observed using the other compound (right). Neutrophil migration towards KC and SDF-1 attractants was impaired by pre-treatment of the cells with the two compounds. These results suggest that the HIPW-conditioned medium contains CXCR2 ligands which could induce neutrophils migration.

MSCs migration towards HIPW-conditioned medium was also investigated. The average results of two independent experiments are presented here. As shown in Fig.4.20 there was a significant difference in number of cells that migrated towards HIPW-conditioned medium (High P) compared to DMEM medium enriched with 1 or 10% FBS, or the Freeze/Thaw medium. However, no significant difference in MSCs migration was observed between HIPW-conditioned medium and sham medium.

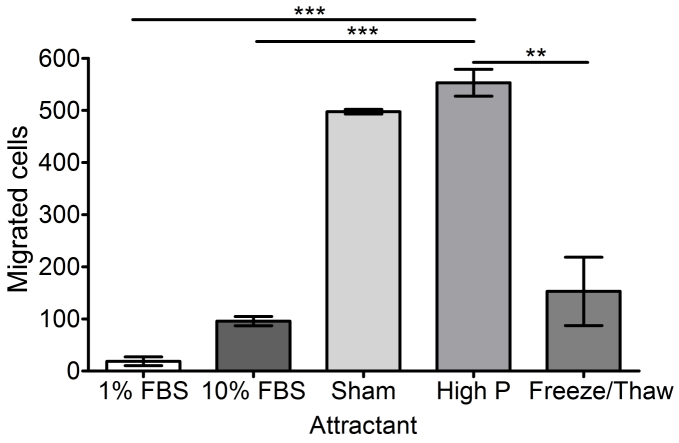

Figure 4.20: **Migration of MSCs to HISP-conditioned medium** The total number of MSCs that migrated towards different attractant media is shown, which is the average of two experiments (E = 2) each performed with N=3 samples (** = $p<0.01$, *** = $p<0.001$). Mean values were analysed using one way ANOVA with Tukey post hoc test. For each sample, 8 independent fields of view were used to count migrated cells and the total number was recorded.

4.3.5 MSCs adherent to a substrate

MSCs *in vivo* are rarely found in suspension. In order to study the effects of HIPWs on adherent cells, the modified system described in Chapter 3 for adherent cells was used. MSCs were grown on glass coverslips which were mounted at the end of the input (front) and output (back) bar of the SHPB system both facing the chamber cavity. Culture medium was inserted in the chamber and a HIPW of low intensity was then generated. Fig. 4.21 shows the metabolic activity measured for sham, Front, and Back samples immediately after the HIPWs experiments were carried out as percentage of the metabolic activity of control samples which were not introduced in the chamber. The decrease in metabolic activity measured for sham samples compared to control can be explained by the damaged caused by the manipulation required to mount the coverslip on the bar inserts (part of the surface of the coverslip was in contact with the screw that was holding it in place). Both groups of samples subjected to HIPW (Front and Back) showed very low levels of metabolic activity, which indicated an average 85% loss in cell viavility. Microscopical analysis of the recoverd cover slip confirmed these results. As is shown in Fig. 4.22, Front and Back coverslip samples were almost completely empty. A few blue-stained nuclei were visible at the lowest magnification (2x) indicating that most of

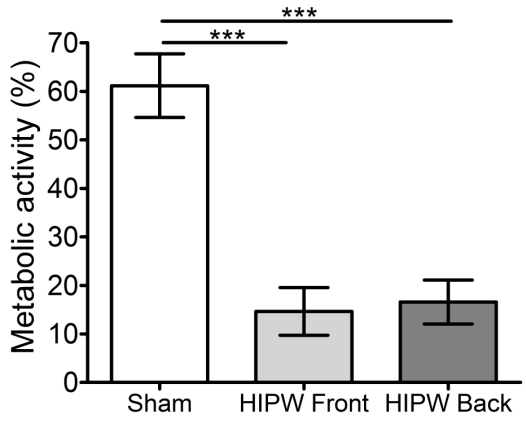

Figure 4.21: **Metabolic activity of adherent MSCs subjected to HIPWs.**The metabolic activity of MSCs adherent to glass coverslips recovered post-HIPWs exposure was assessed using the MTS assay and expressed as the percentage ratio compared to values obtained for control samples not inserted in the chamber. The average of two experiments (E = 2), each performed with N=3, are shown (*** = p<0.001). Mean values were analysed using one way ANOVA with Tukey post hoc test.

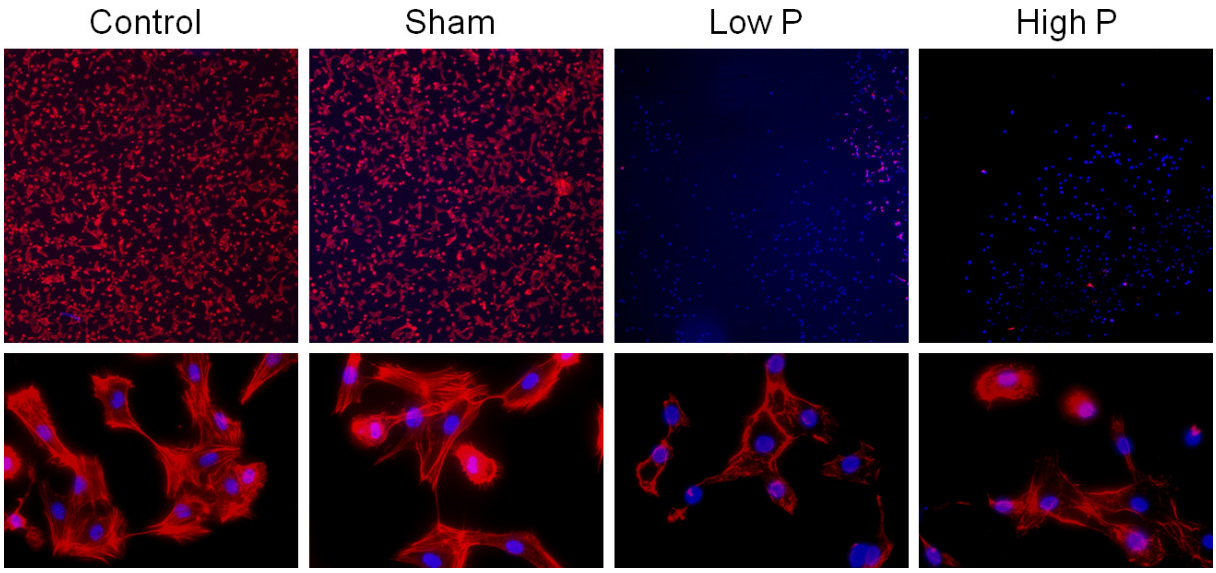

Figure 4.22: **Fluorescent images of adherent MSCs subjected to HIPWs** Images of MSCs adherent to glass coverslips post-HIPW exposure were compared to control and sham samples. Cell nuclei appears blue (DAPI stain) and in actin filaments appear red (Tritc Phalloidin stain). The top row is at 2x magnification and the bottom row 40x magnification.

the cells had been abruptly detached from the coverslips due to the HIPWs while the remaining cells lost their cytoskeleton (stained in red). At higher magnification (40x), the few remaining cells on the coverslips exposed to HIPW showed damage to the actin cytoskeleton. The organised structure of filaments that span within the cellular body seen in control and sham samples was not visible in the Front and Back samples. In the latter samples the actin is displaced outwards with respect to the central nuclei. In addition, the outer layer of the actin filaments appeared to form a close loop in the control and sham samples. Discontinuities were visible in the Front and Back samples, which could be associated with membrane rupture. These results indicate that the lowest level of pressure achievable with the SHPB system is lethal for this type of adherent cells.

4.4 Discussion

Improving the prospects for treatment of injuries arising from high intensity pressure waves is an issue of increasing importance given the nature of the casualties arising in military conflicts and terroristic attacks where explosive devices cause a range of blast injuries. The work presented here aimed to address primary blast injuries through the development of an experimental setup in the form of a highly resilient and biocompatible chamber. This chamber enabled the application of high intensity pressure waves to different cell cultures that could then be subsequently analysed for acute and short term effects. Previous studies of cell damage induced by shock waves generated with ESW or laser facilities have reported variable percentages of cell lyses (5%-95%) and cell death, depending on the number of discharges and their pulses energy [43]. In the experiments presented here cells in suspension were subjected to a single pressure event characterised by multiple peaks with a total duration of approximately 1 ms and peak pressures varying from 15 to 40 MPa, as described in Chapter 3. Cell lysis measured as LDH release for PLB985 and MSCs in suspension subjected to HIPWs showed similar results for the two different cell lines: increasing the peak pressure the amount of LDH release increased. Moreover cell viability was assessed by the trypan blue dye exclusions method as previously described for other shock-induced damage cellular experiments [52, 57]. The experiments performed

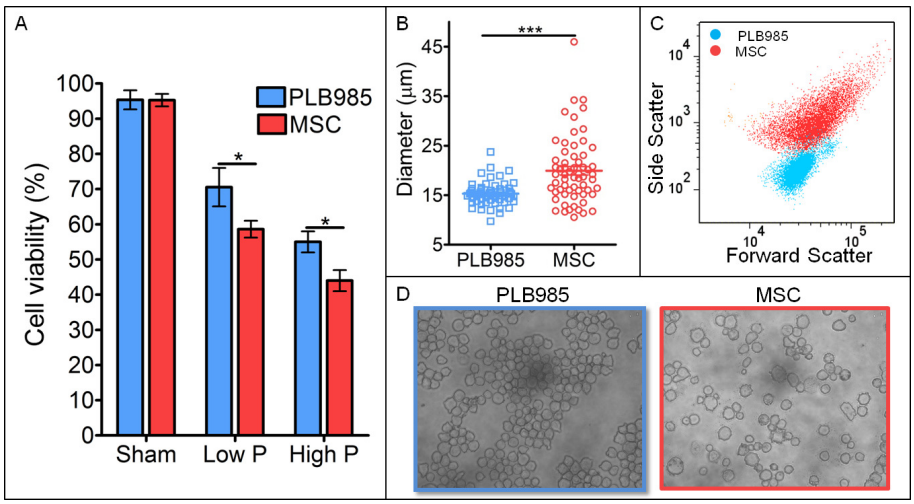

Figure 4.23: **Comparison of cell viability, cell size and granularity of PLB985 cells with MSC subjected to HIPWs**(A) Cell viability for PLB985 cells and MSCs expressed as a percentage of the initial number of cells. The average of three experiments (E = 3), each performed with N=3 for PLB985 cells and N=5 for MSCs, are shown (* = p<0.05, *** = p<0.001). Mean values were analysed using unpaired t test. (B) Cells diameter measured from cytospin of PLB985 and MSCs shown in quadrant (D). (C) FSC-SSC plot of PLB985 cells and MSCs which shows significantly higher granularity for MSCs.

with the SHPB system showed that cell viability was significantly reduced in samples subjected to HIPW for all the different cell types used. In agreement with the cell lysis results, the decrease in cell viability was proportional to the intensity of the pressure wave and independent from initial cell concentration. To confirm these results, the metabolic activity of samples subjected to HIPWs was also analysed with a MTS assay. The results of these experiments confirmed the loss in viability measured with the exclusion method, and that intact cells recovered after the HIPWs experiments were indeed metabolically active. Comparing the results on cell viability for two different cell lines subjected to the same HIPWs it was observed that MSCs were more susceptible to HIPWs compared to PLB985 cells as shown in Fig.4.23 A. These two cell types differ both in size (average diameter: MSCs 19.9 $\pm$ 0.9 μm; PLB985 15.3 $\pm$ 0.3 μm) and granularity (MSC showed higher SCC values in the flow cytometry analysis). These data suggest that both these parameters could be related to the cellular injury threshold. In comparison, results of cell viability for the different cell populations in the bone marrow showed no statistically significant differences between cells with different sizes and granularity. These results are

consistent with the opposite conclusion, namely that neither cell size nor granularity influence the cell injury threshold. However, higher errors were observed for data obtained from HIPW experiments on bone marrow. Cell viability data obtained from MSCs and PLB985 cells were directly assessed using individual cell populations. Cell viability data obtained for the different cell populations of the bone marrow were calculated on the total number of cells recovered and then adjusted for the different proportions of populations based upon the percentage distribution determined using flow cytometry. This last method could hence not take in account losses in viability of the individual cell populations, since it is assumed that the percentage distribution is measured on viable cells, and results for populations like MSCs and HSPCs could also be incorrect due to the very low percentage of cells that can be found in the bone marrow. Previous studies on the effects of pressure waves on cells reported that cellular injury threshold is a characteristic of the specific cell type [56], and that different cellular components have different injury thresholds, with the plasma membrane being the most susceptible to injury [52].

High speed photography of HIPW experiments (Chapter 3, section 3.5.4.6) indicated that, following the pressure wave, air bubbles formed and collapsed inside the liquid suspension. The images suggest that cavitation takes place for approximately 30 ms after the passage of the pressure wave. This result must be taken into consideration if a mechanism of cell damage is to be defined: although a correlation between the peak pressure and the level of damage in terms of viability of the cells was observed, cavitation could have also contributed to the lysis of cells in suspension, as previously reported for ESW and laser shock experiments [43, 51, 52].

Short term effects of HIPWs on MSCs in suspension were studied for their effects on cell metabolic activity and differentiation potential. Controversial results have been previously reported on the effects of mechanical stimuli on MSCs proliferation and differentiation. Scaglione et al. [114] reported a decrease in cell proliferation and an increase in expression of some osteogenic genes in 2D MSCs culture subjected to shear flow. Maul et al. [115] observed no osteogenic or adipogenic differentiation in MSCs subjected to cyclic hydrostatic pressure or laminar shear stress when cultured in normal cell culture medium. In

both studies the mechanical stimuli were applied on adherent MSCs and were repeated and prolonged. In our experiments we were interested in simulating a single pressure event, relevant to blast injuries, and assess if MSCs metabolic activity or osteogenic differentiation was enhanced. This is because an increase in the number of progenitor cells with osteogenic potential was observed in the tissue extracted from patients that later developed HO [109]. However, no significant differences in metabolic activity were observed between sham samples and samples subjected to HIPWs when cultured up to 72 h in fresh DMEM medium. Also, cell cycle analysis revealed no changes in the percentage of cells in the different cycle phases for samples subjected to HIPW compared to sham samples. Moreover, no differences in ALP activity were observed between sham and HIPW samples when cells were cultured in osteogenic medium or DMEM culture medium for 7 days. One can therefore speculate that the increase in number of osteoprogenitor cells in the wounded tissue is not directly related to the mechanical blast stimulus on the cells themselves, but possibly to the effects of the blast medium surrounding the wounded tissue. The effects of the HIPW conditioned medium on healthy cells were studied in terms of metabolic activity and migration potential. No significant conclusions could be drawn from the study of the effects of the HIPW conditioned medium on the metabolic activity of healthy cells as the different experiments yielded contradictory results. Moroever, although a significant increase in MSC migration was observed towards HIPW-conditioned medium compared to control DMEM medium, no significant differences were observed compared to sham samples. These data suggest that no significant changes in the content of migration factors occur in the conditioned medium of sham and HIPWs samples.

The migration of neutrophils towards HIPW-conditioned medium was investigated. In these experiments neutrophil migration towards HIPW-conditioned medium was significantly increased compared to sham medium. Migration towards HIPW-conditioned medium was partially reduced when neutrophils were pretreated with SB265610, while no changes in migration were observed for neutrophils pretreated with AMD3100. These results suggest that the HIPWs conditioned medium may contain ligands for the CXCR2 receptor but not for the CXCR4 receptor. Bone marrow MSCs are known to secrete vari-

able levels of the chemokine CXCL1 in the medium, hence this could be one of the factors released by HIPWs exposed cells which can induce neutrophil migration. However, other chemokines could be released into the HIPW-conditioned medium such as HMGB1 [116], a damage associated molecular pattern released by necrotic cells known to affect proliferation and differentiation of MSCs. The analysis of the different molecules released in the HIPW-conditioned medium is beyond the scope of this research, however these preliminary results suggest that blast-induced release of inflammatory, differentiation or growth factors is likely to be the mechanism by which primary blast pathologies develop. These data are consistent with data obtained by Potter et al. [26] who collected the wound effluent from traumatised muscles that later developed HO and showed an increase in cell differentiation when MSCs were cultured with this medium.

The experiments discussed so far were performed on cells in suspension. However, most cells are anchorage-dependent, hence their morphology and structure depend on the solid support to which they adhere. In order to create the dynamic mechanical loading conditions associated with primary blast trauma in adherent cell culture models, MSCs were grown in a 2D structure on glass coverslips which were then mounted at the end of the input and output bars of the SHPB system. Results showed that the pressure generated with the SHPB system were almost lethal for adherent MSCs. Low levels of metabolic activity were recorded for HIPW-exposed samples. Fluorescent microscopy analysis showed that most of the cells had been ripped off the glass coverslip and the few that were still adherent had evident cytoskeleton damage. These results suggest the need for developing a different type of experiment to simulate primary blast injury on adherent cells which will be presented in the next chapter.

In conclusion, the system developed to generate HIPWs-induced cell injury has successfully demonstrated variable levels of cell damage in cell suspensions and can be used as a platform to generate pressure-induced release of cellular factors. Limitations of the system are represented by the lowest and highest levels of pressure that can be generated in the chamber, the presence of cavitation as a source of cellular damage and the risk of sample contamination during the loading of samples in the chamber in a non-sterile

environment. These limitations could be overcome by using polycarbonate bars to achieve lower pressures, embedding cells in a gel-like structure (which could reduce the cavitation seen in the liquid) and building an ad-hoc sterile laminar flow workstation around the SHPB system to protect samples from airborne contamination.

Future work should include the study of the effects of HIPW-conditioned medium generated from different cell types on the proliferation, differentiation and migration potential of MSCs. Moreover the system could be used to study other cell types associated with primary blast injuries such as blast lung or traumatic brain injury.

Chapter 5

Shock tube for *in vitro* overpressure experiments

5.1 Introduction

5.1.1 Overview of the shock tube

The shock tube is a device used to generate planar shock waves in test gases in order to simulate explosions and their effects. Initial applications focused on the investigation of hydrodynamics of shock propagations, tests of aerodynamics, chemical kinetic measurements, heat transfer studies etc. [117], and more recently shock tubes have been used in biomedical research to study how biological specimens are affected by blast waves [37, 59, 60]. A simple shock tube, as shown in Fig. 5.1 a, is composed of a high pressure section (driver section) and a low pressure section (driven section) divided by a diaphragm. The sudden rupture of the diaphragm, due to the buildup of high pressures behind it, up to the diaphragm bursting pressure P_4, generates a compression wave in the low pressure gas (at initial pressure P_1 and temperature T_1), that rapidly steepens to a shock front travelling at the shock velocity W_s. Simultaneously, a rarefaction (expansion) wave travels back into the high pressure driver gas. This wave is not a discontinuous jump in pressure as the shock front, but a smooth transition between the shock pressure and the driver pressure [118]. The front of the expansion wave travels at the speed of sound

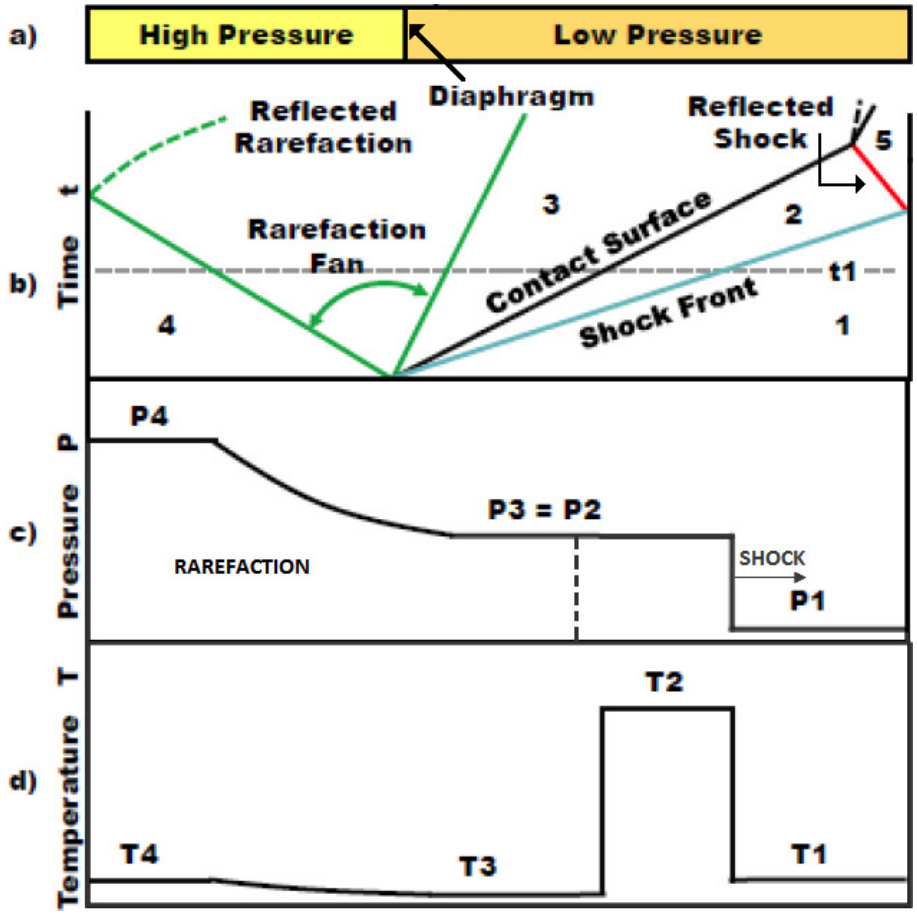

Figure 5.1: **An idealised shock tube.** Reproduced from [118]. a) simple schematic of a shock tube highlighting the high and low pressure gases regions; b) shock, rarefaction, contact and reflected waves formed along the shock tube following the diaphragm rupture; c) pressure profile along the length of the tube once the diaphragm has burst; d) temperature of the gases inside the shock tube

of the driver gas while the tail travels much slower, giving rise to a rarefaction fan, as shown in Fig. 5.1 b. The contact surface between the driven gas and the driver gas moves along the tube behind the shock front. Pressure and temperature in the region between the shock front and the contact surface are denoted by the subscript 2, while the region between the contact surface and the rarefaction fan is described by the subscript 3. If the shock tube is in a closed configuration, the shock wave can reflects back from the shock tube end giving rise to a reflected shock which increases the pressure and temperature of the driven gas to values denoted by P_5 and T_5 [118].

5.1.2 The ideal gas description of a shock tube

The laws of conservation of mass, momentum, and energy are used to relate the state variables before and immediately after the shock front in the driven gas. Under the assumptions that the driven and driver gases are ideal, the diaphragm rupture is instantaneous and there are no friction or radiative losses in the gas flow, the conservation equations are:

$$\rho_1(W_s - \nu_1) = \rho_2(W_s - \nu_2) \tag{5.1}$$

$$P_1 + \rho_1(W_s - \nu_1)^2 = P_2 + \rho_2(W_s - \nu_2)^2 \tag{5.2}$$

$$H_1 + 1/2(W_s - \nu_1)^2 = H_2 + 1/2(W_s - \nu_2)^2 \tag{5.3}$$

where ρ, ν, P and H are the density, particle velocity, pressure and enthalpy per unit mass of the driven gas and the subscripts 1 and 2 denote respectively the states ahead and behind the shock front [118]. In the case of an ideal gas, the entalphy H, which represent the total energy of a thermodynamic system including the internal energy U and the work done by the system, PV, can be expressed as:

$$H = (\frac{\gamma}{\gamma - 1})RT \tag{5.4}$$

where γ is the specific heat ratio and R is the universal gas constant per unit mass of gas. For air at room temperature, γ has a value of 7/5.

According to arguments presented by Gaydon and Hurle [119], the conservation equations can be manipulated to formulate relations between the state variables P, ρ and T in the region ahead and behind the shock front in terms of the Mach number M and the specific heat ratio. M is defined as the ratio of the velocity of the flow in the gas and the local speed of sound a, and for the gas in the unshocked state equals to

$$M_1 = \frac{(W_s - \nu_1)}{a_1} \tag{5.5}$$

The sound speed in the unshocked gas is defined as $a_1 = \sqrt{\gamma R T_1}$. Hence, the pressure, temperature and density in the shock front of an ideal gas can be calculated knowing the pressure, temperature and density in the unshocked state and the shock velocity using the equations:

$$\frac{P_2}{P_1} = \frac{2\gamma M_1^2 - (\gamma - 1)}{(\gamma + 1)} \tag{5.6}$$

$$\frac{\rho_2}{\rho_1} = \frac{M_1^2(\gamma + 1)}{(\gamma - 1)M_1^2 + 2} \tag{5.7}$$

$$\frac{T_2}{T_1} = \frac{(\gamma M_1^2 - \frac{\gamma - 1}{2})(\frac{M_1^2(\gamma - 1)}{2} + 1)}{(\frac{\gamma + 1}{2})^2 M_1^2} \tag{5.8}$$

Moreover, the relationship between the bursting pressure P_4 or the pressure behind the reflected pressure P_5 and the initial pressure of the driven gas P_1 can be expressed as:

$$\frac{P_4}{P_1} = \frac{2\gamma_1 M_1^2 - (\gamma_1 - 1)}{(\gamma_1 + 1)}[1 - \frac{(\gamma_4 - 1)a_1}{(\gamma_1 - 1)a_4}(M_1 - \frac{1}{M_1})]^{-(\frac{2\gamma_4}{\gamma_4 - 1})} \tag{5.9}$$

$$\frac{P_5}{P_1} = (\frac{2\gamma_1 M_1^2 - (\gamma_1 - 1)}{(\gamma_1 + 1)})(\frac{(3\gamma_1 - 1)M_1^2 - 2(\gamma_1 - 1)}{(\gamma_1 - 1)M_1^2 + 2}) \tag{5.10}$$

These equations can be used to design experiments through prediction of the pressure state developed in the shock front, hence giving indications of the stimulus that a specimen would be subjected to when positioned at the end of the shock tube. However, in real experiments gases are not ideal, diaphragm rupture is not instantaneous and the presence of obstacles in the shock tube such as a sample can introduce friction and induce turbulence, hence generating a deviation from the theoretical values of pressure. For these reasons, dynamic pressure sensors need to be used in order to accurately monitor the shock evolution along the tube and within the specimen of interest.

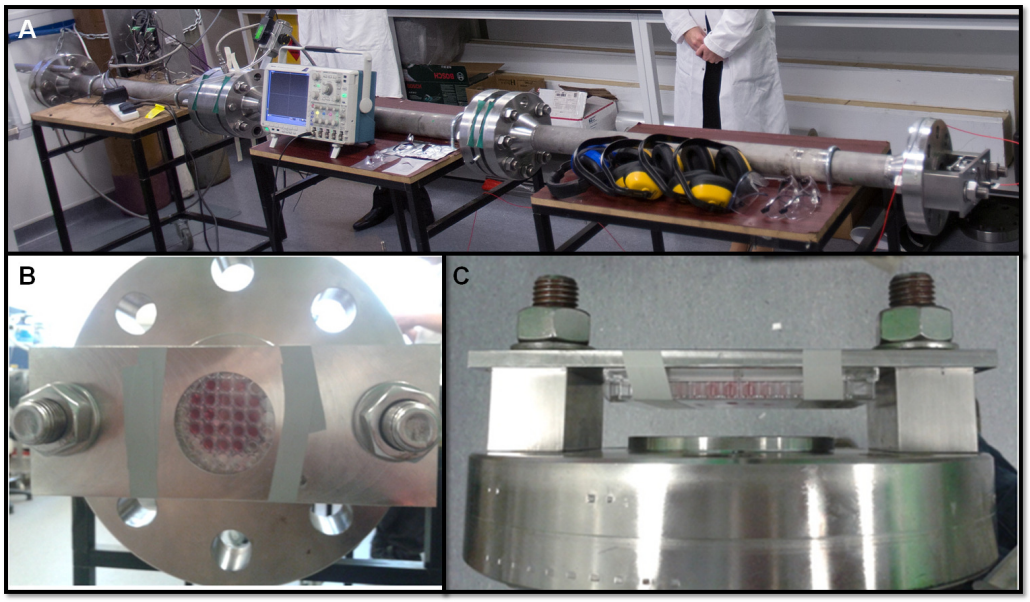

Figure 5.2: **CBIS's shock tube** Photographs of CBIS shock tube (A) and *in vitro* assembly with a tissue culture plate hold by tape on a steel support at the open end of the shock tube (B,C)

5.2 Materials & methods

5.2.1 The CBIS shock tube

The CBIS's shock tube was designed by Dr D. Chapman and consists of three 1.22 m long stainless steel tube sections connected by flanges in which pressure transducers, o-rings and vents are embedded. Rubber nitrile gaskets were used to improve the sealing at joinings. The tube internal and external diameters are 59 and 73 mm respectively. The total length of the tube in the standard configuration is approximately 3 m, with the first meter of the tube serving as the high pressure driver section, separated from the low pressure driven section by the diaphragm breech. The driver and breech sections of the shock tube are pressurised from a standard gas cylinder of dry air to a maximum pressure of 18.2 bar (for safety reasons). The shock tube is charged and operated from a remote control box, connected to the shock tube and gas cylinder using flexible pressure hosing. Pressure transducers enable the static pressure in the driver and breech sections to be monitored from the control box. Mylar and aluminium membranes of varying thicknesses are used for generating increasing levels of blast overpressures. Two dynamic pressure sensors, Dytran - 2300V1 and Dytran - 2300C4 are installed respectively along the driven

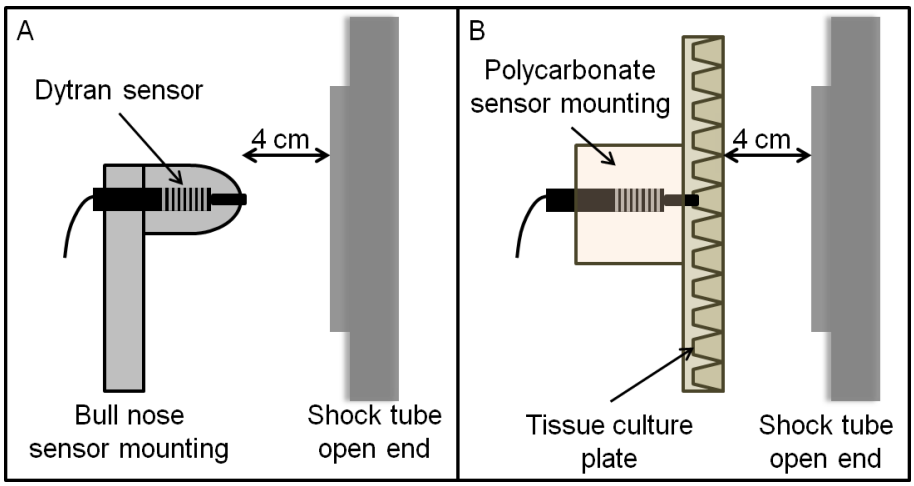

Figure 5.3: **Sensor mounting configurations.** The pressure at the open end of the shock tube is measured either in air using the bull nose configuration (A), where the sensor is mounted in a bull nose steel support, or in liquid, inside the tissue culture plate (B), where the sensor is mounted in a custom made polycarbonate cylinder which has been attached to the bottom of the culture plate with an epoxy bonding agent

section oriented laterally (sensors 1) and head-on (sensor 2) to the shock tube to monitor the evolution of the shock wave generated by the sudden rupture of a diaphragm.

In the experiments reported here, sensor 2 was either mounted on a bull nose or on a custom made support, as shown in Fig 5.3, to measure the pressure developed at the open end of the shock tube or within the plates used in the *in vitro* experiments. Sensor 1 was connected to the oscilloscope through a current source, while signal from sensor 2 was amplified before being connected to the oscilloscope. Data were acquired for 4 ms with acquisition rate of 25 mega-samples/s and triggered by the rising edge of sensor 1. The output voltage was converted to pressure using the calibration factor provided by the manufacturer for sensor 1 (21.04), while sensitivity of sensor 2 was manually set using the amplification box to a value of 100.

5.2.2 *In vitro* set up and characterisation

Fortyeight well tissue culture plates filled with 720 μl of water were secured in the vertical position at a distance of 4 cm from the last flange of the shock tube in the open configuration: the plates were secured with tape on a custome made stainless steel support (designed by Dr J. Wilgeroth) either in the front (with the bottom of the plate in contact

with the metal support) or back (with the bottom of the plate facing the shock tube open end) configurations as shown in Fig. 5.2 B and C. Two different materials were used to seal the plates during the overpressure experiments: a non permeable and a gas permeable tape (Cornig). Shock experiments were performed with diaphragm of different materials and thicknesses to determine the maximum overpressure the set up could withstand, as well as to compare the two different plate's sealing membranes. High speed photography was used to investigate the formation of cavitation during the overpressure experiments.

5.2.3 Cell culture overpressure experiments

MSCs were cultured up to passage 3 as described in Chapter 4. The day before the overpressure experiments, cells in suspension were plated in 96 well tissue culture plates at a concentration of 10^4 cells per well (9 replicates per plate), covered with 200 μl of DMEM medium containing 1% (v/v) FCS and 1% (v/v) PenStrep. Cell were let adhere overnight in an incubator at 37 °C and 5% CO_2. Just prior to the experiment, the culture medium was removed from the wells and replaced with 360 μl of fresh DMEM medium. Each plate was sealed with a non permeable adhesive membrane (Cornig) trying to avoid any air bubble formation. After exposure to the overpressure the medium from each well was removed and replaced with 200 μl of fresh DMEM medium. The MTS assay was used, as described in section 4.2.6.1, to investigate cell metabolic activity at different time points (3, 24 and 48 h) after the overpressure. Results were compared to metabolic activity of sham samples, which were handled as the samples subjected to overpressure but without operating the shock tube. Moreover, cell differentiation potential was investigated with the ALP assay 7 days after the shock experiments for samples cultured in osteogenic differentiation or DMEM culture media, as described in section 4.2.9.2. Values of ALP activity were expressed as mean ± standard error and statistical analysis was carried out by one way ANOVA using GraphPad Prism software (GraphPad Software Inc., La Jolla, California, USA).

Material	Thickness	Burst Pressure	Reflected Shock Pressure
	μm	bar	kPa
Aluminium	40	1.8 ± 0.1	40 ± 5
Aluminium	80	3.0 ± 0.1	160 ± 10
Mylar	23	2.2 ± 0.1	50 ± 5
Mylar	50	4.4 ± 0.1	110 ± 10
Mylar	125	9.5 ± 0.1	270 ± 15

Table 5.1: **Performance of different diaphragm materials and thicknesses.** The average burst driving pressure and the reflected shock pressure measured from three experiments for each type of diaphragm with the shock tube in the open configuration

5.3 Results

5.3.1 Shock tube's pressure output

A full characterisation of the operation of the shock tube is beyond the scope of this thesis and the topic of another PhD student's research within the CBIS group. Hence, this study has focused on measuring the pressure profiles developed along the shock tube and inside the biological sample holder when the device was fired in the open configuration, which is relevant to experiments performed to study the effects of a single blast overpressure on biological samples. Initial experiments were performed to determine the conditions under which *in vitro* overpressure experiments could be performed without damaging the tissue culture plates and allowing recovery of uncontaminated biological samples. Two different diaphragm membranes (annealed aluminium foils and Mylar film of different thicknesses) were used to generate increasing levels of overpressure. In Table 5.1 a summary of the values of burst pressure and reflected shock pressure measured in the open configuration, with sensor 2 mounted on the bull nose support, as a function of the diaphragm material and thickness. Aluminium foils bursted at lower pressures compared to Mylar films of the same thickness, hence generating lower reflected shock pressures. Moreover, the burst process of the aluminium foils was associated with fragmentation which generated shrapnels that travelled along the shock tube. These fragments could reach the sample positioned at the open end of the shock tube, causing damage to the adhesive film used to seal the tissue culture plates. Consequently, only Mylar films were used to generate overpressures for *in vitro* experiments. It was observed that tissue culture plates broke

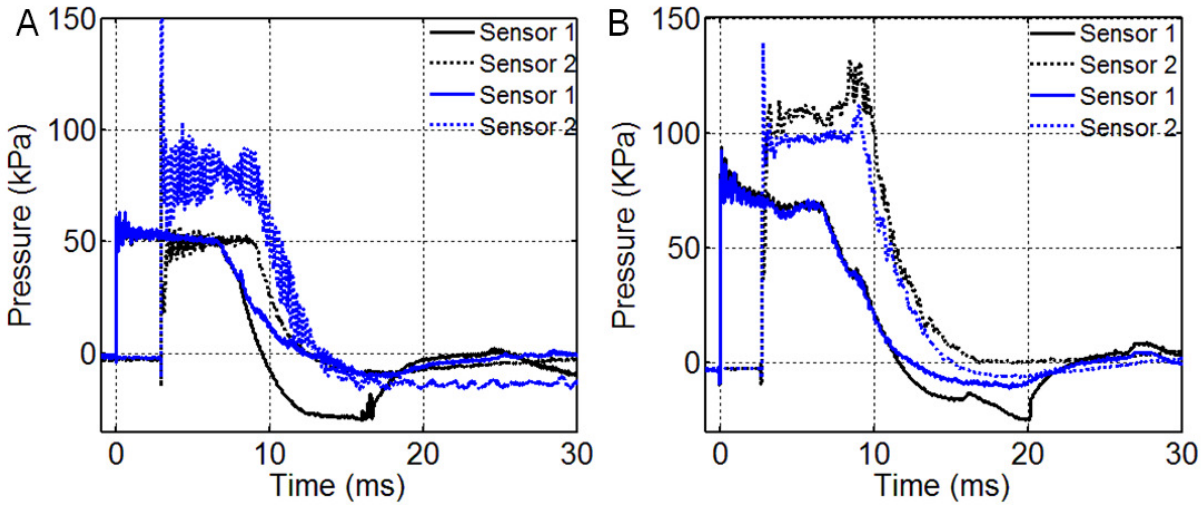

Figure 5.4: **Pressure profiles along the shock tube** The overpressure measured by the lateral sensor (1) and head-on sensor (2) when mounted on the bull nose (black) or in the tissue culture plate (blue) respectively for Mylar 23 (left) and Mylar 50 (right) bursting diaphragms.

when subjected to an overpressure of 270 kPa generated by the rupture of a 125 μm thick Mylar diaphragm. Hence the characterisation of the *in vitro* system was conducted with Mylar diaphragms of 23 and 50 μm thickness.

In Fig. 5.4 the pressure history measured at the mid length of the tube (sensor 1) and at the opend end (sensor 2), with sensor 2 mounted respectively on the bull nose support (black), or within the unsealed tissue culture plate (blue) for experiments performed with Mylar diaphragms of different thickness (23 μm on the left and 50 μm on the right). Thicker diaphragms produced higher overpressures as recorded in each configuration by sensors 1 and 2. Moreover, while the intial rise and step portion of the pressure traces measured at sensor 1 was identical for the different configurations, the exponential decay part of the curves changed significantly when sensor 2 was mounted at the open end of the tube either on the bull nose or on the tissue culture plate support. This affected the duration of the positive phase as well as the shape of the negative phase as measured by sensor 1 for experiments performed with diaphragms of different thickness. However, the output pressure measured with sensor 2 at the open end of the shock tube with the two different sensor mountings changed only in terms of intensity, suggesting that varying the diaphragm thickness or the sample configuration, would have simply varied the intensity

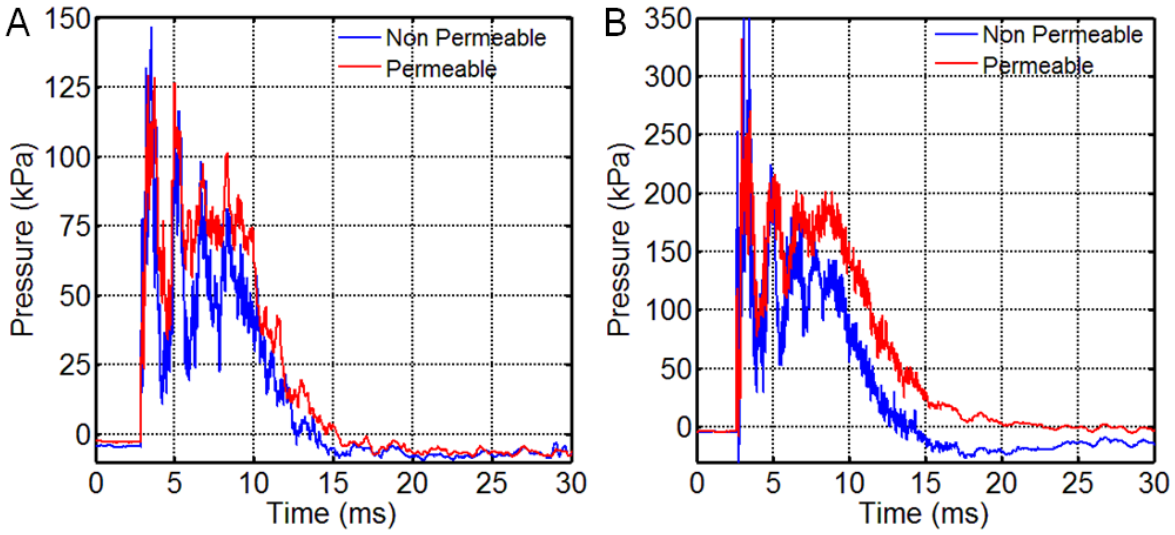

Figure 5.5: **Pressure in the *in vitro* system** Pressure profiles developed within the tissue culture plate filled with liquid and sealed with a non permeable (blue) or gas permeable (red) membrane respectively for Mylar 23 (left) and Mylar 50 (right) bursting diaphragms.

of the shock pressure, hence allowing the comparison of the effects of different overpressures on biological samples.

In order to evaluate the overpressure sensed by the cells in the *in vitro* configuration, experiments were performed with a tissue culture plate filled with water and sealed with two different types of membrane (non permeable or permeable), before being positioned in front of the open end of the shock tube. Sensor 2 was mounted within one of the wells and sealed with teflon tape, so that the end face of the sensor would sit in the same position of the cell monolayer. The pressure history recorded by sensor 2, for experiments performed with diaphragms of different thicknesses (Mylar 23 and 50 μm), are presented in Fig. 5.5. All the traces are characterised by an intial sharp rise in pressure followed by a series of oscillations around a plateau value of pressure which then evolves in an exponential decay. Comparing the two plots, the pressure generated within the liquid-filled well by the external overpressure was higher for experiments performed with thicker diaphragms, as expected. The two types of membrane produced comparable levels of overpressure, with the permeable membrane correspondent to slightly higher values in the plateau region. Moreover, the non permeable membrane was associated with larger oscillations around the plateau value. This could be related to the different mechanical properties of the

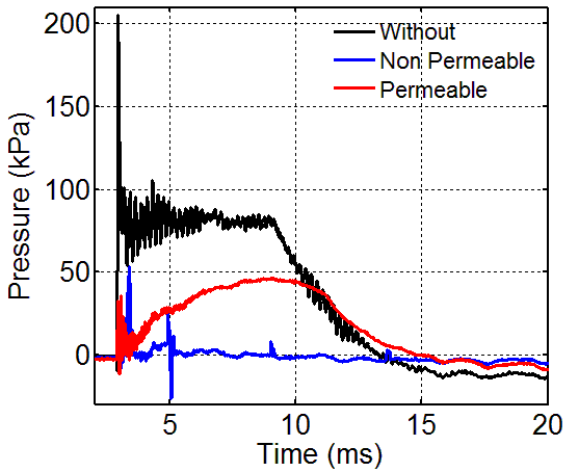

Figure 5.6: **Comparison of different sealing membranes** Pressure profiles developed behind different sealing membranes (red and blue) when mounted on an empty tissue culture plate compared to the pressure profile developed within an unsealed plate.

sealing membranes, but also to the fact that pressure generated in the well when sealed with the permeble membrane was due not only to the energy coupling between the membrane and the liquid, but also to the overpressure in the gas which could flow inside the well. In Fig. 5.6 the pressure developed within the plate when not filled with liquid and sealed or not with the two different membranes. The pressure developed in the air-filled well behind the non permeable membrane was almost negligible compared to the values of pressure measured in the well when the plate was not sealed. On the contrary, the permeable membrane allowed significant gas flow inside the well which generated a rise in pressure as shown by the red curve, which had total duration comparable to the pressure developed in the open well, but lower intensity and slower rise. These results suggest that although the pressure measured in the liqid-filled wells when sealed with the two different membranes are comparable, the mechanisms of pressure generation could be substantially different. Moreover, it was observed that the non permeable plate ensured perfect sealing during the overpressure experiments, while the permeable membrane allowed liquid to leak once the values of pressure had returned to the ambient one. The two configurations could be used to represent different physiological scenarios: the non permeable one, to simulate the effects of overpressure on tissues such as bone, skin, muscle etc., while the permeable one to replicate the effects of blast overpressure on gas filled organs, such as

	Peak pressure	**Plateau pressure**	**Duration**	**Impulse**
	kPa	kPa	ms	kPa ms
Non Perm.	150.7 ± 20.29	59.86 ± 3.68	9.33 ± 0.46	466.2 ± 42.1
Perm.	155.2 ± 18.32	78.90 ± 4.01	11.48 ± 1.52	660.8 ± 49.5
Non Perm.	398.8 ± 5.162	131.50 ± 8.34	10.05 ± 0.54	1056.0 ± 134.1
Perm.	366.1 ± 37.10	166.81 ± 3.37	17.57 ± 2.81	1643.0 ± 23.0

Table 5.2: **Shock parameters for *in vitro* overpressure experiments** Average values of peak pressure, plateau pressure, positive phase duration and pressure impulse as measured from sensor 2 pressure profile traces when mounted inside the water-filled tissue culture plate. Values represent mean and standard deviation of three experiments.

lung, trachea, ears etc. In the present study, the non permeable membrane was chosen to subject mesenchymal stem cells harvested from the bone marrow of balb/c mice to controlled overpressure. Furthermore, several parameters were identified that could affect the biological samples: peak overpressure, average plateau overpressure, positive phase duration and overpressure impulse (calculated as the area under the curve of the positive phase). The values of this parameters for experiments performed with the two different sealing membranes and two different diaphragm thicknesses are summarised in Table 5.2. Finally, high speed photography was used to investigate if cavitation was induced within the liquid-filled wells by the shock overpressure. Tissue culture plates were mounted at the open end of the shock tube either with the sealing membrane directly facing the tube flange (front) or facing the steal plate's support (back). As shown in Fig. 5.7 in both configurations, air bubbles generated at the edges of the wells and expanded towards the centre, before collapsing or retrieve towards the edges. Moreover, if an air bubble was trapped in the well before the overpressure, the shock stimulus induced the bubble to increase in size before collapsing.

5.3.2 Effects of shock overpressure on stem cells

Preliminary experiments were performed to study the effects of blast overpressure on MSCs when adherent to a substrate. Levels of cell respiration were measured with the MTS assay at different time points after the cell monolayers were subjected to overpressure due to the rupture of a 50 μm Mylar diaphragm. The graph in Fig. 5.8 shows the average

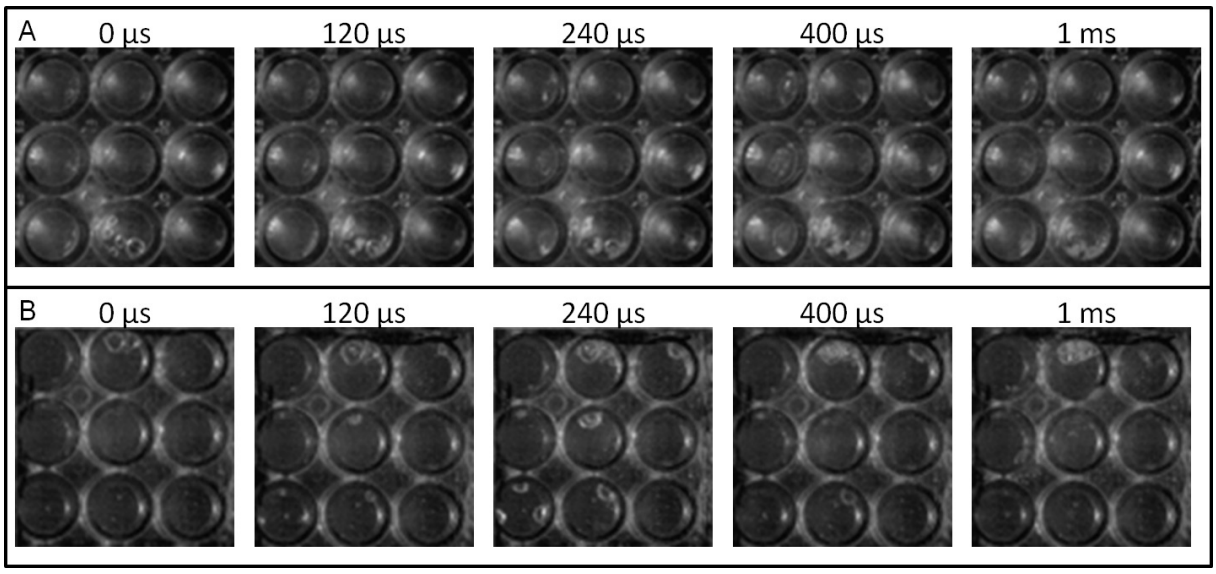

Figure 5.7: **High speed photography of *in vitro* shock experiments** Still images at different time points for shock tube-induced overpressure in tissue culture plates sealed with non permeable gas membrane. In A the plate faces the open end of the shock tube, while in B the bottom of the plate is first exposed to the shock wave.

levels of cell respiration at 3, 24 and 48 hours. Samples subjected to overpressure in the back configuration were associated with significantly lower levels of respiration (Dunnett's Multiple Comparison Test) 3 hours after the overpressure experiments compared to sham samples. However, when a linear fit was applied to determine if cell respiration had been affected by the overpressure, no significant differences were observed between the three groups. The differentiation potential of MSCs subjected to overpressure was also investigated. Samples recovered from the shock experiments were cultured either in the ostegenic medium or in the control medium for one week and the amount of pNPP produced by the cells, normalised to the level of cell respiration, was compared to sham samples. The results are presented in Fig. 5.9. No significant differences were observed between shocked and unshocked samples when cultured in osteogenic medium, whereas there was a significant increase in ALP activity in samples subjected to overpressure and then cultured in control medium compared to sham samples. This result suggests that the pressure stimulus could potentially stimulate osteogenic differentiation in MSCs, however more experiments are needed to confirm this hypothesis.

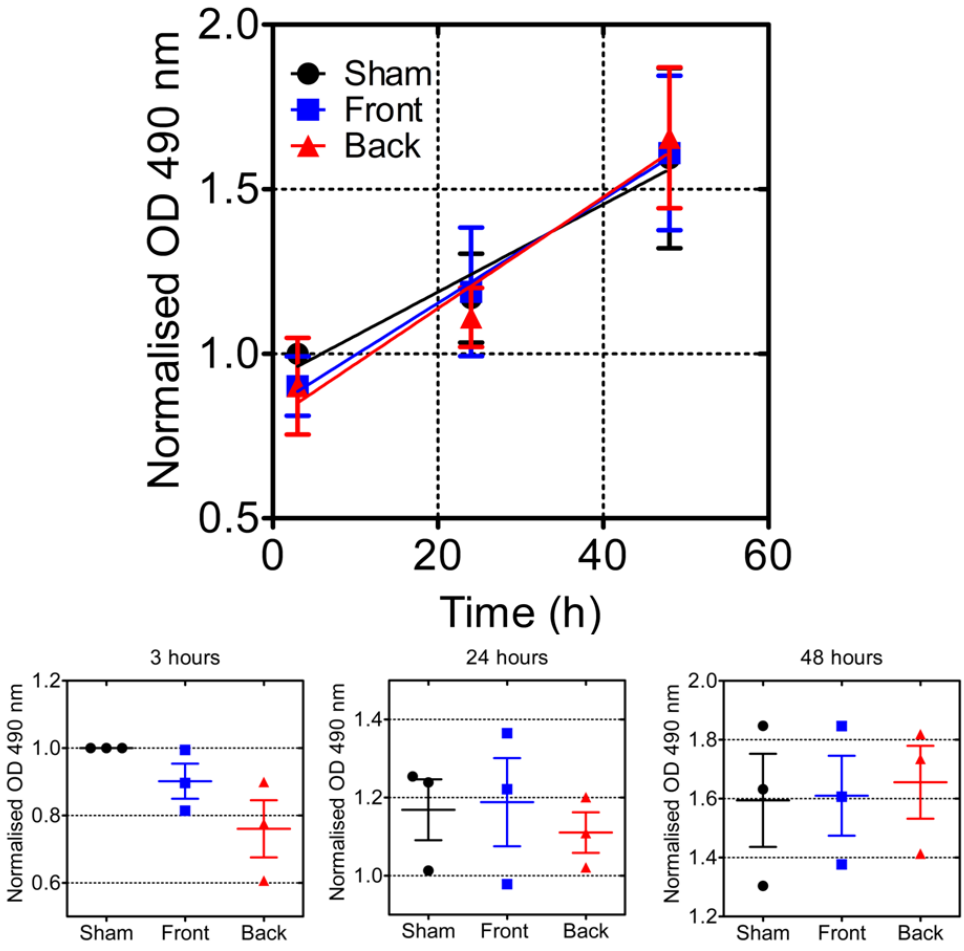

Figure 5.8: **Viability and metabolic activity of MSCs following blast overpressure** Cell respiration was evaluated with the MTS assay and measured in terms of optical density (OD 490 nm) for samples subjected to ovepressure CBIS shock tube at 3, 24 and 48 hours after the shock experiments. The average of two experiments (E = 3), each performed with N=9, are shown. Mean values were analysed using one way ANOVA followed by Dunnet's multiple comparison tests.

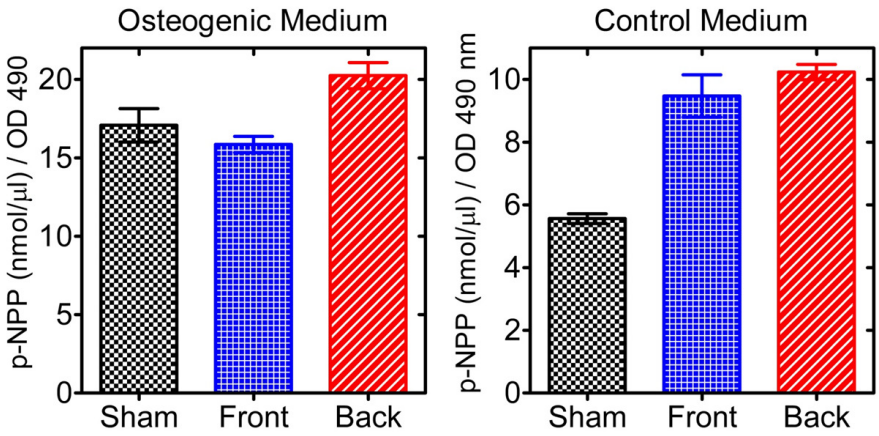

Figure 5.9: **Osteogenic differentiation of MSCs subjected to shock overpressure** The amount of pNPP produced by cells subjected to overpressure was measured 7 days after the shock experiments and normalised by the values of cell respiration at the same time point. The results represent the average of one experiment (E = 1) performed with three samples per condition(N = 3).

5.4 Discussion

In vitro models are an important tool to study pressure-mediated effects on live biological samples. Few studies have focused on the response of cultured cells and tissues to mechanical inputs that simulate primary blast conditions [22]. *In vitro* models have the potential to improve access to the biological and mechanical parameters associated with primary blast-induced damage, elucidating the molecular and biochemical changes that are the basis of traumatic and long term pathologies seen in blast victims. In the past few years two research groups have developed shock tube *in vitro* systems to subject cell culture to overpressure similar to those experienced in the battlefield [59, 60]. Arun et al [59,61] developed a tissue culture plate-based *in vitro* shock system to study the effects of overpressure on neuronal cells in the context of TBI studies. They used gas permeable membranes to seal the plates and performed different cell based assays to assess the damage induced by the mechanical stimulus. They reported the contradictory result that samples subjected to multiple overpressures had sustained less damage in terms of cell viability and their system characterisation lacked the measurement of the actual pressure sensed by the cell monolayers within the tissue culture plates. Bass et al. [58, 60] developed a shock tube for both *in vivo* and *in vitro* studies. They designed a fluid-filled *in vitro* receiver in which biological samples, sealed in a plastic bag, were suspended. The

authors used pressure transducers positioned in front and behind the biological sample holder to characterise the parameters of the mechanical stimulus, and different neuronal cell cultures to investigate the effects of overpressure in accordance to TBI studies. They observed delayed cell death in hyppocampal slices subjected to peak incident pressures in the order of 500 kPa and with a positive duration of approximately 1 ms, compared to sham samples, but they didn't see changes in number of dead cells in bEnd.3 cell cultures exposed to similar overpressures compared to sham samples [60]. These results suggest that cellular injury depends not only on the mechanical parameters of the pressure stimulus but also on the type of cell and sample configuration used in the overpressure experiments.

In the study presented in this chapter a setup similar to the one developed by Arun et al. [59] has been used to subject MSCs to shock tube-generated overpressures. The research focused on the characterisation of the pressure profile developed within the tissue culture plate, as well as the comparison of different sealing membranes for the *in vitro* system. The peak pressure, average pressure plateau, positive phase duration and impulse for experiments performed with non permable or gas permeable sealing membranes were calculaated from pressure profiles measured within the tissue culture plate filled with water following the rupture of Mylar diaphragms of different thicknesses. All these parameters could be important in determinig a relation between the mechanical stimulus and changes in biological functions induced in cell monolayers. Preliminary experiments were performed to study the effects of shock tube-generated overpressure on the viability and differentiation potential of MSCs monolayers. It was observed that depending on the plate orientation with respect to the open end of the shock tube, cell metabolic activity was affected 3 hours after the overpressure experiments, with samples facing the shock tube with the bottom of the plate (back configuration) associated with lower level of cell respiration post shock. However, cell viability was restored after 24 hours and no changes in cell metaboic activity were observed up to 48 hours in samples subjected to overpressures of 131.50 $\pm$ 8.34 kPa and duration of approximately 10 ms. A single experiment in which the osteogenic differentiation potential of MSCs following overpressure

was examined, showed elevated levels of ALP in samples subjected to the shock stimulus and the cultured in control medium compared to sham samples. This result suggests that the mechanical stimulus could potentially affect the ability of MSCs to initiate the differentiation process. Previous studies reported the influence of cyclic stretch, cyclic pressure, and laminar shear stress on the differentiation of MSCs towards smooth muscle cells and endotelial cells [115], as well as the upregulation of MSCs osteogenesis under cyclic tension [120]. Although many more experiments are necessary to understand the relation between the pressure stimulus and changes in biological functions in cells, this research has provided a solid platform to study primary blast-induced biological effects on MSCs and the preliminary results reinforce the hypothesis that MSCs could be involved in blast induced Heterotopic Ossification.

Chapter 6

Mechanical compression of porcine skin

6.1 Introduction

To develop biofidelic models of blast injuries it is necessary to define the mechanical properties and structural changes of wounded tissues at high-strain rates. In order to maintain a strong synergism with the research being undertaken within CBIS, skin tissue was chosen to be studied, because it is associated with trauma to the extremities. Several studies have been conducted to determine the mechanical properties of skin under physiological conditions, however there have been limited studies addressing the mechanical properties in compression, of skin tissue excised from different anatomical locations, at high loading rates. Moreover, recovery of the tissue specimens post compression for morphological analysis has not been a common practice in biomechanical tests. In this chapter a summary of the the mechanical properties of skin and the results from compressive experiments performed at different strain rates and on two different skin samples will be presented. Moreover, preliminary histological studies on the recovered samples will be discussed.

6.1.1 Anatomy and functions of the skin

The skin is the heaviest organ of the human body representing in average 15% of the human weight. This organ has several important roles among which providing the body with a protective barrier against external threats such as harmful microorganisms and chemicals as well as sun ultraviolet rays. It also plays an important role in the body thermoregulation, excretion of waste products and sensorial functions. Moreover, it prevents internal tissues from exposure to traumatic injuries. Skin consists of three layers, as shown in Fig. 6.1: epidermis, dermis and hypodermis. The epidermis is the thin outer layer of the skin with thickness varying from 0.06 to 1.0 mm throughout the body [121]. It comprises several sublayers, each with their own distinct role. The stratum germinativum, the inner layer, is mainly composed of basal keratinocytes and melanocytes, which respectively provide strength and toughness and give the skin its brown pigmentation. In this layer cells continuously divide and once new cells are formed they migrate upwards towards the stratum corneum. During their journey to the outer layer keratinocytes die and are filled with keratin, a tough, fibrous protein. The stratum corneum is mainly composed of dead, keratinized cells which are constantly shed and replaced by new ones. The dermis is the thick, 1 to 4 mm [121], inner supportive layer of the skin constituted by two sublayers: the papillary layer, the upper level, which is made of closely interwoven thin fibres in which lyes an extensive network of blood vessels and the reticular layer, the lower level, which is made of thick, loosen and randomly oriented collagen fibres and which contains different type of sensory receptors, hair follicles and glands. In the papillary layer type III collagen fibrils of 20-40 nm in diameter are arranged in large fibres with diameters varying from 0.3 to 3 μm. The reticular layer is mostly composed of type I collagen fibrils of 60-100 nm in diameter which are bundled in fibres of 10-40 μm in diameter [122]. In addition to collagen, elastic tissue is found in the dermis with elastin fibres of different diameters and lengths forming a three dimensional network which extends from the papillary to the reticular layer [122]. Collagen and elastin are both produced by fibroblasts, a group of cells that are scattered throughout the dermis and their networks are embedded in an amorphous gel-like substance, called the ground substance, which comprises pro-

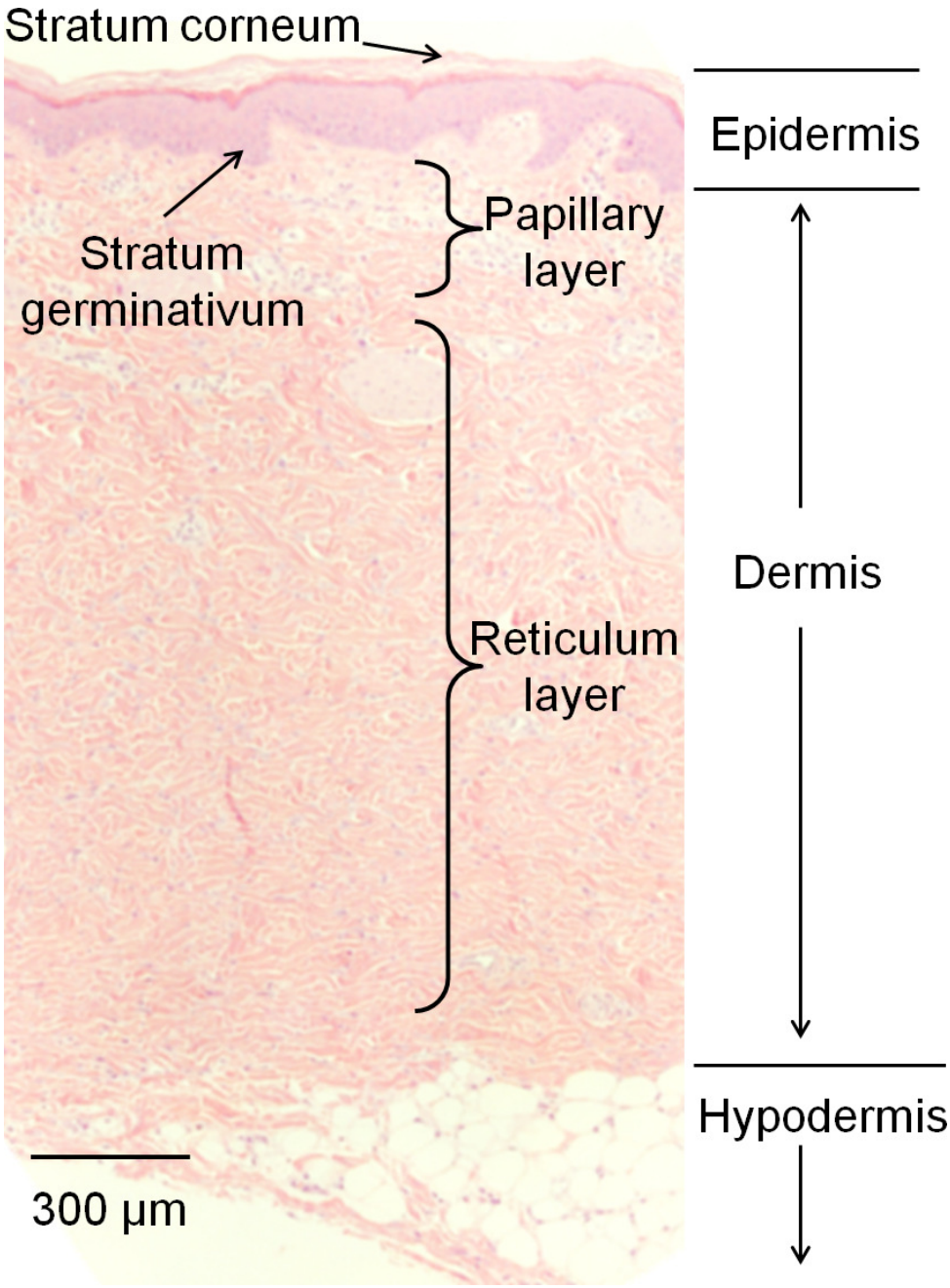

Figure 6.1: **Cross-section of the different skin layers** Histological image of porcine skin cut throughout the tissue thickness. Epidermal, dermal and hypodermal layers are identified, as well as some of the major sublayers.

teoglycans, glycosaminoglycans and glycoproteins [123]. The ground substance acts as a lubricant during movement of the collagen fibres and contributes to direct collagen fibre formation [123]. Finally, the hypodermis, also known as the subcutaneous layer, is the most inner layer of the skin and is composed of fat and collagen cells.

6.1.2 Mechanical properties of the skin

The mechanical properties of skin have been studied both *in vivo* and *in vitro*. *In vivo* experiments comprise tension [124, 125], suction [126, 127], torsion [128] and indentation methods [129,130]. For *in vivo* experiments the mechanical properties of skin are thought to be mostly related to the response of the dermis to the applied external forces, and limited values of stress and strain can be explored. *In vitro* experiments, uniaxial tensile [122,131–134] or compressive tests [65,135], allow samples to be tested up to failure in various environmental conditions and the different skin layers can be tested individually. However, long term functional information cannot be obtained from *in vitro* tests. A very important aspect of *in vitro* studies is the tissue preservation method. Different studies have been conducted to investigate the tissue preservation methods on the mechanical properties of the tissue. Ralis demonstrated that freezing quadriceps femoris and calcaneal tendons caused flexion deformity, while after thawing samples were characterised by greater deformability in all joints of the specimen [136]. Moreover Zhang *et al.*, demonstrated significant differences in brain samples tested in uniaxial compression at at high strain when stored at 4 °C or 37°C for up to 4 hours post mortem [137]. Generally, it is accepted that excised tissues should be tested within 4-5 hours post mortem and that good levels of humidity and fluids should be maintained during preservation and testing, but no definitive guidelines have been drawn on the tissue preservation method. Due to the poor availability of fresh human tissue, *in vitro* mechanical tests are generally performed on animal samples. In the case of skin, pig has been found to be the best human simulant, both in terms of morphology and mechanical properties [133].

Several factors have been found to affect the mechanical properties of skin among which the location from where samples were excised [138], sample orientation [138], age, temper-

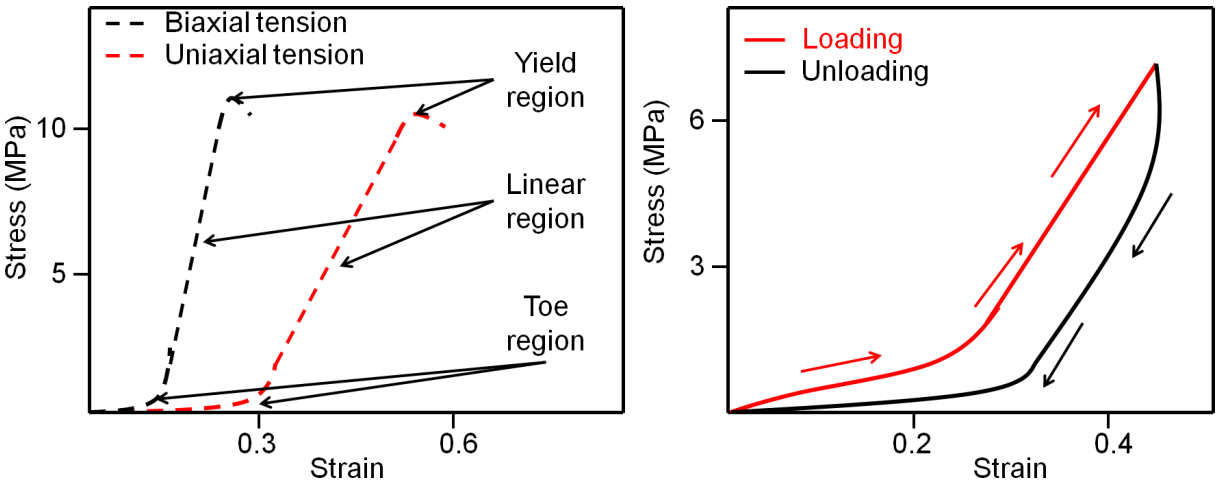

Figure 6.2: **Generalised stress-strain curves for skin** Left, schematic of uniaxial and biaxial tensile stress strain curve for excised skin. Right, idealised loading and unloading response of skin in uniaxial tension experiments

ature [134,139] and strain rate [65,133]. Pioneering studies by Langer showed that skin is anisotropic and in a state of biaxial passive pretension: lines of maximum tension could be determined from cadavers by puncturing circular holes at short distances from each other into the skin and measuring the longer axes of the resultant ellipsoidal holes [140]. This preexisting tension is due to the intricate networks of collagen and elastin fibres in the dermis. These two components are indeed responsible for the passive mechanical properties of skin. Oxlund *et al.* demonstrated that elastin plays a major role in the mechanical response of skin at low values of stress and strain [131]. Specifically, they conducted *in vitro* uniaxial tension experiments on rat skin samples which were treated or not with an elastase solution to degrade the elastin fibres network. The authors observed that samples treated with the elastase solution showed increased extensibility at low values of stress, while no difference in the maximum yield stress and strain were observed between the two group of samples, proving that elastic fibres are responsible for the load bearing at strains lower than 30% [131], while collagen fibres contributes to the mechanical properties of skin at larger strains. These results are in good agreement with previous studies by Vogel who demonstrated a correlation between the tensile strength and the collagen content in rat skin [141].

6.1.2.1 Stress-strain curve

Generalised uniaxial and biaxial tensile stress strain curves for skin samples are presented in Fig. 6.2. The initial linear portion of the toe region corresponds to the passive mechanical response of the stretched elastin fibres. The collagen network is initially in a wavy configuration and at rest but in the final portion of the toe region collagen fibres start to straighten and align parallel to one another, which corresponds to an increase in stiffness of the material. The linear region exhibits a linear response to increasing strain as collagen fibril stretch and slip within the crosslinked collagen fibres providing resistance to the deformation. Finally, in the yield region, the collagen fibres begin to slide past one another as the intermolecular cross-links fail, corresponding to fibre defibrillation.

6.1.2.2 Viscoelastic behaviour of skin

If skin samples are subjected to load cycles, stretched at a steady rate up to a desired stress then unloaded with the same velocity, hysteresis can be observed, as shown in Fig. 6.2 B. The area between the loading and unloading curves represents the energy lost by the system and can be used as a measure of the tissue viscosity. Moreover, skin undergoes stress-relaxation when subjected to constant strain, while shows creep when subjected to constant stress [142]. The viscous properties of skin are believed to be due to the interaction between collagen fibres and the ground substance. Mins *et al.* performed stress-strain and stress relaxation experiments on connective tissue treated to remove the ground substance [143]. The authors reported a decrease in relaxation in correspondence of treated samples compared to the control, supporting the hypothesis that viscosity is related to the resistance collagen fibres experience while they stretch through the ground substance. Dunn *et al.* and Silver *et al.* characterised the elastic and viscous response of skin performing *in vitro* stress relaxation experiments on excised cadaveric human samples [122, 132]. In these experiments, the elastic and viscous stress strain curves for skin are compared to other connective tissues such as tendons and the authors conclude that the differences in the mechanical responses of these connective tissues are due to differences in the structure and organisation of the collagen fibres.

More recent studies by Zhang *et al.* adopt a surface wave method to determine the viscoelastic material properties of human skin *in vivo* [144]. In their experiments, a small force, generated by a mechanical shaker, is applied to the skin and the resulting surface vibration is measured using a laser vibrometer. The authors measured the shear elasticity and shear viscosity at different sites of the arm and on the palm of the hand and found significant differences in viscoelasticity between the different sites [144]. *In vitro* uniaxial tensile experiments on excised samples demonstrated that other mechanical properties such as ultimate tensile stress, strain energy and elastic modulus were significantly different for samples excised from different region of the back [138]. In their study the authors also demonstrated the strong anisotropy of skin, showing different stress strain curves for sample excised from adjacent locations of the back but with different orientation with respect to Langer's Lines [138].

6.1.2.3 Strain-rate and temperature effects

The mechanical response of skin has been shown to be strain rate dependent both in tension [133] and in compression [65]. In both papers the authors performed uniaxial tests on freshly excised porcine skin at strain rates varying from 0.004 to 4000 s^{-1} using a range of devices, hydraulic or screw driven testing machines and modified SHPB systems. The authors found that increasing the strain rate the tissue stiffness increased, and Lim *et al.* also reported clear distinction in the mechanical response of skin excised in two orthogonal directions, with the samples parallel to the spine stiffer but less strain rate sensitive than the sample excised in the perpendicular direction [133]. High strain rate experiments were also performed by Saraf et al, who used a modified SHPB systems to measure the dynamic bulk response of soft human tissues [64]. In these experiments, cylindrical tissue specimens were confined between the Hopkinson bars by a jacket. Experiments were performed varying the impact velocities, each of which allowed to determine values of the volumetric strain and the correspondent maximum stress sustained by the samples. A linear fit of the volumetric and stress data was employed by the authors to determine the bulk modulus of stomach, liver, heart and lung [145]. Finally, Xu *et al.* and Zhou *et al.*

studied the mechanical properties of skin at various temperature [134, 139]. They showed that increasing the temperature the stress necessary to reach a desired strain value is lower, compared to samples tested in physiological conditions (37 °C). They suggest two possible mechanism for this behavior: the loss in strength due to denaturation of collagen fibres and the change in viscoelastic properties due to the change in water content [134].

6.1.3 Biomechanical modeling of the skin

Several constitutive models have been used to describe the mechanical behaviour of soft biological tissues. Skin has been described using linear elastic, hyperelastic and viscoelastic models. The linear elastic model is the simplest constitutive model which assume a linear relation between stress and strain. In the case of an anisotropic material the relation between stress and strain is described in a matrix form as $[\sigma] = [C][\varepsilon]$ where $[\sigma]$ is the stress matrix, [C] is the elastic stiffness matrix and $[\varepsilon]$ is the strain matrix. For an anisotropic material the elastic stiffness matrix contains 21 material constants, which are reduced to 12 if the material is assumed to be orthotropic while a two parameter (Young's modulus and Poisson's ratio) relation is valid if the material is considered isotropic. In the case of skin the isotropic assumption has been largely adopted [122, 126, 129, 130] and the linear model has been generally used for low values of strain to fit the stress strain data obtained from uniaxial experiments and to determine the Young's modulus. Silver *et al.* used a bilinear approximation to describe the stress strain response of human skin in *in vitro* uniaxial tension and reported values of Young's modulus of 0.1 MPa and 18.8 MPa respectively for the initial linear portion of the stress strain curve (toe region) and for the high strain region (linear region) [122]. Delalleau *et al.* calculated the elastic constant and the Poisson's ratio from data obtained from *in vivo* indentation experiments on human skin to be respectively 5.67 kPa and 0.48 [129]. Diridollou *et al.* reported values of Young's modulus of 129 ± 88 kPa for *in vivo* suction tests on human skin. In a recent study Pailler-Mattei *et al.* [130], propose a two layers model in which each skin layer is represented by a spring characterised by a specific stiffness. The experimental data obtained from indentation tests are used by the authors to determine the elastic

constants of the dermis and the hypodermis layers which are reported to be respectively 35 kPa and 2 kPa. These results highlight the large variability in the values of Young's modulus calculated with different experimental methods and different samples. Moreover, the stress strain relationship for uniaxial tensile and compressive *in vitro* experiments has shown strong non-linearity. Hence a more complex constitutive model was necessary to describe the behavior of skin.

6.1.3.1 Hyperelastic models of the skin

Several hyperelastic models have been used to represent the mechanical behaviour of skin both *in vitro* uniaxial tension and compression as well as *in vivo* experiments. The most widely used is the Ogden model [65, 125, 133, 134, 139]. In this model a strain energy function is used to describe the work done per unit volume to deform a material from a stress free reference state to a loaded state. The Ogden's strain energy potential is defined as:

$$W(\lambda_1, \lambda_2, \lambda_3) = \sum_{i=1}^{N} \frac{2\mu_i}{\alpha_i}(\bar{\lambda}_1^{\alpha_i} + \bar{\lambda}_2^{\alpha_i} + \bar{\lambda}_3^{\alpha_i} - 3) + \sum_{i=1}^{N} \frac{1}{D_i}(J-1)^{2i} \tag{6.1}$$

where $\bar{\lambda}_k$ (k =1, 2, 3) are the principal deviatoric stretches, with $\bar{\lambda}_k = \mathrm{J}^{-\frac{1}{3}}\lambda_k$, J = $\lambda_1\lambda_2\lambda_3$ is the volumetric ratio, λ_k (k =1, 2, 3) are the principal stretches, μ_i are the shear parameters, α_i are the exponential parameters and D_i are the bulk parameters. For an incompressible material the principal stretches satisfy the constrain $\lambda_1\lambda_2\lambda_3 = 1$ [146], hence the second sum in equation 6.1 is 0. The principal stresses σ_k (k =1, 2, 3) are related to the principal stretches through W in the form:

$$\sigma_k = \lambda_k \frac{\partial W}{\partial \lambda_k} - p \tag{6.2}$$

where p is a hydrostatic pressure. In a uniaxial compression test with the loading direction along the x_1 axis and no other external forces the specimen is in a plane stress condition and $\sigma_2 = \sigma_3 = 0$. Moreover, the incompressibility constraint imposes that $\lambda_2 = \lambda_3 = \lambda^{-1/2}$ hence the stress in the direction of loading can be expressed as a function of the stretch

by the equation

$$\sigma = \sum_{i=1}^{N} \frac{2\mu_i}{\alpha_i}(\lambda^{\alpha_i - 1} - \lambda^{-1/2\alpha_i - 1}) \tag{6.3}$$

where μ and α respectively represents the physical parameters for shear modulus and strain hardening exponent. In the several studies conducted on skin, it was reported that one term, hence N = 1, in equation 6.3 was sufficient to obtain a good fit to the experimental data. In table 6.1 the values of μ and α reported in literature for tensile and compression experiments at different strain rates and with various sample orientations are reported. Shergold *et al.* [65] and Lim *et al.* [133] report constant values for the strain

Author	**Exp. type**	**Tissue origin**	**Orientation**	**Strain rate**	**Temperature**	μ N mm^{-2}	α
Shergold	Compression	-	-	0.004	RT	0.4	12
Shergold	Compression	-	-	0.4	RT	1.2	12
Shergold	Compression	-	-	40	RT	2.2	12
Shergold	Compression	-	-	4000	RT	7.5	12
Lim	Tension	abdomen	// spine	0.005	RT	10	11
Lim	Tension	abdomen	// spine	0.5	RT	20	11
Lim	Tension	abdomen	// spine	1700	RT	180	11
Lim	Tension	abdomen	// spine	2500	RT	230	11
Lim	Tension	abdomen	// spine	3500	RT	300	11
Lim	Tension	abdomen	$\perp$ spine	0.005	RT	3	7
Lim	Tension	abdomen	$\perp$ spine	0.5	RT	8	7
Lim	Tension	abdomen	$\perp$ spine	1700	RT	40	7
Lim	Tension	abdomen	$\perp$ spine	2500	RT	200	7
Lim	Tension	abdomen	$\perp$ spine	3500	RT	370	7
Zhou	Tension	belly	-	0.25%	45 °C	0.0002	10.464
Zhou	Tension	belly	-	0.5%	45 °C	0.00028	10.189
Zhou	Tension	belly	-	1%	45 °C	0.00093	8.907
Zhou	Tension	belly	-	2.5%	45 °C	0.00227	7.796
Zhou	Tension	belly	-	5%	45 °C	0.00313	7.772
Zhou	Tension	belly	-	10%	45 °C	0.00136	9.156
Zhou	Tension	belly	-	1%	10 °C	0.003759	8.982
Zhou	Tension	belly	-	1%	15 °C	0.003909	8.582
Zhou	Tension	belly	-	1%	45 °C	0.000934	8.907
Zhou	Tension	belly	-	1%	50 °C	0.001169	8.504
Zhou	Tension	belly	-	1%	60 °C	0.000368	9.677

Table 6.1: Ogden parameters reported in literature for tension and compression experiments performed with fresh pig skin excised from different areas, at different strain rates and temperatures

hardening exponent α and values of the shear stress μ that increase in correspondence of increasing strain rate. Moreover, the two studies show values of α in the same order of magnitude, while there is a difference of one order of magnitude in the values of μ. In contrast, Zhou *et al.* [134] report values of α and μ very different from the other authors

and also their results don't reveal any trend between the estimated parameters and the experimental variables (strain rate and temperature). These differences could have arisen from differences in sample preparation, sample testing or minimisation algorithms used to determine the Ogden's parameters.

Other hyperelastic models used to fit *in vitro* compression or tension experiments on skin samples are the Mooney-Rivlin [65], the Fung [138] and the Gent [138] models. For completeness the stress-stretch relations as represented by these models for uniaxial experiments are reported here:

$$\sigma^M = 2(\lambda - \frac{1}{\lambda^2})(C_1 + \frac{C_2}{\lambda}) \tag{6.4}$$

$$\sigma^F = \mu \exp^{b(\lambda^2 + \frac{2}{\lambda} - 3)}(\lambda - \frac{1}{\lambda^2}) \tag{6.5}$$

$$\sigma^G = \frac{\mu J_m}{J_m - \lambda^2 - 2/\lambda}(\lambda - \frac{1}{\lambda^2}) \tag{6.6}$$

where C_1 and C_2 are material constants, μ is the initial shear modulus, b is a parameter associated with strain stiffening and J_m is a parameter associated with limited chain extensibility, all of which must be determined experimentally.

6.1.3.2 Visco-elastic models of the skin

In order to capture the time-dependent behaviour of skin in creep and stress relaxation experiments several viscoelastic models have been employed to characterise the mechanical properties of such tissue. The simplest viscoelastic models used to describe biological tissues are the Maxwell, Voigt and Standard Linear Solid (SLS) models [147]. They all employ Hookean spring and Newtonian dashpot elements in parallel or in series as shown in Fig. 6.3, which represent respectively the elastic and the viscous components. In a Maxwell model, each element is subjected to the same stress, while the total strain is the sum of the strain in each element. On the contrary, in the Voigt model each element experience the same strain and the total stress is the sum of the stresses of each element. The SLS model is a combination of the other two models. From these considerations the

equations that describe the stress strain relation for each model can be obtained:

$$k\dot{\varepsilon} = \dot{\sigma} + \frac{k}{\eta}\sigma \tag{6.7}$$

$$\sigma = k\varepsilon + \eta\dot{\varepsilon} \tag{6.8}$$

$$\dot{\sigma} + \frac{k_1}{\eta}\sigma = (k_1 + k_2)\dot{\varepsilon} + \frac{k_1 k_2}{\eta}\varepsilon \tag{6.9}$$

where the constants k and η are respectively the material elastic constant and the damping coefficient. Several variation and combinations of these simple viscoelastic models have been used to describe the mechanical response of skin in *in vitro* and *in vivo* experiments. Jamison *et al.* [148] performed creep relaxation and tensile experiments on guinea pig skin samples. They adopted a three elements viscous model composed by a Voigt model in series with a damping element and they report values of the elastic and damping constants for different types and orientation of the skin tissue samples. In a more recent study Khatyr *et al.* [149] propose a more complex model composed of three main parts: an elastic part in series with a simple Voigt part followed by a series of five Voigt parts in series which represent respectively the tissue elastic part, the short term viscous part and a spectrum which the authors claim comes into play for long term effects. They obtain the elastic and damping constants for different testing orientations for *in vivo* experiments performed on human skin. Moreover, they propose a methodology to obtain the material properties for a viscoelastic ortothropic model of skin from the results obtained from the viscoelastic modeling of uniaxial tests performed with different orientations [149]. For the ortothropic model, they report values of elastic moduli $E_1 = 657$ kPa and E_2=130 kPa and shear modulus G_{12} =132 kPa and they conclude that the ortothropic model enables the simulation of skin anisotropy in 80% of the patients [149]. Holt *et al.* [150] characterised the mechanical behavior of human skin under low-magnitude shear loads and used a modified Voigt viscoelastic model to determine the values of the elastic and viscous moduli from creep shear experiments on skin and dermis biopsy specimens. The authors report narrow values of these two parameters for a large range of loading frequecies. Moreover they observe strain hardening in experiments performed with whole skin specimen and

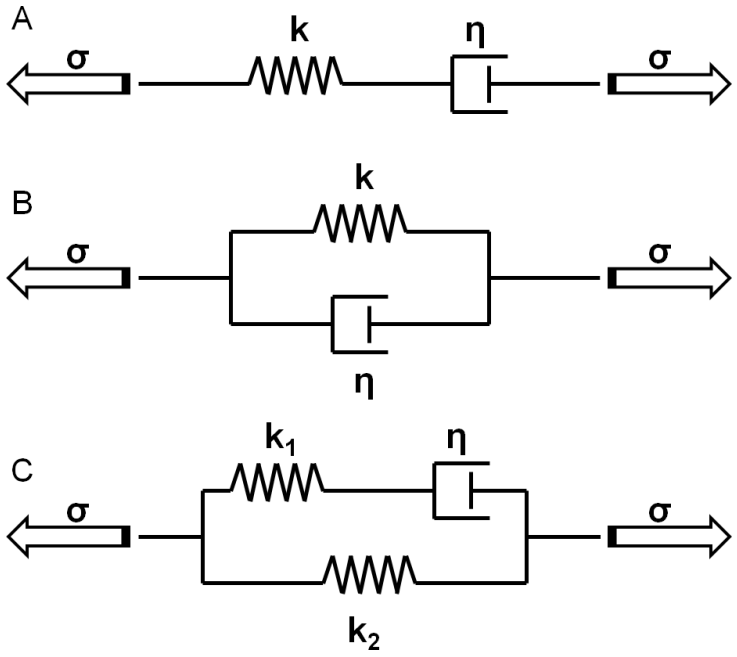

Figure 6.3: **Basic viscoelastic models** Schematic of (A) Maxwell, (B) Voigt and (C) Standard Linear Solid viscoelastic models

stress softening in the dermis-only spcimens. From this, they conclude that the epidermis is responsible for the rigid elastic behavior of the skin, while the dermis provides the viscous response [150].

6.2 Materials & methods

6.2.1 Skin sample preparation

Skin samples were obtained from the rump and the thigh of a weaned pig (6-8 weeks old), sourced from a Specific Pathogen Free (SPF) closed herd serologically negative against influenza virus. The pig was sacrificed by intravenous administration of sodium pentobarbitone (0.8 mg/kg i.v. to effect) by a collaborator in the Department of Veterinary Medicine, Cambridge Veterinary School, University of Cambridge. Hair were removed with a razor blade and rectangular sheets of tissue were harvested from each anatomical area of interest as shown in the schematic in Fig. 6.4. Eight needles were used to keep the tissue stretched on a plastic board while the adipose layer was gently removed from it with a scalpel, paying attention not to damage the dermis layer. Cylindrical specimens

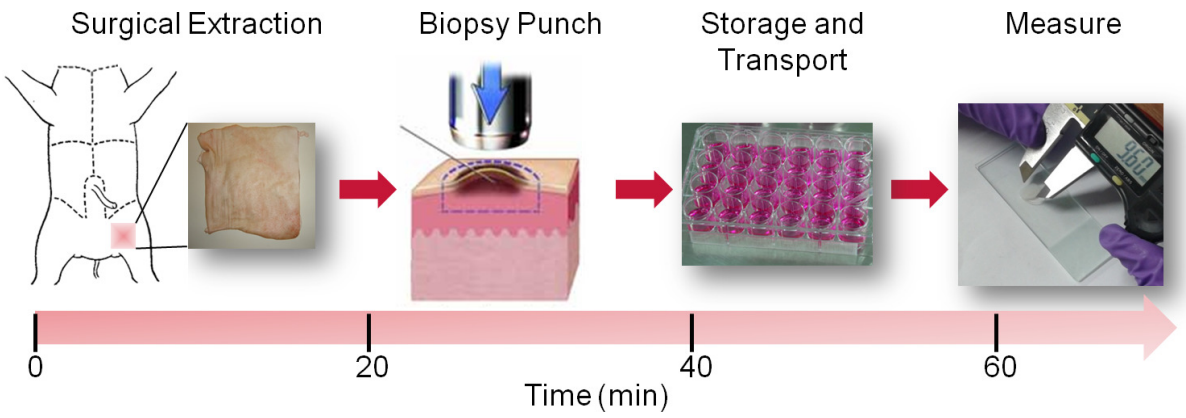

Figure 6.4: **Skin samples preparation** Schematic representing the different steps of the sample preparation as a function of time since the animal was sacrificed.

were obtained using biopsy punches of different diameters (8 mm and 12.7 mm). The specimens were either stored in phosphate buffered saline solution (PBS) at 4 °C until mechanical tests were performed (fresh specimens) or fixed in a 4% formaldehyde in PBS solution for long term preservation (fixed specimens). Fresh specimens were tested within 5 hours from the tissue harvest to prevent rigor mortis. Fixed specimen were rinsed in PBS to eliminate any residual of formaldehyde before they were mechanically tested. Moreover, prior to each mechanical test, samples were gently tapped with a tissue paper to remove excess liquid and then positioned between two microscope slides to measure their thickness and diameter with a calliper.

6.2.2 Compression experiments

Skin tissue was mechanically tested in compression in two different configurations: confined compression and unconfined compression. Confined compression experiments were performed with tissue specimens of the same diameter of the SHPB bars. The SHPB system was equipped with 500 mm long and 12.7 mm in diameter magnesium AZM bars in order to reduce the mechanical impedance mismatch between the bars and the skin samples thereby maximising signal transmission. Two Kulite type AFP-500-90 gauges were coaxially located halfway along the bar length and diametrically opposite to remove effects of flexural bar vibration. The samples were positioned between the input and the output bars and a polycarbonate tube was slided along the bars to completely confine

the specimen. The bars were then gently squeezed in order to ensure contact between the tissue, the bars and the confinement jacket. Experiments were performed with striker bar impact velocities varying from 4.4 ± 0.1 ms^{-1} to 7.3 ± 0.1 ms^{-1}.

In unconfined compression experiments each tissue sample was compressed between two smooth metallic rods or plates and was free to expand radially. Low and medium strain rate experiments (0.001 s^{-1} and 1.0 s^{-1}) were performed with an Instron 5566 machine, see Fig. 3.13 for schematic, which is an electromechanical load frame used to compress material samples at known force and deformation rate. High strain rate experiments (6000 - 9000 s^{-1}) were performed with the SHPB system equipped as for confined experiments. In these experiments the sample weight was also measured before and after compression to verify sample volume conservation and samples were recovered and kept at room temperature in a 4% formaldehyde in PBS solution after compression for subsequent histological analysis. During the SHPB compression experiments the bar strain was recorded with a Tektronics TDS540 8-bit digital oscilloscope with acquisition rate of 10 MHz. During the quasi static compression experiments the load and the extenstion measured by the load cell of the Instron machine were recorded with acquisition rate of 100 Hz.

In order to minimise the level of friction during each compression experiment, a thin layer of lubricant (Vaseline, Johnson & Johnson) was applied to the ends of the Hopkinson bars or to the Instron plates with a cotton bud.

6.2.3 Data analysis

Confined compression experiments were analysed with the SHPB data analysis routine developed in Matlab, previously described in Chapter 3. Briefly, the sample and bar parameters were inserted for each individual experiment, the file containing the gauges traces was loaded in the application and the start point of the incident wave was selected with the provided cursor. Wave dispersion correction was included in the analysis to ensure good waves alignment. “Confined Test” was chosen from the pop up menu in the “Results” panel to calculate the stress strain history and the results were saved in a .xls file. In addition to the stress history, the maximum stress developed in the chamber and

the correspondent volumetric strain were calculated for each specimen according to Saraf *et al.* [64].

Unconfined compression experiments performed with the SHPB system were analysed using the application developed in Matlab as previously described. Experiments performed with the Instron machine were manually analysed. The load was used to calculate the instantaneous true and engineering stress defined respectively as

$$\sigma_{ENG}(t) = \frac{F(t)}{A_0} \tag{6.10}$$

$$\sigma_{TRUE}(t) = \frac{F(t)}{A_s(t)} \tag{6.11}$$

where F(t) is the load measured by the Instron machine, A_0 is the initial sample's surface area and $A_s(t)$ is the instantaneous sample's surface area calculated assuming sample volume conservation.

6.2.4 Histology

Tissue samples after compression were kindly processed by the technicians of the Department of Veterinary Medicine, Cambridge Veterinary School, University of Cambridge. Briefly, samples were sectioned in two along the main cylinder axis to allow visualisation along the straining direction. Samples were dehydrated through a series of graded ethanol baths to displace the water and then infiltrated with paraffin wax. The infiltrated tissues were then embedded into wax blocks and sectioned in 5 μ thick slices using a microtome. These thin slices were floated on the surface of the 37 °C water bath and then transferred onto the surface of clean glass slides. The slides with paraffin sections were placed on the warming block in a 65 °C oven for 15 minutes to bond the tissue to the glass and stored overnight at room temperature for subsequent staining. Two different stains were adopted to study the morphology of unconfined compressed samples: Haematoxylin and Eosin and Masson's trichrome stains. The first one is a widely used stain in histology and uses two dyes to differentially colour various components. Specifically, haematoxylin, in combination with a mordant, reacts with negatively charged, basophilic components

in the tissue, such as nucleic acids in the cell nucleus, which result in a blue stain. On the other hand, eosin reacts with positively charged, acidophilic cell components, such as proteins in the cytoplasm and produces a variety of red and pink shades as a result.
Masson's trichrome is a three-colour staining protocol usually used to differentiate between collagen and smooth muscle in tumors, or to measure changes in amount of collagen present in connective tissues. The staining principle of trichrome stains is based on the size and affinity of the different dyes: the smallest dye molecule will stain the less porous tissues, but whenever a dye of large molecular size is able to penetrate, it will compete to stain the already stained tissue on the basis of it's affinity to the tissue. In the case of the Masson's trichrome stain, first a Weigert's hematoxylin solution, with a dye of small molecular weight, is used to stain the cellular nuclei black. Then, a plasma stain solution, with dye of intermediate molecular weight, is used to stain red/orange the entire tissue. Then a polyacid, which has a large molecular weight, is applied to differentially remove the plasma stain from specific tissues such as collagen, which are then stained with a light green or aniline blue solution.

6.2.5 Constitutive skin tissue modeling

Experimentally obtained stress-strain curves for porcine skin samples harvested from the rump and the thigh and subjected to uniaxial compression at different strain rates were fitted with different two parameters hyperelastic constitutive models. Strain values were converted for each specimen into stretch values using the simple relation $\lambda(t) = 1 - \varepsilon(t)$. Stress data were smoothed with a moving average filter, with the filter span set at 20. A Curve Fitting Tool available in MATLAB was used to calculate the best fitting values of the two parameters for the one term Ogden model, the Fung model and the Gent model. The Trust-Region algorithm was chosen to determine the best fit values of the parameters, because it allowed to define the lower and upper constrains on the parameters values, set respectively at 0 and ∞. The goodness of the fit was evaluated with respect to the root mean square error and the R-square values.

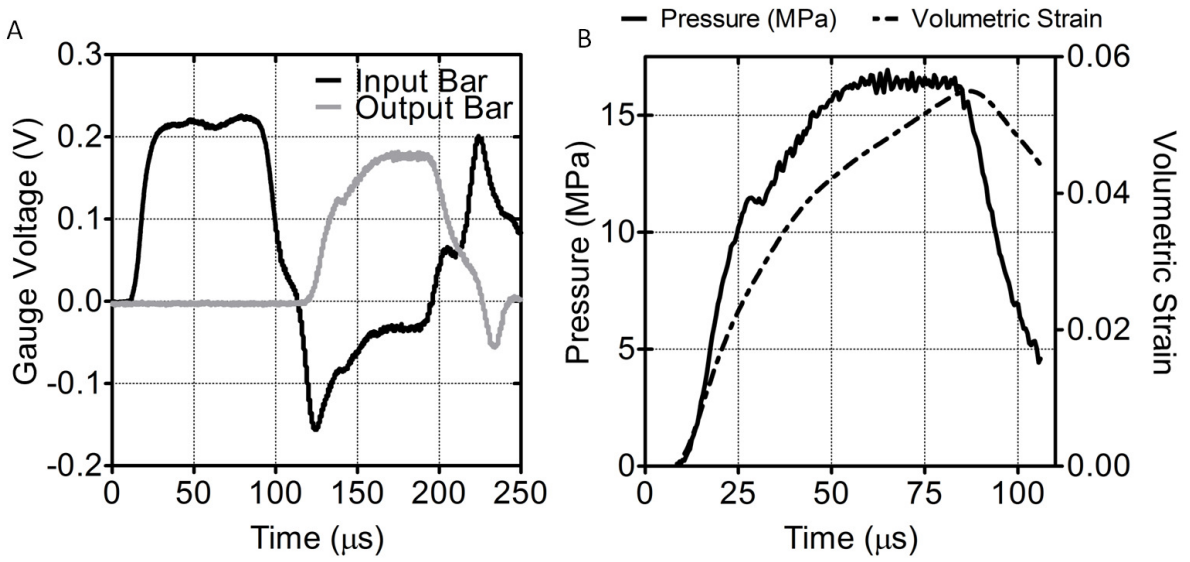

Figure 6.5: **Skin response under confined compression** A, Typical SHPB input and output bar traces for confined compression experiments on skin samples. B, Pressure and volumetric strain of a skin sample under confined compression with strain rate of 3500 s^{-1}

6.3 Results

6.3.1 Confined compression

Fresh and fixed skin specimens excised from the posterior legs of two pigs and cut into cylinders of 12.7 mm in diameter and thickness varying from 1.5 to 1.9 mm were tested in confined compression using the Cavendish Laboratory SHPB apparatus. The applied strain rate ranged between 1500 and 3500 s^{-1}, while the duration of the compressive pulse was approximately 90 μs. The typical input and output bar strain gauges signals for a compressive test on skin are presented in Fig. 6.5 A. These raw data show that a constant stress state is reached during compression as indicated by the plateau of the output signal after the initial rise, hence suggesting that an hydrostatic pressure state was achieved. However, as shown in Fig. 6.5 B, the volumetric strain doesn't reach a steady value until close to the end of the compressive pulse, suggesting that damage to the tissue might have occurred, or that complete confinement was reached only after an initial simple compression. This might be due to inaccuracy in sample preparation, specifically due to the loss in pretension of the skin specimens after the cylindrical samples

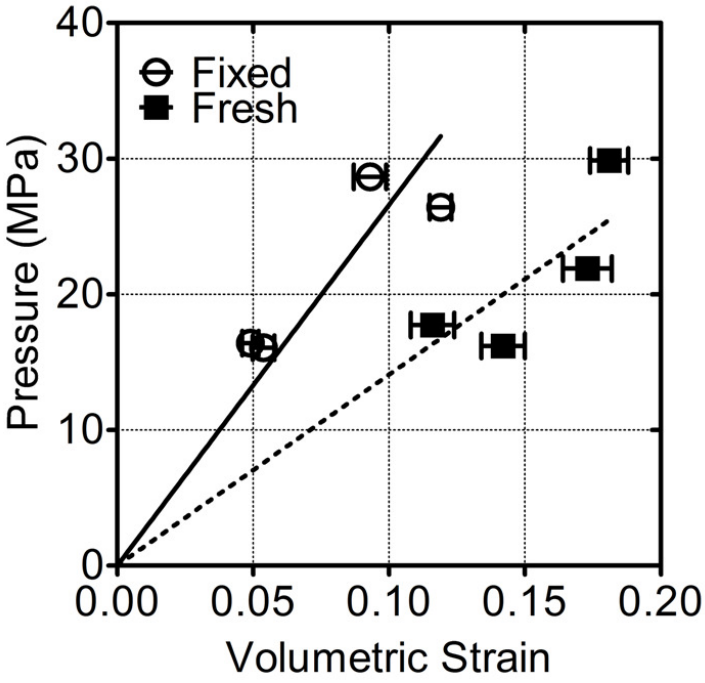

Figure 6.6: **Results from dynamic confined compression of skin's experiments** Pressure vs volumetric strain for dynamic confined compression of fresh and fixed porcine skin samples. Data represent the average of two experiments (E=2) each performed to N=3. The error bars represent the standard error.

were cut from the main tissue sheet, causing a small change in size. Hence, in order to generate a pressure-volumetric strain curve for the tissue, the average value of stress was measured in the plateau region, and the volumetric strain was measure from the data points correspondent in time to the stress plateau. This resulted in large errors on the volumetric strain, as shown in Fig. 6.6, where the pressure and volumetric strain value for each independent test are presented. Only a small number of data points are presented here, due to the limited number of samples available and also to the fact that only tests in which a steady stress state was achieved were used to determine the bulk modulus of the tissue. Due to these limitations, the dynamic bulk modulus of the tissue in the two different conditions was determined using a simple linear approximation, as suggested by Saraf *et al.* [64]. In this approximation the values of dynamic bulk modulus for fixed and fresh porcine skin were respectively 0.26 ± 0.03 GPa and 0.14 ± 0.01 GPa, which are in the same order of magnitude of values of bulk modulus measured by Saraf *et al.* for the stomach reported to be 0.48 GPa. It is evident that tissue preservation methods can significantly influence the material properties of the samples. In this case, the process

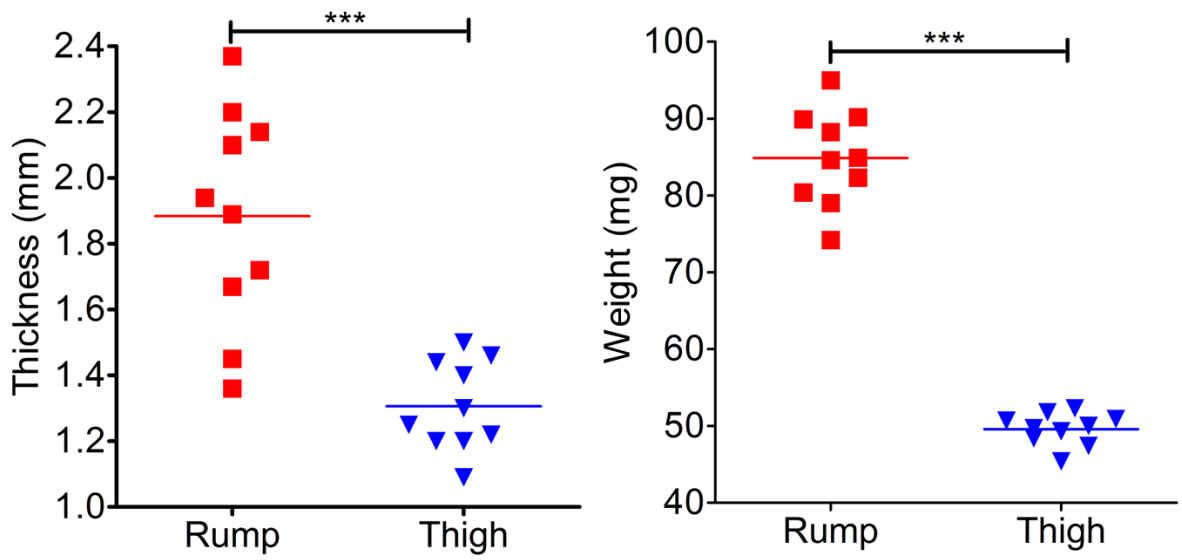

Figure 6.7: **Differences in skin phenotypes as a function of anatomical area** Thickness and weight of porcine skin measured before compression experiments from samples harvested from the rump and the thigh of the posterior limbs of a pig. Data represent the N=10 individual values measured for one experiment (E=1). Average data were analysed with unpaired t test.

of fixation clearly resulted in an increase in stiffness of the tissue. This was due to the covalent cross-linking bonds created between proteins in the tissue in the presence of the fixative agent formalin which provided additional rigidity to the tissue.

6.3.2 Unconfined compression

Fresh skin specimens harvested from the rump and the thigh of a pig were tested in compression at different strain rates. Tissue specimens were cut into cylinders with a 8 mm diameter biopsy punch. The thickness and weight of each sample was measured before each compression test. As shown in Fig. 6.7 specimens from the rump were thicker and as a consequence the weight was also larger, compared to samples collected from the thigh. High strain rates experiments were performed with the Cavendish Laboratory SHPB apparatus with strain rates in the range of 6000-9000 s^{-1}. A typical SHPB output signal for unconfined experiments on skin is presented in Fig. 6.8 A. The output signal, which is related to the stress developed in the sample, shows the typical J form of a biological tissue. As previously discussed in Chapter 3, stress equilibrium must be reached within the specimen in a time significantly lower than the total duration of the experiment.

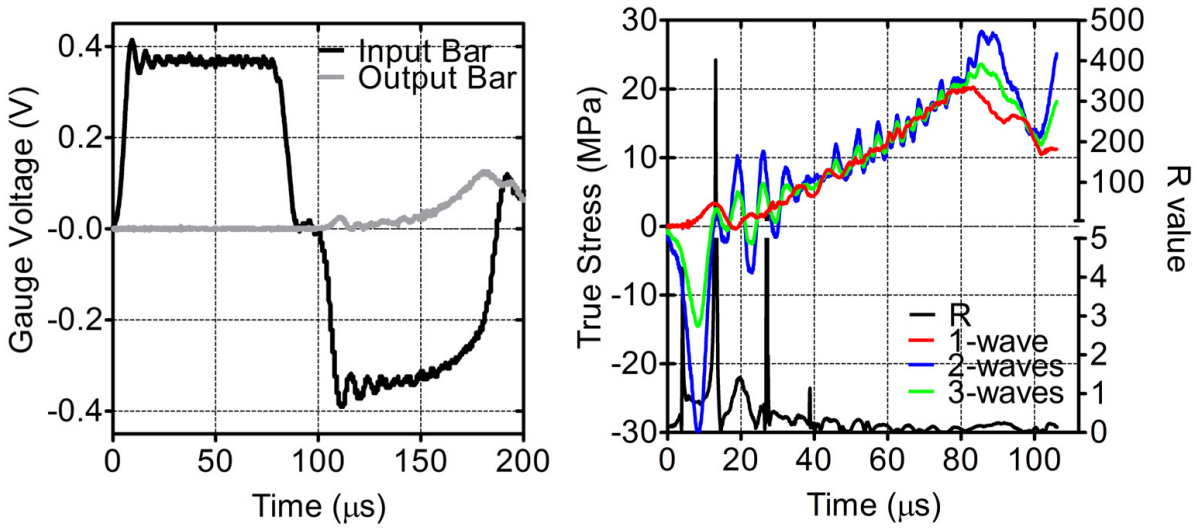

Figure 6.8: **Results from high strain rate uniaxial compression of skin** Left, typical SHPB strain gauges signal for an unconfined uniaxial compression experiment on a skin sample harvested from the rump. Right, analysis of stress equilibrium evaluated comparing the results from 1-, 2- and 3-waves data analysis. The values of the adimensional parameter R as a function of time are also plotted for completeness

In Fig. 6.8 B, a comparison of the 1-,2- and 3-waves analysis as well as the R values for a typical SHPB compression experiment on skin show that stress equilibrium was reached approximately within 25 μs from the origin of the stress pulse. The gauges signals were analysed using the routine developed in Matlab for unconfined specimens as described in Chapter 3. Wave dispersion correction was incorporated into the data analysis. As shown in Fig. 6.9, the incident, reflected and transmitted pulses were cut and time shifted in order to represent the signal at the bars-specimen interface. The wave dispersion correction didn't seem to have a significant effect on the raw data or on the final stress strain curve. The only difference observable between the dispersed and undispersed stress values was the amplitude of the initial oscillation, which seemed to be amplified by the wave dispersion algorithm. This initial pulse is related to the sample radial inertia. Although the sample geometry was chosen to minimise the influence of inertia on the output signals, the contribution of inertia to the measured stress values could be neglected only after the first 20 μs of the experiments.

Medium and low strain rate experiments were performed with an Instron 5566 machine at respectively 60.00 mm/min and 0.06 mm/min which corresponded approximately to

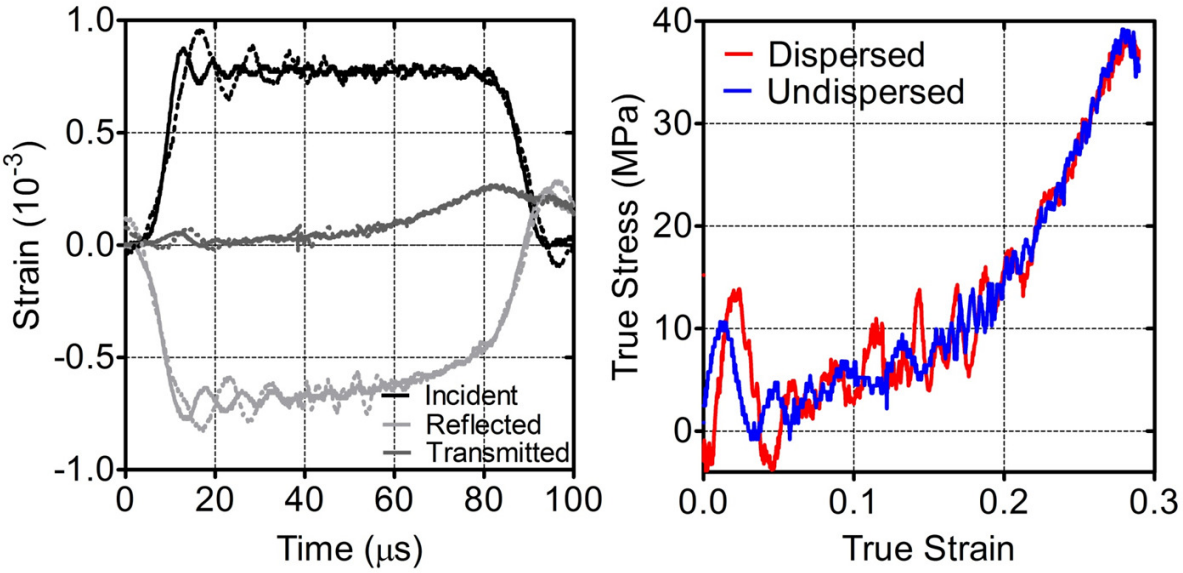

Figure 6.9: **Effects of dispersion correction** Left, the full lines represent the signals measured at the strain gauges while the dotted lines represent the signals dispersed backwards or forwards at the sample-bar interfaces. Right, the effects of the dispersion correction algorithm are evaluated comparing the stress-strain curve calculated for a uniaxially compressed skin sample

strain rates of 1.0 and 0.001 s^{-1}. The load and extension data, as shown in Fig. 6.10, were recorded from the Instron 5566 load cell and converted into engineering stress and strain values. To be able to compare the data acquired at different strain rates, the stress and strain curves for SHPB experiments were also calculated with engineering values, hence with respect to the initial sample dimensions. The results for experiments performed on tissue samples collected from the rump and the thigh regions of the posterior pig legs are shown in the top section of Fig. 6.11 for the different strain rates. The curves show that the stress-strain response of the pig skin is non-linear and with a J-shape, as previously reported in literature [65, 133, 134]. Repeated compressive experiments at the different strain rates showed limited scatter, with the tests at the highest strain rate associated with the larger variability between repeats, possibly due to the difficulty in replicating exactly the same experimental conditions in a high strain rate test. Strain rates effects are clearly observable in the stress-strain response for both groups of samples harvested from different regions. Increasing the strain rate, the stress-strain curves maintain the same J-shape but shift upwards and leftwards, suggesting that skin tissue increases its stiffness at high strain rate. Moreover, two regions can be identified in the stress-strain curves

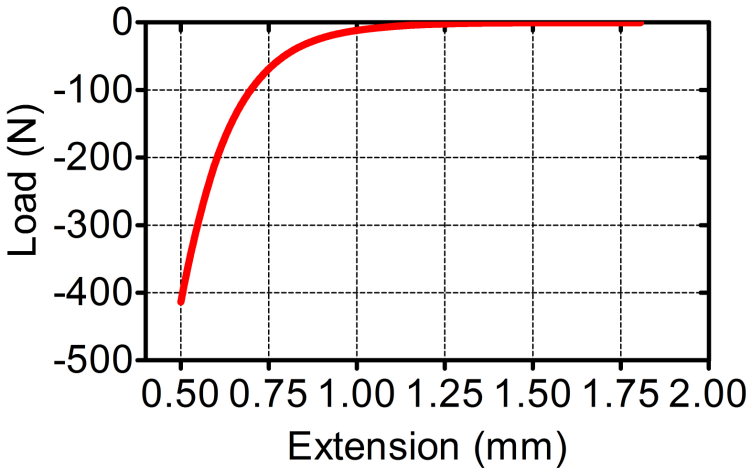

Figure 6.10: **Typical load-extension curve obtained from quasi-static uniaxial compression of skin samples** The values of load and extension were recorded from the Instron 5566 load cell during the compression of a rump skin sample at a speed of 6 mm min^{-1}

of experiments at low and medium strain rates: an initial linear response at low values of strain, which corresponds to the deformation of the elastin fibres in the tissue, and a non-linear response at higher values of strain, which can be related to the movement and deformation of the collagen bundles. The transition between these two regions is shifted leftwards with increasing strain rates, suggesting that both elastin and collagen are strain rate-dependent components. It is not possible to clearly observe the initial linear portion of the curve in the stress strain results at high strain rates because of the influence of inertia on the stress values and also because the specimens are known to be in equilibrium only after the first 20 μs of the compression test. However, a qualitative analysis shows that a transition between the two parts of the curve at high strain rates occurs at values of strain in the range 0.3 - 0.4 for samples harvested from the thigh and 0.2 - 0.3 for samples harvested from the rump. In the lower section of Fig. 6.11, the same results are plotted for each strain rate to compare the stress strain response of the skin samples harvested from different areas. In all three cases, low, medium and high strain rates, the curves for the rump samples are shifted leftwards compared to the thigh samples, suggesting that rump samples are stiffer and with higher strength. Moreover the transition region is shifted to lower values of strain for rump samples, suggesting that the response of collagen

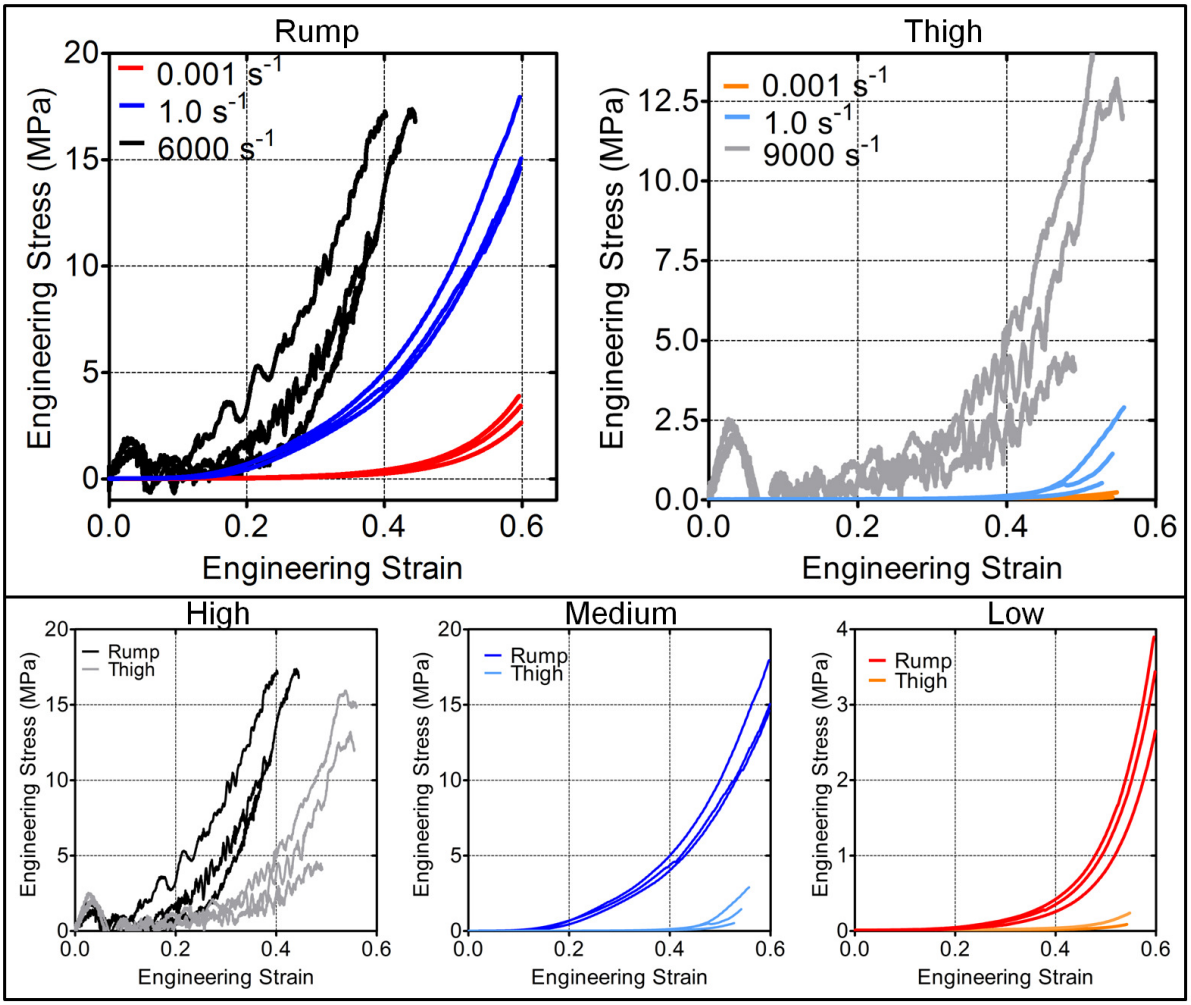

Figure 6.11: **Results from uniaxial compression of rump and thigh skin at different strain rates** Engineering stress-strain curves for skin samples harvested from the rump (top left) and the thigh (top right) of a pig at strain rates of 0.001. 1.0 and 6000/9000 s^{-1}. In the bottom panel the same results are plotted to compare the stress-strain response of skin harvested from rump and skin at each strain rate (High: 6000/9000 s^{-1}, Medium: 1 s^{-1}, Low: 0.001 s^{-1})

fibres in this tissue prevails on the response of the elastin fibres. This observation is in agreement with the geometrical characterisation of the specimens: samples from the rump are significantly thicker than samples from the thigh. Assuming that the thickness of the epidermal layer is the same for the two type of samples, the difference in thickness is associated with a difference in the dermal layer, hence in the content of collagen bundles. This can be evaluated with a histological analysis as discussed in the next section.

6.3.3 Histology

Histological analysis of skin tissues harvested from the rump and the thigh areas of the posterior limb of a pig showed significant morphological differences. As shown in Fig. 6.12 the thickness of the tissue excised from the rump (epidermal and dermal layers) is significantly larger than the thickness of the tissue from the thigh. A quantitative image analysis on three independent specimen for each group, with ten measurement each, showed that the average thickness of samples from the rump and the thigh was respectively 2.54 $\pm$ 0.29 mm and 1.72 $\pm$ 0.38 mm. Moreover, analysis of the same samples at higher magnifications showed that the thickness of the whole epidermal layer for skin from the rump and the thigh areas was respectively 138 $\pm$ 15 μm and 91 $\pm$ 11 μm, while the thickness of the stratum corneum are respectively 34.8 $\pm$ 4.2 μm and 23.0 $\pm$ 4.3 μm. These results suggest that the main difference between tissue harvested from the rump and the thigh is the thickness of the dermal layer. A comparison between samples recovered after the compression tests at different strain rates and samples loaded into the mechanical apparati but not subjected to compression (sham) is shown in Fig. 6.13, 6.14, 6.15 for the rump samples and Fig. 6.16, 6.17, 6.18 for the thigh samples, where H&E stain of the tissue specimens at different magnifications are presented. A qualitative analysis of these images showed that rump specimen subjected to quasi static compression (strain rates 0.001 and 1.0 s^{-1}) up to a strain in the range of 0.6 - 0.7 were not able to recover their initial thickness, while samples subjected to high strain rate compression didn't show any significant difference compared to the sham samples. It is important to notice that the maximum strain achieved in the high strain rate experiments for one single compressive

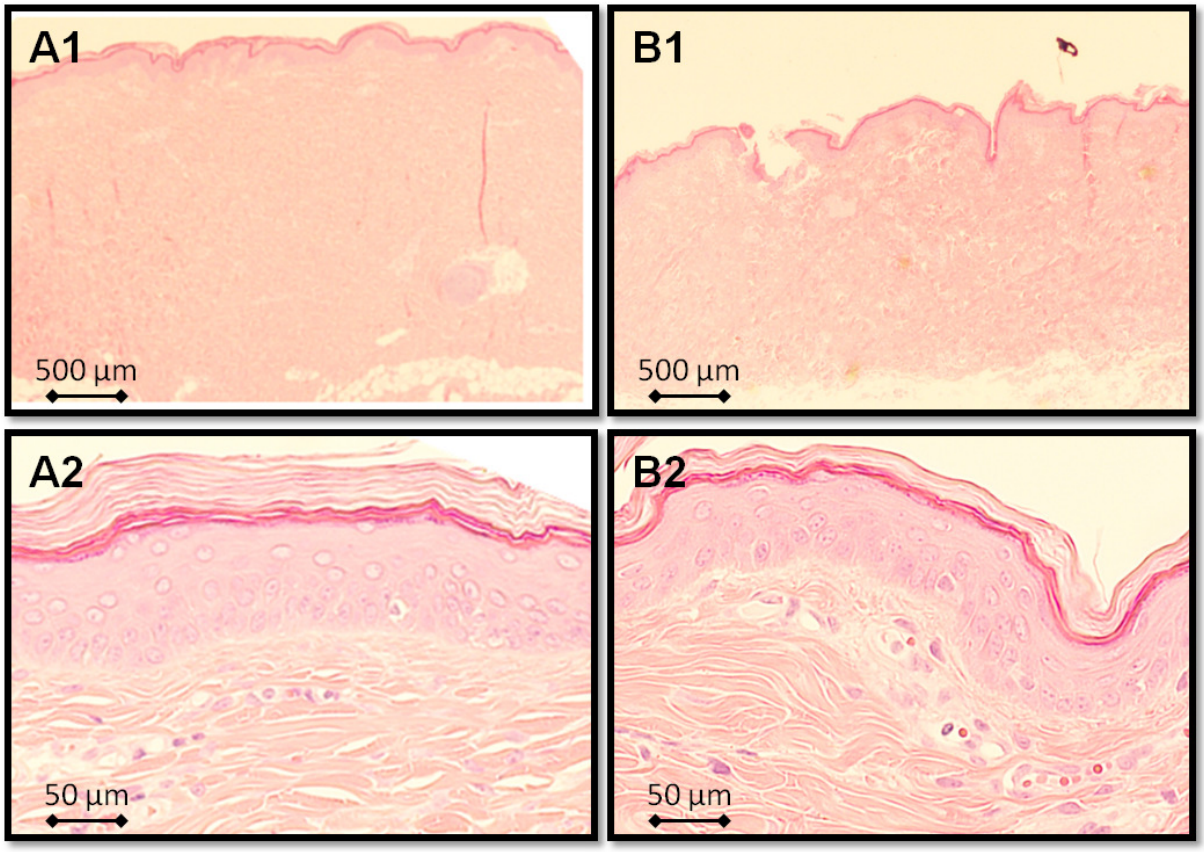

Figure 6.12: **Histological comparison of skin sample harvested from different anatomical areas** H&E stain of uncompressed skin samples harvested from the rump and the thigh at two magnifications

pulse was approximately 0.4, however, because of the lack of a momentum trap system, the specimens were actually subjected to multiple compressive pulses, which would have increase the final strain values to the range achieved in the quasi static experiments. Moreover, images at high magnifications showed that cellular nuclei assumed a squeezed elongated shape in the rump samples subjected to low and medium strain rate compression, particularly in proximity of the basal epidermal layer, while cells maintained their round shape in samples compressed at high strain rate. In the case of specimen harvested from the thigh no significant differences in thickness were observed in the recovered samples after compression at any strain rate, while the same change in shape of the cell nuclei highlighted for rump samples was observed in thigh samples compressed at low and medium strain rates. The change in thickness in rump samples subjected to low and medium strain rates is associate with a delamination of the collagen network, as shown by the increased distribution of white empty spaces between the pink collagen bundles in the dermal layer. This delamination appears to have a preferential orientation, perpendicular to the straining direction. In the thigh samples, although no delamination could be observed, a preferential orientation of the collagen bundles in the upper dermal layer could be hypothesized.

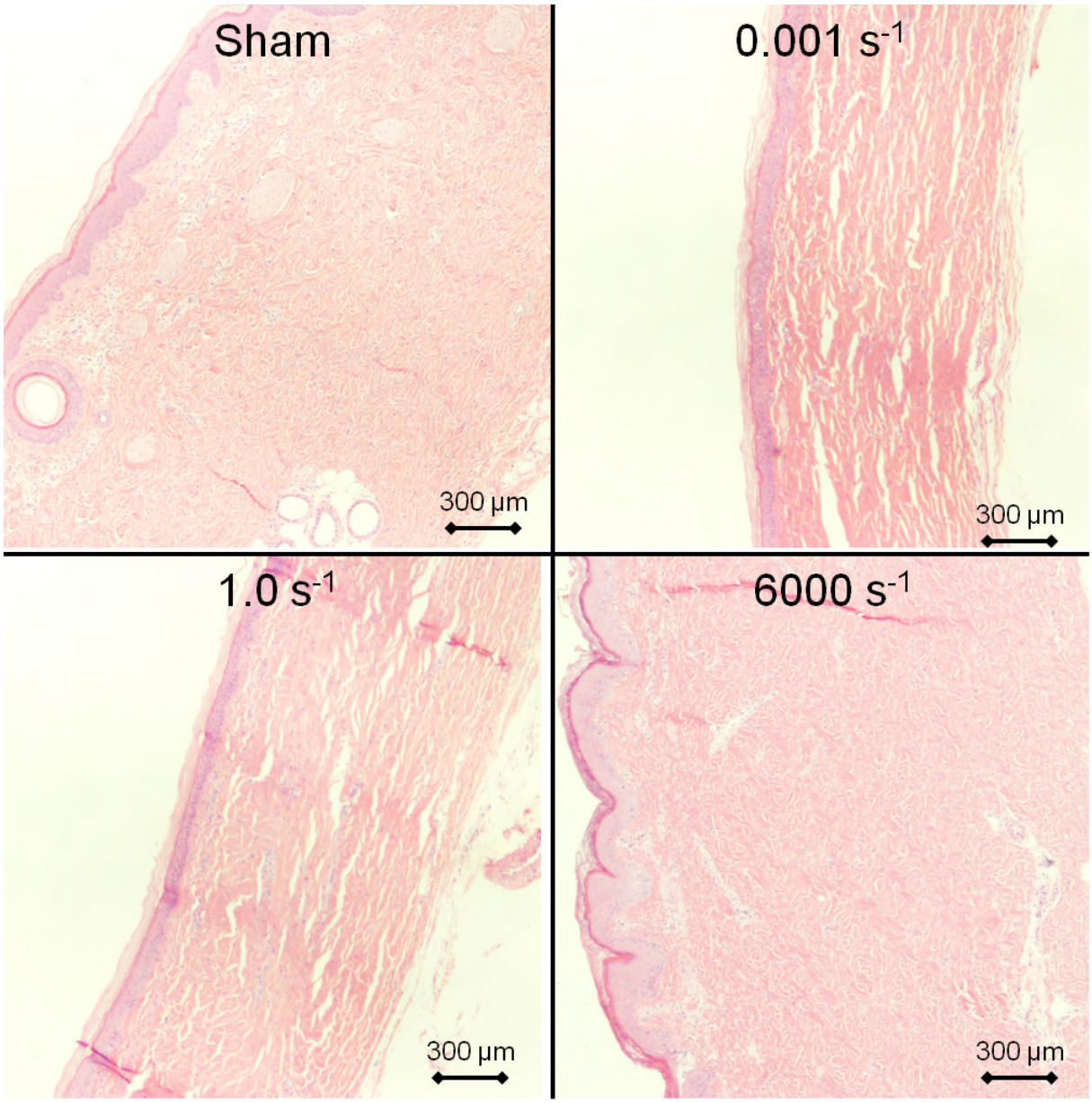

Figure 6.13: **Analysis of histological changes in porcine skin due to compression: Rump 4x** H&E stain of porcine skin samples harvested from the rump and recovered after compression at strain rates of 0.001, 1.0 and 6000 s^{-1} compared to uncompressed (sham) samples

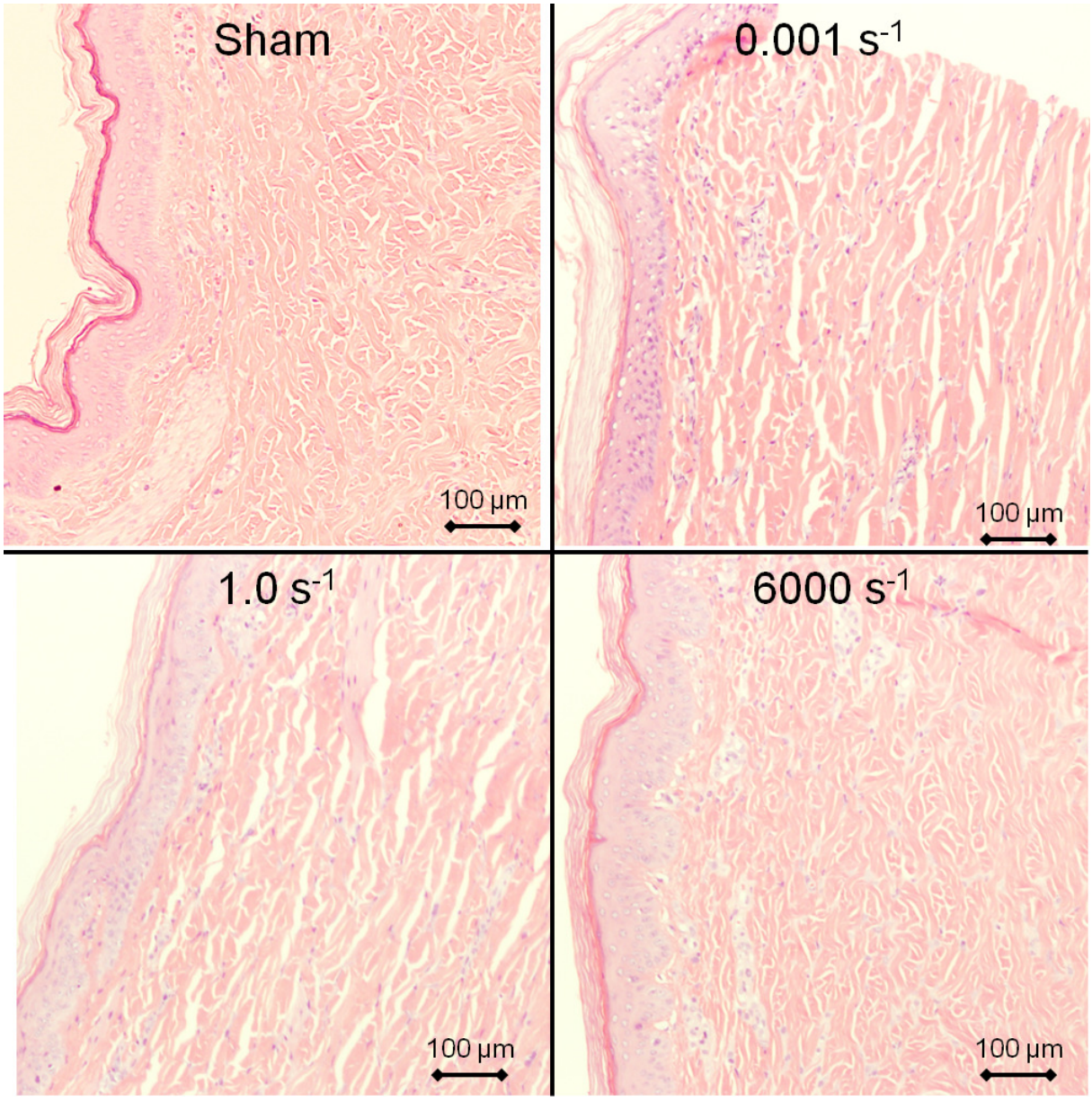

Figure 6.14: **Analysis of histological changes in porcine skin due to compression: Rump 10x** H&E stain of porcine skin samples harvested from the rump and recovered after compression at strain rates of 0.001, 1.0 and 6000 s^{-1} compared to uncompressed (sham) samples

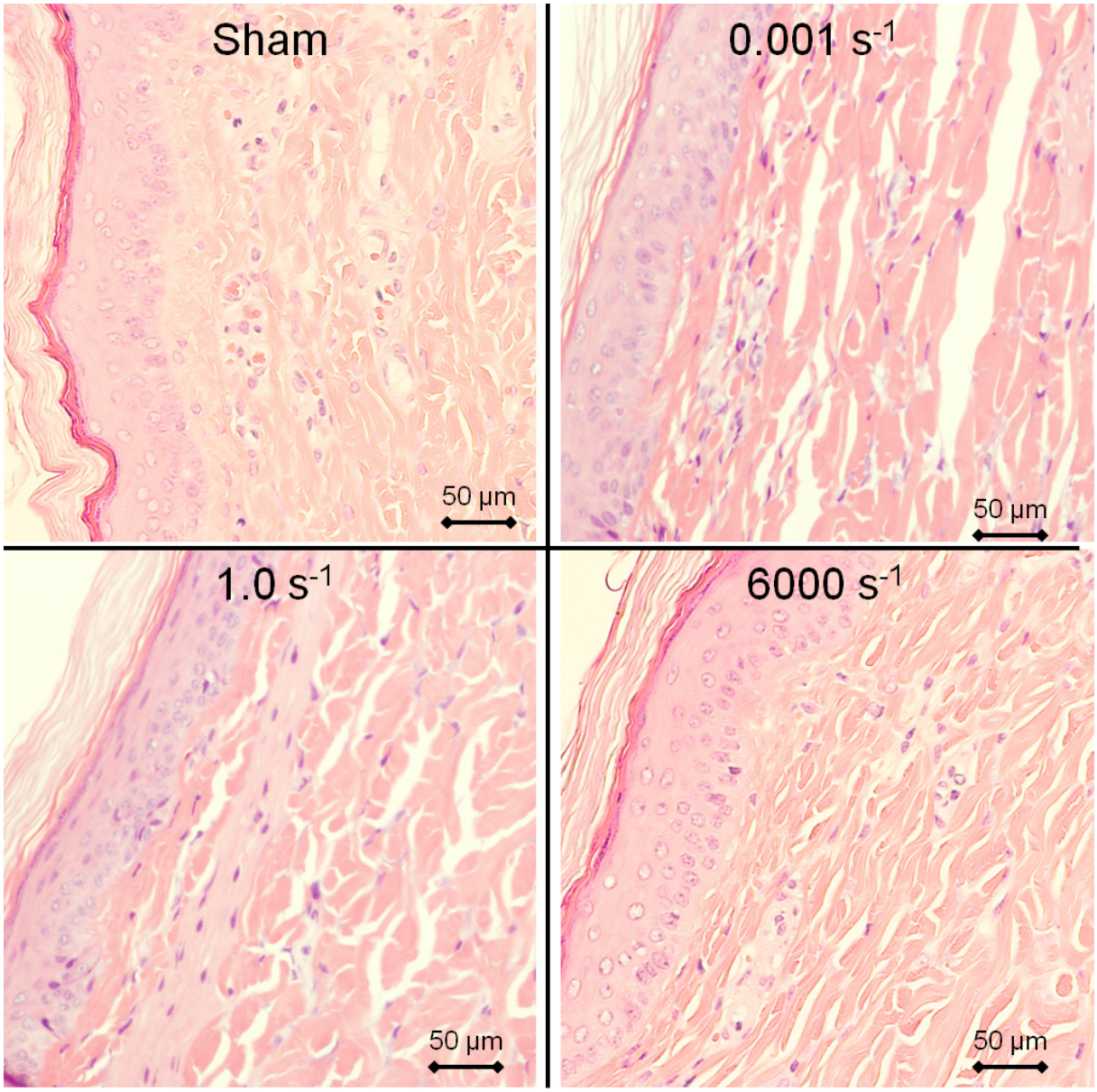

Figure 6.15: **Analysis of histological changes in porcine skin due to compression: Rump 20x** H&E stain of porcine skin samples harvested from the rump and recovered after compression at strain rates of 0.001, 1.0 and 6000 s^{-1} compared to uncompressed (sham) samples

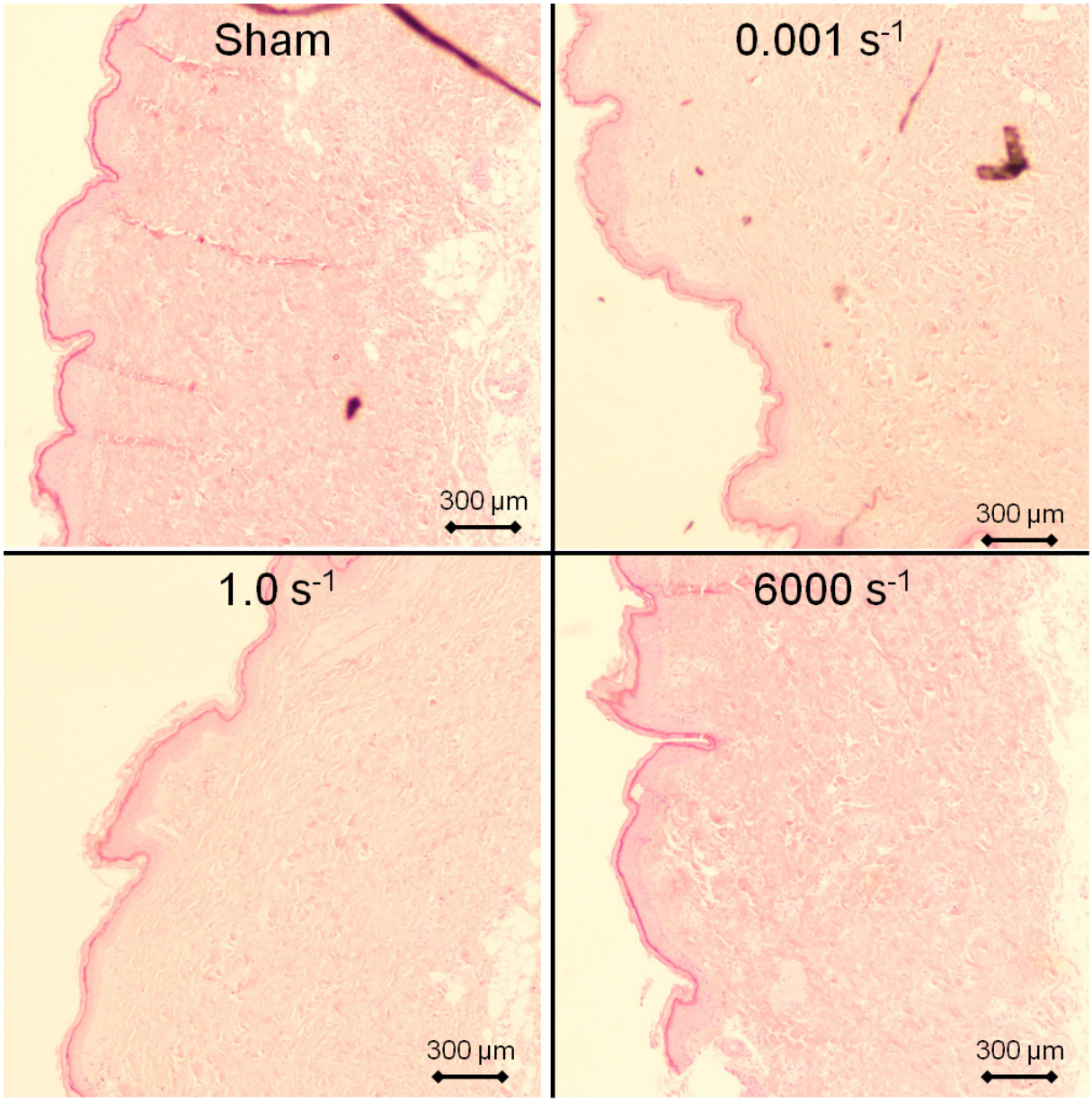

Figure 6.16: **Analysis of histological changes in porcine skin due to compression: Thigh 4x** H&E stain of porcine skin samples harvested from the thigh and recovered after compression at strain rates of 0.001, 1.0 and 6000 s^{-1} compared to uncompressed (sham) samples

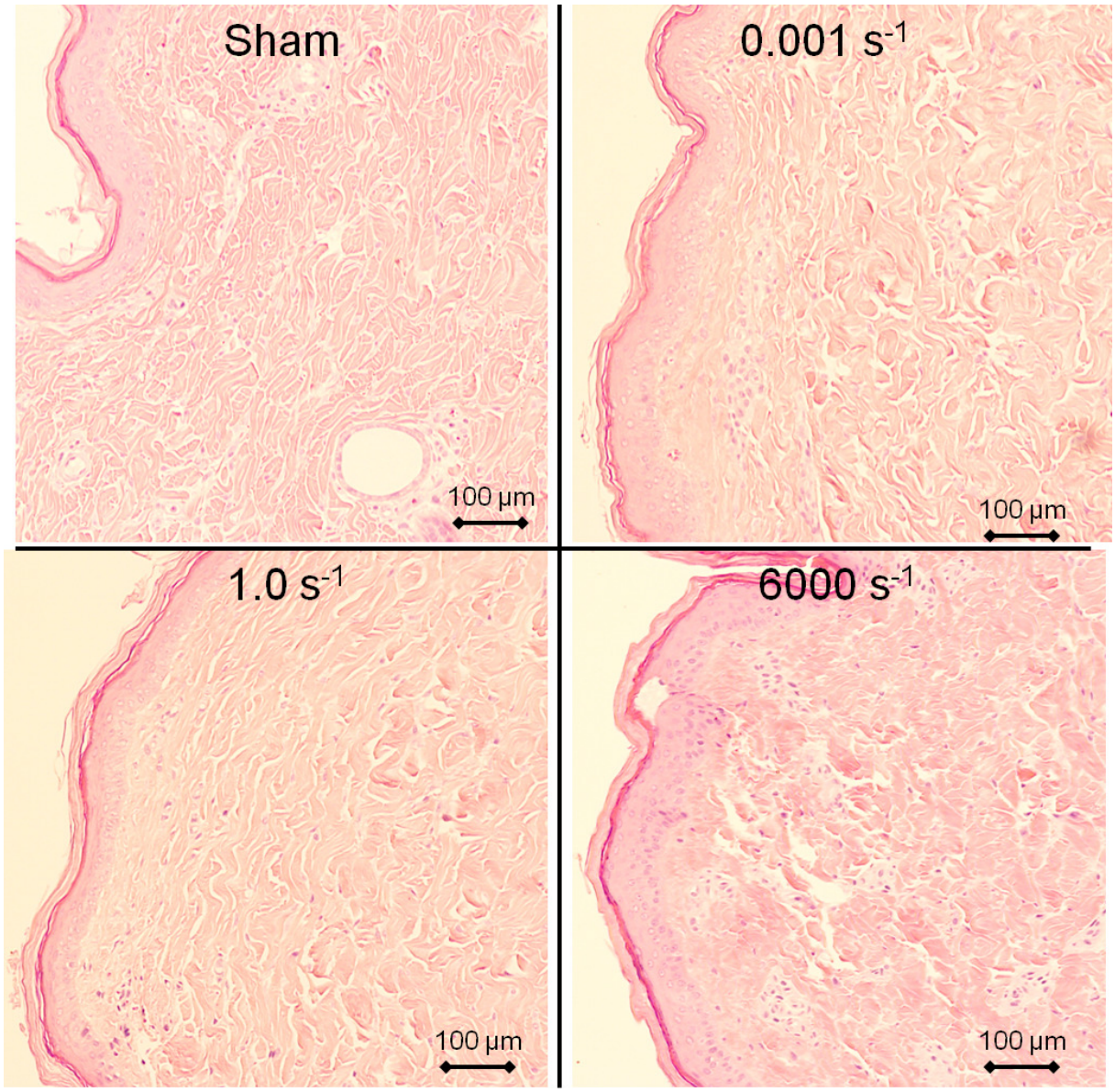

Figure 6.17: **Analysis of histological changes in porcine skin due to compression: Thigh 10x** H&E stain of porcine skin samples harvested from the thigh and recovered after compression at strain rates of 0.001, 1.0 and 6000 s^{-1} compared to uncompressed (sham) samples

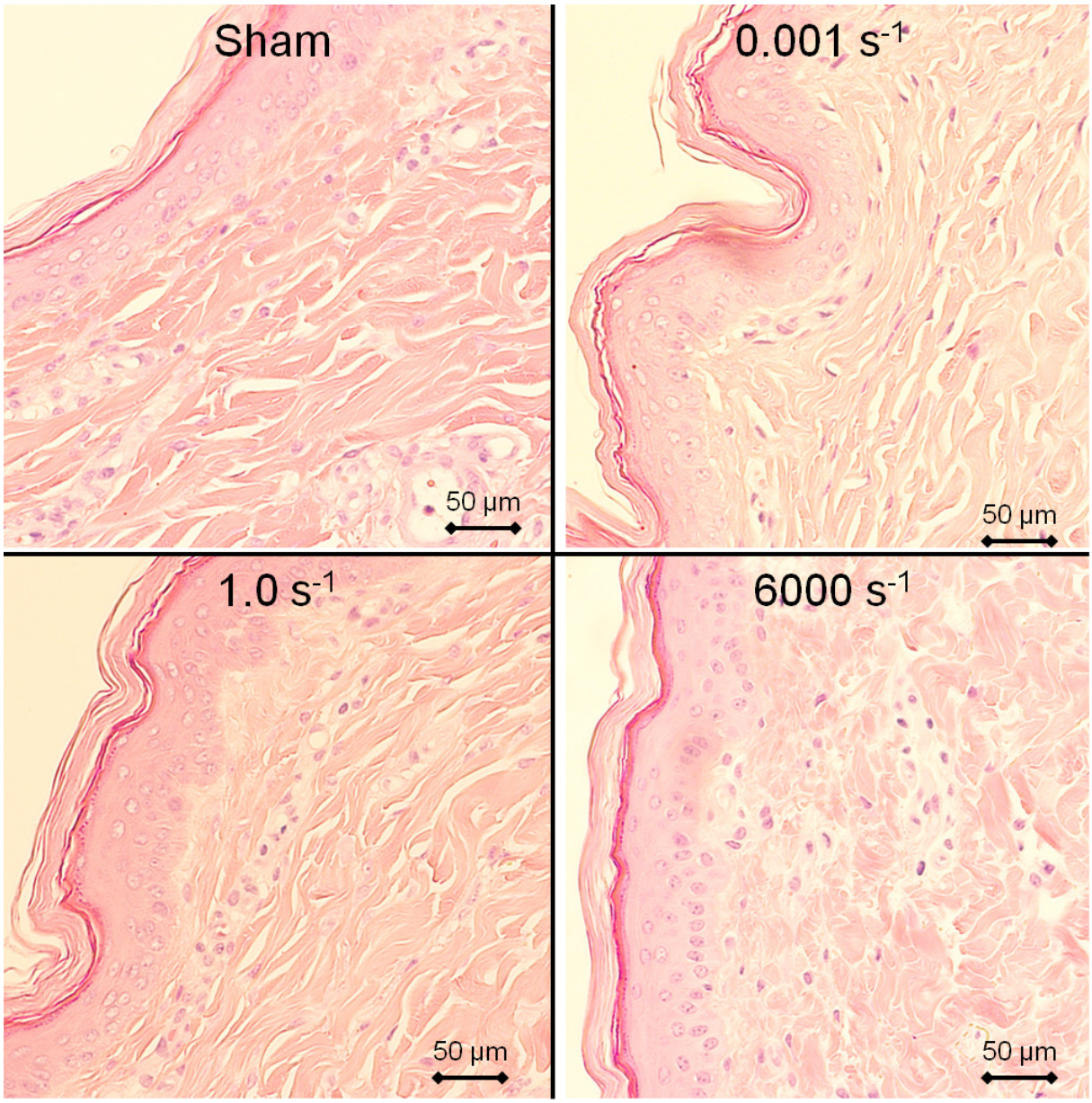

Figure 6.18: **Analysis of histological changes in porcine skin due to compression: Thigh 20x** H&E stain of porcine skin samples harvested from the thigh and recovered after compression at strain rates of 0.001, 1.0 and 6000 s^{-1} compared to uncompressed (sham) samples

In order to gather more information regarding changes in the collagen matrix following the mechanical tests, samples were stained using a Masson's trichrome stain. The results for rump samples compressed at different strain rates are shown in Fig. 6.19, 6.20 at two different magnifications. Significant differences are observed between samples compressed at low and medium strain rates compared to sham samples. Specifically, the orange stain is present both in the stratum corneum and dermal layers of the compressed samples while only the stratum corneum of the sham samples is stained orange. This implies that the last die used in the multistep staining procedure, the blue dye with large molecular weight, was not able to penetrate entirely the collagen network and stain all the collagen bundles in the dermal layer of the compressed samples. This suggests that the collagen network following the mechanical test at low and medium strain rates has undergone significant structural changes associated with the reduction in distance between collagen bundles which corresponded to smaller pore sizes generated during the fixation of the tissue, and possibly suggesting damage to the ground substance in which the collagen bundles are immersed. Moreover, previous observations of changes in the shape on the cellular nuclei in samples compressed at low and medium strain rates are confirmed by images of the Masson's trichrome stain. Cellular nuclei are stained in black/dark blue and as shown in Fig. 6.20 they show a squeezed elongated shape in samples compressed at low and medium strain rates, while they have a more round shape in sham samples and samples compressed at high strain rate. The only difference between samples compressed at high strain rates and sham samples is the intensity of the blue stain in the dermal layer. This, however, is most likely correlated to small differences in the time of immersion of the samples in the light green stain.

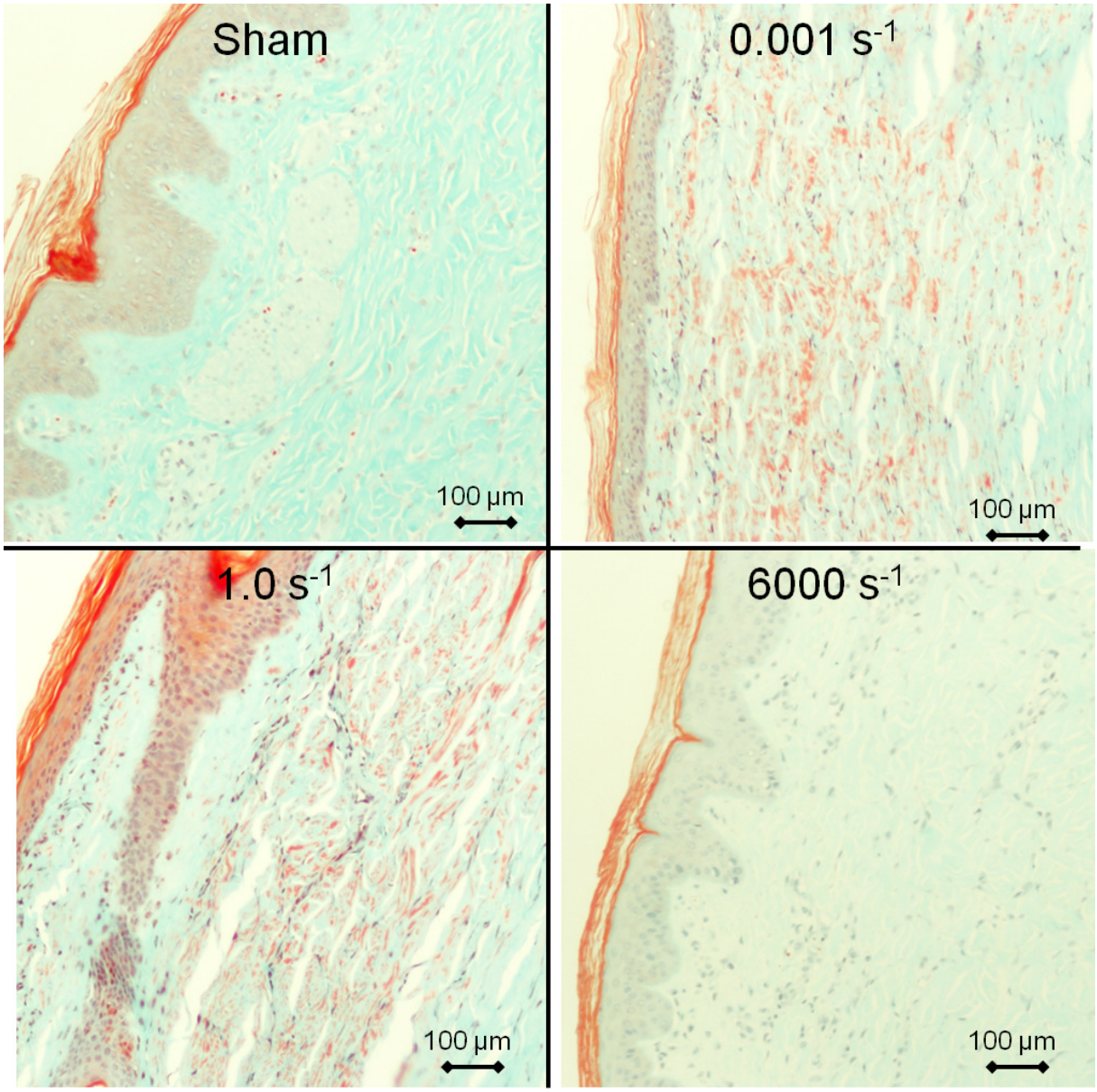

Figure 6.19: **Analysis of histological changes in porcine skin due to compression: Rump 10x** Masson's trichrome stain of porcine skin samples harvested from the rump and recovered after compression at strain rates of 0.001, 1.0 and 6000 s^{-1} compared to uncompressed (sham) samples

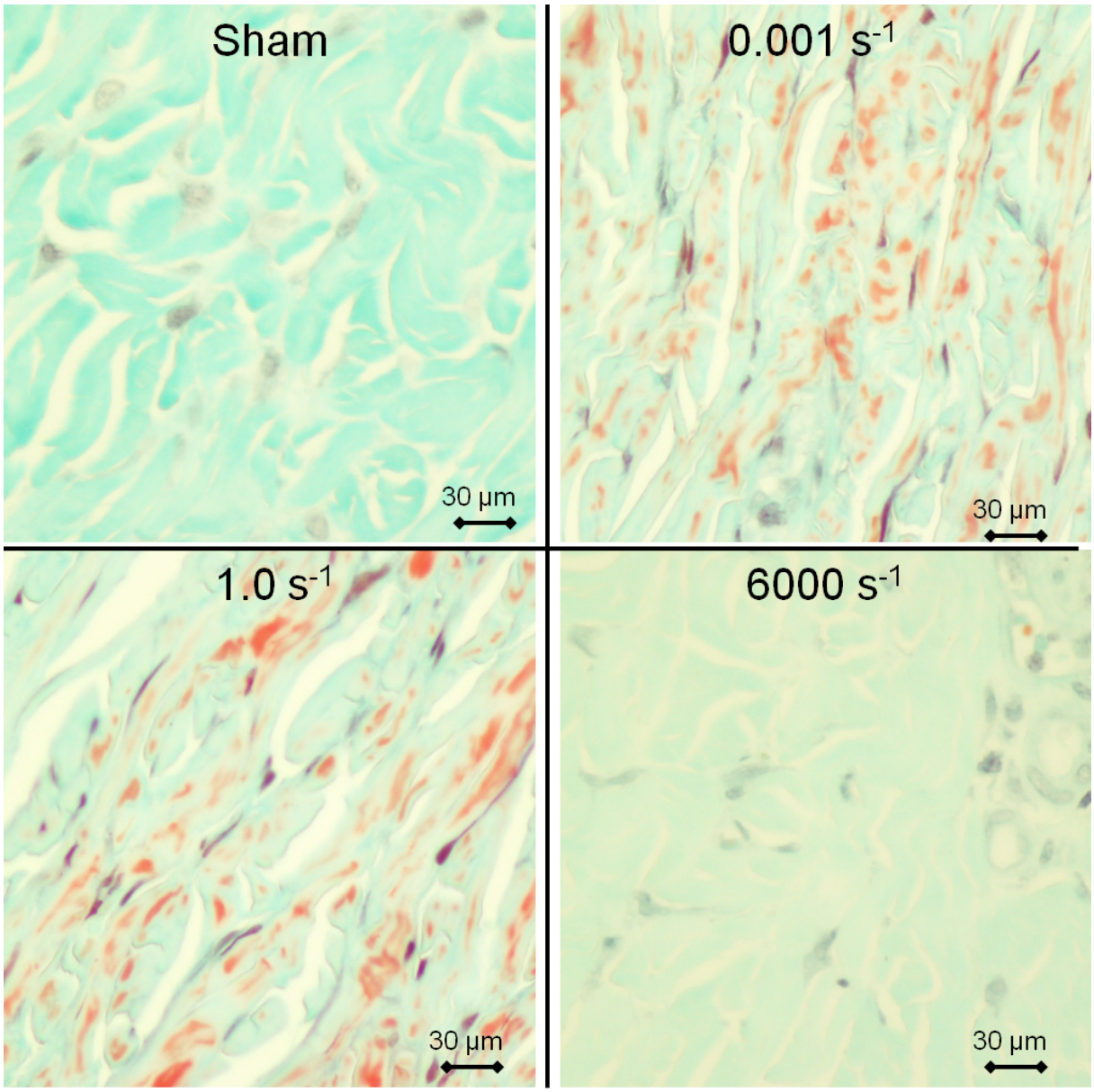

Figure 6.20: **Analysis of histological changes in porcine skin due to compression: Rump 40x** Masson's trichrome stain of porcine skin samples harvested from the rump and recovered after compression at strain rates of 0.001, 1.0 and 6000 s^{-1} compared to uncompressed (sham) samples

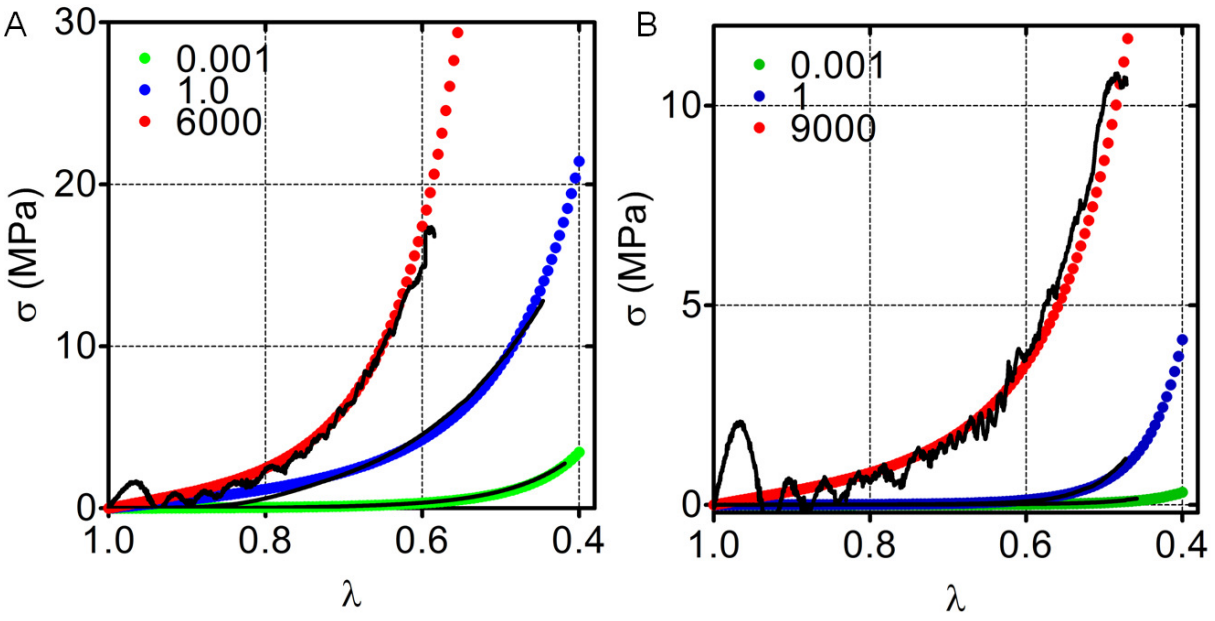

Figure 6.21: **Stress-stretch curves for skin samples** In colours, stress-stretch curves fitted with a one parameter Ogden model for uniaxial compression of skin samples harvested from the rump (A) and the thigh (B) at different strain rates. In black average engineering stress-stretch curves calculated from the experimental results (E=1, N=3).

6.3.4 Tissue modeling

Three hyperelastic models were used to fit the stress-stretch curves obtained from independent compression experiments at different strain rates. In Fig. 6.21 the average experimentally obtained data and the correspondent curves fitted using a one term Ogden model are presented for compression experiments on rump and thigh skin samples at three different strain rates. The Ogden model reproduces the J-shape response of the tissue at each strain rate. A comparison of the goodness of the fit among the results obtained from three different hyperelastic models (Ogden, Fung and Gent) indicated that the Ogden model best described the skin response in compression both for rump and thigh samples, as shown by the values of R^2 summarised in Table 6.2

	Ogden	**Fung**	**Gent**
Rump	98.8 ± 0.9	98.7 ± 0.9	97.8 ± 0.9
Thigh	97.5 ± 3.7	97.0 ± 3.5	95.8 ± 3.3

Table 6.2: Average R^2 values obtained from fittings of stress-stretch curves with Ogden, Fung and Gent models

The average values of the fitting parameters for the three different models are shown

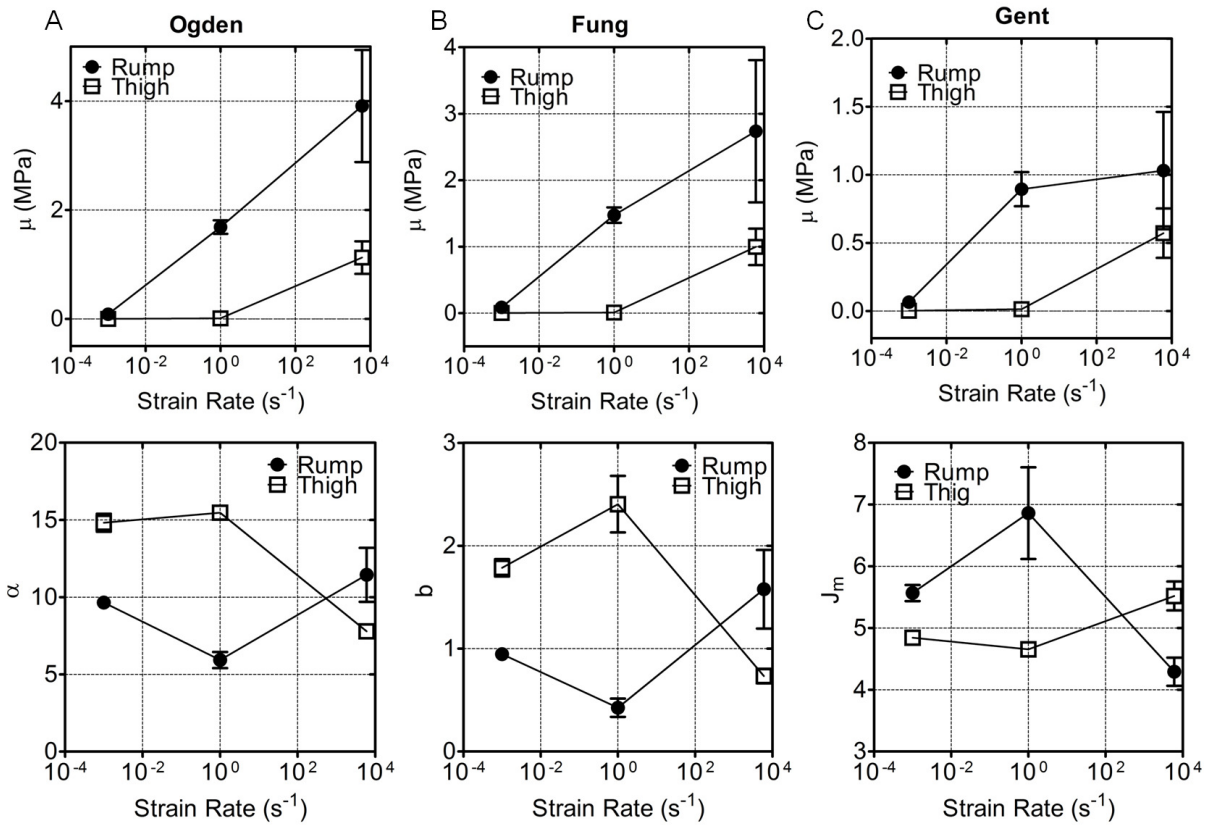

Figure 6.22: **Skin constitutive parameters** Shear stress μ, strain hardening α and b, and chain extensibility J_m parameters calculated with a best fit algorithm for Ogden, Fung and Gent models from experimentally obtained stress-stretch curves for rump and thigh samples as a function of the strain rate. Data are presented as average values of one experiment performed with N=3. Error bars represent standard error.

in Fig. 6.22 as a function of the strain rate. As previously reported in literature [65, 133] the best fit values for the shear stress parameter μ increased with increasing strain rate both for rump and thigh specimens, for all the three different models. However, significant differences were observed in the values of μ for the samples harvested from the two different anatomical regions, with rump samples associated with higher shear stress values at each strain rate. Moreover, the Ogden and Fung models returned similar values of shear stress at each strain rate, while the best fit values obtained with the Gent model were significantly lower. No significant trends were observed in the values of the strain hardening parameters α and b respectively of the Ogden and Fung models, as well as in the case of the chain extensibility parameter J_m of the Gent model with respect to the strain rate.

6.4 Discussion

In this chapter the mechanical response of confined or unconfined porcine skin in compression at different strain rates has been investigated. *In vitro* studies were chosen over *in vivo* studies because they offered the opportunity to compress the material up to high values of strain and strain rate, and also to recover the samples post compression for morphological analysis. Initial studies on confined specimens showed that tissue preservation had an important role in the measured mechanical properties of the tissue such as the bulk modulus.

In unconfined experiments, fresh skin samples were harvested from two different anatomical regions to highlight the significant differences in phenotype and mechanical properties of skin depending on the location of the body from which it was harvested. Previous studies had reported differences in mechanical properties of skin in tension as a function of orientation with respect to the Langer's lines [138,149], while only one study was found which reported differences in mechanical properties of rat skin harvested from different areas when subjected to compression [135]. However, rat skin does not represent a good simulant of human skin, hence the necessity of performing compression experiments on porcine skin harvested from different areas.

Analysis of the phenotype of skin harvested from the rump and the thigh showed that samples from the two anatomical regions had significantly different thickness, with specimens from the rump thicker than specimens from the thigh. Moreover, the dermis was the skin layer that mostly contributed in the difference in thickness between the samples. Also, specimens of the same diameter showed different weight indicating that skin samples harvested from the rump had higher density of collagen fibres compared to samples harvested from the thigh. The mechanical response of these specimen was investigated in compression at strain rates of 0.001, 1.0 and 6000-9000 s^{-1} using an Instron 5566 for low and medium strain rates and a SHPB system for high strain rate experiments. Results showed that the mechanical response of skin in compression was strongly dependent on the strain rate of loading and on the anatomical region from which the samples were collected. As previously reported [65, 133, 139], pig skin stiffens and strengthens with in-

creasing strain rate over the full range explored. This behaviour was observed for the two groups of specimens harvested from the rump and thigh. Comparison of the mechanical response of the two skin groups when compressed at the same strain rate showed that skin from the rump was stiffer than skin from the thigh. These results support the hypothesis that the constitutive behaviour of skin primarily depends on the structure and density of the collagen network that lies within the dermal layer [65]. Another phenotypic characteristics which could contribute to the differences in mechanical properties observed in compression between the two group of skin samples is the number and dimension of hair follicles embedded in the dermal layer [135]. A qualitative analysis of the skin tissue before harvest indicated that the rump area was characterised by thicker and denser hair, therefore suggesting that the hair follicles embedded in the dermal layer of these samples were larger and more frequent. However, a quantitative relation between mechanical properties and hair density could not be drawn as very few hair follicles were present in the histological sections of samples recovered post compression and analysed with microscopy.

Rarely histological techniques have been adopted to investigate the mechanisms of damage and deformation of tissue samples subjected to mechanical tests. Wang *et al.* [135] used a H&E staining of skin samples before the compression tests to characterise their morphology and found that skin sections from mice of different age showed that the thickness of the epidermal layer was similar among groups while the thickness of the dermal and hypodermal layers varied among age groups and hair-cycle stages [135]. Moreover, they reported different thicknesses for samples harvested from different areas of the hind limb and they showed that anatomical location significantly impacted skin stiffness [135]. In the study reported here, H&E staining of skin samples harvested from the rump and the thigh pre compression highlighted phenotypic differences between the two samples, such as thickness of the dermal layer, which could be related to the mechanical response of the tissues in compression. Moreover, H&E staining of samples harvested from the rump and recovered after mechanical test showed that samples compressed quasi statically did not recover the initial thickness and that long and thick white stripes perpendicular to the

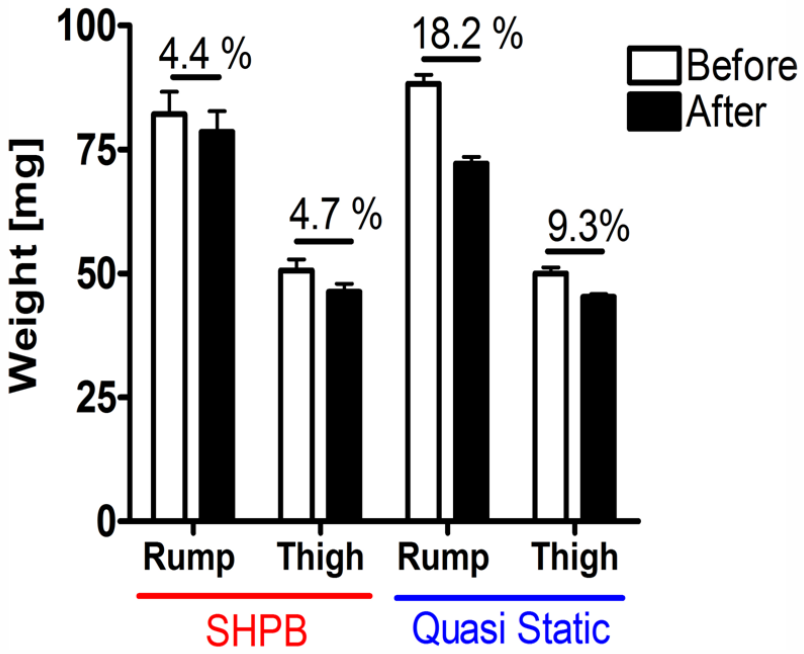

Figure 6.23: **Water loss in compression experiments** The loss in water content was evaluated measuring the weight loss in skin samples due to compression experiments. The values reported on each set of column represent the percentage loss of weight for rump and thigh samples for experiments at high (SHPB) and low (Quasi Static) strain rates. Data represent average values of one experiment (E=1) performed with N=3 samples per condition.

direction of compression appeared in the samples compressed at 0.001 and 1 s^{-1}, while no significant differences were observed in samples compressed at high strain rate compared to sham samples. These results suggest that slow compression of samples allowed a re-organisation and possibly damage to the collagen network, while during high strain rate compression the collagen fibres had no time to slide within the ground substance and less damage was associated with the mechanical process. Moreover, low and medium strain rate experiments were associated with high loss of water during compression, as shown in Fig. 6.23, compared to high strain rate experiments. This could also be associated with increased levels of damage observed in the specimens compressed with the Instron 5566 machine in the form of delamination of the collagen bundles associated with large white spaces present in the histological sections of these specimens. These results suggest that future studies should be performed with specimen completely immersed in a liquid

solution, in order to prevent liquid loss during compression. Infiltration of low molecular weight die in the Masson's trichrome stain of samples compressed quasi statically suggested rupture of structural elements (e.g. collagen fibres, elastin) which formed smaller pores when crosslinked in the fixation stage hence excluding the larger blue molecules to stain the tissue where damaged. These results confirmed the observations that damage occurred at the level of the structural network within the dermal layer of sample compressed at low and medium strain rates. In future studies, interrupted test (e.g. fixing the maximum level of strain) at different strain rates, associated with post compression histology, could provide more information regarding the mechanical parameters that are associated with tissue damage such as strain rate, maximum strain, maximum stress.

The measured constitutive response of skin harvested from different anatomical regions at different strain rates was modeled using three different isotropic hyperelastic models, the Ogden, the Fung and the Gent models. Although skin is known to be anisotropic, in the case of uniaxial compression the isotropic approximation is acceptable since mechanical tests are performed in the through thickness direction, and the results represents an average of the mechanical response of skin in its major plane [65], hence loosing information about the tissue orientation. The three hyperelastic models used two parameter to fit the experimentally obtained stress stretch curve for skin in compression at different strain rates. The common parameter between the models is the shear modulus μ. The values of μ increase with strain rate for all the three different models used. It has been suggested that this parameter is related to the mechanisms of bending and shearing of the collagen fibres within the ground substance when they poses resistance to rearrangement, hence its dependence on the strain rate of loading [65, 133]. Previous results obtained from compression of porcine skin [65] reported values of μ similar to the one obtained for the samples harvested from the rump when fitted with a one term Ogden model. This model also reported the best goodness of fit, expressed in terms of the values R^2 among the hyperelastic models investigated. However, the values for the strain hardening exponent α calculated with a non-linear best fit method, although in the same order of magnitude, were not constant with respect to the strain rate as reported in previous studies [65, 133].

Zhou *et al.* [134] also reported variable values of the parameter α but did not suggest an explanation for this phenomenon. Shergold *et al.* [65] suggest that α is related to the geometrical reorganisation of the collagen network and the authors suggest that this phenomenon is not dependent on the strain rate. However, in the present study, histological analysis of compressed tissue specimens suggested differences in network structure following compression at different strain rates, but a relation between strain rate and the parameter α was not observed. Moreover, significant differences in the values of the fitting parameters were observed for skin specimens harvested from different anatomical regions, suggesting that a constitutive model of skin might also need to take into account sample thickness or collagen content to better represent the tissue behaviour. Future studies should include tensile tests on skin samples from the same anatomical regions at the different strain rates, electron microscopy of recovered samples to gather more information regarding the damage mechanisms at the microscopical level of collagen and elastin fibres in conjunction with interrupted mechanical tests. These studies would allow the formulation of a more complete set of modeling parameters which could be used in finite element modeling of traumatic or non-traumatic tissue injury.

Chapter 7

Conclusions

7.1 Summary of thesis achievements

The research presented in this thesis focused on the development and characterisation of experimental platforms to investigate the effects of primary blast on live biological samples. Early animal studies, reported in literature, focused on determining injury and survivability thresholds as a function of the peak pressure and duration of the blast stimulus [10, 32]. In these studies, animals were subjected to a blast wave generated either via detonation of explosives or with a shock tube and the values of the pressure stimulus were measured in air just before and after the test subject. The upper limit of human survivability curves was found to correspond to values of pressure of few MPa for short pulses (in the order of hundreds of microseconds - few millisenconds in duration). Longer pulses (tens to hundreds of milliseconds in duration) were survivable if associated with values of peak pressure in the order of tens - few hundreds kPa [10, 32]. The apparati developed in this thesis to study primary blast effects on biological samples were able to generate pressure stimuli in two different regimes. The SHPB system delivered pressure waves in the order of tens of MPa with a total duration of a millisecond, while the shock tube could generate pulses as long as ten millisenconds with the peak pressure ranging from fifty to hundreds of kPa. Although these values correlated well with the spectra of stimuli categorised as survivable by animal experiments, there are no reported values of pressure/stress generated within the test subjects, probably due to the difficulty to

perform such experiments. Stress transmission depends on the density and mechanical impedance of the different biological tissues subjected to the blast wave and can vary also as a function of the position and distance of the subject with respect to the explosion. Future studies should focus on the correlation between the pressure values of the external stimulus and the actual stresses experienced *in vivo*.

A confined SHPB system was designed and implemented, which enabled the generation and characterisation of dynamic pressure pulses in a controlled environment on cells. Data analysis software was developed to automate calculations of the pressure pulses generated within the confinement chamber. A dispersion correction algorithm was implemented within the data analysis software: although dispersion was limited in the SHPB system, due to the geometry of the bars, the correction algorithm allowed better wave alignment during data analysis. The peak pressures achieved with the current system ranged from 10 - 40 MPa with a total duration of approximately 1 ms. The pressure profile was characterised by multiple subsequent pressure pulses of varying, but reproducible, amplitudes. The confinement chamber was designed to allow recovery of the biological samples for further analysis.

Cell pressurisation experiments were conducted on three different samples: PLB985 cells, bone marrow and MSCs. It was observed that, for all samples, viability was reduced, following the high intensity pressure wave event, to levels proportional to the peak pressure and pressure impulse. The loss in viability was associated with cell lysis, detected by measuring the levels of LDH released into the cell medium following the pressure event. The recovered intact cells were analysed to confirm their viability: they showed normal levels of metabolic activity compared to control samples. The cell medium recovered after the pressure experiments (referred to in the text as HIPW-conditioned medium) showed contradictory effects when used to culture fresh MSCs: the level of metabolic activity of the cells was either unchanged for the three consecutive days of experiments (E=2) or cells cultured in HIPW-conditioned medium showed increased levels of metabolic activity compared to sham (E=2). No definitive conclusions could be formulated from these experiments. The HIPW-conditioned medium showed chemotactic potential for neutrophils: a

significant increase in neutrophil migration was observed towards the HIPW-conditioned medium compared to the controls. These results taken together suggest that pressure stimuli on the order of tens of MPa and with a duration of 1 ms can induce damage in live cells in suspension. In addition, long term functional effects are possibly related to signals that the cells (dead or viable) release in the medium following the pressure event. The SHPB confined system was further modified to allow pressurisation experiments on cell monolayers. However, both the system characterisation and the preliminary biological analysis indicated that the set up was not adequate: classical SHPB theory could not be applied due to the presence of extra mechanical components and almost complete cell death was observed in MSCs monolayers subjected to the lowest pressure achievable with the bars currently available. Hence, alternative types of experiments were sought.

Shock tubes have been largely used in animal studies of blast injuries but only in the last three years researchers adopted this system to study the effects of primary blast on cells. A shock tube-bio set up, similar to the one developed by Arun *et al.* [59], was developed and characterised. Briefly, a tissue culture plate filled with liquid was positioned at the open end of the shock tube. Diaphragms of different thickness were used to generate increasing levels of overpressure, and a pressure sensor embedded in the tissue culture plate was used to characterise the pressure stimulus generated within the wells. Preliminary experiments on MSC monolayers showed that, for an overpressure of approximately 130 kPa and duration of 10 ms, limited cellular damage occurred. These results indicate that the shock tube platform can be used to study the effects of primary blast of low intensity on cell monolayers.

Finally, the SHPB system, coupled with quasi-static experiments, was used to investigate the mechanical properties of skin over a range of strain rates. It was observed that samples harvested from different anatomical regions displayed different stress-strain curves, and that tissue stiffness increased at higher strain rates. Three hyperelastic models were used to fit the experimental data: the Ogden model returned the best fit, as previously reported in literature. Histological analysis of recovered tissue samples indicated changes in tissue morphology, following compression, were suggestive of collagen damage. This

result highlights the potential of the histological technique in understanding the mechanisms of deformation and damage in soft biological tissues.
Overall this research provides a framework for primary blast injury studies on live biological samples.

7.2 Future work

The experimental platforms (confined SHPB and Shock Tube-bio set up) developed and characterised in this thesis will enable research of primary blast injuries to be extended to a wider variety of cellular types and tissues. Specifically, future work should focus on identifying a molecular signature of primary blast injuries, such as blast lung and traumatic brain injury, through analysis of the cells and cell medium recovered post pressurisation of single or multiple cell populations. This could help inform clinicians about early detection biomarkers, as well as facilitate the development of targeted treatments for unique pathologies associated with blast injuries. Further pressurisation studies on immobilised cells in gel-like 3D structures using the SHPB platform would provide more information about the role of mechanotransduction in blast injuries and help to establish a link between cellular and tissue studies. Finally, the confined SHPB platforms could be used to study the mechanical properties of non-Newtonian liquids at high pressures and strain rates.

Bibliography

[1] Ramasamy, A., Hill, A.M., and Clasper , J.C., Improvised explosive devices: pathophysiology, injury profiles and current medical management, *J. R. Army Med. Corps* (2009), **155**: 265–272

[2] Ramasamy, A., Harrison, S.E., Clasper, J.C., and Stewart, M.P.M., Injuries from roadside improvised explosive devices, *J. Trauma* (2008), **65**: 910–914

[3] Stuhmiller, J.H., Phillips III, Y.Y., and Richmond, D.R., *The physics and mechanisms of primary blast injury*, pp. 241–270, Office of the Surgeon General (1991)

[4] Wolf, S.J., Bebarta, V.S., Pans, P.T., and Cantrilli, S.V., Blast injuries, *Lancet* (2009), **374**: 405–415

[5] Freidlander, F.G., The diffraction of sound pulses. diffraction by a semi-infinite plate, *Proc. R. Soc. Lond. A* (1946), **186**: 322–344

[6] Proud, W.G., The physical basis of explosion and blast injury processes, *J R Army Med Corps* (2013), **159**: i4–i9

[7] Salas, M.D., The curious events leading to the theory of shock waves, *Shock Waves* (2007), **16**: 477–487

[8] Elsayed, N.M., Toxicology of blast overpressure, *Toxicology* (1997), **121**: 1–15

[9] White, C.S., The scope of blast and shock biology and problem areas in relating physical and biological parameters, in *Defence Atomic Support Agency Report, DASA 1856* (1966)

[10] Bowen, I.G., Fletcher, E.R., and Richmond, D.R., Estimate of man's tolerance to direct effects of air blast, in *Defence Atomic Support Agency Report, DASA 2113* (1968)

[11] Stewart, C., Jagoda, A., and Howell, J.M., Blast injuries: preparing for the inevitable, *Emergency Medicine Practice* (2006), **8**: 1–28

[12] Peleg, K., Aharonson-Daniel, L., Stein, M., Michaelson, M., Klueger, Y., Simon, D., and Noji, E.K., Gunshot and explosion injuries: characteristics, outcomes, and implications for care of terror-related injuries in israel, *Ann. Surg.* (2004), **239**: 311–318

[13] Owens, B., Kragh, J.F., Wenke, J.C., Macaitis, J., Wade, C.E., and Holcomb, J.B., Combat wounds in operation iraqi freedom and operation enduring freedom, *J. Orth. Trauma* (2008), **64**: 295–299

[14] Ramasamy, A., Masouros, S.D., Newell, N., Hill, A.M., Proud, W.G., Brown, K.A., Bull, A.M.J., and Clasper, J.C., In-vehicle extremity injuries from improvised explosive devices: current and future foci, *Phil. Trans. R. Soc. B* (2011), **366**: 160–170

[15] Ramasamy, A., Hill, A.M., Masouros, S.D., Gibb, I., Bull, A.M.J., and Clasper, J.C., Blast-related fracture patterns: a forensic biomechanical approach, *J. R. Soc. Interface* (2010), **8**: 689–698

[16] Zioupos, P., Hansen, U., Currey, J.D., Gibb, I., Bull, A.M.J., and Clasper, J.C., Microcracking damage and the fracture process in relation to strain rate in human cortical bone tensile failure, *J. Biomech.* (2008), **41**: 2932–2939

[17] Elsayed, N.M. and Atkins, J.L. (Eds.), *Explosion and Blast-related injuries*, Elsevier Inc (2008)

[18] Stinner, D.J., Burns, T.C., Kirk, K.L., Scoville, C.R., Ficke, J.R., and Hsu, J.R., Prevalence of late amputations during the current conflicts in Afghanistan and Iraq, *Mil. Med* (2010), **175**: 1027–1029

[19] Forsberg, J.A. and Potter, B.K., Heterotopic ossification in wartime wounds, *J. Surg. Orthop Adv.* (2010), **19**: 54–61

[20] Zuckerman, S., Vulnerability of human targets to fragmenting and blast weapons, in *Textbook of air armament*, Air Publication (1952) pp. 1–243

[21] Hill, J.F., Blast injury with particular reference to recent terrorist bombing incidents, *Ann. R. Coll. Surg. Engl.* (1979), **61**: 4–11

[22] Chen, Y.C., Smith, D.H., and Meaney, D.F., *In vitro* approaches for studying blast-induced traumatic brain injury, *J. Neurotrauma* (2009), **26**: 861–876

[23] Yun, H.C., Branstetter, J.G., and Murray, C.K., Osteomyelitis in military personnel wounded in Iraq and Afghanistan, *J. Trauma* (2008), **64**: 163–168

[24] Schneiderman, A.I., Braver, E.R., and Kang, H.K., Understanding sequelae of injury mechanisms and mild traumatic brain injury incurred during the conflicts in Iraq and Afghanistan: persistent postconcussive symptoms and posttraumatic stress disorder, *Am. J. Epidemiol* (2008), **167**: 1446–1452

[25] Brohi, K., Trauma induced coagulopathy, *J. R. Army Med. Corps* (2009), **155**: 320–322

[26] Potter, B.K., Forsberg, J.A., Davis, T.A., Evans, K.N., Hawksworth, J.S., Tadaki, D., Brown, T.S., Crane, N.J., Burns, T.C., O'Brien, F.P., and Elster, E.A., Heterotopic ossification following combat-related trauma, *J. Bone Joint Surg. Am.* (2010), **92**: 74–89

[27] Brown, K.V., Dharm-Datta, S., Potter, K., Etherington, J., Mistlin, A., Hsu, J.R., and Clasper, J.C., Comparison of development of heterotopic ossification in injured us and uk armed services personnel with combat-related amputatons: preliminary findings and hypotheses regarding causality, *J. Trauma* (2010), **69**: S116–S122

[28] Jackson, W.M., Aragon, A.B., Bulken-Hoover, J.D., Nesti, L.J., and Tuan, R.S., Putative heterotopic ossification progenitor cells derived from traumatized muscle, *J. Orthop. Res.* (2009), **27**: 1645–1651

[29] Nesti, L.J., Jackson, W.M., Shanti, R.M., Koehler, S.M., Aragon, A.B., Bailey, J.R., Sracic, M.K., Freedman, B.A., Giuliani, J.R., and Tuan, R.S., Differentiation potential of multipotent progenitor cells derived from war-traumatized muscle tissue, *J. Bone Joint Surg. Am.* (2008), **90**: 2390–2398

[30] Lounev, V.Y., Ramachandran, R., Wosczyna, M.N., Yamamoto, M., Maidment, A.D.A., Shore, E.M., Glaser, D.L., Goldhamer, D.J., and Kaplan, F.S., Identification of progenitor cells that contribute to heterotopic skeletogenesis, *J. Bone Joint Surg. Am.* (2009), **91**: 652–663

[31] Richmond, D.R. and White, C.S., A tentative estimantion of man's tolerances to overpressure from air blast, in *The Symposium on Effectiveness Analysis Techniques for Non-Nuclear Warheads Against Surface Targets*, U. S. Naval Weapons Laboratory, Dahlgren, Virginia (October, 1962)

[32] Bass, C.R., Rafaels, K.A., and Salzar, R.S., Pulmonary injury risk assessment for short-duration blasts, *The Journal of Trauma Injury, Infection, and Critical Care* (2008), **65**: 604–615

[33] Dodd, K.T., Mundie, T.G., Lagutchik, M.S., and Morris, J.R., Cardiopulmonary effects of high-impulse noise exposure, *J. Trauma* (1997), **43**: 656–666

[34] Mundie, T.G., Dodd, K.T., Lagutchik, M.S., and Morris, J.R., Effects of blast exposure on exercise performance in sheep, *J. Trauma* (2000), **48**: 1115–1121

[35] Cernak, I., Wang, Z., Jiang, J., Bian, X., and Savic, J., Ultrastructural and functional characteristics of blast injury-induced neurotrauma, *J. Trauma* (2000), **50**: 695–706

[36] Elsayed, N.M. and Gorbunov, N.V., Interplay between high energy impulse noise (blast) and antioxidants in the lung, *Toxicology* (2003), **189**: 63–74

[37] Reneer, D.V., Hisel, R.D., Hoffman, J.M., Kryscio, R.J., Lusk, B.T., and Geddes, J.W., A multi-mode shock tube for investigation of blast-induced traumatic brain injury, *J. Neurotrauma* (2011), **28**: 95–104

[38] Hull, J.B. and Cooper, G.J., Pattern and mechanism of traumatic amputation by explosive blast, *J. Trauma* (1996), **40**: 198S–205S

[39] Serbest, G., Horwitz, J., and Barbee, K., The effect of poloxamer-188 on neuronal recovery from mechanical injury, *J. Neurotrauma* (2005), **22**: 119–132

[40] Blackman, B.R., Barbee, K.A., and Thibault, L.E., *In vitro* cell shearing device to investigate the dynamic response of cells in a controlled hydrodynamic environment, *Ann. Biomed. Eng.* (2000), **28**: 363–372

[41] Ellis, E.F., Mckinney, J.S., Willoughby, K.A., Liang, S., and Povlishock, J.T., A new model for rapid stretch-induced injury of cells in culture: characterization of the model using astrocytes, *J. Neurotrauma* (1995), **12**: 325–344

[42] Ellis, E.F., Willoughby, K.A., Spark, S.A., and Chen, T., S100b protein is released from rat neonatal neurons, astrocytes, and microglia by in vitro trauma and anti-s100 increases trauma-induced delayed neuronal injury and negates the protective effect of exogenous s100b on neurons, *J. Neurochem.* (2007), **101**: 1463–1470

[43] Delius, M., Medical applications and bioeffects of extracorporeal shock wave, *Shock Waves* (1994), **4**: 55–72

[44] van Leeuwen, M.T., Zwerver, J., and van der Akker-Scheek, I., Extracorporeal shockwave therapy for patellar tendinopathy: a review of the literature, *Br. J. Sports Med.* (2009), **43**: 163–168

[45] Schelling, G., Delius, M., Gschwender, M., Grafe, P., and Gambhiler, S., Extracorporeal shock wave stimulate frog sciatic nerves indirectly via a cavitation-mediated mechanism, *Biophys. J.* (1994), **66**: 133–140

[46] Ogden, J.A., Alvarez, R.G., Levitt, R., and Marlow, M., Shock wave therapy (orthotripsy) in musculoskeletal disorders, *Clin. Orthop. Relat. Res.* (2001), **387**: 22–40

[47] Tamma, R., dell'Endice, S., Notarnicola, A., Moretti, L., Patella, S., Patella, V., Zallone, A., and Moretti, B., Extracorporeal shock waves stimulate osteoblast activities, *Ultrasound Med. Biol.* (2009), **35**: 2093–2100

[48] Delius, M., Ueberle, F., and Gambhiler, S., Acoustic energy determines haemoglobin release from erythrocytes by extracorporeal shock waves in vitro, *Ultrasound Med. Biol.* (1995), **21**: 707–710

[49] Wang, F.S., Yang, K.D., Chen, R.F., Wang, C.J., and Sheen-Chen, S.M., Extracorporeal shock wave promotes growth and differentiation of bone-marrow stromal cells towards osteoprogenitors associated with induction of tgf-β1, *J. Bone Joint. Surg. Am.* (2002), **84-B**: 457–461

[50] Delius, M., Twenty years of shock wave research at the institute for surgical research, *Eur. Surg. Res.* (2002), **34**: 30–36

[51] Br*ü*mmer, F., Br*ä*uner, T., H*ü*lser, D.F., and Wieland, W., Biological effects of shock waves, *World J. Urol.* (1990), **8**: 224–232,

[52] Steinbach, P., Hofst*ä*dter, F., Nicolai, H., R*ö*ssler, W., and Wieland, W., In vitro investigations on cellular damage induced by high energy shock waves, *Ultrasound Med. Biol.* (1992), **18**: 691–699

[53] Kodama, T., Hamblin, M.R., and Doukas, A.G., Cytoplasmatic molecular delivery with shock waves: importance of impulse, *Biophys. J.* (2000), **79**: 1821–1832

[54] Howard, D. and Sturtevant, B., In vitro study of the mechanical effects of shock-wave lithotripsy, *Ultrasound Med. Biol.* (1997), **23**: 1107–1122

[55] Ganzenm*ü*ller, G.C., Hiermaier, S., and Steinhauser, M.O., Shock-wave induced damage in lipid bilayers: a dissipative particle dynamics simulation study, *Soft Matter* (2011), **7**: 4307–4317

[56] Doukas, A.G. and Flotte, T.J., Physical characteristics and biological effects of laser-induced stress waves, *Ultrasound Med. Bio.* (1996), **22**: 151–164

[57] Sondén, A., Svensson, B., Roman, N., Östmark, H., Brismar, B., Palmblad, J., and Kjellström, B.T., Laser-induced shock wave endothelial cell injury, *Lasers. Surg. Med.* (2000), **26**: 364–375

[58] Panzer, M.B., Matthews, K.A., Yu, A.W., Morrison III, B., Meaney, D.F., and Bass, C.R., A multiscale approach to blast neurotrauma modeling: part i – development of novel test devices for in vivo and invitroblast injury models, *Front Neurol.* (2012), **3**: 1–11

[59] Arun, P., Spadaro, J., John, J., Gharavi, R.B., Bentley, T.B., and Nambiar, M.P., Studies on blast traumatic brain injury using *in vitro* model with shock tube, *Neuroreport* (2011), **22**: 379–384

[60] Effgen, G.B., Hue, C.D., Vogel III, E., Panzer, M.B., Meaney, D.F., Matthews, K.A., Bass, C.R., and Morrison III, B., A multiscale approach to blast neurotrauma modeling: part ii: methodology for inducing blast injury to in vitro models, *Front Neurol.* (2012), **3**: 1–10

[61] Arun, P., Abu-Taleb, R., Valiyaveettil, M., Wang, Y., Long, J.B., and Nambiar, M.P., Transient changes in neuronal cell membrane permeability after blast exposure, *NeuroReport* (2012), **23**: 342–346

[62] Leung, L.Y., VandeVord, P.J., Leonardi Dal Cengio, A., Bir, C., Yang, K.H., and King, A.I., Blast Related Neurotrauma: A review of Cellular Injury, *Mol. Cell. Bio.* (2008), **5**: 155–168

[63] Nienaber, M., Lee, J.S., Feng, R., and Lim, J.Y., Impulsive pressurization of neuronal cells for traumatic brain injury study, *J O V E* (2011), **56**: e2723 1–4

[64] Saraf, H., Ramesh, K.T., Lennon, A.M., and Merkle, A.C., Measurement of the dynamic bulk resposnse and shear response of soft human tissues, *Exp. Mech.* (2007), **47**: 439–449

[65] Shergold, O., Fleck, N., and Radford, D., The uniaxial stress versus strain response of pig skin and silicone rubber at low and high strain rates, *Int. J. Imp. Eng.* (2006), **32**: 1384–1402

[66] Song, B., Chen, W., Ge, Y., and Weerasooriya, T., Dynamic and quasi-static response of porcine muscle, *J. Biomech.* (2007), **40**: 2999–3005

[67] Tanabe, Y. and Kobayashi, K., Anysotropy in the dynamic non-linear viscoelastic properties of bovine compact bone, *J. Mater. Sci. Mater. Med.* (1994), **5**: 397–401

[68] Shazly, M., Kayacan, R., Prakash, V., and Davy, D., Failure of equine compact bone under impact loading, in *ICF XI - 11th International Conference on Fracture* (2005)

[69] Pilcher, A., Wang, X., Kaltz, Z., Garrison, J.G., Niebur, G.L., Song, B., Cheng, M., and Chen, W., High strain rate testing of bovine trabecular bone, *J. Biomech. Eng.* (2010), **132**: 081012:1–7

[70] Pervin, F. and Chen, W.W., Dynamic mechanical response of bovine gray matter and white matter brain tissue under compression, *J. Mater. Sci. Mater. Med.* (1994), **5**: 397–401

[71] Rubin, R. and Strayer, D.S., *Rubin's pathology. Clinicopathologic foundations of medicine*, pp. 1–46, Lippincot William & Wilkins (2008)

[72] Trump, B.F. and Berezesky, I.K., Calcium-mediated cell injury and cell death, *FASEB J.* (1995), **9**: 219–228

[73] Cobb, J.P., Hotchkiss, R.S., Karl, I.E., and Buchman, T.G., Mechanisms of cell injury and death, *Br. J. Anaesth.* (1996), **77**: 3–10

[74] Trump, B.F., Berezesky, I.K., Sato, T., Laiho, K.U., Phelps, P.C., and DeClaris, N., Cell calcium, cell injury and cell death, *Environmental Health Perspectives* (1984), **57**: 281–287

[75] Alberts, B., Bray, D., Hopkin, K., Johnson, A., Lewis, J., Raff, M., Roberts, K., and Walter, P., *Essential Cell Biology*, Garland Science (2010)

[76] Potten, C. and Wilson, J., *Apoptosis. The life and death of cells*, chap. 2, pp. 20–38, Cambridge University Press (2004)

[77] Hopkinson, B., A method of measuring the pressure produced in the detonation of high explosives or by the impact of bullets, *Phil. Trans. R. Soc. A* (1914), **213**: 437–456

[78] Kolsky, H., An investigation of the mechanical properties of materials at very high rates of loading, *Proc. Phys. Soc. B* (1949), **62**: 676–700

[79] Gray III, G.T., *ASM Handbook*, chap. Classic split-Hoplinson pressure bar testing, pp. 462–476, ASM Int (2000)

[80] Gray III, G.T., High-strain-rate testing of materials: The split hopkinson pressure bar, in *Characterization of Materials* (Edited by E.N. Kaufmann), chap. 2 (2012)

[81] Gama, B.A., Lopatnikov, S.L., and Gillespie Jr, J.W., Hopkinson bar experimental techinique: a critical review, *Appl. Mech. Rev.* (2004), **57**: 223–250

[82] Chen, W. and Ravichandran, G., Dynamic compressive behaviour of ceramics under lateral confinement, *J. Phys. IV France* (1994), **4**: C8 177–182

[83] Bragov, A.M., Lomunov, A.K., Sergeichev, I.V., tsembelis, K., and Proud, W.G., Determination of physicomechanical properties of soft soil from medium to high strain rates, *Int. J. Impact. Eng.* (2008), **35**: 967–976

[84] Ramesh, K.T., *High strain rate and impact experiments*, chap. 33, pp. 1–30, Springer (2009)

[85] Meyers, M.A., *Dynamic Behaviour of Materials*, Wiley Interscience (1994)

[86] Drodge, D.R., *Mechanical properties of energetic composites*, University of Cambridge (2009)

[87] Chree, C., The equations of an isotropic elastic solid in polar and cylindrical coordinates: Their solution and application., *Transactions of the Cambridge Philisophical Society* (1889), **14**: 250–369

[88] Bancroft, D., The velocity of longitudinal waves in cylindrical bars, *Phys. Rev.* (1941), **59**: 558–593

[89] Li, W. and Lambros, J., Determination of the dynamic response of brittle composites by the use of the split hopkinson pressure bar, *Exp. Mech.* (1999), **59**: 1097–1107

[90] Gong, J.C., Malvern, L.E., and Jenkins, D.A., Dispersion investigation in the split hopkinson pressure bar, *J. Eng. Mater. Technol.* (1990), **112**: 309–314

[91] Gorham, D.A., Specimen inertia in high strain-rate compression, *J. Phys. D: Appl. Phys.* (1989), **22**: 1888–1893

[92] Kenner, V., The fluid hopkinson bar, *Exp. Mech.* (1980), **20**: 226–232

[93] A$\mathring{h}$rström, B., Lindqvist, S., Höglund, E., and Sundin, K., Modified split hopkinson pressure bar method for determination of the dilatation-pressure relationship of lubricants used in elastohydrodynamic lubrication, *Proc. Inst. Mech. Eng., Part J: J. Eng. Trib.* (2002), **216**: 63–73

[94] Ogawa, K., Dynamic behaviour of viscous fluid at high rate of shear using through bar method, *J. Phys. IV France* (2003), **110**: 435–440

[95] Lim, A.S., Lopatnikov, S.L., and Gillespie Jr., J.W., Development of the split-hopkinson pressure bar technique for viscous fluid characterization, *Polymer Testing* (2009), **28**: 891–900

[96] Ritenour, A.E., Dorlac, W.C., Fang, R., Woods, T., Jenkins, D.H., Flaherty, S.F., Wade, C.E., and Holcomb, J.B., Complications after fasciotomy revision and delayed compartment release in combat patients, *The Journal of Trauma Injury, Infection, and Critical Care* (2007), **64**: S153–S162

[97] Forsberg, J.A., Pepek, J.M., Wagner, S., Wilson, K., Flint, J., and Andersen, R.C., Heterotopic ossification in high-energy wartime extremity injuries: prevalence and risk factors, *J. Bone. Joint Surg. Am.* (2008), **91**: 31–38

[98] Brown, D., Kogan, S., Lagasses, E., Weissmans, I., Alcalay, M., Pelicci, P.G., Atwater, S., and Bishop, J.M., A pmlrarα transgene initiates murine acute promyelocytic leukemia, *Proc. Natl. Acad. Sci. USA* (1997), **94**: 2551–2556

[99] Badami, C.D., Livingston, D.H., Sifri, Z.C., Caputo, F.J., Bonilla, L., Mohr, A.M., and Deitch, E.A., Hematopoietic progenitor cells mobilize to the site of injury after trauma and hemorrhagic shock in rats, *The Journal of Trauma Injury, Infection, and Critical Care* (2007), **63**: 596–602

[100] Uccelli, A., Moretta, L., and Pistoia, V., Mesenchymal stem cells in health and disease, *Nat. Rev. Immunol.* (2008), **8**: 726–736

[101] Caplan, A.I. and Bruder, S.P., Mesenchymal stem cells: building blocks for molecular medicine in the 21st century, *Trends Mol. Med.* (2001), **7**: 259–264

[102] Liu, Z.J., Zhuge, Y., and Velazquez, O.C., Trafficking and differentiation of mesenchymal stem cells, *J. Cell. Biochem.* (2009), **106**: 984–991

[103] Kolf, C.M., Cho, E., and Tuan, R.S., Biology of adult mesenchymal stem cells: regulation of niche, self-renewal and differentiation, *Arthritis Research & Therapy* (2007), **9**: 1–10

[104] Baddoo, M., Hill, K., Wilkinson, R., Gaupp, D., Hughes, C., Kopen, G.C., and Phinney, D.G., Characterization of mesenchymal stem cells isolated from murine bone marrow by negative selection, *J. Cell. Biochem.* (2003), **89**: 1235–1249

[105] Chamberlain, G., Fox, J., Ashton, B., and Middleton, J., Concive review: mesenchymal stem cells: their phenotype, differentiation capacity, immunological features, and potential for homing, *Stem Cells* (2007), **25**: 2739–2749

[106] Fong, E.L.S., Chan, C.K., and Goodman, S.B., Stem cell homing in musculoskeletal injury, *Biomaterials* (2011), **32**: 395–409

[107] Li, L. and Jiang, J., Regulatory factors of mesenchymal stem cell migration into injured tissues and their signal transduction mechanisms, *Front. Med.* (2011), **5**: 33–39

[108] Sasaki, M., Abe, R., Fujita, Y., Ando, S., Inokuma, D., and Shimizu, H., Mesenchymal stem cells are recruited into wounded skin and contribute to wound repair by transdifferentiation into multiple skin cell type, *J. Immunol.* (2008), **180**: 2581–2587

[109] Davis, T.A., O'Brien, F.P., Anam, K., Grijalva, S., Potter, B.K., and Elster, E.A., Heterotopic ossification in complex orthopaedic combat wounds. quantification and characterization of osteogenic precursor cell activity in traumatized muscle, *J Bone Joint Surg Am* (2011), **93**: 1122–1132

[110] Rieseberg, M., Kasper, C., Reardon, K.F., and Scheper, T., Flow cytometry in biotechnology, *Appl. Microbiol. Biotechnol.* (2001), **56**: 350–360

[111] Baumgarth, N. and Roederer, M., Blast injury with particular reference to recent terrorist bombing incidents, *Journal of Immunological Methods* (2000), **243**: 77–97

[112] Tung, J.W., Heydari, K., Tirouvanziam, R., Sahaf, B., Parks, D.R., Herzenberg, L.A., and Herzenberg, L.A., Modern flow cytometry: A practical approach, *Clinics in Laboratory Medicine* (2007), **27**: 453–v

[113] Huang, Z., Nelson, E.R., Smith, R.L., and Goodman, S.B., The sequential expression profiles of growth factors from osteroprogenitors to osteoblasts in vitro, *Tissue Engineering* (2007), **13**: 2311–2320

[114] Scaglione, S., Wendt, D., Miggino, S., Papadimitropoulos, A., Fato, M., Quarto, R., and Martin, I., Effects of fluid flow and calcium phosphate coating on human bone marrow stromal cells cultured in a defined 2d model system, *Journal of Biomedical Materials Research Part A* (2008), **86**: 411–419

[115] Maul, T.M., Chew, D.W., Nieponice, A., and Vorp, D.A., Mechanical stimuli differentially control stem cell behavior: morphology, proliferation, and differentiation, *Biomechanics and Modelling in Mechanobiology* (2011), **10**: 939–953

[116] Meng, E., Guo, Z., Wang, H., Jin, J., Wang, J., Wang, H., Wu, C., and Wang, L., High mobility group box 1 protein inhibits the proliferation of human mesenchymal stem cells and promotes their migration and differentiation along osteoblastic pathway, *Stem Cells and Development* (2008), **17**: 805–814

[117] Rogers, M., The shock tube: Talisman, tool or techniques?, Seattle, Washington, USA (1997) pp. 3–11

[118] Chapman, D.J., *Design of Shock Tube Facility* (2010)

[119] Gaydon, A.G. and Hurle, I.R., *The Shock Tube In High-Temperature Chemical Physics*, London: Chapman and Hall Ltd. (1963)

[120] Jagodzinski, M., Drescher, M., Zeichen, J., Hankemeier, S., Krettek, C., Bosch, U., and van Griensven, M., Effects of cyclic longitudinal mechanical strain and dexamethasone on osteogenic differentiation of human bone marrow cells, *European Cells and Materials* (2004), **7**: 35–41

[121] Silver, F.H., Siperko, L.M., and Seehra, G.P., Mechanobiology of force transduction in dermal tissue, *Skin Research and Technology* (2003), **9**: 3–23

[122] Silver, F.H., Freeman, J.W., and DeVore, D., Viscoelastic properties of human skin and processed dermis, *Skin Research and Technology* (2001), **7**: 18–23

[123] Hussain, S.H., Kinthongkul, B., and Humphreys, T.R., The biomechanical properties of the skin, *Dermatol. Surg.* (2013), **39**: 193–203

[124] Manschot, J.F.M. and Brakkee, J.M., The measurement and modelling of the mechanical properties of human skin, *J. Biomech.* (1985), **19**: 511–515

[125] Flynn, C., Taberner, A., and Nielsen, P., Mechanical characterisation of in vivo human skin using a 3D force-sensitive micro-robot and finite element analysis, *Biomech. Model. Mechanobio.* (2011), **10**: 27–38

[126] Diridollou, S., Patat, F., Gens, F., Vaillant, L., Black, D., Lagarde, J.M., Gall, Y., and Berson, M., In vivo model of the mechanical properties of the human skin under suction, *Skin Research and Technology* (2000), **6**: 214–221

[127] Piérard, G.E., Piérard, S., Delvenne, P., and Piérard-Franchimont, C., *In vivo* evaluation of the skin tensile strength by the suction method: pilot study coping with hysteresis and creep extension, *ISRN Dermatology* (2013), **2013**: 841217–841223

[128] Batisse, D., Bazin, R., Baldeweck, T., Querleux, B., and Lévêque, J.L., Influence of age on the wrinkling capacities of skin, *Skin Research and Technology* (2002), **8**: 148–54

[129] Delalleau, A., Josse, G., Lagarde, J.M., Zahouani, H., and Bergheau, J.M., Characterization of the mechanical properties of skin by inverse analysis combined with the indentation test, *J. Biomech.* (2006), **39**: 1603–1610

[130] Pailler-Mattei, C., Bec, S., and Zahouani, H., *In vivo* measurements of the elastic mechanical properties of human skin by indentation tests, *Med. Eng. & Phys.* (2008), **30**: 599–606

[131] Oxlund, H., Manschott, J., and Vildik, A., The role of elastin in the mechanical properties of skin, *J. Biomech.* (1988), **21**: 213–218

[132] Dunn, M.G. and Silver, F.H., Viscoelastic behavior of human connective tissues: relative contribution of viscous and elastic components, *Connective Tissue Research* (1983), **12**: 59–70

[133] Lim, J., Hong, J., Chen, W.W., and Weerasooriya, T., Mechanical response of pig skin under dynamic tensile loading, *Int. J. Imp. Eng.* (2011), **38**: 130–135

[134] Zhou, B., Xu, F., Chen, C.Q., and Lu, T.J., Strain rate sensitivity of skin tissue under thermomechanical loading, *Philos. Trans. A Math. Phys. Eng. Sci.* (2010), **368**: 679–690

[135] Wang, Y., Marshall, K.L., Baba, Y., Gerling, G.J., and Lumpkin, E.a., Hyperelastic material properties of mouse skin under compression, *PloS one* (2013), **8**: e67439

[136] Ralis, Freezing of orthopaedic specimens before mechanical testing, *J. Bone Joint Surg. Am.* (1989), **71**: 55–57

[137] Zhang, J., Yoganandan, N., Pintar, F.a., Guan, Y., Shender, B., Paskoff, G., and Laud, P., Effects of tissue preservation temperature on high strain-rate material properties of brain, *J. Biomech.* (2011), **44**: 391–396

[138] Annaidh, A.N., Ottenio, M., Bruyère, K., Destrade, M., Gilchrist, M.D., and Cédex, B., Mechanical Properties of Excised Human Skin, in *6th World Congress of Biomechanics IFMBE Proceedings*, Singapore (2010) pp. 1000,1003

[139] Xu, F., Lu, T.J., and Seffen, K.A., Compressive behavior of skin tissue, *J. Mech. Med. Bio.* (2009), **9**: 81–104

[140] Wilhelmy, B.J., Blackwell, S.J., and Phillips, L.G., Langer's lines: to use or not to use, *Plastic and Reconstructive Surgery* (1999), **104**: 208–214

[141] Vogel, H.G., Correlation between tensile strength and collagen content in rat skin. effect of age and cortisol treatment, *Connective Tissue Research* (1974), **2**: 177–182

[142] Edwards, C. and Marks, R., Evaluation of biomechanical properties of human skin, *Clinics in dermatology* (1995), **13**: 375–80

[143] Minns, R.J., Soden, P.D., and Jackson, D.S., The role of the fibrous components and ground substance in the mechanical properties of biological tissues: a preliminary investigation, *J. Biomech.* (1973), **6**: 153–65

[144] Zhang, X., Kinnick, R.R., Pittelkow, M.R., and Greenleaf, J.F., Skin viscoelasticity with surface wave method, in *2008 IEEE Ultrasonics Symposium*, Ieee (2008) pp. 651–653

[145] Saraf, H., Ramesh, K.T., Lennon, A.M., Merkle, A.C., and Roberts, J.C., Mechanical properties of soft human tissues under dynamic loading, *J. Biomech.* (2007), **40**: 1960–1967

[146] Ogden, R.W., Saccomandi, G., and Sgura, I., Fitting hyperelastic models to experimental data, *Computational Mechanics* (2004), **34**: 484–502

[147] Korhonen, R.K. and Saarakkala, S., *Theoretical Biomechanics*, chap. Biomechanics and Modeling of Skeletal Soft Tissues, pp. 113–132, InTech (2011)

[148] Jamison, C.E., Marangoni, R.D., and Glaser, A.A., Viscoelastic properties of soft tissue by discrete model characterisation, *J. Biomech.* (1968), **1**: 33–46

[149] Khatyr, F., Imberdis, C., Vescovo, P., Varchon, D., and Lagarde, J.m., Model of the viscoelastic behaviour of skin in vivo and study of anisotropy, *Skin Research and Technology* (2004), **10**: 96–103

[150] Holt, B., Tripathi, A., and Morgan, J., Viscoelastic response of human skin to low magnitude physiologically relevant shear, *J. Biomech.* (2008), **41**: 2689–2695

Appendix

- Matlab code of Calibration GUI:

```
function varargout = CalibrationGui(varargin)
% CALIBRATIONGUI MATLAB code for CalibrationGui.fig
% Begin initialization code - DO NOT EDIT
gui_Singleton = 1;
gui_State = struct('gui_Name',       mfilename, ...
                   'gui_Singleton',  gui_Singleton, ...
                   'gui_OpeningFcn', @CalibrationGui_OpeningFcn, ...
                   'gui_OutputFcn',  @CalibrationGui_OutputFcn, ...
                   'gui_LayoutFcn',  [] , ...
                   'gui_Callback',   []);
if nargin && ischar(varargin{1})
    gui_State.gui_Callback = str2func(varargin{1});
end

if nargout
    [varargout{1:nargout}] = gui_mainfcn(gui_State, varargin{:});
else
    gui_mainfcn(gui_State, varargin{:});
end
% End initialization code - DO NOT EDIT

% --- Executes just before CalibrationGui is made visible.
function CalibrationGui_OpeningFcn(hObject, eventdata, handles, varargin)
handles.output = hObject;

% Update handles structure
guidata(hObject, handles);

% --- Outputs from this function are returned to the command line.
function varargout = CalibrationGui_OutputFcn(hObject, eventdata, handles)

varargout{1} = handles.output;

function mass_Callback(hObject, eventdata, handles)

% --- Executes during object creation, after setting all properties.
function mass_CreateFcn(hObject, eventdata, handles)
if ispc && isequal(get(hObject,'BackgroundColor'),
get(0,'defaultUicontrolBackgroundColor'))
    set(hObject,'BackgroundColor','white');
end

function impedance_Callback(hObject, eventdata, handles)

% --- Executes during object creation, after setting all properties.
function impedance_CreateFcn(hObject, eventdata, handles)
```

```
if ispc && isequal(get(hObject,'BackgroundColor'),
get(0,'defaultUicontrolBackgroundColor'))
    set(hObject,'BackgroundColor','white');
end

function diameter_Callback(hObject, eventdata, handles)

% --- Executes during object creation, after setting all properties.
function diameter_CreateFcn(hObject, eventdata, handles)

if ispc && isequal(get(hObject,'BackgroundColor'),
get(0,'defaultUicontrolBackgroundColor'))
    set(hObject,'BackgroundColor','white');
end

function edit4_Callback(hObject, eventdata, handles)

% --- Executes during object creation, after setting all properties.
function edit4_CreateFcn(hObject, eventdata, handles)

if ispc && isequal(get(hObject,'BackgroundColor'),
get(0,'defaultUicontrolBackgroundColor'))
    set(hObject,'BackgroundColor','white');
end

function distancelasers_Callback(hObject, eventdata, handles)

% --- Executes during object creation, after setting all properties.
function distancelasers_CreateFcn(hObject, eventdata, handles)

if ispc && isequal(get(hObject,'BackgroundColor'),
get(0,'defaultUicontrolBackgroundColor'))
    set(hObject,'BackgroundColor','white');
end

function timelasers_Callback(hObject, eventdata, handles)

% --- Executes during object creation, after setting all properties.
function timelasers_CreateFcn(hObject, eventdata, handles)

if ispc && isequal(get(hObject,'BackgroundColor'),
get(0,'defaultUicontrolBackgroundColor'))
    set(hObject,'BackgroundColor','white');
end

function firingpressure_Callback(hObject, eventdata, handles)

% --- Executes during object creation, after setting all properties.
function firingpressure_CreateFcn(hObject, eventdata, handles)

if ispc && isequal(get(hObject,'BackgroundColor'),
get(0,'defaultUicontrolBackgroundColor'))
    set(hObject,'BackgroundColor','white');
end

function Fbar_Callback(hObject, eventdata, handles)
```

```
% --- Executes during object creation, after setting all properties.
function Fbar_CreateFcn(hObject, eventdata, handles)

if ispc && isequal(get(hObject,'BackgroundColor'),
get(0,'defaultUicontrolBackgroundColor'))
    set(hObject,'BackgroundColor','white');
end

function FbarV_Callback(hObject, eventdata, handles)

% --- Executes during object creation, after setting all properties.
function FbarV_CreateFcn(hObject, eventdata, handles)

if ispc && isequal(get(hObject,'BackgroundColor'),
get(0,'defaultUicontrolBackgroundColor'))
    set(hObject,'BackgroundColor','white');
end

function data_table_CellSelectionCallback(hObject, eventdata, handles)

% --- Executes on button press in pushbutton1.
function pushbutton1_Callback(hObject, eventdata, handles)

fileName = uigetfile('*.*');
set(handles.filename, 'string', fileName)
filename_Callback(hObject, eventdata, handles)
data = xlsread(fileName);
axes(handles.axes1)
t = data(18:length(data),1);
ch1 = data(18:length(data),3);
plot(t,ch1);
xlim([0.5*10^(-4) 2*10^(-4)]);
xlabel('Time (s)');
ylabel('Voltage (V)');
grid on;

function filename_Callback(hObject, eventdata, handles)

% --- Executes during object creation, after setting all properties.
function filename_CreateFcn(hObject, eventdata, handles)

if ispc && isequal(get(hObject,'BackgroundColor'),
get(0,'defaultUicontrolBackgroundColor'))
    set(hObject,'BackgroundColor','white');
end

% --- Executes on button press in calcforce.
function calcforce_Callback(hObject, eventdata, handles)
mass = get(handles.mass, 'string');
diameter = get(handles.diameter, 'string');
impedance = get(handles.impedance, 'string');
intV = get(handles.intV, 'string');
avgV = get(handles.avgV, 'string');
distance = get(handles.distancelasers, 'string');
time = get(handles.timelasers, 'string');


mass = str2num(mass);
diameter = str2num(diameter);
```

```
impedance = str2num(impedance);
intV = str2num(intV);
avgV = str2num(avgV);
impact_v = get(handles.velocity, 'string');
impact_v = str2num(impact_v);
distance = str2num(distance);
time = str2num(time);

area = (diameter/2)^2*pi()*10^(-6);

if time ~=0
    impact_v = distance/time;
    set(handles.velocity, 'string', impact_v);
end

if (intV ~=0 && avgV ~=0)
    Fbar = (2*mass*impact_v)/((intV/avgV)+((2*mass)/(area*impedance)));
    Fbarstring = num2str(Fbar,'%f');
    set(handles.Fbar, 'string', Fbarstring)
end

% --- Executes on button press in integration.
function integration_Callback(hObject, eventdata, handles)

axes(handles.axes1)

%Cursor to select limit of integration

x1 = ginput(1);
x2 = ginput(1);

filename = get(handles.filename, 'string');
data = xlsread(filename);
t = data(18:length(data),1);
ch1 = data(18:length(data),3);

%Find the indexes correspondent to the selection
i=1;
while t(i) < x1(1)
    i = i + 1;
end
j=i;
while t(j) < x2(1)
    j = j+1;
end

hold on
lh1 = line([t(i) t(i)],[0 max(ch1)], 'Color', [1 0 0]);
lh2 = line([t(j) t(j)],[0 max(ch1)], 'Color', [1 0 0]);

%define handles for limits of integration
handles.lh1 = lh1;
handles.lh2 = lh2;

intV= trapz(t(i:j),ch1(i:j));
intV = num2str(intV);

set(handles.intV, 'string', intV);
guidata(hObject,handles)
```

```
% --- Executes on button press in AverageV.
function AverageV_Callback(hObject, eventdata, handles)
axes(handles.axes1)

%Cursor to select limit of integration
x1 = ginput(1);
x2 = ginput(1);

filename = get(handles.filename, 'string');
data = xlsread(filename);
t = data(18:length(data),1);
ch1 = data(18:length(data),3);

%Find the indexes correspondent to the selection
i=1;
while t(i) < x1
    i = i + 1;
end
j=i;
while t(j) < x2
    j = j+1;
end

hold on
la1 = line([t(i) t(i)],[0 max(ch1)], 'Color', [1 1 0]);
la2 = line([t(j) t(j)],[0 max(ch1)], 'Color', [1 1 0]);

handles.la1 = la1;
handles.la2 = la2;

avgV= mean(ch1(i:j));
avgV = num2str(avgV);

set(handles.avgV, 'string', avgV);
hold off
guidata(hObject,handles)

function intV_Callback(hObject, eventdata, handles)

% --- Executes during object creation, after setting all properties.
function intV_CreateFcn(hObject, eventdata, handles)

if ispc && isequal(get(hObject,'BackgroundColor'),
get(0,'defaultUicontrolBackgroundColor'))
    set(hObject,'BackgroundColor','white');
end

function avgV_Callback(hObject, eventdata, handles)

% --- Executes during object creation, after setting all properties.
function avgV_CreateFcn(hObject, eventdata, handles)

if ispc && isequal(get(hObject,'BackgroundColor'),
get(0,'defaultUicontrolBackgroundColor'))
    set(hObject,'BackgroundColor','white');
end
```

```
% --- Executes when entered data in editable cell(s) in tabledata.
function tabledata_CellEditCallback(hObject, eventdata, handles)

% --- Executes on button press in loadtable.
function loadtable_Callback(hObject, eventdata, handles)
% hObject    handle to loadtable (see GCBO)
% eventdata  reserved - to be defined in a future version of MATLAB
% handles    structure with handles and user data (see GUIDATA)
data = get(handles.tabledata , 'data')
k = 1;
while (data(k,1) ~= 0)
    k = k +1;
end

Fbar = get(handles.Fbar, 'string');
avgV = get(handles.avgV, 'string');
firingp = get(handles.firingpressure, 'string');
impactv = get(handles.velocity, 'string');

Fbar = str2num(Fbar);
avgV = str2num(avgV);
firingp = str2num(firingp);
impactv = str2num(impactv);
vector = [firingp impactv Fbar avgV];
data(k,:) = vector;
set(handles.tabledata, 'data', data);

function velocity_Callback(hObject, eventdata, handles)

% --- Executes during object creation, after setting all properties.
function velocity_CreateFcn(hObject, eventdata, handles)

if ispc && isequal(get(hObject,'BackgroundColor'),
get(0,'defaultUicontrolBackgroundColor'))
    set(hObject,'BackgroundColor','white');
end

function kvalue_Callback(hObject, eventdata, handles)

% --- Executes during object creation, after setting all properties.
function kvalue_CreateFcn(hObject, eventdata, handles)
if ispc && isequal(get(hObject,'BackgroundColor'),
get(0,'defaultUicontrolBackgroundColor'))
    set(hObject,'BackgroundColor','white');
end

function bvalue_Callback(hObject, eventdata, handles)

% --- Executes during object creation, after setting all properties.
function bvalue_CreateFcn(hObject, eventdata, handles)

if ispc && isequal(get(hObject,'BackgroundColor'),
get(0,'defaultUicontrolBackgroundColor'))
    set(hObject,'BackgroundColor','white');
end

% --- Executes on button press in cleartable.
function cleartable_Callback(hObject, eventdata, handles)
data = zeros(10,4);
```

```
set(handles.tabledata, 'data', data);

% --- Executes on button press in caclkb.
function caclkb_Callback(hObject, eventdata, handles)

data = get(handles.tabledata , 'data');
k = 1;
while (data(k,1) ~= 0)
    k = k +1;
end

for jj = 1:(k-1)
    F_V(jj) = data(jj,3)/data(jj,4);
    V(jj) = data(jj,4);
    FiringP(jj) = data(jj,1);
    ImpactV(jj) = data(jj,2);
end
axes(handles.axes2)
hold off
plot(V,F_V,'*');
V = V';
F_V = F_V';

[fitobject,G] = fit(V,F_V,'poly1');
hold on
plot (fitobject);
xlabel('Voltage (V)');
ylabel('Force/Voltage (N/V)');
legend('Data', 'Linear Fit','Location','NorthWest');
p1 = fitobject.p1;
p2 = fitobject.p2;

k = num2str(p2);
b = num2str(p1/p2);

set(handles.kvalue, 'string', k);
set(handles.bvalue, 'string', b);

axes(handles.axes3)
hold off
plot(FiringP,ImpactV,'*');

FiringP = FiringP';
ImpactV = ImpactV';
[fitobj2,GG] = fit(FiringP,ImpactV,'poly2');
hold on
plot(fitobj2);
xlabel('Firing Pressure (bar)');
ylabel('Impact Velocity (m/s)');
legend('Data','Polynomial Fit');
xlim([0 1]);
ylim([0 15]);

% --- Executes on button press in savedata.
function savedata_Callback(hObject, eventdata, handles)
% Get calibration parameters k and b  values
k = str2double(get(handles.kvalue,'string'));
b = str2double(get(handles.bvalue,'string'));
```

```
%Get data from table
data = get(handles.tabledata , 'data');
kk = 1;
while (data(kk,1) ~= 0)
    kk = kk +1;
end

%Place the table data in correct formatting
for jj = 1:(kk-1)
    F_V(jj) = data(jj,3)/data(jj,4);
    V(jj) = data(jj,4);
    FiringP(jj) = data(jj,1);
    ImpactV(jj) = data(jj,2);
end

calib_data = [k;b];
FiringP = FiringP';
ImpactV = ImpactV';
F_V = F_V';
V = V';
vel_data = [FiringP;ImpactV];

%Save data to .txt file in specified directory
file_name = handles.filename;
folder_name = uigetdir();
file_path = strcat(folder_name,file_name);
fileID = fopen(file_path,'w');
fprintf(fileID,'%6s %9s\r\n','k','b');
fprintf(fileID,'%6.4f %6.4f\r\n',calib_data);
fprintf(fileID,'%23s %23s %23s %23s\r\n','Firing Pressure (bar)','Impact
Velocity (m/s)','Force/Voltage(N/V)','Average Volatege (V)');
for i=1:length(FiringP)
    fprintf(fileID,'%20.4f %20.4f %23.4f
%23.4f\r\n',FiringP(i),ImpactV(i),F_V(i),V(i));
end
fclose(fileID);


scrsz = get(0,'ScreenSize');
%figure1 = figure('visible','on');
figure1 = figure(1);

figure1_name = '\Calibration_fit';
figure1_path = strcat(folder_name,figure1_name);

set(figure1,'Position',[scrsz(1) scrsz(2) scrsz(3)/1.6 scrsz(4)/2.3])


set(gcf,'paperpositionmode','auto');
newhandle = copyobj(handles.axes2,figure1);
f1 = figure1;
legend('Data','Linear Fit','Location','NorthWest');
%legend('Incident','Reflected','Transmitted');
print(f1,'-dbmp',figure1_path);
close(figure1); % clean up by closing it

figure2 = figure(2);
figure2_name = '\Velocity_fit';
figure2_path = strcat(folder_name,figure2_name);
```

```
set(figure2,'Position',[scrsz(1) scrsz(2) scrsz(3)/1.165 scrsz(4)/3])
set(gcf,'paperpositionmode','auto');

newhandle2 = copyobj(handles.axes3,figure2);
f2 = figure2;

%legend('Data','Location','NorthWest');
print( f2,'-dbmp',figure2_path);
close(figure2);

% --- Executes on button press in clearlastentry.
function clearlastentry_Callback(hObject, eventdata, handles)
data = get(handles.tabledata , 'data')
k = 1;
while (data(k,1) ~= 0)
    k = k +1;
end
zero = [0 0 0 0];
data(k-1,:) = zero;

set(handles.tabledata,'data',data);

% --- Executes on button press in resetlimits.
function resetlimits_Callback(hObject, eventdata, handles)
lh1 = handles.lh1;
lh2 = handles.lh2;

la1 = handles.la1;
la2 = handles.la2;

delete(lh1);
delete(lh2);
delete(la1);
delete(la2);

% --- Executes on selection change in popupmenu2.
function popupmenu2_Callback(hObject, eventdata, handles)

str = get(hObject,'String');
val = get(hObject,'Value');
switch str{val};
    case 'Input' % User selects Raw Data figure.
        file_name = '\inputbar_calib_data.txt';
        handles.filename = file_name;

    case 'Output'
        file_name = '\outputbar_calib_data.txt';
         handles.filename = file_name;
end
guidata(hObject,handles)

% --- Executes during object creation, after setting all properties.
function popupmenu2_CreateFcn(hObject, eventdata, handles)

if ispc && isequal(get(hObject,'BackgroundColor'),
get(0,'defaultUicontrolBackgroundColor'))
    set(hObject,'BackgroundColor','white');
end
```

- Matlab code of Data Analysis GUI:

```
function varargout = AnalysisSHPBData(varargin)
% Begin initialization code - DO NOT EDIT
gui_Singleton = 1;
gui_State = struct('gui_Name',       mfilename, ...
                   'gui_Singleton',  gui_Singleton, ...
                   'gui_OpeningFcn', @AnalysisSHPBData_OpeningFcn, ...
                   'gui_OutputFcn',  @AnalysisSHPBData_OutputFcn, ...
                   'gui_LayoutFcn',  [] , ...
                   'gui_Callback',   []);
if nargin && ischar(varargin{1})
    gui_State.gui_Callback = str2func(varargin{1});
end

if nargout
    [varargout{1:nargout}] = gui_mainfcn(gui_State, varargin{:});
else
    gui_mainfcn(gui_State, varargin{:});
end
% End initialization code - DO NOT EDIT

% --- Executes just before AnalysisSHPBData is made visible.
function AnalysisSHPBData_OpeningFcn(hObject, eventdata, handles, varargin)

handles.output = hObject;

% Update handles structure
guidata(hObject, handles);

% --- Outputs from this function are returned to the command line.
function varargout = AnalysisSHPBData_OutputFcn(hObject, eventdata,
handles)

varargout{1} = handles.output;

function filename_Callback(hObject, eventdata, handles)

% --- Executes during object creation, after setting all properties.
function filename_CreateFcn(hObject, eventdata, handles)

if ispc && isequal(get(hObject,'BackgroundColor'),
get(0,'defaultUicontrolBackgroundColor'))
    set(hObject,'BackgroundColor','white');
end

% --- Executes on button press in setfilename.
% --- Allows to select the 'xls' file where the raw data are stored
function setfilename_Callback(hObject, eventdata, handles)

fileName = uigetfile('*.*');
set(handles.filename, 'string', fileName)
data = xlsread(fileName);
h = handles.monkey;
t = data(22:length(data),1);
ch1 = data(22:length(data),2);
ch2 = data(22:length(data),3);
```

```
hold off
axes(h);
p1 = plot(t,ch1);
hold on
p2 = plot(t,ch2);
set(p1,'color',[1 0 0]);
set(p2,'color',[0 0 1]);
xlim([-2.5*10^(-4) 14*10^(-4)]);
xlabel('Time (s)');
ylabel('Voltage (V)');
legend('Input Bar','Output Bar');
grid on;

%calculate duration of pulse as a function of the length of the projectile
bar_c = get(handles.soundspeed,'string');
bar_c = str2num(bar_c);
bar_c = 10^3*bar_c; %in mm/s

strikerlength = get(handles.strikerlength,'string');
strikerlength = str2double(strikerlength);

dT = t(8)-t(7);
t_p = (2*strikerlength/bar_c)/dT; %(microseconds)
window = round((4/3)*t_p);
N = floor(window/2);
T = window*dT;
w_0 = 2*pi()/T;
bar_D = get(handles.bardiameter,'string');
bar_R = str2num(bar_D)/2;

%Assign the vectors to a handle so that you can access them in all the
%functions in the Gui
handles.t = t;
handles.ch1 = ch1;
handles.ch2 = ch2;
handles.fileName = fileName;
handles.N = N;
handles.w_0 = w_0;
handles.bar_R = bar_R;
handles.bar_c = bar_c;
%Save the changes to the handles
guidata(hObject,handles)

% --- Executes on button press in cutwaves.
function cutwaves_Callback(hObject, eventdata, handles)

%data
t = handles.t;
ch1 = handles.ch1;
ch2 = handles.ch2;
cf = get(handles.correctionfactor,'string');
cf = str2num(cf);

%calculate duration of pulse as a function of the length of the projectile
bar_c = get(handles.soundspeed,'string');
bar_c = str2num(bar_c);
bar_c = 10^3*bar_c; %in mm/s

strikerlength = get(handles.strikerlength,'string');
strikerlength = str2double(strikerlength);
```

```
dT = t(8)-t(7);
t_p = (2*strikerlength/bar_c)/dT; %(microseconds)
window = round((4/3)*t_p)*8;

%make the axes labled as monkey the current axis
axes(handles.monkey)

%Cursor to select limit of incident wave
[x1,y1] = ginputc(1, 'Color', 'b', 'LineWidth', 1);

%Find the index correspondent to the selection of the beginnning of the
%incident wave
i=1;
while t(i) < x1(1)
    i = i + 1;
end

%define gauge distance to the sample/bar interface
delta_x1 = 250+cf; %(mm)
delta_x2 = 250; %(mm)

%calculate Tau_s time necessary to travel through the sample thickness as a
%function of sample length and sound speed
sample_c = get(handles.samplesoundspeed,'string');
sample_c = str2num(sample_c);
sample_c = sample_c*10^3;

sample_h = get(handles.sampleheight,'string');
sample_h = str2num(sample_h);

tau_s = (sample_h/sample_c)/dT;

%Define limits for each pulse (incident, reflected and transmitted
% incident wave
A1 = i;
B1 = A1 + window;

% reflected wave
A2 = A1 + round(2*(delta_x1/bar_c)/dT);
B2 = A2 + window;

% transmitted wave
A3 = A1 + round(((delta_x1 +delta_x2)/bar_c)/dT + tau_s);
B3 = A3 + window;

%calibration parameters
k_i = get(handles.k_i,'string');
b_i = get(handles.b_i,'string');
k_o = get(handles.k_o,'string');
b_o = get(handles.b_o,'string');
bar_E = get(handles.barmodulus,'string');
bar_D = get(handles.bardiameter,'string');
bar_R = str2num(bar_D)/2;
k_i = str2num(k_i);
k_o = str2num(k_o);
b_i = str2num(b_i);
b_o = str2num(b_o);
bar_E = str2num(bar_E);
```

```
bar_A = ((bar_R)^(2))*pi();

%Preallocate array
inputbar_strain = zeros(1,length(ch1));
outputbar_strain = zeros(1,length(ch1));
inputbar_stress = zeros(1,length(ch1));
outputbar_stress = zeros(1,length(ch1));

%transform voltage in strain
for ii=1:length(ch1)
   inputbar_strain(ii)=((k_i*ch1(ii))*(1+(b_i*ch1(ii))))/(bar_E*bar_A);
   outputbar_strain(ii)= ((k_o*ch2(ii))*(1+(b_o*ch2(ii))))/(bar_E*bar_A);
   inputbar_stress(ii)=((k_i*ch1(ii))*(1+(b_i*ch1(ii))))/(bar_A);
   outputbar_stress(ii)= ((k_o*ch2(ii))*(1+(b_o*ch2(ii))))/(bar_A);

end

in_strain = inputbar_strain(A1:B1);
re_strain = inputbar_strain(A2:B2)*1.05;
tr_strain = outputbar_strain(A3:B3);

wave dispersion correction
N = floor(window/2);
T = window*dT;
w_0 = 2*pi()/T;
c_0 = bar_c/1000;
delta_t = dT;

%Calculate Fourier's series parameters A0, Ak, Bk for incident, reflected
%and transmitted pulse
A0n_in = zeros(1,2*N);
A0n_re = zeros(1,2*N);
A0n_tr = zeros(1,2*N);

An_in = zeros(1,2*N);
An_re = zeros(1,2*N);
An_tr = zeros(1,2*N);

Ak_in = zeros(1,N);
Ak_re = zeros(1,N);
Ak_tr = zeros(1,N);

Bn_in = zeros(1,2*N);
Bn_re = zeros(1,2*N);
Bn_tr = zeros(1,2*N);

Bk_in = zeros(1,N);
Bk_re = zeros(1,N);
Bk_tr = zeros(1,N);

for n=1:(2*N)
A0n_in(n) = in_strain(n)*delta_t;
A0n_re(n) = re_strain(n)*delta_t;
A0n_tr(n) = tr_strain(n)*delta_t;
end
A0_in = (2/T)*sum(A0n_in);
A0_re = (2/T)*sum(A0n_re);
A0_tr = (2/T)*sum(A0n_tr);
```

```
for k=1:N
    for n=1:(2*N)
        An_in(n) = in_strain(n)*cos(k*w_0*n*delta_t)*delta_t;
        An_re(n) = re_strain(n)*cos(k*w_0*n*delta_t)*delta_t;
        An_tr(n) = tr_strain(n)*cos(k*w_0*n*delta_t)*delta_t;
    end
    Ak_in(k)=(2/T)*sum(An_in);
    Ak_re(k)=(2/T)*sum(An_re);
    Ak_tr(k)=(2/T)*sum(An_tr);
end

for k=1:N
    for n=1:(2*N)
        Bn_in(n) = in_strain(n)*sin(k*w_0*n*delta_t)*delta_t;
        Bn_re(n) = re_strain(n)*sin(k*w_0*n*delta_t)*delta_t;
        Bn_tr(n) = tr_strain(n)*sin(k*w_0*n*delta_t)*delta_t;
    end
    Bk_in(k)=(2/T)*sum(Bn_in);
    Bk_re(k)=(2/T)*sum(Bn_re);
    Bk_tr(k)=(2/T)*sum(Bn_tr);
end

%load values of ck
ck = handles.ck;
l_ck = length(ck);
diff_length = N-l_ck;
if diff_length ~= 0
    for gg = (l_ck+1):N
        ck(gg) = ck(l_ck);
    end
end

Pkf = zeros(1,N);
Pkb = zeros(1,N);

%calculate phase angle shift for each frequency component for forward or
%backward dispersion
for k=1:N
   Pkf(k) = k*w_0*((delta_x1*10^(-3)/ck(k)) - (delta_x1*10^(-3)/c_0));
   Pkb(k) = k*w_0*(((-delta_x1)*10^(-3)/ck(k)) - ((-delta_x1)*10^(-
3)/c_0));
end

%reconstruct the signal at the shifted position and with wave dispersion
%correction

in_strain_k = zeros(1,N);
re_strain_k = zeros(1,N);
tr_strain_k = zeros(1,N);

in_strain_disp = zeros(1,2*N);
re_strain_disp = zeros(1,2*N);
tr_strain_disp = zeros(1,2*N);

for n=1:(2*N)
    for k=1:N
        in_strain_k(k) = Ak_in(k)*cos(k*w_0*n*delta_t - Pkf(k)) +
Bk_in(k)*sin(k*w_0*n*delta_t - Pkf(k));
        re_strain_k(k) = Ak_re(k)*cos(k*w_0*n*delta_t + Pkb(k)) +
Bk_re(k)*sin(k*w_0*n*delta_t + Pkb(k));
```

```
        tr_strain_k(k) = Ak_tr(k)*cos(k*w_0*n*delta_t + Pkb(k)) +
Bk_tr(k)*sin(k*w_0*n*delta_t + Pkb(k));
    end
    in_strain_disp(n) = A0_in/2 + sum(in_strain_k);
    re_strain_disp(n) = A0_re/2 + sum(re_strain_k);
    tr_strain_disp(n) = A0_tr/2 + sum(tr_strain_k);
end

in_stress = in_strain*bar_E;
re_stress = re_strain*bar_E;
tr_stress = tr_strain*bar_E;

for o = 1:length(in_strain)
    RR(o) = (in_stress(o)+re_stress(o)-
tr_stress(o))/(in_stress(o)+re_stress(o)+tr_stress(o));
end

%Make the time start from 0
time = zeros(length(in_strain),1);
T_sampling = t(2)- t(1);

for ii=2:length(in_strain)
     time(ii)=(time(ii-1)+T_sampling);
end

time = time*10^6;
axes(handles.monkey)
hold off
xlim([0 100]);
plota=plot(time,in_strain);
hold on
plotb=plot(time,re_strain);
plotc=plot(time,tr_strain);
grid on;
set(plota,'color',[0 0 0]);
set(plotb,'color',[0 0 1]);
set(plotc,'color',[1 0 0]);
hLeg = legend('Incident','Reflected','Transmitted');
xlabel('Time (us)');
ylabel('Strain');

scrsz = get(0,'ScreenSize');
figure1 = figure('visible','on');
set(figure1,'Position',[1 scrsz(4)/3 scrsz(3)/2 scrsz(4)/2])
newhandle = copyobj(handles.monkey,figure1);
legend('Incident','Reflected','Transmitted');
saveas(figure1,'Threewaves.bmp');
close(figure1) % clean up by closing it

time = time*10^(-6);

handles.in_strain = in_strain;
handles.re_strain = re_strain;
handles.tr_strain = tr_strain;

handles.in_stress = in_stress;
handles.re_stress = re_stress;
handles.tr_stress = tr_stress;
```

```
handles.inputbar_stress = inputbar_stress;
handles.outputbar_stress = outputbar_stress;

handles.RR = RR;
handles.time = time;
% Save the change you made to the structure
guidata(hObject,handles)

% --- Executes on selection change in popupmenu1.
% --- Allows to plot the raw data or the incident, reflected and
% transmitted waves once they have been cut
function popupmenu1_Callback(hObject, eventdata, handles)

str = get(hObject,'String');
val = get(hObject,'Value');
switch str{val};
case 'Raw Data' % User selects Raw Data figure.
    hold off
    h = handles.monkey;
    t = handles.t;
    ch1 = handles.ch1;
    ch2 = handles.ch2;
    axes(h)
    p1 = plot(t,ch1);
    hold on
    p2 = plot(t,ch2);
    set(p1,'color',[1 0 0]);
    set(p2,'color',[0 0 1]);
    %xlim([-0.5*10^(-4) 4*10^(-4)]);
    xlabel('Time (s)');
    ylabel('Voltage (V)');
    legend('Input Bar','Output Bar');
    grid on;

case 'Cut Waves' % User selects Incident reflected and transmitted waves
figure.
    in_strain = handles.in_strain;
    re_strain = handles.re_strain;
    tr_strain = handles.tr_strain;
    time = handles.time;
    time = time*10^6;
    axes(handles.monkey)
    hold off
    plota=plot(time,in_strain);
    hold on
    plotb=plot(time,re_strain);
    plotc=plot(time,tr_strain);
    set(plota,'color',[0 0 0]);
    set(plotb,'color',[0 0 1]);
    set(plotc,'color',[1 0 0]);
    hLeg = legend('Incident','Reflected','Transmitted');
    xlabel('Time (us)');
    ylabel('Strain');
    grid on;

end

% --- Executes on selection change in popupmenu3.
% Select if the analysis has to be performed on samples that were able to
% deform radially (uniaxial stress) or if they were confined (uniaxial
```

```
% strain)
function popupmenu3_Callback(hObject, eventdata, handles)

str = get(hObject,'String');
val = get(hObject,'Value');
switch str{val};
case 'Unconfined' % User selects Raw Data figure.
    confined = 0;
    handles.confined = confined;
case 'Confined' % User selects Raw Data figure.
    confined = 1;
    handles.confined = confined;
end
guidata(hObject,handles)

% --- Executes during object creation, after setting all properties.
function calculate_CreateFcn(hObject, eventdata, handles)

function calculate_Callback(hObject, eventdata, handles)

% Calculate particle velocity, sample istantaneous length and area from
bars' strains
sample_h = get(handles.sampleheight,'string');
sample_h = str2num(sample_h);

sample_d = get(handles.samplediameter,'string');
sample_d = str2num(sample_d);

sample_A = ((sample_d/2)^2)*pi();

in_strain = handles.in_strain;
re_strain = handles.re_strain;
tr_strain = handles.tr_strain;
time = handles.time;

bar_c = get(handles.soundspeed,'string');
bar_c = str2num(bar_c);
bar_c = 10^3*bar_c;

bar_d = get(handles.bardiameter,'string');
bar_d = str2num(bar_d);

bar_A = ((bar_d/2)^2)*pi();

bar_E = get(handles.barmodulus,'string');
bar_E = str2num(bar_E);

bar_den = get(handles.density, 'string');
bar_den = str2num(bar_den);
%convert density to kg/mm3
bar_den = 10^(-9)*bar_den;

T_sampling = time(2)-time(1);

bar_Z = bar_den*bar_c;

deltaU(1)=0;
%calculate relative displacement deltaU of the specimen ends
```

```
for ff=1:length(re_strain);
    deltaU(ff+1)=-2*bar_c*(re_strain(ff)*T_sampling)+deltaU(ff);
    volum_strain(ff) = deltaU(ff)/sample_h;
end

%calculate particle velocity during compression
for kk=1:length(in_strain)
    v_i(kk) = (1/bar_Z)*bar_E*in_strain(kk)*10^3;
    v_r(kk) = (1/bar_Z)*bar_E*re_strain(kk)*10^3;
    v_t(kk) = (1/bar_Z)*bar_E*tr_strain(kk)*10^3;
end

%calculate velocity difference
for xx=1:length(in_strain)
    delta_v1(xx) = 2*v_r(xx);%one wave
    delta_v2(xx) = 2*(v_t(xx)-v_i(xx));%two waves
    delta_v3(xx) = (v_i(xx)+v_r(xx)+v_t(xx));%three waves
end

%calculate instantaneous length and aera
l_s1(1) = sample_h; %initial length, one wave
l_s2(1) = sample_h; %initial length, two waves
l_s3(1) = sample_h; %initial length, three waves
A_s1(1) = sample_A;
A_s2(1) = sample_A;
A_s3(1) = sample_A;
for ll=1:length(time)
    l_s1(ll+1) = l_s1(ll)+(delta_v1(ll)*T_sampling);
    A_s1(ll+1)= sample_A*sample_h/l_s1(ll);
    l_s2(ll+1) = l_s2(ll)+(delta_v2(ll)*T_sampling);
    A_s2(ll+1)= sample_A*sample_h/l_s2(ll);
    l_s3(ll+1) = l_s3(ll)+(delta_v3(ll)*T_sampling);
    A_s3(ll+1)= sample_A*sample_h/l_s3(ll);
end

%calculate sample strain rate
for dd=1:length(time)
    s_sr1(dd) = -(delta_v1(dd)/l_s1(dd));
    s_sr11(dd) = -2*bar_c*re_strain(dd)/l_s1(1);
    s_sr2(dd) = -(delta_v2(dd)/l_s2(dd));
    s_sr3(dd) = -(delta_v3(dd)/l_s3(dd));
end

%calculate sample true strain
s_truestrain1(1) = 0;
s_truestrain2(1) = 0;
s_truestrain3(1) = 0;
for ww=1:(length(time)-2)
    s_truestrain1(ww+1) = s_truestrain1(ww)+s_sr1(ww)*T_sampling;
    s_truestrain2(ww+1) = s_truestrain2(ww)+s_sr2(ww)*T_sampling;
    s_truestrain3(ww+1) = s_truestrain3(ww)+s_sr3(ww)*T_sampling;
end

%calculate sample engineering strain
for w=1:(length(time)-1)
    s_engstrain1(w) = 1 - (l_s1(w)/sample_h);
    s_engstrain2(w) = 1 - (l_s2(w)/sample_h);
    s_engstrain3(w) = 1 - (l_s3(w)/sample_h);
end
```

```
confined = handles.confined;
if confined == 0
    %Calculate sample stress when sample is free to deform radially
    for ll=1:(length(time)-1)
        sample_stress_1(ll) = (bar_A*bar_E/A_s1(ll))*tr_strain(ll);
        sample_stress_eng(ll) = (bar_A*bar_E/sample_A)*tr_strain(ll);
        sample_stress_2(ll) =
(bar_A*bar_E/A_s1(ll))*(in_strain(ll)+re_strain(ll));
        sample_stress_3(ll) =
(bar_A*bar_E/(2*A_s1(ll)))*(in_strain(ll)+re_strain(ll)+tr_strain(ll));
    end
    hold off
    axes(handles.axes2)
    plotb = plot(s_truestrain1, sample_stress_1);
    hold on
    plota = plot(s_engstrain1, sample_stress_eng);
    %plotc = plot(s_truestrain1, sample_stress_3);
    grid on
    set(plota,'color',[0 0 0]);
    set(plotb,'color',[1 0 0]);
    %set(plotc,'color',[0 0 1]);
    xlabel('Strain');
    ylabel('Stress (MPa)');
    legend('True Stress-Strain','Eng Stress Strain');

    handles.sample_stress_1 = sample_stress_1;
    handles.sample_stress_2 = sample_stress_2;
    handles.sample_stress_3 = sample_stress_3;
    handles.sample_stress_eng = sample_stress_eng;
    handles.s_engstrain1 = s_engstrain1;
    handles.s_engstrain2 = s_engstrain2;
    handles.s_engstrain3 = s_engstrain3;

    %Calculate sample stress when sample is not free to deform radially
    else if confined ==1
        for ll=1:(length(time)-1)
            sample_stress_conf(ll) = (bar_A*bar_E/sample_A)*tr_strain(ll);
            sample_stress_2(ll) =
(bar_A*bar_E/sample_A)*(in_strain(ll)+re_strain(ll));
            sample_stress_3(ll) =
(bar_A*bar_E/(2*sample_A))*(in_strain(ll)+re_strain(ll)+tr_strain(ll));
        end
        %Calculate pressure and volumetric strain data for bulk modulus
        %evaluation
        [maxstress,index] = max(sample_stress_conf);
        maxstress=num2str(maxstress);
        set(handles.maxstress,'string',maxstress);

        final_volum_strain = volum_strain(index);
        final_volum_strain = num2str(final_volum_strain);
        set(handles.volstrain,'string',final_volum_strain);

        hold off
        axes(handles.axes2)
        plota = plot(time(1:(length(time)-1)), sample_stress_conf);
        grid on
        set(plota,'color',[0 0 0]);
        xlabel('Time');
        ylabel('Pressure (MPa)');
        handles.s_volum_strain = final_volum_strain;
```

```
        handles.s_stress_conf = sample_stress_conf;
        handles.sample_stress_2 = sample_stress_2;
        handles.sample_stress_3 = sample_stress_3;
        end
end

handles.time = time;
handles.s_sr1 = s_sr1;
handles.s_truestrain1 = s_truestrain1;
handles.s_truestrain2 = s_truestrain2;
handles.s_truestrain3 = s_truestrain3;
handles.s_inst_length = l_s1;

% Save the change you made to the structure
guidata(hObject,handles)

% --- Executes on selection change in popupmenu2.
function popupmenu2_Callback(hObject, eventdata, handles)

% True Stress vs Time
% Strain Rate vs Time
% Engineering Stress vs Engineering Strain

time = handles.time;
s_sr1 = handles.s_sr1;
s_truestrain1 = handles.s_truestrain1;

confined = handles.confined;
if confined == 0
    sample_stress_1 = handles.sample_stress_1;
    sample_stress_2 = handles.sample_stress_2;
    sample_stress_3 = handles.sample_stress_3;
    s_engstrain1 = handles.s_engstrain1;
    s_engstrain2 = handles.s_engstrain2;
    s_engstrain3 = handles.s_engstrain3;

else if confined ==1
    volum_strain = handles.s_volum_strain;
    sample_stress_1 = handles.s_stress_conf;
    sample_stress_2 = handles.sample_stress_2;
    sample_stress_3 = handles.sample_stress_3;
    end
end

h = handles.axes2;

str = get(hObject,'String');
val = get(hObject,'Value');
switch str{val};
case 'True Stress vs True Strain' % User selects True Stress vs True Strain
figure.

    hold off
    axes(h)
    p1 = plot(s_truestrain1,sample_stress_1);
    set(p1,'color',[0 0 0]);
    xlabel('Trues Strain');
    ylabel('True Stress (MPa)');
    grid on;
```

```
case 'Strain Rate vs Time' % User selects Strain Rate vs Time figure.

    hold off
    axes(h)
    plota=plot(time,s_sr1);
    set(plota,'color',[0 0 0]);
    xlabel('Time (s)');
    ylabel('Strain Rate (1/s)');
    grid on;

case 'Three Waves Analysis' % User selects Strain Rate vs Time figure.

    hold off
    axes(h)
    plota=plot(time(1:(length(time)-1)),sample_stress_1);
    hold on
    plotb=plot(time(1:(length(time)-1)),sample_stress_2);
    plotc=plot(time(1:(length(time)-1)),sample_stress_3);
    set(plota,'color',[0 0 0]);
    set(plotb,'color',[1 0 0]);
    set(plotc,'color',[0 0 1]);
    xlabel('Time (s)');
    ylabel('Stress (MPa)');
    legend('1-wave','2-waves','3-waves');
    grid on;

case 'Pressure vs Time' % User selects Strain Rate vs Time figure.

    hold off
    axes(h)
    plota=plot(time(1:(length(time)-1)),sample_stress_conf);
    set(plota,'color',[0 0 0]);
    xlabel('Time (s)');
    ylabel('Pressure (MPa)');
    grid on;

 case 'Volumetric Strain vs Time' % User selects Strain Rate vs Time
figure.

    hold off
    axes(h)
    plota=plot(time,volum_strain);
    set(plota,'color',[0 0 0]);
    xlabel('Time (s)');
    ylabel('Volumetric Strain');
    grid on;

  case 'Smoothed' % User selects Smoothed Stress vs Strain figure.

    smoothnumber = handles.smoothn;
    if smoothnumber ~= 0
        sample_stress_1_smoothed = handles.sample_stress_1_smoothed;
        hold off
        axes(h)
        plota=plot(s_truestrain1,sample_stress_1_smoothed);
        set(plota,'color',[0 0 0]);
        xlabel('True Strain');
        ylabel('True Stress Smoothed (MPa)');
```

```
        grid on;

    else if smoothnumber == 0
        hold off
        axes(h)
        p1 = plot(s_truestrain1,sample_stress_1);
        set(p1,'color',[0 0 0]);
        xlabel('Trues Strain');
        ylabel('True Stress (MPa)');
        grid on;
        end
    end

end

% --- Executes on button press in savedata.
function savedata_Callback(hObject, eventdata, handles)

confined = handles.confined;
if confined == 0;

    time = handles.time';
    s_sr1 = handles.s_sr1;
    s_truestrain1 = handles.s_truestrain1;
    sample_stress_1 = handles.sample_stress_1;
    sample_stress_2 = handles.sample_stress_2;
    sample_stress_3 = handles.sample_stress_3;
    sample_stress_eng = handles.sample_stress_eng;
    sample_eng_stress = handles.sample_stress_eng;
    s_engstrain1 = handles.s_engstrain1;
    s_engstrain2 = handles.s_engstrain2;
    s_engstrain3 = handles.s_engstrain3;
    h = handles.axes2;
    l_s1 = handles.s_inst_length;

    file_name = handles.fileName;
    file_name = ['\results',file_name];
    folder_name = uigetdir();
    file_path = strcat(folder_name,file_name);

    M = [time; s_sr1];
    M = M';
    C = [s_truestrain1; s_engstrain1; sample_stress_1; sample_eng_stress;
sample_stress_2;sample_stress_3];
    C=C';


    d = {'Time (s)', 'Strain Rate', 'True Strain', 'Eng Strain', 'True
Stress', 'Eng Stress', 'Stress 2 waves', 'Stress 3 waves (MPa)', 'Sample
Length'};

  xlswrite(file_path,d,1,'A1');
    xlswrite(file_path,M,1,'A2');
    xlswrite(file_path,C,1,'C2');



elseif confined ==1
    inputbar_stress = handles.inputbar_stress;
```

```
    outputbar_stress = handles.outputbar_stress;
    in_strain = handles.in_strain;
    re_strain = handles.re_strain;
    tr_strain = handles.tr_strain;
    in_stress = handles.in_stress;
    re_stress = handles.re_stress;
    tr_stress = handles.tr_stress;
    RR = handles.RR;
    s_sr1 = handles.s_sr1;
    sample_pressure = handles.s_stress_conf;
    sample_stress_2 = handles.sample_stress_2;
    sample_stress_3 = handles.sample_stress_3;
    time = handles.time';
    %smoothnumber = handles.smoothn;
    file_name = handles.fileName;
    file_name = ['\results',file_name];
    folder_name = uigetdir();
    file_path = strcat(folder_name,file_name);

    F = [inputbar_stress(1:50:32000);outputbar_stress(1:50:32000)];
    F = F';

    C = [sample_pressure(1:50:length(sample_pressure))
;sample_stress_2(1:50:length(sample_pressure));sample_stress_3(1:50:length(
sample_pressure))];
    C = C';
    M = [time(1:50:length(sample_pressure));
s_sr1(1:50:length(sample_pressure));
in_strain(1:50:length(sample_pressure));
re_strain(1:50:length(sample_pressure));
tr_strain(1:50:length(sample_pressure));
in_stress(1:50:length(sample_pressure));
re_stress(1:50:length(sample_pressure));tr_stress(1:50:length(sample_pressu
re)); RR(1:50:length(sample_pressure))];
    M = M';
    d = {'Time (s)', 'Strain Rate', 'Incident Strain', 'Reflected Strain',
'Transmitted Strain', 'Incident Stress', 'Reflected Stress', 'Transmitted
Stress', 'R','Pressure (MPa)', 'Pressure 2-wave (MPa)','Pressure 3-
wave(MPa)','Input Bar Stress (MPa)', 'Output Bar Stress (MPa)'};

    xlswrite(file_path,d,1,'A1');
    xlswrite(file_path,M,1,'A2');
    xlswrite(file_path,C,1,'J2');
    xlswrite(file_path,F,1,'M2');

end

% --- Executes on button press in smooth.
function smooth_Callback(hObject, eventdata, handles)
% hObject    handle to smooth (see GCBO)
% eventdata  reserved - to be defined in a future version of MATLAB
% handles    structure with handles and user data (see GUIDATA)
confined = handles.confined;

    if confined == 0;
    time = handles.time';
    s_sr1 = handles.s_sr1;
    s_truestrain1 = handles.s_truestrain1;
    sample_stress_1 = handles.sample_stress_1;
    sample_stress_2 = handles.sample_stress_2;
```

```
    sample_stress_3 = handles.sample_stress_3;
    sample_stress_eng = handles.sample_stress_eng;
    sample_eng_stress = handles.sample_stress_eng;
    s_engstrain1 = handles.s_engstrain1;
    s_engstrain2 = handles.s_engstrain2;
    s_engstrain3 = handles.s_engstrain3;
    h = handles.axes2;
    l_s1 = handles.s_inst_length;

    smoothnumber = get(handles.smoothnumber1,'string');
    smoothnumber=str2num(smoothnumber);
        if smoothnumber ~= 0
            sample_stress_1_smoothed =
smooth(sample_stress_1,smoothnumber);
        end

    elseif confined ==1
    smoothnumber = get(handles.smoothnumber1,'string');
    smoothnumber=str2num(smoothnumber);
    sample_pressure = handles.s_stress_conf;
    time = handles.time';
        if smoothnumber ~= 0
            sample_stress_1_smoothed =
smooth(sample_pressure,smoothnumber);
        end
    end
handles.sample_stress_1_smoothed = sample_stress_1_smoothed;
handles.smoothn = smoothnumber;
% Save the change you made to the structure
guidata(hObject,handles)

% --- Executes on button press in ckfile.
function ckfile_Callback(hObject, eventdata, handles)

ck_fileName = uigetfile('*.*');
set(handles.ckfilename, 'string', ck_fileName)
ck_data = xlsread(ck_fileName);
ck = ck_data(:,1);

handles.ck = ck;
guidata(hObject,handles)

% --- Executes on button press in calculateCk.
function calculateCk_Callback(hObject, eventdata, handles)
% hObject    handle to calculateCk (see GCBO)
% eventdata  reserved - to be defined in a future version of MATLAB
% handles    structure with handles and user data (see GUIDATA)
bar_R = handles.bar_R;
bar_c = handles.bar_c;
bar_c = bar_c/1000;
N = handles.N;
w_0 = handles.w_0;

poissonratio = get(handles.poissonratio,'string');
poissonratio = str2num(poissonratio);

if poissonratio == 0.29
    A = 0.57594;
    B = 0.42555;
    C = 21.326;
```

```
    D = 19.224;
    E = -7.3258;
    F = 2.4713;
elseif poissonratio == 0.34
    A = 0.57594;
    B = 0.42555;
    C = 21.326;
    D = 19.224;
    E = -7.3258;
    F = 2.4713;
end

bar_R = bar_R*10^(-3);
syms z
for k=1:N
lkk(k) = solve((2*pi()*bar_c/(w_0*k))*( A + B/(C*(bar_R/z)^4 +
D*(bar_R/z)^3 - E*(bar_R/z)^2 + F*(bar_R/z)^1.5 + 1)) -
z,z,'PrincipalValue',true);
end
lk = double(lkk);
for k=1:N
ck(k) = k*w_0*lk(k)/(2*pi());
end
ck=ck';
lk=lk';

%save ck values to .xls
ck_name = get(handles.ckfilename1,'string');
folder_name = uigetdir();
file_name = ['\',ck_name];
file_path = strcat(folder_name,file_name);

d = {'ck','lambda k','N', 'w_0'};

xlswrite(file_path,d,1,'A1');
xlswrite(file_path,ck,1,'A2');
xlswrite(file_path,lk,1,'B2');
xlswrite(file_path,N,1,'C2');
xlswrite(file_path,w_0,1,'D2');



guidata(hObject,handles)
```

RE: Reproduction of image

PNAS Permissions [PNASPermissions@nas.edu]
Sent: 05 November 2013 19:17
To: Bo, Chiara

Permission is granted for your use of the figure as described in your message. Please cite the full journal references and include "Copyright (copyright year) National Academy of Sciences, U.S.A." (because this material published between 1993 and 2008, a copyright notice is needed). Let us know if you have any questions.

Best regards,
Kay McLaughlin for
Diane Sullenberger
Executive Editor
PNAS

From: Bo, Chiara [mailto:c.bo10@imperial.ac.uk]
Sent: Tuesday, November 05, 2013 11:13 AM
To: PNAS Permissions
Subject: Reproduction of image

Dear PNAS Permissions Editor ,

my name is Chiara Bo, I am a PhD Student at the Institute of Shock Physics, Imperial College London.
My contact details are:

Rm 730 Blackett Laboratory,
Imperial College London,
Prince Consort Road,
London, SW7 2AZ, United Kingdom.
Mobile +44 795 868 0102
e-mail: c.bo10@imperial.ac.uk

I would like to reproduce in my PhD thesis titled: "Investigation of the Effects of High Pressure Pulses on Biological Samples"

part of a figure from the article:

PNAS **March 18, 1997** vol. 94 no. 6**2551-2556**

titled:

A PMLRARa transgene initiates murine acute promyelocytic leukemia

written by

DIANE BROWN, SCOTT KOGAN, ERIC LAGASSE, IRVING WEISSMAN, MYRIAM ALCALAY,
PIER GIUSEPPE PELICCI, SUSAN ATWATER, AND J. MICHAEL BISHOP

in page 2554

FIG. 3. Murine APL. (a and b) Bone marrow isolates.

Thank you for your consideration.

Yours sincerely,

Chiara Bo